Stellar clustering and outflows in dwarf galaxies

Jessica May Hislop

München 2022

Stellar clustering and outflows in dwarf galaxies

Jessica May Hislop

Dissertation
der Fakultät für Physik
der Ludwig-Maximilians-Universität
München

vorgelegt von
Jessica May Hislop
aus Shoreham-by-Sea, United Kingdom

München, den 30. August, 2022

Erstgutachter: Prof. Dr. Volker Springel

Zweitgutachter: PD Dr. Klaus Dolag

Tag der mündlichen Prüfung: 21. Oktober, 2022

Contents

List of Figures

List of Tables

Zusammenfassung

Die Häufung der Sternentstehung und die draus folgende Rückkopplung hat einen bedeutenden Einfluss auf die Regulierung der Sternentstehung indem sie die Dichten und Temperaturen des umgebenden interstellaren Mediums verändert und Ausströmungen aus der Galaxie beeinflusst. Die Entwicklung von Zwerggalaxien ist wegen ihrer geringen Masse besonders von Rückkopplungseffekten abhängig und eignet sich daher gut, um den Einfluss der Sternhaufenbildung und von Rückkopplungseffekten in der Galaxienentwicklung zu verstehen.

In dieser Arbeit untersuche ich die Bildung von Sternhaufen und Ausströmungen aus der Galaxie in hochauflösenden Simulationen von isolierten Zwerggalaxien. Ich untersuche den Einfluss der Parameter der stellaren Rückkopplung und Sternentstehung, welche nicht aufgelöste Physik modellieren, um die Auswirkungen auf galaktisch gemittelte und kleinskalige Eigenschaften des interstellaren Mediums und die Sternhaufenbildung zu quantifizieren. Ich komme zu dem Ergebnis, dass die Details der Modellierung der Sternentstehung einen starken Einfluss auf die räumlichen und dynamischen Eigenschaften der gebildeten Sternhaufen haben und damit ihre zukünftige Entwicklung beeinflussen. Ich untersuche auch, wie sich die Sternhaufenbildung und die stellaren Rückkopplungen auf das umgebende interstellare Medium und die Umgebungsdichten von Supernovae auswirken, sowie die daraus resultierenden Auswirkungen auf galaktische Eigenschaften wie Sternentstehungsraten und Ausströmungen.

Die in dieser Arbeit vorgestellten Simulationen beinhalten die Effekte der Eigengravitation, Nichtgleichgewichtsheizung und -kühlung, chemische Prozesse, die Abschirmung vom zeitlich und räumlich variierenden interstellaren Strahlungsfeld sowie ein dichte- und temperaturabhängiges Sternentstehungsmodell. Mit einer minimalen baryonischen Teilchenmasse von 4 $M_\odot$ und einer räumlichen Auflösung von unter einem Parsec werden einzelne massereiche Sterne aufgelöst, deren individueller Strahlungsbeitrag durch Photoionisation berücksichtigt wird und deren Kernkollaps-Supernovae sowie Metallanreicherung modelliert wird.

Die Änderung der Dichten, bei denen Sterne entstehen, kann durch die Änderung des Parameters für die Sternentstehungseffizienz pro Freifallzeit des Sternentstehungsmodels variert werden und ist ein effektiver Weg, um die Haufenbildungseigenschaften der Sterne signifikant zu verändern. Sterne bilden sich aus dichten, kalten Gaswolken und wenn eine Gaswolke vor der Sternentstehung auf eine sehr hohe Dichte kollabieren kann, führt dies zu stark gebundenen, kompakten Sternhaufen. Umgekehrt sind die entstehenden Sternhaufen diffuser und ausgedehnter, wenn die Wolke zu weniger hohen Dichten kollabiert. Die Größe und Oberflächendichte der Sternhaufen hat einen starken Einfluss auf ihre Anfälligkeit für Störungen durch den Ausstoß von Gas, stellare Rückkopplungseffekte und Gezeitenwechselwirkungen.

Um Effekte wie unaufgelöste Turbulenzen im Sterne formenden Gas und dynamische Effekte

aus Zweikörper Wechselwirkungen zu modellieren, erhalten neu entstehende Sternteilchen einen kleinen Geschwindigkeitsstoß in eine zufällige Richtung.

Außerdem untersuche ich die Auswirkungen der Photoionisation und der Supernova- Rückkopplung. Ich zeige, dass Photoionisation die Dichten in den Sternentstehungsgebieten sowie die Umgebungsdichten der Supernovae, die einige Millionen Jahre später explodieren, reguliert. Durch den Vergleich der Modelle mit unterschiedlicher stellarer Rückkopplung und Sternhaufeneigenschaften ist es möglich zu unterscheiden, was für die Beeinflussung der Ausströmungen aus der Galaxie maßgeblich ist. Eine Änderung der stellaren Rückkopplung führt zu einer grundlegenden Veränderung sowohl der Dichten als auch des Anteils des Gases in jeder Phase des interstellaren Mediums und hat einen erheblichen Einfluss auf die Sternhaufenbildung und die Ausströmungen aus der Galaxie.

Abstract

The clustering of star formation and subsequent stellar feedback has a significant impact on regulating star formation by altering the densities and temperatures of the surrounding interstellar medium as well as influencing galactic outflows. Dwarf galaxies, owing to their low masses, are particularly impacted by feedback and are thus an ideal setup for understanding the role of stellar clustering and feedback in galaxy evolution.

In this thesis, I explore star cluster formation and galactic outflows in high resolution simulations of isolated dwarf galaxies. I examine the effect of the sub-resolution models of star formation and stellar feedback in order to quantify the impact on the globally averaged properties, the small scales of the interstellar medium and the clustering of stars. I find that the way in which we model star formation heavily impacts the spatial and dynamical properties of the formed star clusters, influencing their future evolution. I also observe how stellar clustering and stellar feedback affect the surrounding interstellar medium, the ambient densities of supernovae and the subsequent impact on galactic scale quantities such as star formation rates and outflows.

The simulations presented in this thesis incorporate self-gravity, non-equilibrium heating, cooling and chemistry processes, shielding from a temporally and spatially varying interstellar radiation field and a density and temperature dependent star formation model. With a minimum baryonic particle mass of 4 $M_\odot$ and sub-parsec spatial resolution, we resolve individual massive stars, of which we follow the radiation input from photoionisation and core-collapse supernovae explosions, as well as metal enrichment.

Altering the densities at which stars form, which can be controlled by changing the star formation efficiency per free-fall time in the sub-resolution modelling of star formation, is an effective way to significantly change the clustering properties of the stars. Stars form from dense and cold clouds of gas, and allowing a gas cloud to collapse to very high densities before star formation results in highly bound, compact star clusters. Conversely, should the cloud not collapse to such high densities, the resultant star clusters are more diffuse and extended. The size and surface densities of the star clusters have a strong impact on their susceptibility to being disrupted by gas expulsion, stellar feedback effects and tidal interactions. To explore this further, I implement a small randomly orientated velocity kick to the newly formed star particles in order to mimic effects such as unresolved turbulence in star forming gas and dynamical effects from binary interactions.

Additionally, I study the impact of photoionisation and supernova feedback. I demonstrate the effect of photoionising feedback and its ability to regulate the densities within star forming regions as well as the ambient densities of the supernovae that explode some millions of years later.

Comparing the models with different stellar feedback and stellar clustering allows for disentangling what is responsible for influencing the outflow properties of the galaxy. Changing the stellar feedback implemented fundamentally alters both the densities and the fraction of gas in each phase of the interstellar medium, having a substantial effect on stellar clustering as well as galactic outflows.

"And what is even more remarkable, the stars which have been called 'nebulous' by every astronomer to this time, turn out to be groups of small stars wonderfully arranged."

Galileo Galilei

1 Introduction

The first documented observation of a star cluster was by Galilei (1610). In *Sidereus Nuncius*, the first published examination of the night sky with a telescope, he presented his findings of the *Praesepe Nebula*. Previously observed only with the naked eye as a misty patch on the night sky containing two bright stars, Galilei discovered that this nebula was actually a collection of several faint stars clustered together. Over 400 years later, we continue to study and understand how stars are formed in our Universe. It is now known that the majority of stars are not born in isolation, and understanding the physical processes that shape star formation in galaxies is central to our understanding of galaxy formation and evolution.

Star formation in galaxies is a complex process acting on a wide range of scales. Stars form from sub-parsec scale clumps of cold, dense gas, one of the components of the galactic-wide interstellar medium populating a galaxy on scales of hundreds of parsecs. This interstellar medium is then influenced by the injection of mass, energy and momentum into the gas from newly formed stars, preventing future star formation as well as driving large scale outflows that remove gas from the galaxy altogether.

In this thesis, I aim to show why the clustering of stars is such an important detail of galaxies in terms of its impact on shaping galaxies from the small scales of the interstellar medium and star formation to the large kiloparsec scale galactic outflows, and how the physical processes of stellar feedback shape galaxy evolution.

1.1 Dwarf galaxies

Low mass galaxies ($M_* < 10^9$ $M_\odot$), commonly described as 'Dwarf galaxies', are the most numerous galaxies in our local Universe, making up approximately 80 per cent of galaxies within the local volume (Dale et al., 2009; McConnachie, 2012; Karachentsev and Kaisina, 2019). In the hierarchical picture of galaxy formation, lower mass galaxies experience multiple mergers in various mass ratios in order to build the most massive galaxies we observe at the present day (Baugh et al., 1996a,b; Neistein et al., 2006; Conroy et al., 2007). Whilst many dwarf galaxies formed in the high redshift Universe have ended up as present day massive galaxies, there are also a population of dwarfs at the present day that have lived their lives relatively undisturbed (Henkel et al., 2017). For this reason, dwarf galaxies are interesting objects to study due to their small size and luminosities, as well as the fact that they are typically low metallicity (Tremonti et al., 2004; Hunter et al., 2012). Additionally, their low mass makes them particularly susceptible to the effects of their own star formation and feedback processes due to their shallow potential wells, providing an intriguing test bed for understanding the physics at play at these scales. From the perspective of simulating galaxies at very high resolution, dwarf galaxies are also naturally desirable due to their lower mass, as well as also the appropriateness of evolving these galaxies in isolation.

1.2 The interstellar medium

The interstellar medium (ISM) is dynamic, constantly changing in space and time. The ISM is the medium out of which stars are born and into which they deposit energy, momentum and metals. The properties of the ISM dictate when and where stars are born, as well as the densities and environments in which these stars evolve, which has a strong influence on future star formation as well as outflow properties. Processes in the ISM span a large range of scales, from entire galaxies down to the sites of individual star formation (Hacar et al., 2022).

The ISM consists of roughly 70 per cent hydrogen (H), 28 per cent helium (He), and 2 per cent heavier elements (Klessen and Glover, 2016). Various observational probes are used to understand the various different temperatures and states of the ISM, allowing us also to link the properties of the gas to star formation and feedback (Tacconi et al., 2020). We typically distinguish the different phases of the ISM by the chemical state of hydrogen. HII regions are ionised bubbles of gas which are a result of stellar feedback processes, and they dominate the volume occupied within the ISM. These regions are observed by looking at hydrogen recombination lines or the fine structure lines of ionised heavy atoms (Klessen and Glover, 2016). HI is atomic gas, and is best studied using the 21cm hyperfine structure hydrogen line. We also observe molecular hydrogen (H_2), most often in dense clouds with sufficient radiation shielding to allow H atoms to remain bound together, in structures known as molecular clouds. The majority of the mass in the ISM is in this molecular gas and the neutral atomic gas.

The ISM is multi-phase, meaning that the gas in the ISM can be separated into distinct thermal and chemical regimes. This was initially suggested by Field et al. (1969) where they suggested a two-phase ISM, as if we assume that the atomic gas in the ISM is in thermal equilibrium, there

Phase	Temperature [K]	f_V	n_H [cm^{-3}]	Heating / Ionisation / Cooling Observed by
H_2 clouds	10-50	10^{-4}	10^2 - 10^6	Photoelectrons, Cosmic Rays Cosmic Rays CO line emission CI fine structure line emission CO 2.6-mm emission dust FIR emission
CNM	100	0.01	30	Photoelectrons Starlight & Cosmic Rays Fine structure line emission HI 21-cm emission & absorption Optical, UV absorption lines
WNM	5000	0.4	0.6	Photoelectrons Starlight, Cosmic Rays Optical line emission Fine structure line emission HI 21-cm emission & absorption Optical, UV absorption lines
HII regions	10^4	0.1	0.3 - 10^4	Photoelectrons from H, He Photoionisation Optical line emission Free-free emission Fine-structure line emission Optical line emission Thermal radio continuum
HIM	$>10^{5.5}$	0.5	0.004	Shock-heating Collisional ionisation Adiabatic expansion X-ray emission UV, X-ray emission Radio synchrotron emission

Table 1.1: The different phases of the ISM, adapted from Draine (2011).

is a wide range of pressures with two thermally stable solutions for dense cold (T ~ 100 K) gas, commonly denoted as the Cold Neutral Medium (CNM), as well as diffuse warm (T ~ 10^4 K) gas, labelled the Warm Neutral Medium (WNM). For the intermediate temperatures, gas will either cool and become more dense or become more diffuse in order to reach one of the stable regimes. McKee and Ostriker (1977) then added another phase to this, the Hot Ionised Medium (HIM), by noting that supernovae exploding in the ISM would result in larger, hot (T ~ 10^6 K) ionised bubbles of gas, with relatively long cooling times. An additional phase of the ISM is that of the gas that occupies HII regions, ionised gas with temperatures of ~ 10^4 K, sometimes referred to as the Warm Ionised Medium (WIM). The final phase of the ISM is the H_2 that resides in cold, dense gas in molecular clouds. This therefore summarises the current picture of the ISM, split into five phases. I summarise the properties as well as the relative contributions of the different phases to the ISM in Table 1.1, which was adapted from Draine (2011). The transfer between the different phases, as well as the relative fractions of these occupying the volume and mass in galaxies is still being understood.

1.3 Formation & evolution of star clusters

In the discussion of the ISM, I have already introduced the concept that stars and their feedback are responsible for dictating most of these phases. I will now explain, somewhat chronologically, the 'story' of stars forming in clusters from molecular clouds, to star formation, to the onset of stellar feedback, and the subsequent destruction of their parent molecular clouds. I then discuss the future evolution of the formed population of star clusters and their contribution towards the future evolution of the galaxy as a whole.

1.3.1 Molecular Clouds

Molecular clouds are groups of gas particles which have sufficient column density to shield themselves from the interstellar radiation field, and remain in this configuration for long enough to form H_2. The main formation mechanism for this H_2 in the ISM occurs on the surfaces of dust grains, where the higher the density of the gas, the shorter the timescale for H_2.

The molecular gas distribution in a galaxy is not smooth, but is instead arranged in clumps, with masses ranging from hundreds to millions of solar masses and radii on the order of parsecs to tens of parsecs (Barnes et al., 2021). Their distribution within a galaxy follows a power-law mass function (Heyer and Dame, 2015).

To understand the formation of stars from molecular clouds, we can consider spherical cloud in hydrostatic equilibrium, such that

$$\frac{dp}{dr} = -\frac{G\rho(r)M(r)}{r^2}, \tag{1.1}$$

where r is the radius of the cloud, $M(r)$ is the mass enclosed within radius r, p is the pressure, $\rho(r)$ is the density at r, and G is the gravitational constant. The pressure here is temperature dependent, thus for a given temperature, should the mass exceed the threshold value, the cloud will collapse. This threshold mass is known as the Jeans mass, which can be derived by taking the condition for collapse of a spherical cloud such that the sound crossing time must exceed the free-fall time, where

$$t_s = \frac{R}{c_s} = \sqrt{\frac{m}{\gamma k_B T}} R, \tag{1.2}$$

where t_s is the the sound crossing time, which is the time it takes sound waves generated from pressure exerted on the collapsing gas cloud to travel through the cloud and back in order to re-balance the pressure, R is the radius of the cloud, c_s is the sound-speed of the gas, γ is the adiabatic index, k_B is the Boltzmann constant, T is the temperature of the gas and m is the particle mass.

To find the turnover point at which collapse will happen, we balance this sound crossing time with the free-fall time:

$$t_{ff} = \sqrt{\frac{3\pi}{32 G \rho}}, \tag{1.3}$$

which is the timescale for gravitational collapse.

The radius at which $t_s = t_{ff}$ gives the Jeans length R_J

$$R_J = t_{ff} c_s, \tag{1.4}$$

from which we can also deduce the Jeans mass, which is simply the mass of a sphere with radius R_J and average density ρ_0. Extracting out the constants and considering a fixed mass, we find

$$M_J \propto T^{3/2} \rho^{-1/2}, \tag{1.5}$$

meaning the Jeans mass decreases as a cloud cools and becomes more dense. Once the cloud collapses further than this threshold, it is on its way to star formation.

1.3.2 Star formation

The star formation process within these molecular clouds appears to be fast (Hartmann, 2001; Elmegreen, 2007), with collapsing cloud cores forming an entire cluster of stars within a Myr. As soon as a molecular cloud begins forming stars, it is a rush to form stars before those stars begin their feedback cycle, aggressively evacuating gas from their surroundings and destroying the molecular cloud.

Star formation is observed to be inefficient, such that a relatively small fraction of gas in a galaxy is converted into stars. Within our own Milky Way galaxy, around 20 per cent of the cold gas is in the form of H_2, with the rest being dominated by neutral atomic hydrogen. Many studies explore the integrated star formation efficiency, that is, the amount of molecular gas that is turned into stars, with values of only a few percent (see e.g. Zuckerman and Palmer, 1974; Williams and McKee, 1997; Kennicutt, 1998; Evans, 1999; Krumholz and Tan, 2007; Evans et al., 2009), however some studies have suggested that dwarf galaxies appear to be slightly more efficient (e.g. Schruba et al., 2012, but see also Bolatto et al., 2011; Jameson et al., 2016; Schruba et al., 2017; Bolatto, 2019). An example of such a dwarf galaxy is the Wolf-Lundmark-Melotte (WLM)

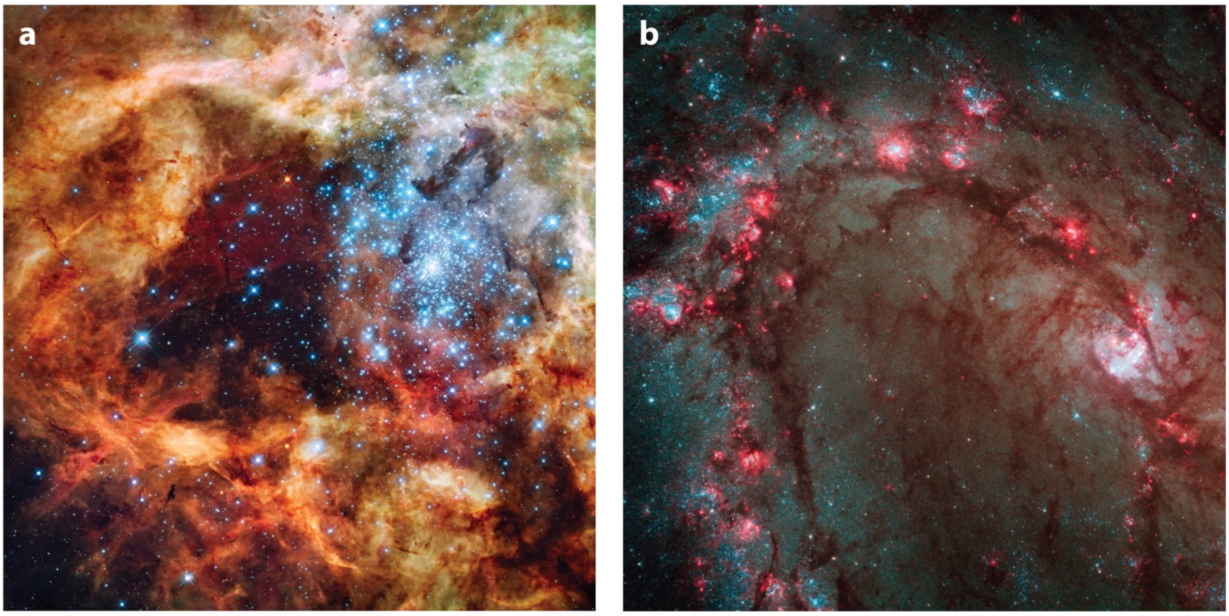

Figure 1.1: (*a*) A 50×50 pc^2 region around the $\sim 10^5$ M$_\odot$ cluster R136 in the 30 Doradus region of the Large Magellanic Cloud, at a distance of $\sim$ 50 kpc. (*b*) Many young star clusters forming in the spiral arms of M83 at a distance of 3.6 Mpc. Image: Portegies Zwart et al. (2010).

(Rubio et al., 2015), which is an appropriate analogue to the simulations presented in this thesis. Nevertheless, galaxies only turn a small fraction of their gas into stars, and the processes that make star formation inefficient can be explained in part by stellar feedback regulating the star formation process on both local and global scales (Cole, 1991; Springel et al., 2005; Dekel and Birnboim, 2006), as discussed later in all chapters of this thesis.

Within a molecular cloud, but more broadly also across much larger star forming regions, a stellar population can be characterised by the initial mass function (IMF), which describes the mass distribution of stars, and remarkably appears to be somewhat universal. As the majority of stars form in groups in giant molecular clouds, a more massive galaxy simply contains more of these star forming units. The mass function describing a newly formed population of stars has been characterised by Salpeter (1955), Kroupa et al. (2001) and Chabrier (2003). As observations resolving individual stars become increasingly powerful, there is also evidence of a deviation from this initial mass function (Larson, 1998; Bartko et al., 2010; Daddi et al., 2010; Marks et al., 2012; Pouteau et al., 2022). The implications of an altered IMF are not minor, as more massive stars for example would mean higher levels of photoionising feedback and supernovae energy injection which has profound effects on not only the small-scale sites of star formation, but also on galactic scale outflows, heavily affecting the future evolution of the galaxy.

1.3.3 Star cluster formation

Star formation is typically clustered (Lada and Lada, 2003; Portegies Zwart et al., 2010), with stars forming from collapsing and fragmenting giant molecular clouds (see e.g. Williams et al., 2022). The result is a group of stars with similar metallicity and ages formed in a single burst of star formation, although some star clusters do show observational evidence of multiple bursts of star formation particularly in massive clusters (e.g. Piotto et al., 2005; Villanova et al., 2007; Peacock et al., 2013). This is also linked with the bursty nature of star formation expected in lower mass galaxies. Massive galaxies such as the Milky Way has shown continuous star formation over many regions of the galaxies at any given time resulting in a roughly constant star formation rate over the last few Gyr (Snaith et al., 2015; Fantin et al., 2021). Dwarf galaxies however, from observations of the Local Group have shown much more bursty star formation histories (Mateo, 1998; Weisz et al., 2011; McQuinn et al., 2012; Shen et al., 2014). This can also be heavily linked with environmental interactions, such as dwarf galaxies with a larger halo (e.g. Besla et al., 2016; Belokurov et al., 2018), as well as internal dynamics. For example, the 30 Doradus region shown in Fig. 1.1 has been suggested to be a result of the direct collision between the SMC and LMC (Besla et al., 2012; Fukui et al., 2017).

Before continuing the discussion of star clusters, we must ask: what is a star cluster? This question goes back as long as Trumpler (1930) on how to distinguish star clusters from multiple systems. The definition presented in Lada and Lada (2003) is a collection of stars with a mass density large enough ($\gtrsim$ 1 $M_\odot/pc^3$) in order to resist tidal disruption in Solar Neighbourhood conditions and with enough stars to avoid N-body evaporation for >100 Myr. Whereas, Portegies Zwart et al. (2010) define a star cluster as simply a set of stars that are gravitationally bound to one another. Another definition could be a group of stars with a significantly higher mass density than in the galactic neighbourhood (~0.1 $M_\odot/pc^3$ near the Sun, McKee et al., 2015). For newly formed star clusters, observationally some of these definitions can be difficult to fulfill as defining a cluster as bound typically involves assuming boundedness if the age of the cluster exceeds a few cluster crossing times, where $t_{cr} = r/\sigma \lesssim 1/\sqrt{G\rho_*}$ (Hills, 1980; Kroupa and Boily, 2002; Baumgardt and Kroupa, 2007; Gieles and Portegies Zwart, 2011). For older star clusters however, all of the definitions listed above are nearly identical in practise. The lack of a universal definition of a star cluster makes comparison of observations and simulations somewhat difficult.

Star cluster masses range from ~ 10^1 - 10^7 $M_\odot$ and half-mass radii from 0.1 up to a few tens of pc with varying stellar densities, from ~ 0.1 to 1000 stars per cubic parsec. The mass and size distribution of star clusters and globular clusters (GCs) in nearby galaxies compiled in a review by Krumholz et al. (2019) is shown in Fig. 1.2. Star clusters can also be characterised in different ways by their mass as well as their location. In this thesis, the term 'star cluster' typically refers to a group of stars which have been formed together and reside embedded in a galaxy. A special category of star clusters within a galaxy is a nuclear star cluster, which we discuss separately later. GCs are star clusters that typically reside outside a galaxy, and tend to also be more massive.

Not all stars are born in star clusters. The exact percentage of stars that are born in clusters is somewhat disputed in both observational and theoretical literature (Larsen and Richtler, 2000; Bastian, 2008; Goddard et al., 2010; Kruijssen, 2012). The fraction of stars in a galaxy which are formed (or currently exist) in identified star clusters is characterised by the cluster formation efficiency (CFE or Γ), such that

$$\Gamma = \frac{M_{*,\mathrm{cl}}(\tau)}{M_*(\tau)}, \tag{1.6}$$

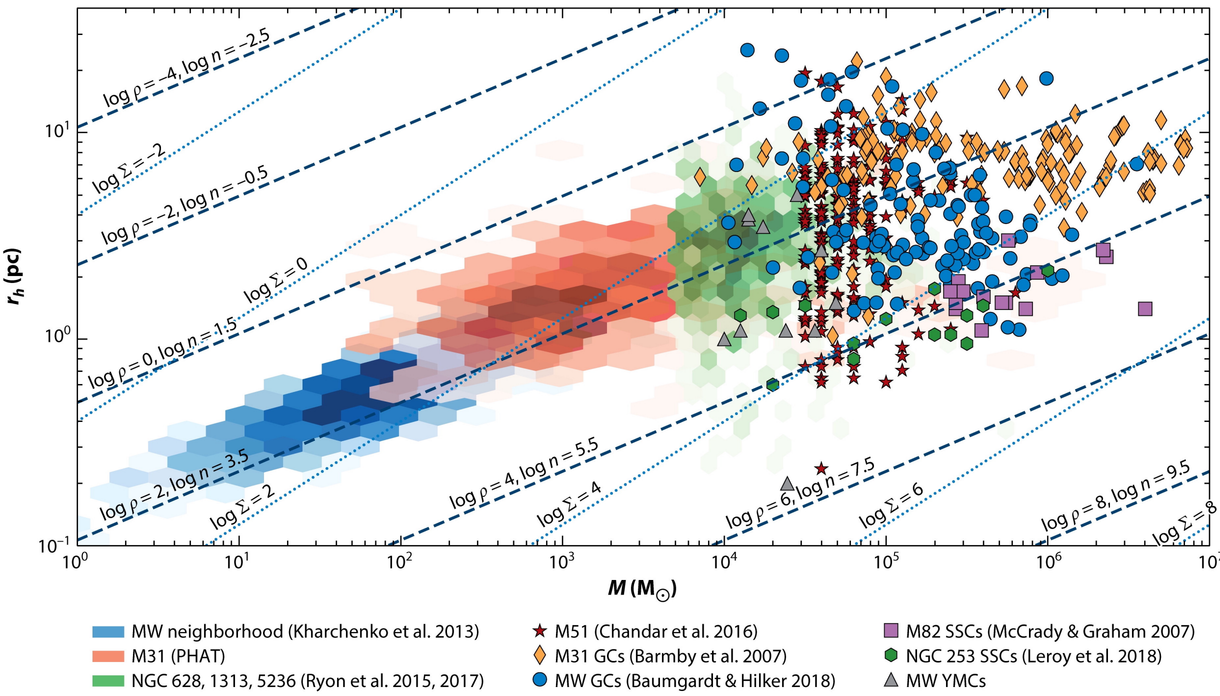

Figure 1.2: Mass-radius relation for star clusters in nearby galaxies. For the Milky Way (MW) clusters and GCs, the half-mass radii or half-number radii is shown, and for all other datasets the half-light radii is shown. Dashed black lines show constant volume density, and dotted blue lines show constant surface density. The hexagonal density plots show the log of the density of clusters in the Milky Way within 2 kpc of the Sun from Kharchenko et al. (2013) (dark blue hexbins), the clusters in M31 from PHAT (red hexbins, Johnson et al., 2012; Fouesneau et al., 2014), and clusters from NGC 628, NGC 1313 and NGC 5236 grouped together from Ryon et al. (2015, 2017) (green hexbins). The other symbols are for clusters in the disk of M51 (dark red stars, Chandar et al., 2016), GCs in M31 (yellow diamons, Barmby et al., 2007), GCs in the Milky Way (blue circles, Baumgardt and Hilker, 2018), super star clusters in M82 (purple squares, McCrady and Graham, 2007), super star clusters in NGC 253 (green hexagons, Leroy et al., 2018) and young massive clusters in the Milky Way (grey triangles, Krumholz et al., 2019). Source: Krumholz et al. (2019).

where $M_{*,\mathrm{cl}}(\tau)$ is the mass in clusters up to some age τ and $M_*(\tau)$ is the total mass formed in stars in the same period. Typically, a timescale of around $\tau = 10$ Myr is used in observational studies.

This fraction can be relatively challenging to observe, as it is naturally heavily dependent on the definition of a star cluster as discussed above. For example, many authors define Γ as the fraction of stars in bound star clusters (e.g. Bastian, 2008; Kruijssen, 2012) whereas other authors drop the bound requirement (e.g. Krumholz et al., 2012). If we assume star clusters are all bound, the definitions are naturally identical. The distribution of stars in a galaxy has significant importance in shaping its further evolution, as the clustering of stars has a strong impact on the properties of the ISM as will be shown particularly in Chapter 5.

Fig. 1.3 shows a collection of observations from Adamo et al. (2020a), where they show the cluster formation efficiency as a function of star formation surface density. For galaxies with high star formation rate surface densities, the cluster formation efficiency approaches 100 per cent, denoting that all stars in the galaxy are born in identified star clusters. This decreases with decreasing star formation rate surface densities (Goddard et al., 2010; Adamo et al., 2011), with cluster formation efficiencies of only a few per cent for star formation rate surface densities on the order of 10^{-3} $\mathrm{M}_\odot$/yr/kpc^2. This quantity is naturally also a function of age (e.g. Chandar et al., 2017), as some fraction of star clusters are destroyed over time by various destruction processes, as discussed in Sec. 1.5. But finding age trends is difficult, as pointed out in Kruijssen and Bastian (2016), as young star cluster observations can easily be contaminated by unbound collections of stars that have not had adequate time to disperse yet.

Within a galaxy, star cluster masses are distributed in a power law mass function, named the cluster mass function (CMF). The CMF is observed to be universal over a broad range of environments and galaxy masses, and follows a power law mass function $\mathrm{d}N/\mathrm{d}M \propto M^\alpha$ with a slope of -2 ± 0.2. A slope of -2 means equal mass per logarithmic bin, corresponding to a completely scale-free distribution (Krumholz et al., 2019).

In observational measurements of the CMF, the lower end of the distribution is often truncated by observational limits, but the few observations that do follow cluster masses down below $\sim 10^3$ $\mathrm{M}_\odot$, even down to 20 $\mathrm{M}_\odot$ also show slopes consistent with -2 (e.g. Lamb et al., 2010). The upper limit, corresponding to the maximum cluster mass in a system appears to be function of the mass of the system (Chandar et al., 2017). Massive clusters ($>10^5$ $\mathrm{M}_\odot$) are expected to be very few for most galaxies according to a power-law mass function. Clusters of these masses are found as expected in massive galaxies such as M82 and the Antennae (O'Connell et al., 1995; Whitmore and Schweizer, 1995; Whitmore et al., 1999; Gallagher and Smith, 1999; Zhang and Fall, 1999; Fall et al., 2005; Melo et al., 2005). Some studies however report an upper truncation of the CMF at some truncation mass M_{trunc}, which is either a hard cut, or characterised as a Schechter function, $dN/dM \propto M^\alpha \exp(-M/M_{\mathrm{trunc}})$ (Bastian, 2008; Larsen, 2009; Bastian et al., 2012; González-Lópezlira et al., 2012; Adamo et al., 2015, 2017).

1.3.4 Nuclear Star Clusters

Nuclear star clusters (NSCs) are the densest stellar structures in the Universe. Defined as a compact, dense group of stars residing in the centre of a galaxy, often hosting a black hole

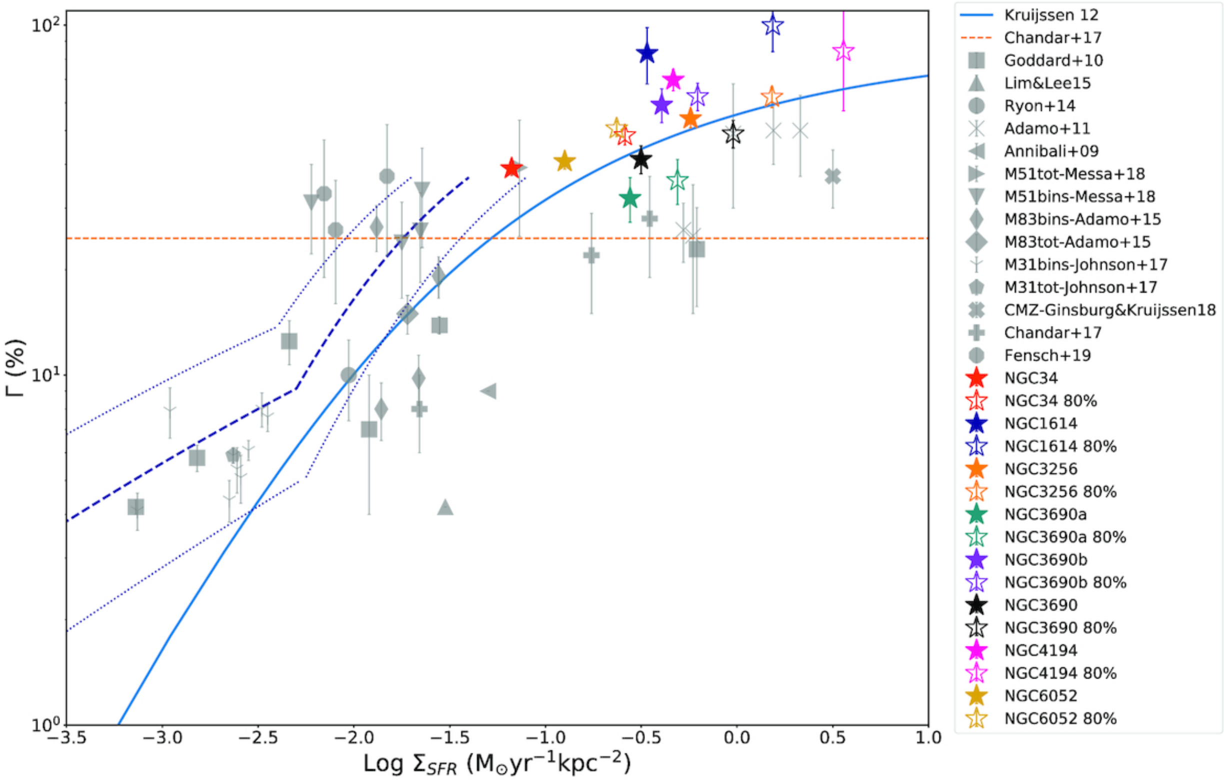

Figure 1.3: Cluster formation efficiency as a function of star formation rate surface density. All coloured points are results from the HiPEEC galaxies presented in Adamo et al. (2020a), with filled and empty star symbols showing total and inner galactic values for Γ, respectively. The grey points show a compilation of literature previous to this study: NGC 4214, NGC 4449, and the Antannae are from Chandar et al. (2017), Large Magellanic Cloud (LMC), Small Magellanic Cloud (SMC), M83-centre, NGC 6946 and the Milky Way (MW) are from Goddard et al. (2010). The solid light blue line shows the Kruijssen (2012) analytical model using the Kennicutt and Evans (2012) $\Sigma_{\rm SFR}$ to $\Sigma_{\rm gas}$ conversion, whilst the dashed and dotted dark blue lines are again the analytic model from Kruijssen (2012), but using the $\Sigma_{\rm SFR}$ to $\Sigma_{\rm gas}$ conversion from Bigiel et al. (2008). The orange horizontal dashed line shows a constant cluster formation efficiency of 24 per cent proposed in Chandar et al. (2017). Source: Adamo et al. (2020a).

(potentially several), we have the privilege of observing a stellar cluster surrounding our own Milky Way black hole, Sagittarius A*. Nuclear star clusters at the basic level are just a star cluster which is in the centre (or nucleus) of its host galaxy, but as noted briefly in Krumholz et al. (2019), they typically co-evolve with central black holes and so have different evolutionary drivers representing a separate physically distinct class. A non-negligible fraction of dwarf galaxies are seen to host nuclear star clusters (Neumayer et al., 2020), and understanding exactly how they came to be there is still an open question. Studying the distinctions between the metallicities and ages of the stars in the NSC and its host galaxy can however give some insight. Fahrion et al. (2022) studied a population of galaxies and found a potential trend with mass, in that lower mass galaxies appeared to have NSCs consistent with accreted GCs, whilst higher mass galaxies host NSCs with more signatures of in-situ star formation, identified by metallicities and stellar ages consistent with their host galaxies.

1.4 Stellar feedback

Now we have looked at where, under what conditions and how star clusters form. On the timeline of star cluster formation, we have formed a population of star clusters within a galaxy, with some still embedded in their parent gas cloud, such as the cluster R136, shown in the left panel of Fig. 1.1. This is a 10^5 $M_\odot$ cluster in the 30 Doradus region which lies at the centre of the Tarantula Nebula of the LMC. When originally discovered, it was believed to be a single stellar object, before being resolved into a group of $\sim 10^5$ stars (Weigelt and Baier, 1985; Massey and Hunter, 1998; Andersen et al., 2009; Campbell et al., 2010). Following from the understanding of this cluster, it was then realised that young massive star clusters were responsible for the giant expanding HII regions found in other galaxies (Lopez et al., 2011), such as in the spiral arms of M83 as shown in the right panel of Fig. 1.1 (van den Bergh, 1971). I will now navigate through the various feedback processes from the stars and the impact that they have on the surrounding gas.

Stellar feedback in the form of winds, ionising photons from massive stars and supernovae combine to regulate the star forming interstellar medium. Whilst stellar feedback can encourage star formation, for example in highly compressed shells on the edges of HII regions or in shocked gas from supernovae, star formation is observed to be relatively inefficient, and therefore stellar feedback plays a predominantly negative role in preventing further star formation, making this a self-regulating process. I discuss the way that the different forms of stellar feedback are implemented in the simulations presented in this thesis in Chapter 2.1, but give a brief physical and observational overview here, following the discussion in Draine (2011).

1.4.1 Photoionising feedback

An O-type star emitting as a blackbody with T = 35000 K emits 32 per cent of its power in $h\nu > I_{\rm H}$ photons. These photons can ionise a substantial fraction of the surrounding gas. The ionised region, known as a HII region surrounding a star has a temperature on the order of 7000 - 15000 K, dependent on the metallicity of the gas and the spectral type of the ionising source.

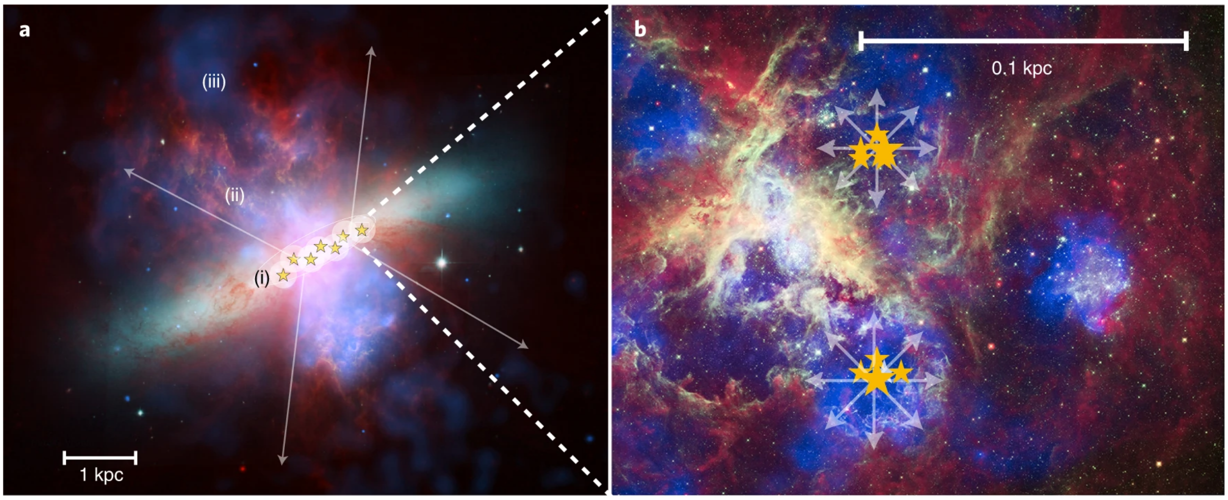

Figure 1.4: Observational images of M82 (a) and the 30 Doradus star forming region in the LMC (b). These images combine Chandra, Spitzer and Hubble Space Telescope imaging. The two images show how feedback impacts galaxies on both galactic scales in M82 and on the scales of star forming regions in 30 Doradus. In these images, white is starlight, red shows infra-red observations (corresponding to temperatures of ~ 300-500 K), orange shows ionised hydrogen (T ~ 10^5 K) and X-ray observations (T ~ 10^6 K) are shown in blue. *Left*: M82 is a starburst galaxy with a mass of ~ 10^{10} $M_{\odot}$, with visible large scale outflows perpendicular to the plane of the disk. M82 image credit: X-ray: NASA/CXC/JHU/D.Strickland; Optical: NASA/ESA/STScI/AURA/The Hubble Heritage Team; IR: NASA/JPL-Caltech/Univ. of AZ/C. Engelbracht. *Right*: 30 Doradus image credit: X-ray: NASA/CXC/PSU/L.Townsley et al.; Optical: NASA/STScI; Infrared: NASA/JPL/PSU/L.Townsley et al. Image taken from: Collins and Read (2022).

In simulations, the HII regions are typically modelled as Strömgren spheres (Strömgren, 1939). I describe in more detail how this is modelled in our simulations in Chapter 2.1. An example of a HII region is seen in panel (*a*) of Fig. 1.1, where the photoionising feedback has heated and cleared the gas surrounding the formed star cluster.

1.4.2 Supernovae

Supernovae are the energetic outburst of a massive star at the end of its life, and can come from different scenarios. Type II supernovae are stars more massive than 8 $M_{\odot}$ that run out of nuclear fuel and core collapse under their own gravity. These supernovae typically explode from 3 to 50 Myr after star formation, dependent on the initial mass of the star. Type Ia supernovae have much longer delay times between the formation of the progenitor star and explosion, as these are thought to result from accretion of material from a binary partner onto a white dwarf star until the white dwarf reaches the Chandrasekhar limit of 1.4 $M_{\odot}$, although there is evidence for other progenitor scenarios of Type Ia supernovae (see e.g. Kirby et al., 2019). We concentrate primarily on Type II supernovae as their frequency in dwarf galaxies is much higher.

When supernovae explode, the injection of energy creates a blastwave, referred to as a supernova remnant, that expands in a series of phases. The first of which is the *free-expansion phase*, where the velocity of the ejecta from the star (~3000 km/s) far exceeds the sound speed of the surrounding material, driving a fast shock into the circumstellar medium. The density of the ejecta also far exceeds the surrounding densities, and so the supernova remnant will continue to expand at nearly constant velocities, hence the name ‘free-expansion’. As the density of the bubble surrounding the star begins to decrease, the external pressure exceeds the thermal pressure within the bubbles, resulting in a reverse-shock. The result is two shockfronts, the original blastwave which is expanding into the surrounding material, and the reverse shock travelling inwards which is slowing and heating the previously cooled material inside the bubble. Following the free-expansion phase, which lasts on the order of a couple of hundred years only, comes the *Sedov-Taylor phase*, where the reverse shock reaches the centre of the supernova remnant, slowing down the evolution of the remnant as it expands adiabatically with velocities on the order of a few hundred km/s. The pressure within the bubble far exceeds the external pressure and the hot gas radiates in X-rays for typical radiation timescales of around 10^4 yr. Following the Sedov-Taylor phase is the *Snowplow phase*, where the remnant energy is dissipated into the surrounding ISM, with modest velocities. The remnant forms a thin, dense shell which cools rapidly, whilst the interior energy of the bubble remains hot. The shockfront gradually slows down, eventually reaching the sound speed of the surrounding ISM on timescales of a few Myr. One particularly stunning example of bubbles driven by SNe is again the 30 Doradus region, but now seen from a wider field of view shown in the right panel (b) of Fig, 1.4. This image shows the effect of consecutive SNe explosions from massive stars on the surrounding ISM as it drives expanding hot bubbles of ionised X-ray emitting gas. Multiple SNe produce overlapping bubbles, often named ‘superbubbles’, with sizes exceeding 100 pc, with the largest of these bubbles requiring hundreds to thousands of SNe to power them.

1.4.3 Stellar winds

Stellar winds inject mass, momentum and energy into the ISM, and are able to carve out large cavities in the surrounding ISM. The most relevant winds come from hot, young, massive O-type stars, red giants and supergiants, as well as planetary nebula progenitors. O-type stars inject energy into the surrounding ISM with velocities on the order of a few thousand km/s, with mass-loss rates on the order of 10^{-6} $M_\odot$/yr (Markova et al., 2004). As already mentioned in Sec. 1.4.1, massive stars will ionise the surrounding ISM creating HII regions, which lowers the ambient medium into which stellar winds will blow. The evolution of the wind undergoes similar phases as the supernova bubbles discussed in Sec. 1.4.2, but the timescales of these phases are extremely short, on the order of years, and becomes radiative very quickly. The shocked wind material is very hot (T ~ 10^7 K) emitting in X-rays with low density, resulting in long cooling timescales. The scales of these winds however are typically well-contained within the HII region created by the same star.

1.4.4 Asymptotic giant branch stars

Asymptotic giant branch (AGB) stars are lower mass stars (<8 $M_\odot$) at the latter stages of its evolution. Observationally, they appear as bright red giants. The core of the star is inert and made from carbon and oxygen, surrounded by a shell of helium undergoing fusion into carbon, followed by a shell of hydrogen fusion to create helium, finally surrounding by a large stellar envelope. In the early phase of AGB stars, the helium shell is undergoing fusion releasing enough energy to cause the star to swell to a red giant. Later in its evolution once the star has exhausted its helium shell, the hydrogen is still producing helium but only in a very thin shell. Once enough helium builds up however, the formed helium shell undergoes a flash, releasing substantial amounts of energy very quickly. This cycle results in thermal pulses of the star, occuring on timescales of 10^4-10^5 yr. These pulsations result in substantial mass loss from the star from stellar winds, on the order of 50 to 70 per cent of its mass (Wood et al., 2004).

1.5 Disruption of molecular clouds and star clusters

The explanation of the destruction of molecular clouds is rather simple following the description of the various feedback processes above. Molecular clouds rarely survive the stellar winds and photoionising feedback emitted by the stars it forms within them (Barnes et al., 2022), and if they do, they certainly not survive the supernovae.

The unbinding, or disruption of star clusters is more challenging. From observations, we saw that a substantial fraction of stars can be born in clusters, looking at ages <10 Myr. In older stellar populations however, only a very small percentage are found in bound star clusters (Bastian and Gieles, 2008; Goddard et al., 2010; Adamo et al., 2011; Johnson et al., 2016), for example Lada and Lada (2003) found that less than 10 per cent of stars formed in embedded clusters ended up in bound clusters after 100 Myr. Within the pair of merging Antennae galaxies, all of the star formation appears to be in clusters, but the majority of these clusters are likely to become unbound (Whitmore, 2003; Fall et al., 2005). Similarly, in M51, Bastian et al. (2012) predict that more than 60 per cent of all young clusters will likely be destroyed within the first tens of Myr of their lives. We can also indirectly infer cluster disruption by a lack of older ($\gtrsim$ Gyr) clusters in the solar neighbourhood Oort (1958); Wielen (1971); Boutloukos and Lamers (2003), as well as in M51, M33 and the Small Magellanic Cloud (SMC; Boutloukos and Lamers, 2003). When comparing the LMC, SMC and the solar neighbourhood, it was noted that the LMC and SMC have more older clusters than the solar neighbourhood, presenting the idea that there are environmentally dependent disruption mechanisms (Gascoigne, 1966; de Grijs and Anders, 2006; Hodge, 1987).

There are three main phases and corresponding typical timescales of cluster disruption (Bastian and Gieles, 2008). Boutloukos and Lamers (2003) derived a ‘disruption time’, $t_{\rm dis}$ for observations of star clusters using the assumption that the disruption time can be parameterised as a function of only the cluster mass, such that

$$t_{\rm dis} = t_4 (M/10^4 {\rm M}_\odot)^\gamma, \tag{1.7}$$

where t_4 is the disruption time of a 10^4 $M_\odot$ cluster.

The first is *Infant mortality*, which describes the unbinding of the cluster due to gas expulsion. This occurs on timescales on the order of 10 Myr (see Bastian and Gieles, 2008, for a review and discussion of this first phase of disruption). Surviving infant mortality has a natural dependency on the relative fractions of stars and gas in the system before gas expansion. When a cluster expels its gas (through processes discussed above), the star cluster must expand to reach virial equilibrium, possibly losing several stars. For clusters with more than 70 per cent of their mass in gas prior to expulsion, a substantial fraction of the stellar mass will be lost through this process and the entire cluster will become unbound in tens of Myr (Tutukov, 1978; Goodwin, 1997a,b; Kroupa and Boily, 2002; Boily and Kroupa, 2003a,b; Bastian and Goodwin, 2006).

If a cluster survives infant mortality, they are now subjected to the effects of *Stellar evolution* on timescales of 100 Myr. Once the cluster age reaches a Gyr, the primary disruption mechanism is then *Tidal relaxation* (see Baumgardt, 2009, for a thorough discussion on the impact of stellar evolution and tidal relaxation on clusters). Additional to all these phases, cluster disruption can occur or be enhanced by additional tidal interactions from passing molecular clouds, the galactic disk and the spiral arms.

1.6 Galactic outflows

The feedback processes discussed above have been shown to strongly influence the evolution and lifespan of star forming molecular clouds, but they can also have a major impact on the galactic-scale properties (Martin, 1998; McQuinn et al., 2019; Keller and Kruijssen, 2022). This topic is the focus of Chapter 5 in this thesis, where the finer details of the specifics of feedback and how outflows are driven is discussed at length. I therefore briefly present here some of the observations and broadly introduce the key points.

Outflows are observed in many galaxies of varying mass and morphologies. One particularly exquisite example of galactic scale outflows is M82, shown in the left panel of Fig. 1.4. The large-scale outflows were first reported by Lynds and Sandage (1963) and Burbidge et al. (1964), where they pondered the question of which processes were capable of driving such large outflows of energy on these scales. Nowadays, owing to much more research done in this field, we have a much more concrete understanding of these processes. There are two primary energy sources responsible for driving galactic outflows: stellar feedback and feedback from active galactic nuclei (AGN). AGN can inject substantial amounts of energy into the surrounding ISM, which are observed to contribute to large scale outflows of gas that can significantly regulate low-mass galaxies (Veilleux et al., 2005, 2020; Silk, 2017; Koudmani et al., 2019, 2021, 2022). However, outflows are also observed in the absence of AGN. Stellar feedback, which is discussed extensively in this thesis, comes in many forms. The most energetic form of stellar feedback is core-collapse supernovae (CCSNe), the end stage of massive stars, which are a driving force behind galactic outflows, particularly in galaxies without AGN (Larson, 1974). Other feedback processes do certainly play a role in driving outflows, but more indirectly as they set the environment in which the CCSNe explode, which are the dominant outflow energy injection into the ISM in the absence of black holes. For now, we ignore the contribution of AGN, as they are not included in the simulations presented in the main chapters of this thesis, but see Koudmani et al. (2022) for a comparison of the contribution from supernovae and AGN in driving outflows.

M82 is a particularly exceptional example of outflows, as it is the only dwarf galaxy in the local Universe with a developed and powerful wind (Rhode et al., 1999). Large scale outflows in M82 have been linked to its highly bursty nature (Konstantopoulos et al., 2009). The winds are conical and moving at velocities of 25-100 kms^{-1}. These galactic winds are also multi-phase (Fielding and Bryan, 2022), with hot (T > 10^5 K), warm (10^3 < T < 10^5 K) and cold (T < 10^3 K) components. There are several regions labelled on the left panel of Fig. 1.4. Region (i) shows active star formation, where bubbles from feedback overlap to form superbubbles (also shown in the right panel (b) of Fig. 1.4). As the superbubbles overlap, they can form a large scale galactic wind seen in region (ii), which is able to remove gas from the disk into the halo and into region (iii), the circumgalactic medium.

To understand the link between star clusters on scales of pc to galactic winds on the scales of kpc, we can recap the feedback processes previously discussed. Stellar feedback begins on pc scales inside star clusters, the stellar winds and photoionising feedback pre-processes the ISM surrounding the stars by heating the gas and lowering the density. This is then followed by CCSNe after some Myr. The first supernova explodes into the photoionised gas, creating a modest bubble, heating the gas and lowering the density further. This process is then enhanced as more and more supernovae explode within or near bubbles. These bubbles overlap, expand to sizes more than 100 pc and merge, creating large superbubbles of low density, hot gas, as seen in the right panel in Fig. 1.4. Many supernovae exploding spatially and temporally nearby therefore have the combined power to drive large expanding bubbles of hot gas that escape the disk with ease.

1.7 Structure of this thesis

This thesis explores the specifics of the star formation prescription as well as stellar feedback on the stellar clustering and outflow properties of dwarf galaxies in high resolution simulations of isolated dwarf galaxies, and we provide insight into understanding how both the galactic and small scale properties are influenced by these processes

Chapter 2 introduces the simulations used in all subsequent chapters and discusses the specifics of the sub-resolution modelling, particularly of star formation and feedback.

Chapter 3 (published as Hislop et al., 2022) presents the effect of the star formation efficiency parameter, which effectively controls the densities at which gas particles are realised into stellar particles. We highlight the importance of understanding the effect of the sub-resolution prescription for star formation on the smaller scale properties. We develop an unbinding routine in order to intricately understand the properties of the star clusters.

Chapter 4 explores two physically motivated alterations to the sub-resolution star formation prescription in order to capture particularly the structural properties of the star cluster population in agreement with observations, as well as understanding the physical processes driving these properties as well as their evolution.

Chapter 5 addresses the question of how supernovae drive outflows, and what is the main driver in setting the outflow properties. We explore separately the effect of stellar clustering and stellar feedback in order to disentangle their relevance and importance in simulations on the scales of dwarf galaxies, which are particularly sensitive to the effects of feedback.

Chapter 6 then shows some preliminary results from isolated dwarf galaxy minor mergers with the inclusion of accurate integration in the central region of the galaxy, with the goal of exploring nuclear star cluster formation. We also briefly describe planned future work beyond this thesis, along with a summary of the overall findings.

"We are all in the gutter, but some of us are looking at the stars."

Oscar Wilde

2

Modelling galaxy formation and evolution with a resolved interstellar medium

Owing to a wealth of different numerical methods as well as different implementations of physical models, one has a rich literature of state-of-the-art simulations in order to explore astrophysical scales from planet formation up to the formation of populations of galaxies comparable with large fractions of the observable Universe. It is discussed extensively in a review from Naab and Ostriker (2017) that many different models with relatively drastically different methods and sub-grid models manage to reproduce remarkably similar results. This is not necessarily helpful in the quest to building a complete picture of galaxy formation in numerical simulations. One example of this is star formation in a galactic context.

In this chapter, I present a biased overview of numerical methods adopted in simulating galaxy formation and evolution, as well as fully introducing the smoothed particle hydrodynamical (SPH) code, SPHGal (Hu et al., 2016) which is the model used in all of these simulations, with the goal of giving a full and detailed description of the adopted methods, along with some caveats and examples of potential future improvements.

2.1 Numerical Methods

In this thesis, all simulations presented have been performed using Gadget-3. I therefore present an overview of numerical methods in general but with a focus towards the methods employed in Gadget-3. I also discuss some limitations of our adopted scheme. It should be noted however that there is no right or wrong answer so long as the limitations and appropriateness of a method to a particular problem are well understood. Several studies have presented interesting overviews and comparisons between a variety of different methods and demonstrate the substantial difference between the different numerical methods (e.g. Frenk et al., 1999; O'Shea et al., 2005; Agertz et al., 2007; Braspenning et al., 2022), including a highly relevant comparison of the model used in this thesis to other widely used codes (Hu et al., 2022b). One might hope that the conclusion to these studies would hint towards the correct method to use, but the issue comes in knowing what is the 'truth' or the correct answer, when there is not one.

2.1.1 N-body methods

Stars are modelled as a collisionless collection of point masses. Stellar interactions in fact are very much collisional, however it has been shown that within a galactic context at least, modelling them in this way is appropriate. Dark matter is modelled as a collisionless fluid, which in SPH is treated by sampling this fluid by a finite set of particles. For these differing reasons, both stars and dark matter are modelled in a similar way.

To model the time evolution of the orbits of a self-gravitating three dimensional fluid, we treat it as a collection of point masses and evolve this system as an N-body problem. The simplest numerical method to solve an N-body problem is direct summation, which evaluates the gravitational potential of these point masses by summing over the individual particle masses. The gravitational potential calculated in this way gives the force, and subsequently the acceleration on each particle, from which the velocities and positions can be updated after some timestep Δt. The potential is calculated such that

$$\Phi(\vec{r}) = -G \sum_i \frac{m_i}{(|\vec{r}_j - \vec{r}_i|^2 + \epsilon^2)^{1/2}}, \tag{2.1}$$

where G is the gravitational constant, m and $\vec{r}$ are the masses and spatial vectors of the respective particles, and ϵ is the gravitational softening (Plummer, 1911). For a larger number of particles, N, direct summation can be extremely computationally expensive.

The spatial tree structure

In order to avoid the high computational demand of N^2 calculations, a spatial tree data structure can be used to group together distant particles, reducing the number of computations needed on each time step significantly. The tree is so-called due to the way that this method is structured. The entire simulation (root) is divided into hierarchical sub-regions (branches) until all particles are occupying a cell (leaves). In Gadget-3, the Barnes and Hut (1986) tree is used, which uses an octree based algorithm, dividing the volume into eight equal cubes and discarding any cubes containing no particles. The force calculations then involves walking the tree (from the root) and summing the force contributions from tree nodes. The centre of mass is calculated for every root. If the position where we want to calculate the force is far away from the root note, we compute only the monopole moment. The gravitational force can then be approximated by the force felt from the total mass of the particles at their centre of mass. If the point where we are calculating the forces is closer however, we also include the monopole moments of the branches and leaves of the respective root note, according to the opening angle of the tree $\theta = l/d$, where l is the size of the node and d is the distance from the point at which the force is being calculate to the centre of mass of the cell. The smaller the value for the opening angle θ, the more accurate the force calculations, but also the more computationally expensive. This tree structure reduces the computational cost to the order of $N \log N$.

Gravitational softening

In Eq. 2.1 we introduced the gravitational softening parameter ϵ. This is used most importantly to avoid a non-zero denominator in the potential calculation. In the absence of gravitational softening in Eq. 2.1, should particles i and j have the same position such that $r_i = r_j$, the result is an infinite acceleration and an infinite velocity change in a given timestep Δt, meaning an infinite change in position. To avoid this, the gravitational softening is introduced to elegantly reduce the consequences of these close interactions by essentially acting as a maximum acceleration a particle can experience. Whilst this acts as a convenient numerical trick, it is not unphysical either when considering at least to first order that the galaxies we are modelling are collisionless systems. The gravitational force from a nearby particle is given by the softened Newtonian potential

$$\Phi(r) = \frac{Gm}{h} W(r/h), \tag{2.2}$$

where h is the smoothing length and W is the softening kernel (Monaghan and Lattanzio, 1985).

The choice of the softening used in a given simulation setup is highly dependent on what is being modelled. Generally speaking however, as a rule of thumb, the softening should be smaller than the mean particle separation by a factor of 10 at least. The description of the Newtonian potential described in equation 2.1 provides the most accurate representation of the true Newtonial potential (for $\epsilon = 0$), however it comes with some disadvantages when it comes to simulating large systems. This calculation requires an $N(N-1)/2$ force computation for N particles in order to compute their spatial evolution over time. It therefore becomes essential to consider optimising this force calculation as simulations increase both in size and resolution.

2.1.2 Smoothed particle hydrodynamics

As discussed above, dark matter and stellar dynamics can be described purely by gravity, but gas is affected additionally by hydrodynamics. The ISM is as a fluid (Draine, 2011), and thus we model it sampled by a discrete set of particles. In Gadget-3, the hydrodynamical forces are calculated using SPH, which was simultaneously introduced by Gingold and Monaghan (1977) and Lucy (1977). We describe here the basics of SPH broadly following a detailed review from Monaghan (1992), as well as the specifics of the implementation in Gadget-3 from Springel et al. (2001); Springel (2005). SPH is just one of the methods that models gas using a Lagrangian approach, whereby a fluid is represented by a finite set of particles.

The fluid equations in Lagrangian form are written as

$$\frac{d\rho}{dt} = -\rho \nabla \cdot \mathbf{v}, \tag{2.3}$$

$$\frac{d\mathbf{v}}{dt} = -\frac{\nabla P}{\rho}, \tag{2.4}$$

$$s = \text{constant}, \tag{2.5}$$

where d/dt is the comoving derivative, s is the entropy function $s \equiv P/\rho^{\gamma}$ where P is pressure, ρ is the density and $\gamma = 5/3$ for an adiabatic equation of state.

Basic equations of SPH

Local averages $\langle f(\mathbf{r})\rangle$ of any quantity $f(\mathbf{r})$ can be estimated by a smoothed kernel weighted integral

$$\langle f(\mathbf{r})\rangle \equiv \int f(\mathbf{r}')W(\mathbf{r}-\mathbf{r}', h)d^3r', \tag{2.6}$$

where $W(\mathbf{r}, h)$ is the kernel function which is usually shaped like a Gaussian distribution with a width h referred to as the smoothing length.

To compute the hydrodynamical forces and the rate of change of internal energy, we must compute the density of the active particles in the simulation as

$$\rho_i = \sum_{j=1}^{N} m_j W(\mathbf{r}_{ij}; h_i), \tag{2.7}$$

where $\mathbf{r}_{ij} \equiv \mathbf{r}_i - \mathbf{r}_j$. h_i here describes the smoothing lengths of each particle, which are necessary to recompute at each timestep. In order to preserve the Lagrangian nature of SPH, the number of neighbours within the smoothing length is ideally kept constant (Nelson and Papaloizou, 1994) in order to reduce noise in SPH estimates of fluid quantities, and so the smoothing length of each particle is adjusted accordingly. W describes the kernel function, which is a function of the relative distances of particles as well as the smoothing length. In Gadget-3, the original cubic spline kernel has been replaced with the Wendland C^4 kernel (Dehnen and Aly, 2012), which tends to be more numerically stable in this regime where the number of neighbours is high (on the order of a 100).

Once the smoothing length and subsequently the density of each particle has been found, the forces can be computed. The equation of motion of a particle i as a function of the pressure and density over its neighbours can be written as

$$\frac{d\mathbf{v}_i}{dt} = -\sum_{j=1}^{N} m_j \left(\frac{P_i}{\rho_i^2} + \frac{P_j}{\rho_j^2} + \Pi_{ij}\right)\nabla_i W(\mathbf{r}_{ij}, h). \tag{2.8}$$

In calculating fluid mixing at contact discontinuities, the hydrodynamical accuracy of SPH is partially dependent on the variables used in the integration of eq. 2.8. Usually, either the density or pressure are paired with the entropy or internal energy (Hopkins, 2013). In the simulations presented in this thesis, we used the pressure-energy implementation such that the pressure is smoothed by construction and has no spurious jumps at contact discontinuities, meaning that fluid instabilities can develop without numerical suppression (Hu et al., 2014). Eq. 2.8 also introduces an artificial viscosity term Π_{ij} (Monaghan, 1997; Springel, 2005), which is introduced to smooth the velocities by inducing an additional repelling force on particles which are separated by a short distance.

Limitations of SPH

SPH is one of the most popular numerical methods owing to its flexibility to a wide range of problems and its ability to achieve a large dynamical range, particularly where gravitational instabilities are important. It well describes the basic dynamics of a fluid whilst conserving mass, momentum and energy. It does however suffer from some issues, most noted is the mixing problems where fluid instabilities are suppressed or prevented (Agertz et al., 2007). Additionally, in situations where the sound speed of the gas is similar or larger than the velocities, SPH tends to be very noisy in these sub-sonic regimes (Bauer and Springel, 2012).

2.2 SPHGal

From here, I describe the numerical implementations adopted in SPHGal (Hu et al., 2014, 2016, 2017), a modified version of Gadget-3 (Springel, 2005) code used for all simulations presented in this thesis. Gadget-3 is a sophisticated hydrodynamical N-body code developed on the hydrodynamical framework of Springel et al. (2001); Springel and Hernquist (2002); Springel (2005). All unresolved astrophysical processes are implemented as sub-resolution models, allowing for the modelling of star formation and stellar feedback for example in simulations with particles representing full populations of stars. In Hu et al. (2016), the original two-phase gas physics using an effective equation of state with a cooling temperature floor (Springel and Hernquist, 2003) has been updated and replaced with non-equilibrium cooling and heating processes including a chemical network for low-temperature gas.

2.2.1 Star Formation

The conditions for star formation in numerical simulations can vary. Commonly used implementations are density or temperature thresholds, or for gas to be virialised or in a convergent flow. The fragmentation conditions of gas can also be approximately characterised by the Jeans (1902) mass,

$$M_{\mathrm{J}} = \frac{\pi^{5/2} c_s^3}{6 G^{3/2} \rho_{\mathrm{gas}}^{1/2}}, \tag{2.9}$$

where c_s is the local sound speed of the gas, G is the gravitational constant and ρ_{gas} is the gas density. The Jeans mass describes the characteristic mass where the self-gravity of the gas cloud exceeds the internal pressure, leading to gravitational collapse.

In the simulations presented in this thesis, for a given gas particle density and temperature, a gas particle becomes eligable for star formation when the Jeans mass satisfies $M_{\mathrm{J}} < N_{\mathrm{thres}} M_{\mathrm{ker}}$, where $M_{\mathrm{ker}} = N_{\mathrm{ngb}} m_{\mathrm{gas}}$ is the SPH kernel mass. We adopt $N_{\mathrm{thres}} = 8$, consistent with Hu et al.

(2017) to properly resolve the Jeans mass for the star-forming gas. We therefore label gas particles with Jeans masses below 8 $M_{\rm ker}$ as 'star-forming'.

For these star-forming gas particles, not all are realised into stars. We adopt a Schmidt (1959)-type star formation prescription, such that the local star formation rate is calculated as

$$\frac{\mathrm{d}\rho_*}{\mathrm{dt}} = \epsilon_{\rm ff}\frac{\rho_{\rm gas}}{t_{\rm ff}}, \tag{2.10}$$

where $\epsilon_{\rm ff}$ is the star formation efficiency per free-fall time, $t_{\rm ff} = \sqrt{3\,\pi/(32\,G\,\rho_{\rm gas})}$ is the gas free-fall time (Binney and Tremaine, 2008), and ρ_* and $\rho_{\rm gas}$ are the stellar and gas volume densities respectively. This $\epsilon_{\rm ff}$ parameter, which varies between 0 and 1, describes the fraction of gas particles eligible for star formation that are realised into stars in a given timestep. It does so in a stochastic manner using a local density-dependent conversion probability

$$1 - \exp\left(- \epsilon_{\rm ff}\frac{\Delta t}{t_{\rm ff}}\right). \tag{2.11}$$

This conversion probability is compared with a randomly generated number drawn from a uniform random number generator during each time step. Should the probability be exceeded, the gas particle is realised into a stellar particle with the same position, velocity and chemical composition as its parent gas particle.

This implementation has been around since the early days of numerical galaxy formation simulations (see e.g. Katz, 1992) and is motivated by the observed inefficiency of star formation on kpc scales in galactic observations (see e.g. Kennicutt, 1998). A typical value for this efficiency is on the order of 2 per cent.

In order to lower the computational expense of our simulations, we enforce an additional star formation threshold introduced in Lahén et al. (2019), whereby gas particles with a Jeans mass less than 0.5 kernel masses are instantaneously formed into stellar particles with a probability of 100 per cent.

When a gas particle is realised into a stellar particle, we stochastically sample from a Kroupa et al. (2001) initial mass function (IMF). For sampled masses above the gas particle resolution adopted of 4 $\mathrm{M}_\odot$, the newly formed stellar particle therefore represents an individual star. For sampled masses below this threshold, the sampled mass is stored until the total sampled mass exceeds 4 $\mathrm{M}_\odot$.

2.2.2 Stellar feedback

Resolving individual massive stars enables the stellar mass-dependent modelling of stellar feedback for different types of stars in the simulation, as well as then being able to quantify the relative effects of each. All stars emit UV radiation, contributing to the interstellar radiation field (ISRF). Massive stars (>8 $\mathrm{M}_\odot$) emit photoionising feedback before ending their lives as core-collapse supernovae.

Radiation

In SPHGal, each young star is an individual source of UV-radiation. The energy emitted by each star in the range of 6-13.6 eV, which dominates the photo-electric heating rate in the ISM, is summed from a given stellar particle (remembering that a stellar particle can represent multiple stars) and the resulting luminosity from each particle is emitted into the surrounding medium. We make use of the assumption of a locally optically thin medium, which is a reasonable approximation for low metallicity dwarf galaxies where the dust content of the ISM is low (<1 per cent of the gas mass). The transfer of radiation can therefore be calculated by summing over radiation field for each star using the inverse square law. For a gas particle, the UV-radiation energy density is given by

$$u_{6-13.6\mathrm{eV}} = \sum_i \frac{L_{i,6-13.6\mathrm{ev}}}{4\pi c r_i^2}, \tag{2.12}$$

where $L_{i,6-13.6\mathrm{ev}}$ is the stellar luminosity which is taken from the BaSeL SED-library (Lejeune et al., 1997; Westera et al., 2002), c is the speed of light and r_i is the distance to each UV-radiating star. By summing along 12 lines of sight accounting for dust and gas absorption and attenuation, we therefore recover an interstellar radiation field, varying in space and time.

We follow photoelectric heating rates from Bakes and Tielens (1994); Wolfire et al. (2003); Bergin et al. (2004) such that

$$\Gamma_{\mathrm{pe}} = 1.3 \times 10^{-24} \epsilon D G_{\mathrm{eff}} n \,\mathrm{ergs^{-1} cm^{-3}}, \tag{2.13}$$

where n is the number density of hydrogen, $G_{\mathrm{eff}} = G_0 \mathrm{e}^{-1.33} D N_{\mathrm{H,tot}}$ is the effective attenuation ration field, D is the dust-to-gas ratio, $N_{\mathrm{H,tot}}$ is the total hydrogen column density and ϵ which is the photoelectric heating rate given by

$$\epsilon = \frac{0.049}{1 + 0.04\psi^{0.73}} + \frac{0.037(T/10^4)^{0.7}}{1 + (2 \times 10^{-4}\psi)}, \tag{2.14}$$

with $\psi = G_{\mathrm{eff}}\sqrt{T}/n^-$, where T is the temperature of the gas and n^- is the electron number density.

Photoionisation

O-type stars emit 32% of their power in $h\nu > I_{\mathrm{H}}$ photons, which can ionise a significant fraction of the surrounding interstellar medium, producing an HII region (Draine, 2011). Dependent on the metallicity of the gas and the temperature of the ionising stars, HII regions are observed to have temperatures on the order of a few 10^4 K (Stasińska, 1990). In our simulations, these HII regions are approximated as Strömgren (1939) spheres, describing an idealised picture of a fully ionised spherical region of uniform density. This approximation allows us to deduce a radius around a photoionising star, such that the rate of ionising photons is in equilibrium with recombination. This Strömgren (1939) radius is then described as

$$R_{S0} \equiv \left(\frac{3Q_0}{4\pi n_{\mathrm{H}}^2 \alpha_B}\right)^{1/3}, \tag{2.15}$$

where Q_0 is the rate of emission of hydrogen-ionising photons ($h\nu > I_H = 13.6$ eV), n_H is the local number density of hydrogen, and α_B is the temperature-dependent hydrogen recombination coefficient, which evaluated at 10^4 K gives $\alpha_{B,T=10^4\ K} = 2.56 \times 10^{-13}$ cm^3 s^{-1}.

In our model, the gas particles within a spherical volume within R_{S0} surrounding each massive star ($M_{initial} > 8\ M_\odot$) are heated to 10^4 K and fully ionised, such that all surrounding molecular and neutral hydrogen is destroyed and transferred to H^+. This approximation holds for a spherical volume of uniform density, however if the density is inhomogeneous, the density of gas estimated at the location of the star may be very different from the density of the neighbouring gas relevant for recombination. Additionally, with two (or more) close-by stars, their Strömgren radii may overlap resulting in double-counting of the photoionised gas. For this reason, the Strömgren sphere is calculated iteratively. With the assumption of ionisation equilibrium, the hydrogen recombination of the neighbouring gas particles should balance the ionising photon budget of the star. Individual neighbouring gas particles each contribute $\beta n_H N_H$ recombinations per second, with the number of hydrogen nuclei $N_H = m_g X_H / m_p$ is the number of hydrogen nuclei and m_g is mass of each gas particle. For each stellar particle, we calculate the total recombination rate R_{rec} by summing over a few of the neighbouring gas particles, giving

$$R_{rec} = \beta \sum_i n_H^i N_H^i. \tag{2.16}$$

In the case of overlapping photoionised regions, any gas particles that have already been photoionised by another star are excluded.

Another consideration is the time scale of photoionisation. In our simulations, the stars begin photoionising the surrounding gas immediately. There would be some delay in the onset of photoionising feedback for a couple of reasons. Firstly, as is explored in Chapter 4, at the densities at which we form stars, the free-fall time of the gas is still on the order of a Myr, meaning that in the fiducial model with no delay time, we do not account for the cloud core collapse timescales of the gas. Additionally, we must ask how long it takes to ionise a H II region, which is considered to be instantaneous in our model. The Strömgren sphere analysis assumes a steady state solution. For an ionising source that turns on instantly surrounded by region of neutral hydrogen, the time to ionise the region is

$$\tau_{ionise} \equiv \frac{(4/3)\pi R_{S0}^3 n_H}{Q_0} = \frac{1}{\alpha_B n_H} = \frac{1.22 \times 10^3 yr}{n_2}, \tag{2.17}$$

where $n_2 \equiv n_H / 10^2$ cm^{-3}. For dense gas surrounding star forming regions, we can deduce that the timescale accounting for the collapse of cloud cores far exceeds the ionising timescale, but can certainly become relevant in lower density environments such as more diffuse H I regions (Draine, 2011).

Even though this is an approximate method, it has been shown to well-capture the physical behaviour of photoionisation, without the computational expense of full radiative transfer methods (see e.g. Rosdahl et al., 2015; Peters et al., 2017).

Core-collapse supernovae

All massive stars with masses greater than 8 $M_\odot$ end their lives as core-collapse supernovae (CCSNe). For a Kroupa et al. (2001) IMF, massive stars account for approximately 20 per cent of the total stellar mass. For every 100 $M_\odot$ formed, that results in approximately one CCSN. In our simulations, every massive star deposits 10^{51} erg of thermal energy into their 100 nearest neighbours at the end of their lives (see e.g. Janka, 2012, for a detailed review on CCSNe), where the lifetimes of all stars are taken from Georgy et al. (2013). As well as depositing energy, the CCSNe also deposit metals into these same neighbours, for which we take the yields for metal enrichment from Chieffi and Limongi (2004). We also take care in the case that the mass of metals distributed to a particle exceeds its own mass by splitting particles that exceed 4 $M_\odot$ following their enrichment. We then offset the position of these two particles by a fifth of the parent smoothing length (in a random isotropic direction) to avoid overlapping particles.

In our simulations, we inject the supernova energy as purely thermal. In simulations which do not resolve individual massive stars, a radially varying fraction of kinetic and thermal energy is used in order to account for the 'overcooling problem', which is where the purely thermal energy gets injected into too many massive gas particles resulting in too modest temperatures. In our particular model, it has been shown that as long as the baryonic mass resolution is below 5 $M_\odot$, the Sedov-Taylor phase is resolved and pure thermal injection recovers well the different evolutionary phases of the supernova remnant (Hu, 2019).

Type Ia supernovae

Type Ia supernovae occur when white dwarf stars accrete material from a binary companion, reaching a sufficient mass to surpass the Chandrasekhar (1931)-limit and explode as a supernova. Following the implementation presented in Aumer et al. (2013), a small fraction of stars with masses lower than 8 $M_\odot$ will explode as Type Ia supernovae with a power-law delay time distribution with $\sim t^{-1}$ where t is the stellar age. Once a star lower than 8 $M_\odot$ has reached the end of its lifetime (according to the stellar lifetimes from Georgy et al., 2013), it becomes a white dwarf star, which then releases mass by sampling the delay time distribution every 50 Myr, as well as metal yields based on Iwamoto et al. (1999). For the isolated low-mass systems considered in this thesis, we currently neglect the contribution from Type Ia supernovae, as only 2 Type Ia supernova progenitors would be produced in a 10^3 $M_\odot$ stellar population (Maoz and Mannucci, 2012), and therefore their contribution in comparison to core-collapse supernovae is very minor for systems in this regime.

Asymptotic giant branch stars

Aysmptotic giant branch (AGB) stars describe the final nuclear-burning phase of all stars in our simulations, other than those that explode as core-collapse supernovae. In our model, the mass returned by AGB stars is modelled with a similar statistical approach to the description of the Type Ia supernovae above. The metal yields are from Karakas (2010), and depend on the stellar metallicity. Additionally kinetic energy is released with outflow velocities of 25 km/s.

2.2.3 Chemistry network

The cooling processes within the ISM depend strongly on the chemical composition of the gas particles. The chemical model used in these simulations closely follows the implementation of the SILCC project Walch et al. (2015); Girichidis et al. (2016) which is based on previous work by Nelson and Langer (1997), Glover and Mac Low (2007) and Glover and Clark (2012). We track the chemical composition of gas and stars following the abundances of 12 elements (H, He, N, C, O, Si, Mg, Fe, S, Ca, Ne and Zn) following the implementation of Aumer et al. (2013), as well as the non-equilibrium evolution of H_2, H^+, H, CO, C^+, O and free electrons. H_2, H^+ and H are followed explicitly, in that their abundances are directly integrated based on the rate equations in the chemistry network. We also include a treatment of carbon chemistry, following Nelson and Langer (1997).

2.2.4 Initial conditions

The setup for most of the simulations in this thesis is an isolated dwarf galaxy, for which we generated the initial conditions using MakeDiskGalaxy (Springel, 2005). The dark matter halo has a virial mass $M_{\rm vir} = 1.98 \times 10^{10}$ M$_\odot$ and a virial radius $R_{\rm vir} = 44$ kpc, following a Hernquist profile with a NFW-equivalent concentration parameter of 10 (Navarro et al., 1997) and a spin parameter of $\lambda = 0.03$. This corresponds to a total halo mass of 2.72×10^{10} M$_\odot$, which is split into 4 million particles, resulting in a dark matter particle mass of 6.8×10^3 M$_\odot$. For these particles we adopt a gravitational softening of 62 pc.

Embedded in the dark matter halo is an exponential baryonic disk of 6×10^7 M$_\odot$, with a gas fraction of 66 per cent resulting in a 4×10^7 M$_\odot$ gas disk and a pre-existing stellar disk of 2×10^7 M$_\odot$. This corresponds to a baryonic fraction of 0.3 per cent, motivated by abundance matching (Moster et al., 2010, 2013). The disk follows an exponential density profile,

$$\rho_{\rm gas} = \frac{M_{\rm gas}}{4\pi R_0^2 z_0} \exp(-R/R_0) \exp(-z/z_0), \tag{2.18}$$

with a scale length $R_0 = 0.73$ kpc and a scale height $z_0 = 0.35$ kpc. The scale length assumes the disc is rotationally supported and that the angular momentum of the disk is 0.3 per cent of the angular momentum of the dark matter halo. The disk scale height is motivated by the fact that dwarf galaxies are generally expected to have a relatively thick disk (Elmegreen and Hunter, 2015). The baryonic particle masses for both gas and stars is 4 M$_\odot$, corresponding to ~ 5 million equal mass inactive stellar particles and ~ 10 million gas particles, for which we use a gravitational softening of 0.1 pc. The metallicity of the gas and stellar particles is set to be 0.1 Z$_\odot$, and the initial temperature of the gas particles is set uniformly to 10^4 K.

Turbulent driving

The initial condition generation described above results in a smooth distribution of gas and stars. Starting a simulation from these conditions results in the gas collapsing rapidly in the z-direction leading to a starburst and creating a hole in the centre of the galaxy (Hu et al., 2016). For

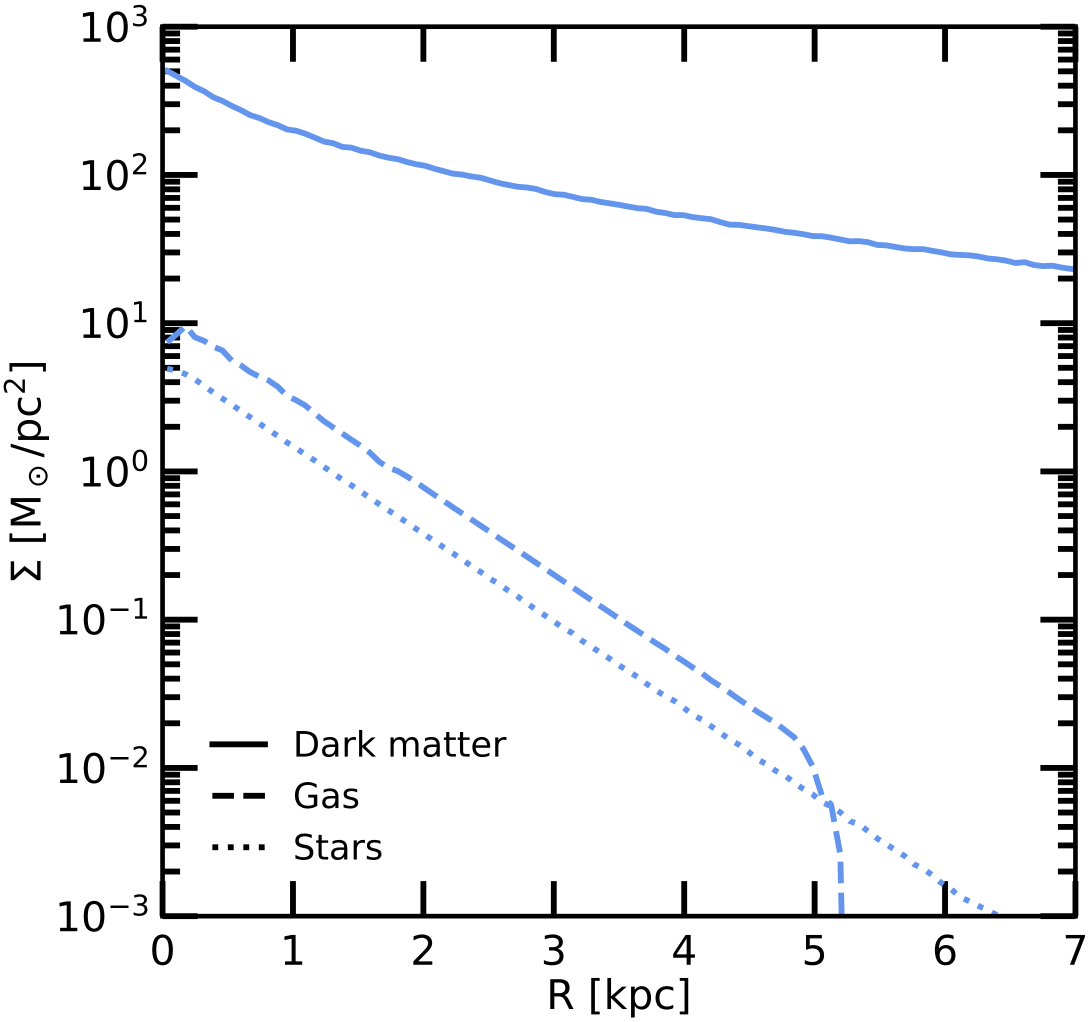

Figure 2.1: Initial conditions for the isolated disk galaxy showing the dark matter (solid line), initial gas distribution (dashed line) and old stellar population (dotted line).

this reason, we introduce some initial turbulent driving into the disk prior to the start of the simulations. Following the generation of the disk as described above, we run the disk with cooling and star formation disabled, and inject 10^{51} erg of energy into overdense gas particles ($n_{\rm gas} > 0.1$ cm^{-3}) and their 100 neighbours for gas particles within a 1 kpc radius from the centre of the disk. This is done in a stochastic fashion, similar to the star formation prescription, with a probability of 2 per cent. After 30 Myr, the result is a gas disk with pre-existing substructure and turbulence, preventing much of the initial collapse of the disk. The density profile for each of the components of the resultant disk galaxy from the initial conditions with the turbulent driving is shown in Fig. 2.1. The exponential profiles of the gas and stars is still visible, however one can notice some small deviations in the gas profile, particularly in the centre due to the turbulent driving creating substructure altering the density profile slightly.

"It is reasonable to hope that in the not too distant future we shall be competent to understand so simple a thing as a star."

Arthur Eddington

3

The challenge of simulating the star cluster population of dwarf galaxies with resolved interstellar medium

We present results on the star cluster properties from a series of high resolution smoothed particles hydrodynamics (SPH) simulations of isolated dwarf galaxies as part of the GRIFFIN project. The simulations at sub-parsec spatial resolution and a minimum particle mass of 4 $M_\odot$ incorporate non-equilibrium heating, cooling and chemistry processes, and realise individual massive stars. The simulations follow feedback channels of massive stars that include the interstellar-radiation field variable in space and time, the radiation input by photo-ionisation and supernova explosions. Varying the star formation efficiency per free-fall time in the range $\epsilon_{\rm ff}$ = 0.2 - 50% neither changes the star formation rates nor the outflow rates. While the environmental densities at star formation change significantly with $\epsilon_{\rm ff}$, the ambient densities of supernovae are independent of $\epsilon_{\rm ff}$ indicating a decoupling of the two processes. At low $\epsilon_{\rm ff}$, gas is allowed to collapse more before star formation, resulting in more massive, and increasingly more bound star clusters are formed, which are typically not destroyed. With increasing $\epsilon_{\rm ff}$ there is a trend for shallower cluster mass functions and the cluster formation efficiency Γ for young bound clusters decreases from 50% to $\sim$ 1% showing evidence for cluster disruption. However, none of our simulations form low mass ($< 10^3$ $M_\odot$) clusters with structural properties in perfect agreement with observations. Traditional star formation models used in galaxy formation simulations based on local free-fall times might therefore be unable to capture star cluster properties without significant fine-tuning.

The content of this chapter is based on the peer-reviewed and published paper Hislop et al. (2022), but includes some small corrections to sec. 3.3.2. All simulations and analysis was performed by the lead author, as well as the vast majority of the paper writing.

3.1 Introduction

Recently there has been significant progress in the optimisation of computer algorithms and in the increased capability of high-performance computing systems. Together with an improved numerical implementation of the physical processes governing the evolution of the galactic interstellar medium (ISM) numerical simulations are able to describe the evolution of entire galaxies including a realistic multi-phase ISM component. This is an important step forward (see e.g. Naab and Ostriker, 2017, for a review) in the understanding of galaxy evolution, as the galactic ISM is the location of all star formation and most of the metal enrichment in the Universe. In addition, the ISM is the driving site for galactic outflows and the origin of most galactic observables at all cosmic epochs.

These next generation simulations have pushed the use of sub-grid models to ever smaller scales. For some cosmological simulations, entire (>100 pc) patches of the ISM are modelled with sub-resolution models (see e.g. Somerville and Davé, 2015, for a review). However, many new high-resolution galaxy formation simulations can resolve the multi-phase ISM structure down to $\sim$ parsec scale. This allows to partially follow important physical processes setting the ISM properties directly, such as the impact of individual supernova (SN) explosions by the approximation of thermal energy injection. Recent simulations also represent the galactic stellar population with increasingly lower mass stellar tracers down to populations of several thousands (e.g. Hopkins et al., 2018; Marinacci et al., 2019; Kretschmer et al., 2022) or several tens to several hundreds solar masses (Hopkins et al., 2011; Renaud et al., 2015; Rosdahl et al., 2015; Dobbs et al., 2017; Agertz et al., 2020; Ma et al., 2020; Jeffreson et al., 2021). The highest resolution studies have even started to trace individual massive stars for isolated galaxy models (e.g. Hu et al., 2016; Emerick et al., 2018; Lahén et al., 2020; Gutcke et al., 2021; Smith et al., 2021; Hirai et al., 2021). While individual stars are the lowest possible resolution element, also these simulations still rely on sub-grid models for estimating the star formation rates, for the sampling of individual stars and, to some degree, for the modelling of their radiation, energy and momentum output. In this study, we focus on the star cluster population properties in simulations of entire galaxies which have the potential to resolve the multi-phase ISM structure as well as the internal structure of star clusters.

The majority of the recent high resolution galaxy formation studies, including those mentioned above assume an underlying simple sub-grid model which estimates the local star formation rate based on the local gas density divided by its free-fall time multiplied with an efficiency $\epsilon_{\rm ff}$ parameter (Schmidt, 1959) [see equation (3.2) below]. The star formation efficiency per free-fall time based sub-grid model is the most commonly adopted model in all numerical galaxy formation research (see e.g. Naab and Ostriker, 2017) and is used with all major simulation methods, i.e. grid codes (e.g. Kravtsov, 1999; Teyssier, 2002; Bryan et al., 2014), moving mesh codes (e.g. Springel, 2010), and particle based hydrodynamics codes (e.g. Springel, 2005; Hopkins, 2015). The different models have varying additional constraints on the properties of the gas particles which become eligible for star formation in the first place. For simulations with resolved ISM this typically refers to the (collapsing) dense and cold gas phase.

The success of this star formation sub-grid model is based on observational evidence at all cosmic epochs that the star formation rate scales with the gas surface density and is an inefficient process (Schmidt, 1959; Kennicutt, 1998; Leroy et al., 2008; Genzel et al., 2010; Tacconi et al., 2013). For typical galaxies the fraction of dense, cold gas turned into stars per free-fall time is low, typically around a few per cent (see e.g. Krumholz et al., 2012) and this simple star formation model easily captures the observed scaling of star formation rate with gas surface density (see e.g. Schaye and Dalla Vecchia, 2008, for a concise overview).

The ability to follow low mass stellar units or even individual stars in galaxy evolution simulations has changed the focus of numerical studies to entire galactic star cluster populations. Together with observationally well determined galactic star cluster properties (see e.g. Portegies Zwart et al., 2010; Krumholz et al., 2019, for reviews) this has opened a new diagnostic window for the small scale structure of the star forming gas and the impact of stellar clustering in galaxy evolution simulations. Star cluster population studies therefore support the scientific validation or falsification of current and novel future theoretical models for the evolution of galaxies with resolved ISM properties.

The origin and impact of clustered star formation is a fundamental question in star formation studies. From observations, we observe star formation to be clustered, although the fraction of stars born in clusters heavily depends on the definition of the cluster (Bressert et al., 2010; Gieles and Portegies Zwart, 2011). Star clusters are observed wherever there is star formation, irrespective of galaxy mass, such as the Small Magellanic Cloud, the Milky Way, or the Antennae galaxies. The stellar clusters are observed to follow uniform cluster mass functions (CMFs) $\mathrm{dN/dM} \propto \mathrm{M}^{\alpha}$ with power law slopes of around $\alpha \sim -2$. The observed normalisations of the CMFs change with the star formation rate of the galaxies and the age of the cluster populations (Fall and Chandar, 2012). Low mass clusters typically disperse quickly, while young massive clusters (YMCs) that we observe today embedded in the ISM might be longer lived and have properties which could make them potential globular cluster progenitors (Longmore et al., 2014; Krumholz et al., 2019).

A fundamental observed property of star clusters is that the number of clusters in star forming galaxies decrease with the age of the cluster population but the slope of the mass function is unchanged (see e.g. Krumholz et al., 2019). There are discussions in the literature whether the cluster formation rate (CFR) follows the global star formation rate, irrespective of galaxy type, meaning that the fraction of stars born in clusters is independent of the star formation rate per unit area (e.g. Chandar et al., 2015; Chandar et al., 2017). Or on the other hand, young star clusters show higher rates of disruption in galaxies with higher gas densities and star formation rates (Bastian et al., 2012) but the fraction of stars born in clusters increases for high star formation rates per unit area (e.g. Kruijssen, 2012; Bastian et al., 2012; Adamo et al., 2020b).

In almost all recent high-resolution galaxy evolution simulations, the normalisation of the star formation rate is regulated by stellar feedback. It becomes independent of the assumed ϵ_{ff} for the dense star forming gas (see e.g. Hopkins et al., 2011, and many other simulations thereafter). However, variations of ϵ_{ff} can change the structure and distribution of newly formed stars, such as cluster sizes, cluster mass functions, and the fraction of stars formed in clusters.

Recently, some of the highest resolution galactic studies have focused on clustering/star cluster properties in galaxy evolution simulations. Renaud et al. (2015) report clusters above 10^5 $\mathrm{M}_{\odot}$ with typical sizes of ~ 5 pc without a clear indication for power-law cluster mass functions. Li et al. (2017) use a cluster formation model combined with a free-fall based star formation model.

They find power law like mass functions for clusters above $\sim 10^3$ $M_\odot$ and cluster formation efficiencies increasing with star formation rate surface densities. In a follow-up study Li et al. (2018) found that the global galactic properties are almost insensitive to changes in $\epsilon_{\rm ff}$ as long as the feedback is sufficient. For low values of $\epsilon_{\rm ff} \leq 0.1$ their cluster age spreads are inconsistently larger than predicted by current observations. They conclude that the range $\epsilon_{\rm ff} = 0.5-1.0$ matches observations best. The cluster formation model, however, does not allow for an investigation of the internal cluster structure.

Assuming a very high local star formation efficiency of $\epsilon_{\rm ff} = 1$, Ma et al. (2020) report cluster mass functions with slope $\alpha \sim -2$ above $10^{4.5}$ $M_\odot$ and typical sizes of ~ 20 pc. These sizes are larger than for observed YMCs in the nearby Universe. High local star formation efficiencies are plausible for dense regions of star forming clouds due to the resemblance of the cloud core mass function and the stellar initial mass function (e.g. Wu et al., 2010; Evans et al., 2014; Heyer et al., 2016; Lee et al., 2016; Vutisalchavakul et al., 2016). In the simulations, "early" stellar feedback before SN explosions then regulates the global efficiencies down to observed values (Hopkins et al., 2020b). However, Ma et al. (2020) report more stellar mass in bound clusters i.e. higher cluster formation efficiencies, in simulations with lower star formation efficiencies. In a recent study, Smith et al. (2021) conclude that the formation of HII regions has the strongest impact on the clustering of SN explosions and the results are independent of the assumed star formation efficiency parameter. Gutcke et al. (2021) also find that SN feedback reduces the clustering of young stars.

On the other hand, Semenov et al. (2018) find a dependence of the galactic depletion time with star formation efficiencies lower than ~ 1 per cent and a decrease of the fraction of star forming gas for efficiencies higher than ~ 1 per cent. In a related study, Semenov et al. (2021) test the effect of variable $\epsilon_{\rm ff}$ and fixed $\epsilon_{\rm ff}$ on the observed spatial de-correlation between star formation and molecular gas (e.g. Kruijssen et al., 2019) with the conclusion that low (~ 1 per cent)/high efficiencies under-/over-predict the spatial decorrelation.

For some of the highest resolution simulations, Lahén et al. (2019) and Lahén et al. (2020) using dwarf merger simulations with 4 $M_\odot$ resolution find clear evidence for power-law star cluster mass functions from a few hundred to $\sim 10^6$ $M_\odot$ with increasing formation efficiency in regions with high gas and star formation rate surface densities. At this resolution, also a first investigation of the internal star cluster rotation/kinematics has become possible (Lahén et al., 2020). These studies have assumed $\epsilon_{\rm ff} = 0.02$ together with a Jeans threshold for immediate star formation. While many star cluster properties for massive clusters ($\gtrsim 10^4$ $M_\odot$) are in good agreement with the observations, the entire star cluster population appears for be more compact than observed, making the observed cluster disruption difficult. In contrast, the results of the model presented in Dobbs et al. (2017) show clear evidence for rapid cluster disruption. However, their simulated clusters have lower densities than observed clusters at a resolution of ~ 300 $M_\odot$ per particle. This would artificially support tidal disruption.

In summary, no high-resolution simulation so far has produced star clusters with formation properties and an evolution history (i.e. disruption) that are in agreement with observations. While power-law mass functions seem to be a general outcome, the star clusters are either too compact and do not dissolve, or when they dissolve they have been too diffuse at their formation.

The aim of this study is to investigate the effect of the star formation efficiency per free-fall time on the properties of star cluster populations in dwarf galaxies. Changing this parameter effectively controls how dense a collection of gas particles is allowed to become before star formation begins, along with the associated stellar feedback. We present a suite of isolated gas-rich dwarf galaxy simulations. These simulations have a gas particle mass resolution of 4 $M_\odot$ and realise individual massive stars with their respective evolutionary tracks as well as modelling their radiation and supernova feedback at sub-parsec spatial resolution. This allows us to realise individual clusters down to the smallest observed cluster masses of $\sim 200\ M_\odot$ in order to examine the effect of varying $\epsilon_{\rm ff}$ on the cluster properties and global galaxy properties.

The simulation suite is a part of the GRIFFIN project[1] (Galaxy Realizations Including Feedback From INdividual massive stars). The aim of this project is to perform galaxy scale simulations of individual galaxies and galaxy mergers (e.g. Lahén et al., 2020) at such high resolution and physical fidelity that individual massive stars can be realised and important feedback processes such as supernova explosions (Steinwandel et al., 2020) can be reliably included to study the formation of a realistic non-equilibrium multi-phase interstellar medium (Hu et al., 2016, 2017; Hu, 2019). As discussed in Naab and Ostriker (2017), the level of detail included in modern numerical simulations is of significant importance as the environmental density of supernova explosions is controlled by stellar clustering as well as stellar feedback processes.

The paper is organised as follows. Sec. 3.2 describes the simulation setup, particularly the star formation model. We describe the global galaxy properties of the simulations in Sec. 3.3 such as the ambient density of star formation and supernovae explosions. We then describe the star cluster analysis. Sec. 3.4 describes how we identify friends-of-friends (FoF) groups and perform an energetic unbinding routine in order to identify bound clusters. We then analyse these FoF groups and bound clusters with a discussion of the CMF, cluster formation efficiency (CFE), ages and sizes. We contrast and discuss these findings on both global and small scales in Section 3.5, before summarising our findings in Section 3.6.

3.2 Methods

3.2.1 Simulation code

All simulations were run using a modified version of the smoothed particle hydrodynamics (SPH) code SPHGal presented in Hu et al. (2014, 2016, 2017), based on GADGET-3 (Springel, 2005). SPHGal is a well tested implementation developed to more appropriately treat fluid mixing, alleviating many of the previously studied difficulties of SPH codes. Gas dynamics are modelled using a pressure–energy formulation (see e.g. Read et al., 2010; Saitoh and Makino, 2013), with the gas properties smoothed over $N_{\rm ngb} = 100$ neighbouring particles using the Wendland C^4 kernel (Wendland, 1995; Dehnen and Aly, 2012). A ‘grad-h’ correction term (Hopkins, 2013) ensures better conservation properties in regions of strongly varying smoothing lengths. The artificial viscosity modelling is updated to better account for converging flows and shear flows (Monaghan, 1997; Springel, 2005; Cullen and Dehnen, 2010). SPHGal also includes artificial conduction of thermal energy in converging gas flows to suppress internal energy discontinuities.

[1]https://wwwmpa.mpa-garching.mpg.de/~naab/griffin-project

Time-stepping is augmented with a limiter to keep neighbouring particles within a time step difference by a factor of four to capture shocks, in particular from SN explosions accurately (see e.g. Saitoh and Makino, 2009; Durier and Dalla Vecchia, 2012). For a more detailed explanation, please see Hu et al. (2014, 2016, 2017).

3.2.2 Initial conditions

All simulations presented in this paper are produced from identical initial conditions, described in Hu et al. (2016). The initial conditions were set up using the method developed in Springel (2005). The dark matter halo follows a Hernquist profile with an NFW-equivalent (Navarro et al., 1997) concentration parameter $c = 10$ with a virial radius $R_{vir} = 44$ kpc and a virial mass $M_{vir} = 2 \times 10^{10}$ $M_\odot$. Embedded in this dark matter halo is a 2×10^7 $M_\odot$ stellar disk as well as a 4×10^7 $M_\odot$ gas disk. The initial disk consists of 4 million dark matter particles, 10 million gas particles and 5 million stellar particles, setting a dark matter particle mass resolution of $m_{DM} = 6.8 \times 10^3$ $M_\odot$ and a baryonic particle mass resolution of $m_{baryonic} = 4$ $M_\odot$. The gravitational softening lengths are $\epsilon_{DM} = 62$ pc and $\epsilon_{baryonic} = 0.1$ pc for the dark matter and baryonic particles, respectively.

In this paper, we present seven simulations, all with identical initial conditions. For six of these simulations, we vary their star formation efficiency per free-fall time ϵ_{ff} between 0 and 50 per cent, which we refer to as `SFE0`, `SFE02`, `SFE2`, `SFE10`, `SFE20` and `SFE50`. We also ran our fiducial model `SFE2` without photoionisation, which we refer to as `SFE2noPI`. For convenience we refer to the simulations with their star formation efficiency percentages in the figures.

3.2.3 Chemistry

Our model for chemistry and cooling closely follows the implementation in the SILCC[2] and the GRIFFIN project (Walch et al., 2015; Girichidis et al., 2016; Hu et al., 2016; Lahén et al., 2019), based on earlier work by Nelson and Langer (1997); Glover and Mac Low (2007); Glover and Clark (2012). We track the chemical composition of gas and stars by following the abundances of 12 elements (H, He, N, C, O, Si, Mg, Fe, S, Ca, Ne and Zn) based on the implementation in Aumer et al. (2013), as well as the non-equilibrium evolution of six chemical species (H_2, H^+, H, CO, C^+, O) and free electrons. The abundances of the first three species are integrated explicitly based on the rate equations within the chemistry network. H^+ is formed via collisional ionisation of hydrogen with free electrons and cosmic rays, and is depleted through electron recombination in the gas phase and on the surfaces of dust grains. H_2 is formed on the surfaces of dust grains and destroyed via interstellar radiation field photodissociation, cosmic ray ionization and collisional dissociation with H_2, H and free electrons.

[2]https://hera.ph1.uni-koeln.de/~silcc/

3.2.4 Cooling & heating

We use a set of non-equilibrium cooling and heating processes, where the processes depend on the local density and temperature of the gas as well as the chemical abundance of species, which may not be in chemical equilibrium. Cooling processes include fine structure lines of C^+, O and Si^+, the rotational and vibrational lines of H_2 and CO, the hydrogen Lyman α line, the collisional dissociation of H_2, collisional ionization of H, and the recombination of H^+. Heating processes include photo-electric heating from an interstellar radiation field, generated by new stars, varying in space and time (Hu et al., 2017), photoelectric effects from dust grains and polycyclic aromatic hydrocarbons, ionization by cosmic rays, photodissociation of H_2, ultraviolet (UV) pumping of H_2, and the formation of H_2. For high-temperature regimes, where $T > 3 \times 10^4$K, the simulations do not follow non-equilibrium cooling and heating processes. Instead, we adopt a cooling function presented in Wiersma et al. (2009) which assumes an optically thin interstellar medium (ISM) that is in ionization equilibrium with a cosmic UV background from Haardt and Madau (2001).

3.2.5 Star formation model

The star formation algorithm samples stellar masses from a Kroupa IMF (Kroupa, 2001) with an upper limit of 50 $M_\odot$. Sampled masses greater than the gas particle mass (4 $M_\odot$) are statistically realised as individual stellar particles. Should the sampled mass be greater than the gas particle mass, the remaining mass is taken from nearby star forming gas particles in order to conserve mass in the simulation. Sampled masses lower than 4 $M_\odot$ are realised as stellar population particles that store the IMF constituents with a mass above 1 $M_\odot$ (see Hu et al., 2016).

Every gas particle has an associated Jeans mass, defined as

$$M_J = \frac{\pi^{5/2} c_s^3}{6 G^{3/2} \rho^{1/2}}, \tag{3.1}$$

where c_s is the local sound speed of the gas, G is the gravitational constant and ρ is the gas density.

A gas particle becomes defined as 'star-forming' only if $M_J < N_{\rm thres} M_{\rm ker}$, where $M_{\rm ker} = N_{\rm ngb} m_{\rm gas}$ is the SPH kernel mass and $N_{\rm thres}$ is a free parameter. As in Hu et al. (2017), we adopt $N_{\rm thres} = 8$ to properly resolve the Jeans mass for the star-forming gas.

For gas particles with Jeans masses between 0.5 $M_{\rm ker}$ and 8 $M_{\rm ker}$ we use a 'Schmidt-type' (Schmidt, 1959) approach to calculate the local star formation rate:

$$\frac{\mathrm{d}\rho_*}{\mathrm{dt}} = \epsilon_{\rm ff} \frac{\rho_{\rm gas}}{t_{\rm ff}}, \tag{3.2}$$

where $\epsilon_{\rm ff}$ is the star formation efficiency per free-fall time, $t_{\rm ff} = \sqrt{3\,\pi/(32\,G\,\rho_{\rm gas})}$ is the gas free-fall time (Binney and Tremaine, 2008), and ρ_* and $\rho_{\rm gas}$ are the stellar and gas volume densities respectively. For gas particles with a $M_J < 0.5$, we enforce instantaneous star formation, as introduced in Lahén et al. (2019).

In this study we explore the effect of varying the star formation efficiency parameter $\epsilon_{\rm ff}$ on the formation of star clusters. In equation (3.2), $\epsilon_{\rm ff}$ is the fraction of 'star-forming' gas which is turned into stars after a gravitational free-fall time. A unit efficiency $\epsilon_{\rm ff} = 1$ describes a star formation rate for which all local star-forming gas is converted into stars on a free fall time. This numerical implementation has its origin in the early days of numerical galaxy formation simulations (see e.g. Katz, 1992) and was motivated by galaxy observations (e.g. Kennicutt, 1998) on kpc scales. Despite higher resolution and physical fidelity of the simulations this star formation model is still being used (see e.g. Semenov et al., 2021). This can be motivated by the finding that a relation between star formation rate and gas density is also valid within star-forming clouds (see e.g. Pokhrel et al., 2021)

By varying $\epsilon_{\rm ff}$, we control how much a region of self-gravitating gas particles is allowed to collapse before stars begin to form. For a collapsing cloud, it is expected that high values of $\epsilon_{\rm ff}$ allow gas particles to be converted into stars while the cloud is still relatively diffuse. Stellar feedback in the form of radiation and SN explosions is more efficient at low densities and might easily disperse the clouds before reaching high densities. A low value of $\epsilon_{\rm ff}$ allows the gas to collapse to higher densities before forming stars. This will generate denser stellar systems and stellar feedback might be less efficient at gas dispersal.

3.2.6 Stellar Feedback

In lower resolution galaxy formation simulations, a star particle typically represents an entire population of stars with an assumed IMF (see e.g. Naab and Ostriker, 2017, for a review). From this, the abundance of massive stars is calculated and subsequently the energy budget of the stellar feedback of each stellar population particle. For the Kroupa IMF used in this study (Kroupa et al., 2001), there is around one type II supernova per 100 $M_\odot$ of formed stars. A given stellar population particle with mass, m_* would inject $(m_*/100\,M_\odot) \times 10^{51}$ erg into the ISM. In the simulations presented here however, we assume a minimum stellar mass of 4 $M_\odot$ representing the low mass part of the IMF. Every massive star expected to form from the assumed IMF is realised individually in the simulation. Therefore, all stars that explode as SN are realised individually. As mentioned in Sec. 3.2.5, particles below 4 $M_\odot$ are realised as stellar population particles with IMF constituents drawn from an IMF with a mass above 1 $M_\odot$.

At this mass resolution and 0.1 pc gravitational force softening in our simulations, individual SNe are well resolved at ambient densities $n < 10\ \mathrm{cm}^{-3}$ (see e.g. Hu et al., 2016, Appendix B). As we show in Section 3.3.2 this corresponds to more than 99 per cent of all SNe in our simulations with photoionisation, and more than 97 per cent for `SFE2noPI`. Explosions at higher ambient density do not capture all details of the Sedov phase but result in the input of the expected amount of radial momentum to the ambient ISM (see Hu et al., 2016; Steinwandel et al., 2020).

We model the photoionisation of hydrogen (PI) by massive stars with a Strömgren approximation assuming the recombination rates balancing the photon production rates. The PI model reproduces well the evolution of D-type fronts (Spitzer, 1998) in good agreement with the StarBench results for different numerical implementations (Bisbas et al., 2015). We note that this model is a good approximation for the local impact of hydrogen ionising radiation but does not accurately follow the radiation field in dwarf galaxies on larger scales (see Emerick et al., 2018, for a discussion).

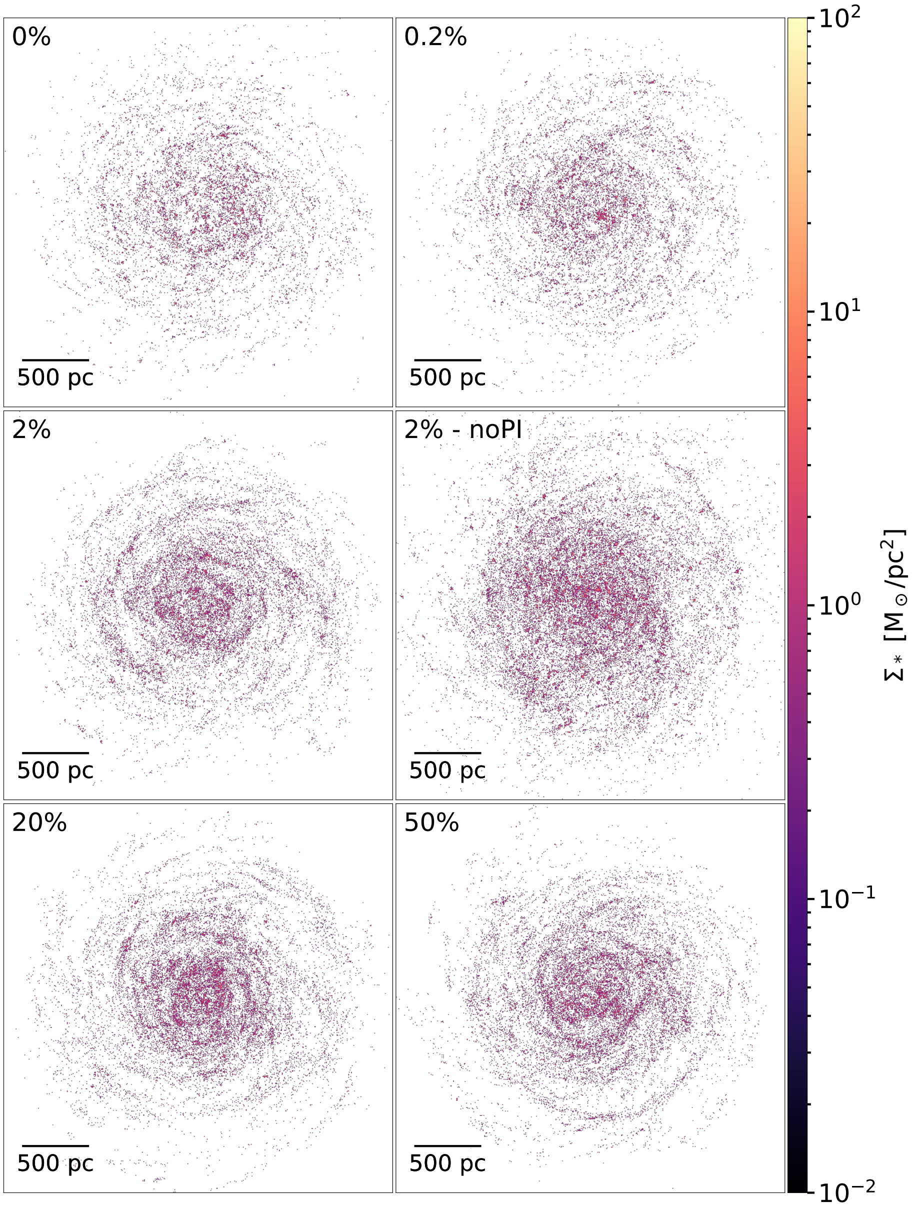

Figure 3.1: Face-on distribution of newly formed stars after 400 Myr for six simulations with increasing star formation efficiency from top left to bottom right. For simulation SFE2 (middle left) we also show the version without the photo-ionisation model, SFE2noPI, (middle right). The stellar surface densities are color coded by $M_\odot/pc^2$. Each image shown is 3×3 kpc^2 plotted with 1024×1024 pixels. Dense and compact star clusters form in the low efficiency simulations with half-mass surface densities as high as 5×10^3 $M_\odot/pc^2$. The most extreme case is SFE2noPI, where we see surface densities as high as 10^4 $M_\odot/pc^2$. At high star formation efficiencies (SFE20 and SFE50, bottom row) the stellar distribution is significantly smoother with fewer and more diffuse visible clusters. This showcases that star formation model parameters and feedback models have a strong impact on stellar clustering.

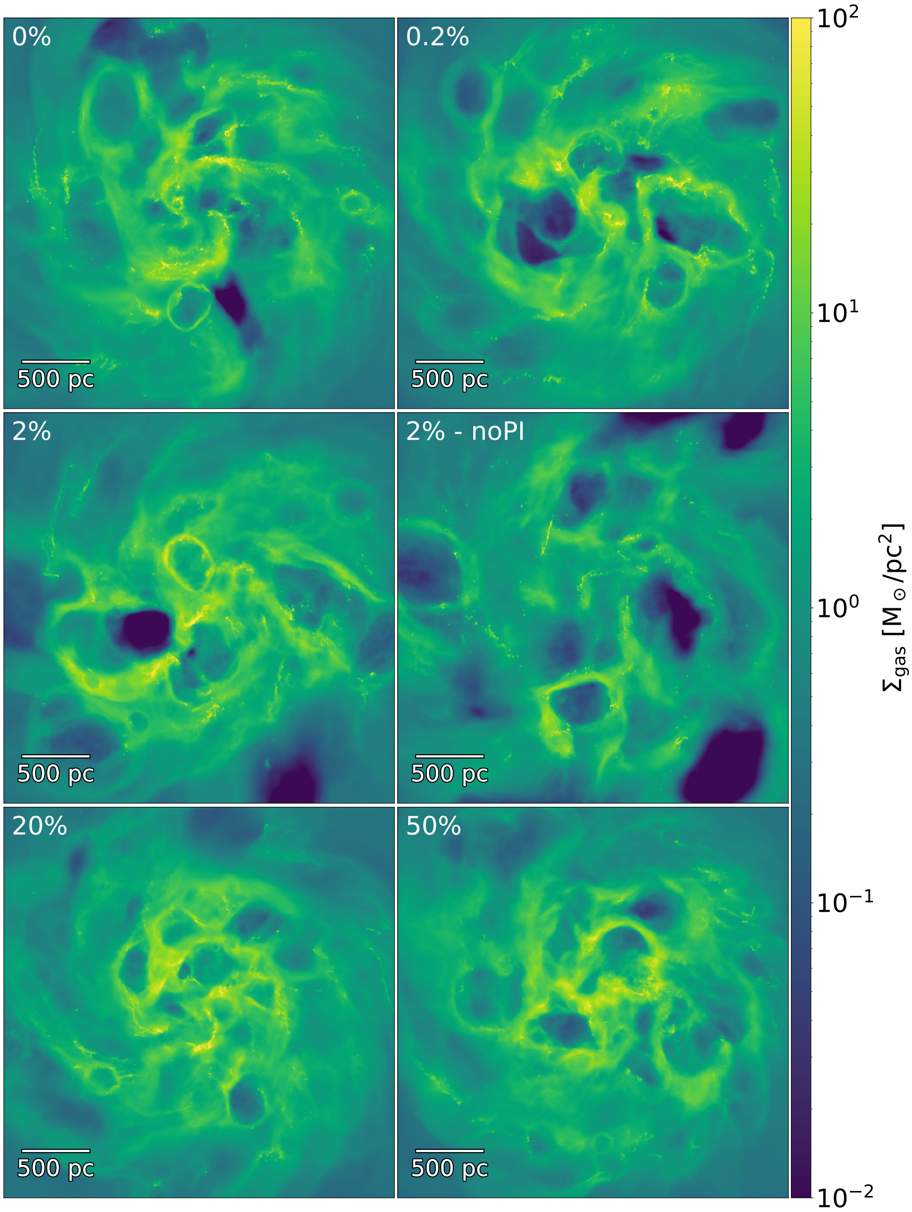

Figure 3.2: Face-on gas surface densities of the six simulations at time t = 400 Myr (see Fig. 3.1 for the stellar distribution). The gas is structured in a diffuse component, dense filaments, and shells generated by photo-ionisation and SN explosions. All simulations with photo-ionisation show similar structure. The `SFE2noPI` model (middle right panel) has less dense gas which is dispersed by the strongly clustered SN feedback from the forming star clusters.

3.3 Galaxy properties

3.3.1 Global properties

In Figs. 3.1 and 3.2 we show the face-on distribution of stars and gas after 400 Myr simulation time for our six simulations. Visually, Fig. 3.1 highlights the differences in the distributions of stars as we increase the star formation efficiency (from the top left panel down to the bottom right panel) as well as the effect of removing the photo-ionisation model (middle right panel). We can see that for low star formation efficiencies (top row), the newly formed stars are more clustered. In contrast, the stellar distributions for the higher star formation efficiency simulations (bottom row) are more smooth, with less clustered star formation. Despite the differences in the stellar distributions, the corresponding gas distributions shown in Fig. 3.2 do not show substantial differences in structure. There might be a slight trend for more low density bubbles in the lower star formation efficiency simulations (top row) in comparison to the higher star formation simulations (bottom row). We also show the 2 per cent model but without photo-ionisation, `SFE2noPI` in the middle right panel of both Figs. 3.1 and 3.2. Here we see significantly stronger clustering in the stellar distribution compared to the corresponding simulation including photo-ionisation, `SFE2`. In addition, about a factor of three more mass in stars has formed in the `SFE2noPI` simulation by t = 400 Myr: $M_*(\texttt{SFE2noPI}) = 1.22 \times 10^6$ $M_\odot$ vs. $M_*(\texttt{SFE2}) = 3.87 \times 10^5$ $M_\odot$. More gas mass has been used up by star formation in the `SFE2noPI` run, which is also reflected in the gas distribution in Fig. 3.2 where we see lower densities in the gas overall as well as more substantial low density bubbles created by strongly clustered SN feedback.

In Fig. 3.3 we show the stellar surface density radial profile of all six simulations at 400 Myr, smoothed over 10 pc. The stellar distributions for the runs with photo-ionisation are very similar, but comparing for example the lowest star formation efficiency `SFE0` with the highest star formation efficiency `SFE50`, we can see that the stellar distribution for the `SFE50` simulation is much smoother. For the same physical model, varying the star formation efficiency therefore does not alter the radial distribution of stars. Instead, it alters how smooth the stellar distribution is. For the `SFE2noPI` run however, we quantitatively see the more efficient transformation of gas into stars by an increased normalisation of the profile. We can also observe the strong clustering in the fluctuations of the surface density.

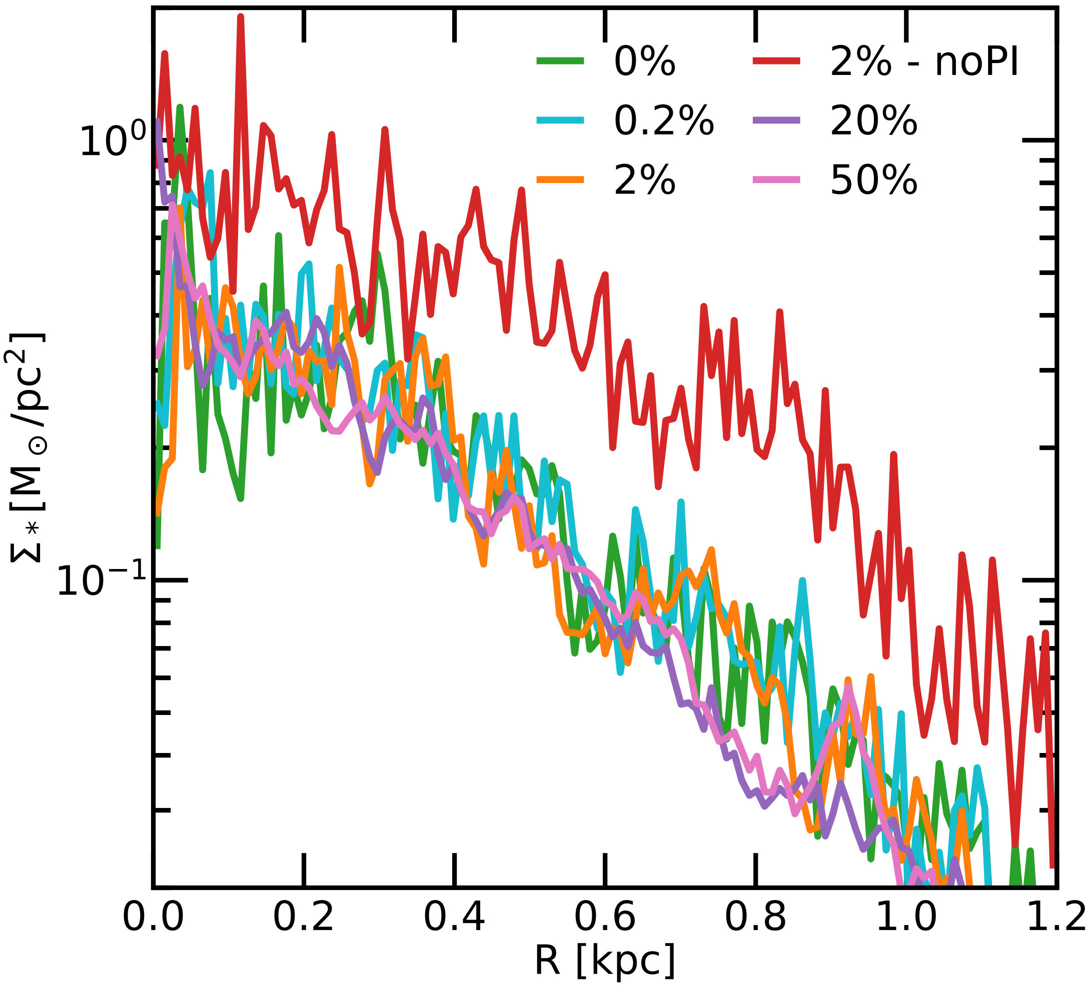

Figure 3.3: Radial stellar surface density profiles for new stars at 400 Myr for each simulation out to 1.2 kpc. The profiles are smoothed over a spatial scale of 10 pc. All simulations apart from `SFE2noPI` have a similar radial structure. The higher star formation efficiencies result in smoother radial profiles which can also be seen qualitatively in Fig. 3.1.

Name	$\epsilon_{\rm ff}$	SFR [10^{-4} M$_\odot$/yr]	η	$f_{\rm SN,A}$	$f_{\rm SN,B}$	α	$\Gamma_{\rm FoF}$	$\Gamma_{\rm BC}$	Age Spread [Myr]	r$_{1/2}$ offset [pc]	$\overline{\rm M_{5mm}}$ [M$_\odot$]	f$_{\rm bound}$
SFE0	**0** %	10 / 8.4	51 / 57	0.64	0.36	-2.9 ± 0.3	0.61	0.57	2.5	-0.7	1933	0.98
SFE02	**0.2** %	10 / 8.6	47 / 52	0.64	0.36	-2.9 ± 0.3	0.59	0.54	2.5	-0.7	2813	0.99
SFE2	**2** %	9.2 / 8.6	54 / 59	0.69	0.31	-2.8 ± 0.3	0.34	0.26	2.6	-0.4	1631	0.88
SFE2noPI	**2** % **- noPI**	25 / 5.6	32 / 124	0.48	0.52	-3.1 ± 0.3	0.64	0.62	3.7	-1.1	5562	0.97
SFE10	**10** %	7.9 / 7.6	50 / 55	0.74	0.26	-1.8 ± 0.3	0.10	0.02	8.1	3.5	526	0.34
SFE20	**20** %	7.9 / 7.2	49 / 52	0.75	0.25	-2.1 ± 0.2	0.10	0.01	6.2	4.9	280	0.30
SFE50	**50** %	7.9 / 7.5	53 / 56	0.75	0.25	-1.7 ± 0.2	0.11	0.02	6.6	8.0	291	0.41

Table 3.1: Summary of simulation properties. $\epsilon_{\rm ff}$: star formation efficiency per free-fall time, no-PI does not allow for HII regions; SFR: average star formation rate calculated between 0-500 Myr / 200-500 Myr; η average mass loading ($\overline{\rm OFR}/\overline{\rm SFR}$) calculated between 0-500 Myr / 200-500 Myr; $f_{\rm SN,A/B}$: fraction of SN exploding at densities higher (A) and lower (B) than $\rho_{\rm ambient} = 10^{-2}$ cm^{-3}; α is the slope of the power-law cluster mass function; $\Gamma_{\rm FoF}$ and $\Gamma_{\rm BC}$: average cluster formation efficiencies for FoF groups and bound clusters (BC) with ages < 10 Myr; Age Spread: average age dispersion of bound clusters; r$_{1/2}$ offset: offset of the half-mass radius from the Brown and Gnedin (2021) relation shown in Fig. 3.13; $\overline{\rm M_{5mm}}$: average mass of the five most massive clusters; $f_{\rm bound}$: fraction of FoF groups identified as bound.

Fig. 3.4 shows the star formation rate (SFR, top panel), outflow rate (OFR, second panel) and the mass loading η for all times in the simulation (third panel) as well as for just 200-500 Myr (bottom panel), defined as the ratio of the outflow rate to the average SFR. All simulations including photo-ionisation settle to similar star formation rates. In the first 50-100 Myr, the peak of the onset of star formation is noticeably higher and slightly delayed at lower star formation efficiencies, as it takes time for the gas to reach the density threshold, but as soon as gas manages to reach the density of 0.5 M_J (discussed in Sec. 3.2.5), we immediately form many stars. This high peak in star formation is then reflected in a strong peak in the outflow rate with a small time lag. This feature is seen in all models, but less so in the higher star formation efficiency runs. Star formation is also more bursty in the `SFE0`, `SFE02` and `SFE2` runs in comparison to the `SFE20` and `SFE50` runs. The reason for this can be explained by comparing the two extreme models, `SFE0` and `SFE50`. For the `SFE50` run, once the gas passes the upper star formation threshold of 8 M_J, these gas particles are defined as star-forming, and statistically 50 per cent per free-fall time of these star forming gas particles will become stars. In this regime, gas does not have to collapse to high densities before forming stars. Neighbouring gas particles will be affected early in the collapse phase by stellar feedback and supernovae after the formation of a star, resulting in a smoother star formation rate. In contrast, the `SFE0` run has no star formation above 0.5 M_J and so gas must collapse to much higher densities before forming stars on a short timescale. The feedback from the formed stars will therefore be more effective in keeping neighbouring star forming gas particles away from that density threshold, drastically halting star formation. This subsequently results in more bursty star formation. Despite these fluctuations, the star formation rates for all models with photo-ionisation stay almost constant across the entire simulation, around 10^{-3} $M_\odot$/yr. The reasons for this are discussed next in Sec. 3.3.2.

Along with the SFR, the outflow rates of each of the simulations with photo-ionisation are very similar, remaining around $4-5\times10^{-2}$ $M_\odot$/yr, showing that the substantial differences in the stellar clustering from the different star formation efficiencies does not seem to effect the outflow rates. Subsequently, the mass loading η of the simulations with photo-ionisation maintain very similar values, keeping a relatively constant value of approximately $\sim 50-60$ from 200 Myr onwards.

For the run without photo-ionisation `SFE2noPI`, things look slightly different. Many stars are formed in the first 150 Myr and then from 200 Myr onwards the star formation is much more bursty, with several periods of no/very low star formation. The outflow rate however remains relatively constant at approximately 7×10^{-2} $M_\odot$/yr as seen in the second panel. When looking at the average mass loading as calculated across the entire simulation as shown in the third panel, we see a slightly lower value in comparison to the runs including photo-ionisation. However, if we only observe the mass loading after 200 Myr and so excluding the initial starburst, we find the mass loading is approximately a factor of two higher in comparison with the same run but including photoionisation (`SFE2`). The values for the SFR and mass loading η are summarised in Table 3.1 where we show both the average values at all times as well as from 200 Myr, excluding any initial starburst in the galaxy. We also check the metallicity of these outflows from each of the simulations and find very little difference. At a typical metallicity of $Z\sim0.13$ $Z_\odot$, the outflows are metal enriched compared to the initial gas phase metallicity of $Z=0.1$ $Z_\odot$.

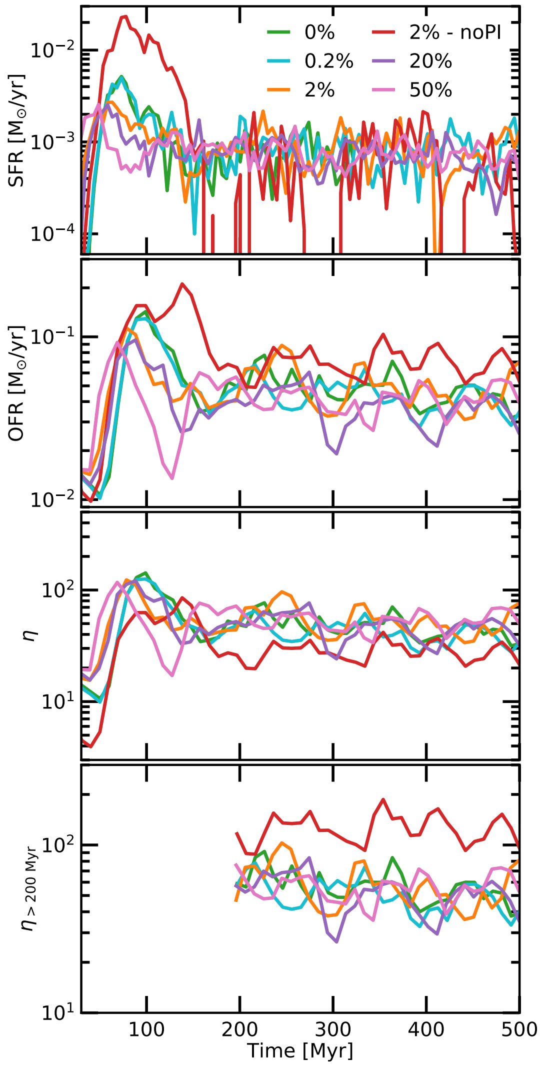

Figure 3.4: *Top panel:* Star formation rates (SFR) for the five different simulations with varying star formation efficiency parameters and the no-photoionisation run. All simulations with photoionisation have similar star formation rates, the one without has a higher average rate and is more bursty. *Second panel:* Gas outflow rate (OFR), which is defined by the gas crossing 500 pc above and below the central disk in 10 Myr intervals. This plot shows relatively similar outflow rates for all simulations at all times during the simulations. In addition we give the average metallicity of the outflowing gas. *Third panel:* Mass loading, η defined as the ratio of the outflow rate to the star formation rate. Here we divide the instantaneous OFR by the average SFR across the entire simulation (0-500 Myr). The simulations show no major differences. *Bottom panel:* Mass loading $\eta_{>200\ \mathrm{Myr}}$ between 200 and 500 Myr. As in the third panel, we show the instantaneous OFR but this time divided by the average SFR between 200-500 Myr, which excludes the initial starburst in each of the simulations. Here we see the mass loading of the run without photo-ionisation (`SFE2noPI`) is a factor of two higher than the corresponding run with photo-ionisation (`SFE2`).

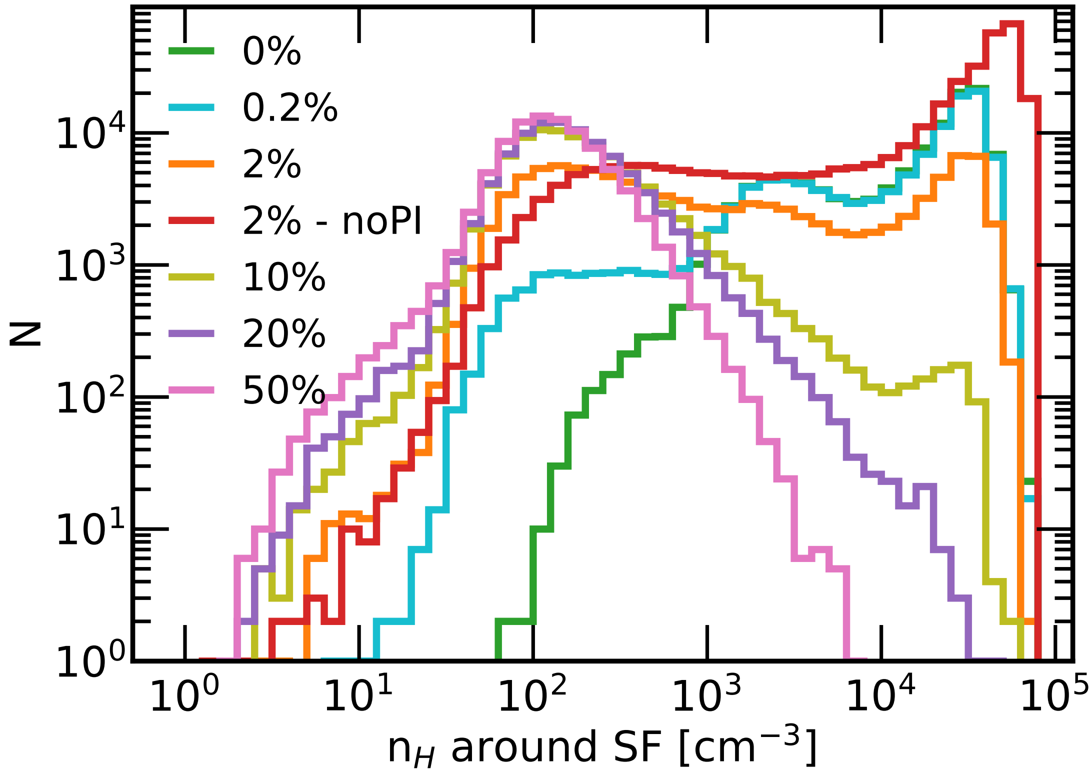

Figure 3.5: Density distribution of gas particles which are turned into stellar particles for all stars present at 400 Myr for all seven simulations. The Jeans threshold of 0.5 M_J is traced by the `SFE0` simulation (0%, green line). For `SFE0`, `SFE02`, `SFE2` and `SFE2noPI` most of the star formation takes place at densities $n_H \gtrsim 10^4\,cm^{-3}$ with more and more extended tails towards lower densities of $\sim 10^2\,cm^{-3}$. In the high efficiency simulations `SFE10`, `SFE20` and `SFE50`, most stars form from gas at densities of $n_H \sim 10^2\,cm^{-3}$ and the gas does not even reach the several orders of magnitudes higher threshold densities of e.g. `SFE0`.

3.3.2 The ISM densities for star formation and supernova explosions

Do we have an explanation for why the star formation model presented here results in similar star formation and outflows rates (see Fig. 3.4) despite the large differences in star formation efficiency? In Fig. 3.5 we show the density distribution of the gas particles which are transformed into stars. These density distributions vary significantly for different models. The density distribution without a free-fall time based star formation `SFE0` (0 %, green), traces the threshold of 0.5 Jeans masses in the SPH kernel for cold gas from a density of $n_H[T = 10\,K] \approx 5 \times 10^2\,cm^{-3}$ to $n_H[T = 100\,K] \approx 5 \times 10^5\,cm^{-3}$. The `SFE02` simulation (0.2 %, blue) has a similar distribution with an emerging lower density tail due to the additional possibility for lower density gas to experience free-fall time based star formation. Still the gas densities peak in the range $\sim 10^4 - 10^5\,cm^{-3}$. In the fiducial `SFE2` run (2%, orange) even more star formation at low densities is possible and the distribution becomes broader with a second lower density peak emerging

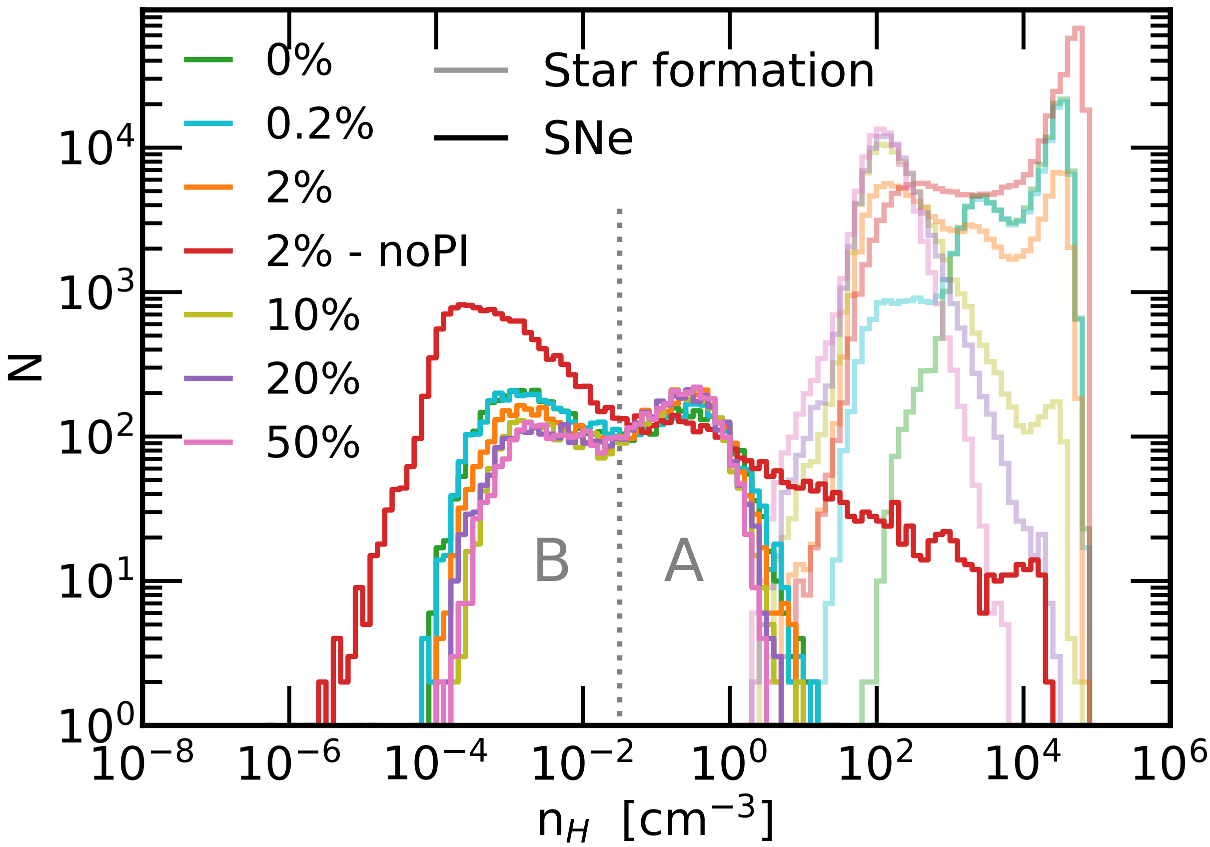

Figure 3.6: Ambient density distributions of SNe explosions within the first 400 Myr (bold lines) compared to the star formation densities from Fig. 3.5. The various simulations are indicated by different colors. The SNe explode at several orders of magnitude lower ambient densities than the stellar birth sites with a double peaked distribution, characteristic for all simulations. One peak (A) is at $\sim 10^{-0.3}$ cm^{-3}, the second peak (B) is at lower densities of $\sim 10^{-3}$ cm^{-3}, and there is a minimum at $\sim 10^{-2}$ cm^{-3}. The `SFE2noPI` (2% - noPI) has a higher SN rate. Less than 2 per cent of the SNe explode at densities higher than $n_H \sim 10$ cm^{-3} indicating that they have no memory of their birth places.

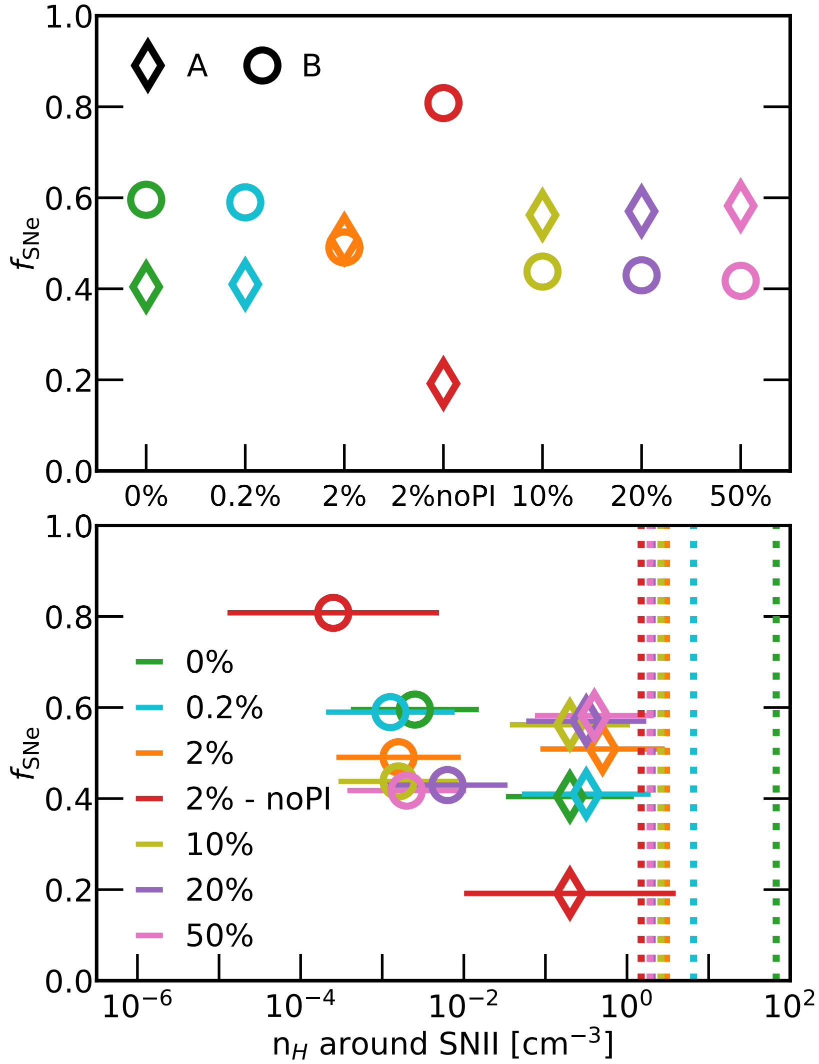

Figure 3.7: *Top panel:* Fraction of SNe exploding at environmental densities higher (A, diamonds) and lower (B, circles) than 10^{-2} cm^{-3} (regions A and B in Fig. 3.6) for the different simulations. SNe at higher ambient densities dominate. With increasing star formation efficiency the fraction of SNe at low environmental densities decreases. This can be connected to lower cluster formation efficiencies (see Sec. 3.4) and therefore less clustered SN events. The simulation without photo-ionisation (red symbols) show an inverted behaviour with the lower ambient densities becoming dominant. *Bottom panel:* Fraction of core collapse SNe in the high (A, diamonds) and low (B, circles) density regime as a function of ambient density. The colour coding is the same as in the top panel. The symbols indicate the density peaks and the horizontal bars show the dispersion. The dotted vertical lines indicate the lowest star formation densities in each of the simulations (see Fig. 3.6). All simulations with photo-ionisation have similar higher (A) and lower (B) density peaks of $\sim 10^{-0.3}$ cm^{-3} and $\sim 10^{-3}$ cm^{-3}, respectively. For the `SFE2noPI` (2% - noPI) simulation, the peaks are shifted to slightly lower ambient densities. In contrast to the other simulations, more than half of the SNe explode at lower densities.

at $\sim$ 100 cm^{-3}. The corresponding simulation without photo-ionisation (red) shows a similar distribution but with a larger fraction of stars forming at densities higher than $\sim$ 100 cm^{-3}. The high star formation efficiency runs `SFE20` and `SFE50` (20%, purple; 50% pink) do not reach high enough star formation densities to hit the Jeans threshold but form all their stars in the free-fall regime between 8 and 0.5 Jeans masses. As a consequence, star formation mostly takes place at gas densities of $\sim$ 100 cm^{-3}. Comparing the models as we decrease $\epsilon_{\rm ff}$ for example from `SFE50` to `SFE10`, we observe an increase in star formation at higher densities above 10^4 cm^{-3} and a decrease in the number of stars formed at lower densities, as we would expect. In summary, the ISM density distributions at which the stars form are qualitatively different when the star formation efficiency is varied.

In Fig. 3.6 we compare the star formation densities shown in Fig. 3.5, now repeated as lightly shaded lines, to the distribution of the ambient ISM densities at which the massive stars explode as supernovae shown as the solid lines. In contrast to the star formation densities, all simulations including photo-ionisation show a similar behaviour for the ambient SN densities. The vast majority of the SNe explode at densities lower than the densities of star formation with two peaks: a first peak (A) at $n_{\rm H} \sim 10^{-0.3}$cm^{-3} and a second peak (B) at lower densities of $n_{\rm H} \sim 10^{-3}$cm^{-3}. For simplicity we have separated the ambient density distributions at a single fiducial density of $n_{\rm H} \sim 10^{-2}$, which approximately corresponds to the local minimum, into a "high" density region A and a "low" density region B. For the simulations with photo-ionisation, the majority of SNe explode at higher ambient densities (region A) while the number becomes about equal for `SFE2noPI` (2% - noPI). The distribution of densities also becomes broader with the exclusion of photo-ionisation. Very few ($\lesssim$ 2 per cent) SNe explode at high densities $n_{\rm H} \gtrsim 10$cm^{-3} while typical stellar birth densities are much higher. An observational study by Hewitt and Yusef-Zadeh (2009) has used masers as signatures of supernovae remnants (SNRs) interacting with molecular clouds. Assuming the survey to be complete, they find around 15 per cent of SNRs are maser emitting. In the simulations, however, we only track the local ambient density at the time of the explosion. Some expanding supernova remnant shells may interact with dense gas thereafter.

In the top panel of Fig. 3.7 we show the fraction of SNE exploding in the high and low ambient density regimes A and B for all simulations. More than 60 per cent explode at higher densities and the fraction is increasing for simulations with high star formation efficiencies. The `SFE2noPI` (2% - nophoto) simulation shows about equal numbers of SNe in both regions. The bottom panel of Fig. 3.7 show the SN fractions as a function of the peak densities in the two regimes. The peak densities are very similar for the simulations including photo-ionisation and slightly lower for the one without. The bars indicate the dispersion in density. The lowest star formation densities indicated by the vertical dashed lines hardly overlap with the densities at explosion time. This indicates that the stars have "forgotten" about their birth environment as soon as they explode as SNe, i.e. the typical massive star explodes in a completely different environment than where it was born and this environment appears to be "universal" and independent of the details of the star formation model. This is a plausible explanation for why the outflow rates of the models with different star formation efficiency are so similar (see Fig.3.4) in all models. The SNe couple to the ISM in a very similar way.

We suggest that most SNe explode at typical ISM densities (region A) for these dwarf galaxy systems, which is dominated by neutral gas in equilibrium. At lower ambient densities (region B in Fig. 3.6) SNe explode in pre-processed environments, mostly affected by previous nearby SNe explosions. Qualitatively, these results agree with previous simulations investigating SN ambient density distributions (e.g. Hu et al., 2017; Peters et al., 2017).

3.4 Identifying Star Clusters and their Properties

In this section we discuss how we identify clusters of stars in our simulations as well as the properties of these clusters in the different simulations. Note here that we primarily only discuss four of the seven simulations previously shown, `SFE02`, `SFE2`, `SFE20` and `SFE50`. The cluster properties from the `SFE0` simulation are very similar to the `SFE02` simulation, whilst the `SFE10` population is very similar to the `SFE20`.

We identify clustered stars in the simulations using a friends-of-friends algorithm (FoF, see e.g. Davis et al., 1985) with a linking length of 5 pc. For each FoF group, which represents a star cluster, we impose a minimum of 35 stars (see e.g. Lada and Lada, 2003) as well as a minimum mass of 200 $M_\odot$ for the analysis. Following the FoF analysis, we perform a binding energy analysis as described in Section 3.4.2 on each of these FoF groups to determine if it is a bound cluster. Throughout this paper, effort is made to distinguish between:

- ***FoF groups***: Physical associations of stars identified by the friends-of-friends algorithm. Observationally, this corresponds to stellar associations and star clusters.

- ***Bound clusters***: Bound groups of stars verified by the unbinding procedure described in Section 3.4.2. These are observed as bound star clusters.

3.4.1 Virial Analysis

To determine if a FoF group is a bound cluster, we perform a virial analysis by calculating the kinetic and potential energies of all stellar particles in a given FoF group. The kinetic energy is calculated using the velocities normalised to the center-of-mass motion of the FoF group. The potential energy is computed directly by calculating the potential between each pair of particles. We only consider stars and exclude gas or dark matter from this analysis. The virial parameter for each FoF group is calculated as $\alpha_{\rm vir} = -U/2K$ where U is the sum of the potential energies and K is the sum of the kinetic energies of all stellar particles within the FoF group. An α parameter of more or equal to one therefore denotes a bound star cluster.

Fig. 3.8 shows the virial parameters of FoF groups with ages less than 20 Myr formed between 200 and 500 Myr in the simulation, prior to the unbinding procedure, described later in Sec. 3.4.2. By plotting the FoF groups younger than 20 Myr, we capture how bound the stellar groups are shortly after their formation.

With increasing star formation efficiency, we see a decrease in total number and a decrease of the typical virial parameter of the FoF groups. It is important to note that plotted here are simply physical associations, and therefore these groups of stars are likely to contain contaminate stars. It is however interesting to see that such a high fraction of identified FoF groups which are still likely to contain contaminating stars have such high virial parameters for the `SFE02` and `SFE2`

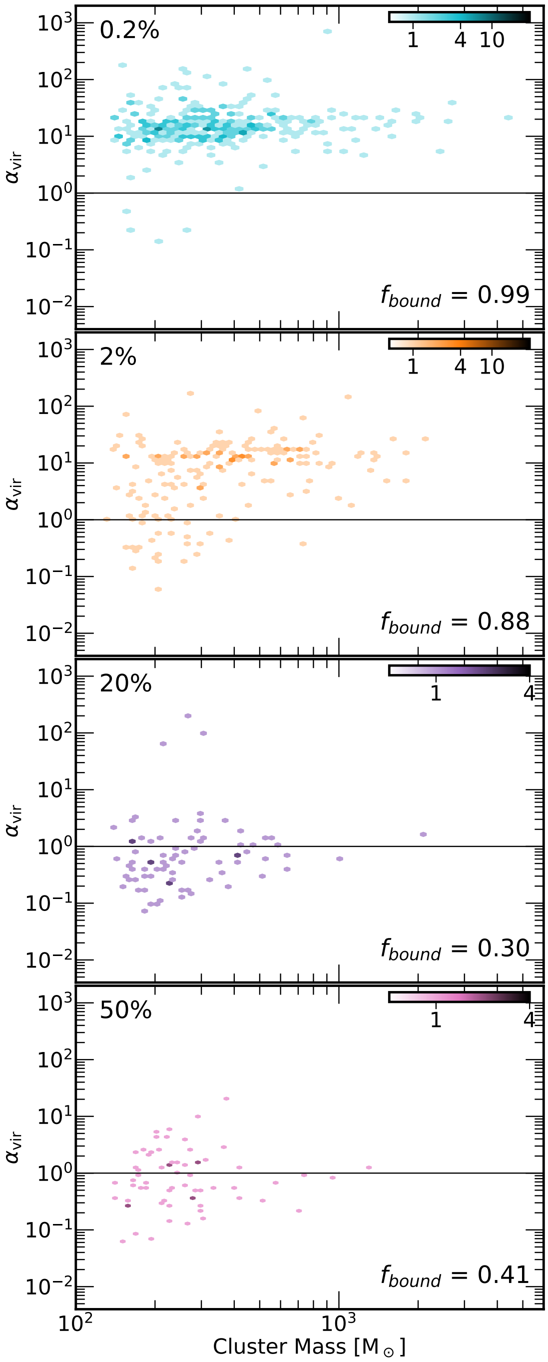

Figure 3.8: Virial parameter $\alpha_{\rm vir}$ as a function of cluster mass for identified FoF groups in four simulations with increasing star formation efficiency from top to bottom. The colourbar shows the number of clusters in each hexbin. We show all FoF groups with stellar ages younger than 20 Myr between 200 and 500 Myr in 20 Myr intervals. The fraction of bound groups (virial parameter larger than unity, horizontal line), $f_{\rm bound}$ decreases from close to unity to $\sim$ 0.4 With increasing star formation efficiency. Also the total number of identified stellar groups decreases.

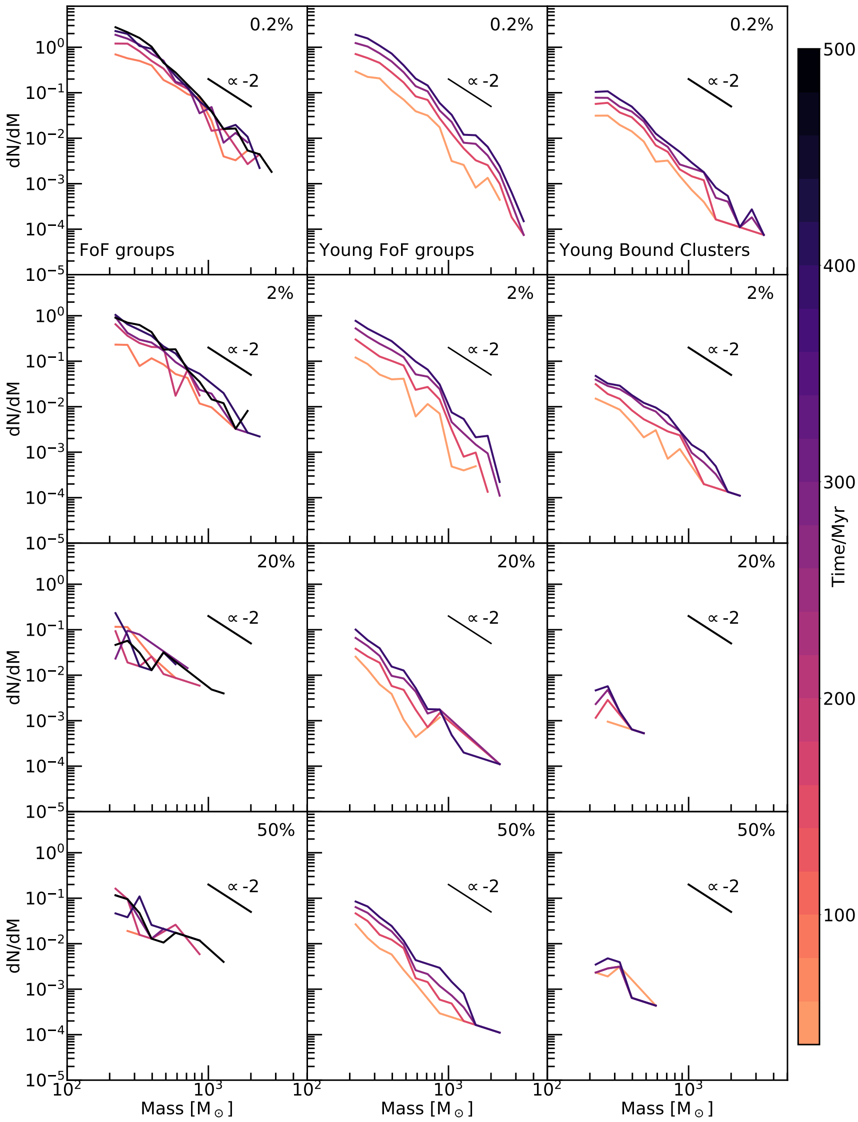

Figure 3.9: Cluster Mass Function (CMF) of all FoF groups and clusters identified in the `SFE02`, `SFE2`, `SFE20` and `SFE50` simulations. The observed slope of around -2 has been added to guide the eye. *First column:* FoF groups of all ages. *Second column:* Young FoF groups with ages less than 20 Myr. *Third column:* Young Bound Clusters with ages less than 20 Myr. The Young Bound Clusters are thus capturing the CMF with which star clusters are born. Due to low number statistics particularly of the `SFE20` and `SFE50` runs, here we have stacked the Young FoF groups and Young Bound Clusters with ages less than 20 Myr in 20 Myr intervals. Each interval contains groups/clusters identified between 100-180 Myr, 200-280 Myr, 300-380 Myr and 400-480 Myr. All of the simulations have CMFs with slopes visually consistent with -2, however the slopes are quantified fully in Figure 3.10. It is important to note that even with stacking, the low number of FoF groups clusters present in the `SFE20` and `SFE50` runs means that making any statements or ruling out any of the models based on the CMF is not possible.

runs. Jumping from SFE2 to SFE20 however shows a steep decrease in the fraction of bound clusters. These higher star formation efficiencies result in a high fraction of FoF groups with virial parameters below 1. Some of these clusters are truly unbound but some are also contaminated with high velocity stars. The unbinding procedure explained in Section 3.4.2 removes these contaminate stars. One can note that the bound fraction increases again from the SFE20 to the SFE50 run, but with a very low number of FoF groups identified in these simulations, this is likely just low number statistics.

3.4.2 Unbinding procedure

As described in Section 3.4.1, we calculate the overall potential and kinetic energies of the FoF groups in order to determine if they are bound. Therefore, following the FoF analysis which identifies physical associations of stars, we perform an energetic analysis of the FoF groups in order to remove contaminating stars (or determine if they are completely unbound). This is done by first sorting the stars by their distance from the centre of mass and then calculating the potential energy of every member of the FoF group in relation to the other members. Working from the outside of the FoF group inwards, a star is defined to be bound if its potential energy exceeds its kinetic energy (normalised to the bulk motion of the overall FoF group in relation to the galaxy). When a star is determined to be unbound, it is removed from the group and the potential energies of the remaining stars are updated to exclude it. This is repeated for all stars within a FoF group. When a FoF group survives this procedure, that is at least 35 members remain (following the definition from Lada and Lada, 2003), the FoF group becomes classified as a bound cluster.

3.4.3 Cluster mass function

In Fig. 3.9 we show the mass function for the SFE02, SFE2, SFE20 & SFE50 simulations (from top to bottom) and FoF groups, young FoF groups and young bound clusters (from left to right). The mass functions are plotted at different times as indicated by the colour bar. For comparison we show a typical mass function with a power-law slope of −2 (e.g. Larsen, 2009; Gieles, 2009; Zhang and Fall, 1999; Vansevičius et al., 2009; Portegies Zwart et al., 2010) in each panel. Such a slope is favoured by observations. We find a very low number of clusters in the SFE20 and SFE50 runs. We therefore decide to stack the young FoF groups together, as well as the bound clusters. The reason for this is simply to increase the number of clusters. Without stacking, for the SFE20 and SFE50 runs, identifying a slope becomes difficult. The second and third columns therefore show the stacked cluster mass function (CMF) of young FoF groups and young bound clusters, respectively, with average ages of less than 20 Myr. The third column therefore captures the CMF in which bound clusters form.

The average slopes from Fig. 3.9 are summarised in Fig. 3.10, showing the slope α of the CMF plotted as a function of the star formation rate surface density $\Sigma_{\rm SFR}$. The $\Sigma_{\rm SFR}$ is calculated within a circle of 1 kpc placed over the face-on disk and 500 pc above and below the plane of the disk. This encompasses >99% of star formation in the disk for all simulations. For α, we see that increasing the star formation efficiency parameter results in shallower slope. We find that both the slope of the FoF groups as well as the bound clusters are both in agreement with −2, implying that this slope is universal and not just for bound structures. This ties into the hierarchical distribution of star formation where clouds, stellar associations as well as bound star clusters all broadly follow a slope of −2 (Elmegreen, 2011). As mentioned, a slope of approximately −2 is the broadly accepted value of the cluster mass function of observed star clusters, however there is some variation in the literature. Adamo et al. (2020a) find a slope of between -1.5 and -2 for a population of star clusters within the Hubble imaging Probe of Extreme Environments and Clusters (HiPEEC) survey. Chandar et al. (2017) find a slope of −2 is consistent for a range of masses of objects, and it is worth noting that they also split their clusters by age and find no change in the slope, only in the normalisation of the CMF. From our simulations, young bound clusters formed in the `SFE20` and `SFE50` runs have slopes close to −2, therefore from the CMF alone, this supports a higher value for $\epsilon_{\rm ff}$. This, however, is based on a small number of clusters. Something to consider is that observations are naturally biased towards more massive clusters. However, when correctly taking incompleteness into account, there should not be a large effect on the slope of the CMF.

3.4.4 Cluster formation efficiency

In the top panel of Fig. 3.11 we show the time evolution of the total mass of stars formed (dashed lines) as well as the total mass of stars in bound clusters (solid lines) and the mass in young bound clusters with ages younger than 10 Myr (dotted lines). For the low star formation efficiency runs (blue and orange), we see a similar trend. The mass in bound clusters (all ages, solid line) increases steadily with the mass of stars formed (dashed line), indicating we have a constant fraction of stars in bound clusters at any given time. This is shown quantitatively in the bottom panel by the open circles which show the fraction of mass in bound clusters of all ages. We observe a roughly constant fraction of ~ 0.5 for the `SFE02` and ~ 0.2 for the `SFE2` run. The cluster formation efficiency (CFE, Γ) is usually defined as the fraction of the mass in young stars that have formed in clusters (see e.g. Elmegreen and Efremov, 1997; Kruijssen, 2012), which is shown in the bottom panel of Fig. 3.11 with filled circles. For the low efficiency runs, this value remains roughly constant (solid blue and orange circles, bottom panel of Fig. 3.11) indicating that newly formed clusters, which are all very bound (see Fig.3.8), are not disrupted. For the high efficiency runs `SFE20` and `SFE50`, the situation is quite different. Both the mass in bound clusters at all ages (pink and purple solid lines, top panel of Fig. 3.11) and the mass of newly formed clusters (pink and purple dotted lines) stay constant. The total mass in young bound clusters remains constant, whilst the stellar mass steadily increases. We see that the fraction mass formed in young clusters (filled pink and purple circles, bottom panel of Fig. 3.11) stays roughly constant, whilst the overall mass in clusters decreases (open pink and purple circles). This is clear evidence for the disruption of bound clusters in these simulations. We also find in 46 per cent and 17 per cent of snaps in the `SFE20` and `SFE50` runs we do not identify any clusters at all. Qualitatively, we have seen this behaviour already Fig. 3.1 where the stellar distribution is more smooth for the higher SFE runs. Clusters with a lower virial parameter are less bound (see Fig. 3.8) and therefore more susceptible to internal and external disruption processes.

We take the average CFE between 300 and 500 Myr from Fig. 3.11 and show this as a function of the corresponding average star formation rate surface density $\Sigma_{\rm SFR}$ in Fig. 3.12 for

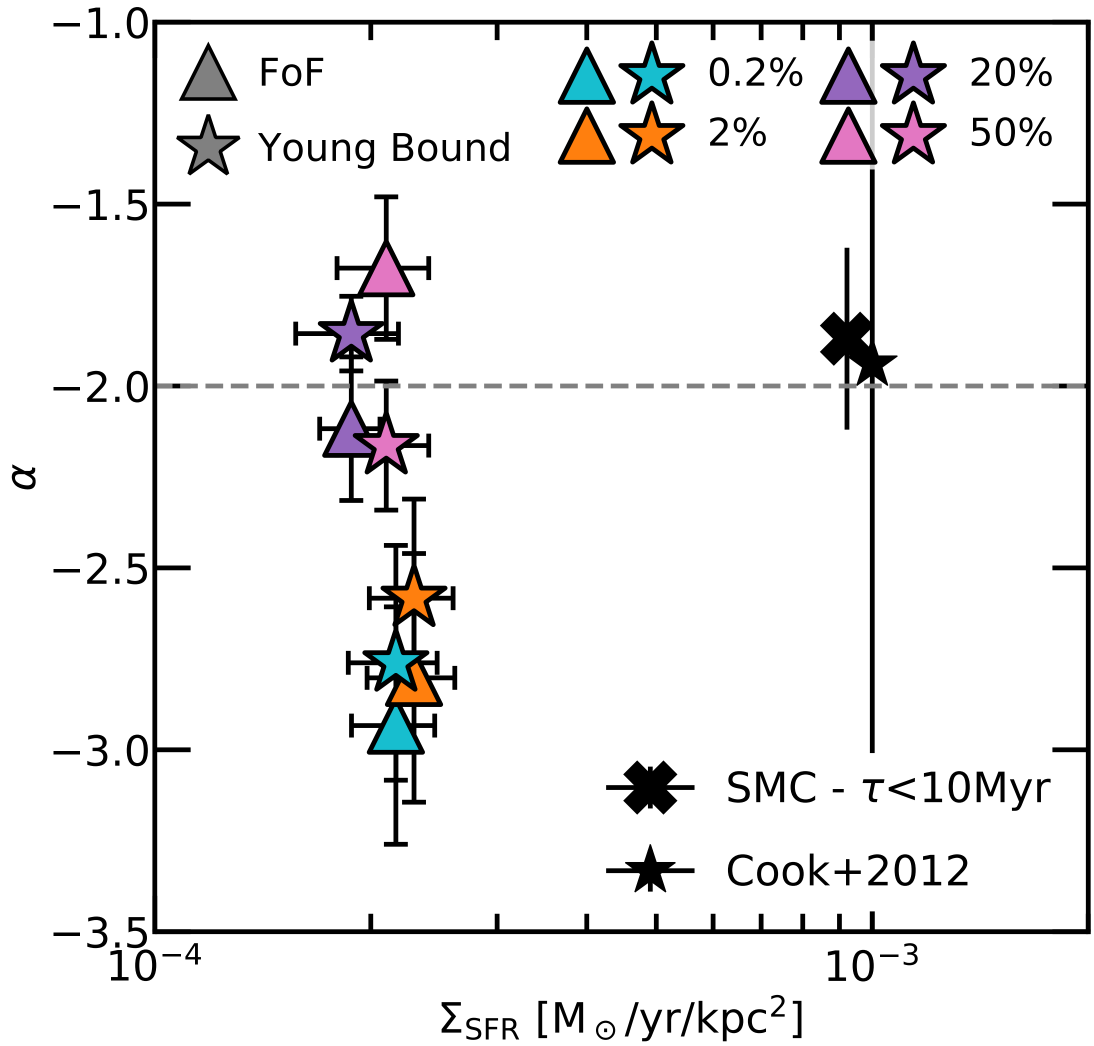

Figure 3.10: The slope, α of the cluster mass function (dN/dM) as a function of the star formation rate surface density. Both quantities are averaged between 300 to 500 Myr. The slope is shown for FoF groups (triangles) and bound clusters younger than 10 Myr in age (stars) with the colours representing the different simulations. Vertical error bars here show the standard deviation from the fit of α and horizontal error bars show the standard deviation of the mean Σ_{SFR} averaged over 300-500 Myr. We see that lower ϵ_{ff} results in steeper slopes of the cluster mass function.

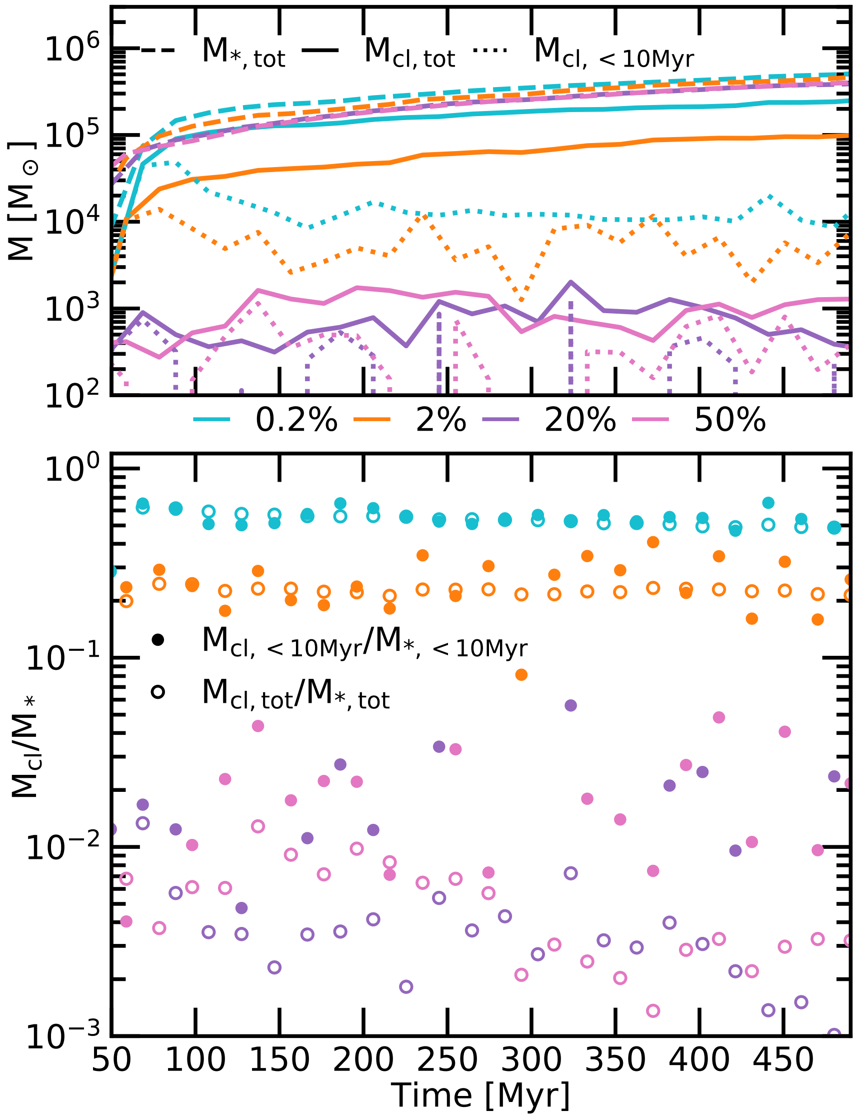

Figure 3.11: *Top panel:* Time evolution of the total mass of newly formed stars (dashed line), stellar mass in bound clusters (solid line) and stellar mass in young bound clusters with ages less than 10 Myr (dotted line). At low star formation efficiencies, `SFE02` and `SFE2`, the total mass in clusters (solid line) follows the stellar mass build up as the clusters are not disrupted. For the higher efficiency runs (`SFE20` and `SFE50`) the mass in bound clusters at all ages stays constant, indicating the disruption of bound clusters. *Bottom panel:* Time evolution of the mass in clusters as a fraction of the total stellar mass. Filled circles show the cluster formation efficiency, defined as the fraction of young (<10 Myr) stellar mass in bound clusters. Open circles represent the fraction of mass in bound clusters of all ages. We do not identify any young clusters in 46 per cent and 17 per cent of the time for the `SFE20` and `SFE50` runs respectively.

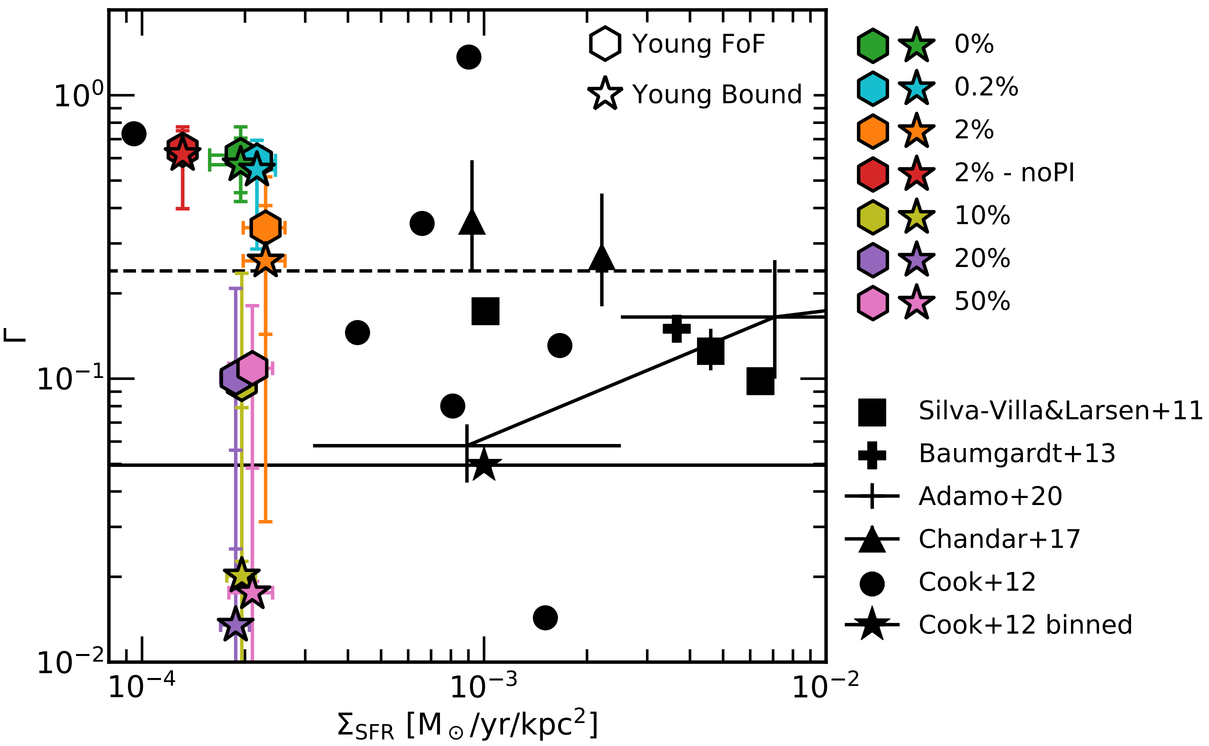

Figure 3.12: Average cluster formation efficiency Γ for each model for young FoF groups (crosses) and young bound clusters (circles) as a function of average star formation rate surface density, Σ_{SFR}. Averages are calculated by taking the cluster formation efficiency of FoF groups or bound clusters with ages younger than 20 Myr at 20 Myr intervals in the simulations between 300 and 500 Myr. We show observational data of NGC6946, NGC45, and NGC7793 (Silva-Villa and Larsen, 2011), LMC (Baumgardt et al., 2013) as well as the median of a collection of data compiled in a review by Adamo et al. (2020b) for young clusters with ages younger than 10 Myr. We also show data for the SMC and LMC from Chandar et al. (2017), who find a constant Γ ∼ 24 per cent, irrespective of Σ_{SFR} for clusters with ages 1-10 Myr (dashed horizonal line). Individual observations of young (<10 Myr) clusters in nearby dwarf galaxies from Cook et al. (2012) hint at a negative trend between Γ and Σ_{SFR}. The median of the data from Cook et al. (2012) binned between $10^{-4.5}$ and 10^{-2} in Σ_{SFR} is also shown.

all simulations presented in this paper. $\Sigma_{\rm SFR}$ is calculated as described in 3.4.3 and the CMF is calculated over the same area, which is a cylinder with radius of 1 kpc and a height of 500 pc. We show the young FoF groups (hexagons) as well as young bound clusters (stars). For the lowest star formation efficiencies, `SFE0` (green) and `SFE02` (blue), more than ~ 50 % of stars are born in FoF groups or bound clusters (most FoF groups are bound, see Fig. 3.8). In contrast, the `SFE10`, `SFE20` and `SFE50` runs (lime green, pink and purple) have averages of only $\sim 1-2$ per cent for young bound clusters and ~ 10 per cent for young FoF groups. For these high efficiency simulations, most young FoF groups are not bound (see Fig. 3.8). The observational data in Fig. 3.12 show the median of data compiled in a recent review by Adamo et al. (2020b), which reveals a positive correlation between Γ and $\Sigma_{\rm SFR}$ for young clusters (<10 Myr). It is important to note however that not all observational literature supports this relation. Chandar et al. (2017) comment on the fact that for data at high $\Sigma_{\rm SFR}$, Γ is preferentially estimated on short time scales (e.g. 1-10 Myr), whilst data at low $\Sigma_{\rm SFR}$ is estimated over a longer time scale, up to 100 Myr. Accounting for this, when only considering newly formed stars over an age range of $1-10$ Myr, they find a constant Γ of around 24 per cent, irrespective of $\Sigma_{\rm SFR}$, shown as the dashed horizontal line. The observational results have made varying assumptions on the definition of clusters, details of which are discussed in a recent review by Adamo et al. (2020b). We also include data for young (<10 Myr) clusters from Cook et al. (2012) who look at local dwarf galaxies. Their data hint at a negative correlation between Γ and $\Sigma_{\rm SFR}$, which is in slight tension with Adamo et al. (2020b). However, as is discussed in both these studies, cluster formation is highly stochastic and heavily dependent on the evolutionary phase of each individual galaxy. The majority of observational data suggest a positive correlation between Γ and $\Sigma_{\rm SFR}$, however the significant scatter means that none of our simulations with differing values of $\epsilon_{\rm ff}$ can necessarily be ruled out by Γ alone.

Linking back to the global properties discussed in Sec. 3.3.1, it is interesting to remind ourselves that with these different cluster formation efficiencies leading to very different clustering properties, we do not see an effect on the outflow properties.

3.4.5 Cluster ages

Observations of the age spreads of star clusters are challenging as projection effects can introduce contamination from older stars. From a variety of objects studied in the literature, an appropriate upper limit for the expected age spread would be approximately 5 Myr (Longmore et al., 2014). We look at the age spreads of the bound clusters in the simulations, which are shown in Table 3.1. In the `SFE02` and `SFE2` models where we also have the most clusters, the majority of clusters have age spreads of less than 5 Myr, but some have spreads of up to $20-30$ Myr. For the `SFE20` and `SFE50` models, we have less bound clusters overall to examine, but these clusters have wider age spreads. This provides some support against these models with higher star formation efficiencies as the star formation histories of the individual clusters are more extended.

3.4.6 Cluster sizes

In Fig. 3.13 we show, from top to bottom, the half mass radius $r_{1/2}$, half mass surface density $\Sigma_{1/2}$ and total surface density $\Sigma_{\rm tot}$, defined as the density of the region containing 90 per cent

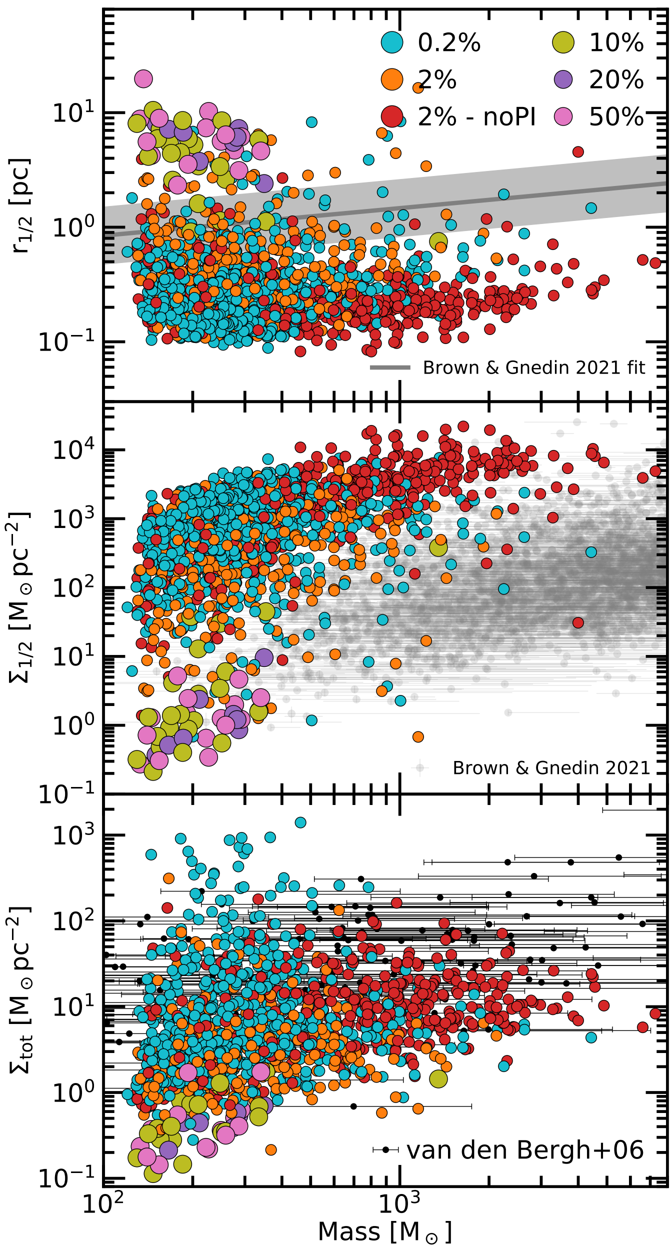

Figure 3.13: *Top panel:* Half-mass radius of bound clusters as a function of cluster mass for `SFE02`, `SFE2`, `SFE2noPI`, `SFE10`, `SFE20` and `SFE50`. The sizes of the symbols for the `SFE10`, `SFE20` and `SFE50` runs have been artificially increased for visual clarity. The solid line indicates the best fit relation with scatter from LEGUS observations of 31 galaxies presented in Brown and Gnedin (2021). *Middle panel:* Half-mass surface density of bound clusters. Observations from Brown and Gnedin (2021) are shown for comparison. *Bottom panel:* Total surface density of bound clusters as a function of their total mass. Observations from van den Bergh (2006) are shown for comparison.

of the cluster mass, as a function of total cluster mass for the bound clusters identified in the simulations. In the `SFE20` and `SFE50` runs, we see that the clusters are more extended with half mass radii of around 3-10 pc, in comparison to the `SFE02` and `SFE2` runs which have half mass radii mostly an order of magnitude lower, around 0.1-1 pc. The `SFE10` run shows clusters with similar sizes to the `SFE20` and `SFE50` with a few more compact clusters with $r_{1/2}$ of around 1 pc. The `SFE10`, `SFE20` and `SFE50` runs also have lower surface densities consistent with their lower virial parameters (see Fig. 3.8). For comparison we show the recently published mass-size relation from Brown and Gnedin (2021). It appears that the simulated clusters are either too small for low star formation efficiencies or too large for high star formation efficiencies. The half-mass surface densities of the low star formation efficiency simulations seem to be lower than observed (middle panel of Fig. 3.13), while the total surface densities (bottom panel) seem consistent with observations. This indicates that clusters produced in simulations with low $\epsilon_{\rm ff}$ below 10^3 $M_\odot$ are too compact compared to observations. The situation improves for the few simulated clusters at higher mass (see also Lahén et al., 2020, for simulated clusters in a starburst environment). The clusters from the `SFE10`, `SFE20` and `SFE50` runs are likely too diffuse. We discussed previously in Section 3.4.4 that there is cluster disruption in the higher star formation efficiency models. Observationally, it is expected that star clusters disrupt, and capturing these disruption properties appears to be a challenge of these galaxy formation simulations. If we do observe cluster disruption in these runs, it is likely due to the fact that the surface densities were too low at formation. It is worth noting as a caveat however that the cluster sizes and properties are likely heavily affected by the fact that the interactions between the stars are softened, reducing dynamical effects such as two-body relaxation. Discussion of this as well as proposed solutions are discussed in Sec. 3.5.2.

3.5 Discussion

3.5.1 Star formation and outflow rates

For the same set of physical processes included in the simulations, the choice of $\epsilon_{\rm ff}$ significantly changes the properties of the forming star clusters but has little impact on the global galaxy properties such as SFR or mass loading. This is in agreement with previous studies (see Sec. 3.1). When excluding photo-ionisation, we form significantly more clusters. However, the peaks in the ambient supernova densities only slightly change. After the initial starburst, mass loading is increased by approximately a factor of two, which is in agreement with the simulations shown in Smith et al. (2021), indicating that stronger stellar clustering in their model without HII regions leads to higher mass loading factors, also by a factor of approximately two. Their modelling of heating/cooling, star formation, and HII regions is similar to the one used here. Smith et al. (2021) also find that the exclusion of photo-ionisation increases the maximum ambient densities at which SN explode quite substantially as well as broadening the distribution of ambient densities, in agreement with Hu et al. (2017) as well as our findings.

Over the entire simulation, a substantial part of the regulation of star formation is done by HII regions, which also result in smoother star formation histories. This conclusion seems very robust as it has also been put forward by earlier studies with varying setups and simulation codes (see e.g. Hopkins et al., 2011; Peters et al., 2017; Butler et al., 2017; Hopkins et al., 2018; Haid et al., 2019; Kannan et al., 2020; Hopkins et al., 2020b; Smith et al., 2021; Rathjen et al., 2021). The formation of HII regions also reduces clustering and cluster growth (e.g. Guillard et al., 2018; Smith et al., 2021; Rathjen et al., 2021). We note however that beyond the initial starburst, the SFE2noPI simulation has a lower star formation rate.

3.5.2 Star cluster disruption

As this study shows, the observed star cluster mass function can be successfully reproduced with high-resolution galaxy evolution simulations. Also the fraction of stars forming in clusters can be controlled by varying the star formation efficiency. However, another fundamental star cluster property cannot be modelled yet, which is the relatively rapid destruction of star clusters after formation (see e.g. Portegies Zwart et al., 2010; Krumholz et al., 2019). In our study, only simulations with very high $\epsilon_{\rm ff}$ values show signs of cluster disruption. These clusters however, are too diffuse compared to observations and can therefore easily be dispersed by tides, which are naturally included in the simulations. The simulated clusters presented in Dobbs et al. (2017) show similar properties. No high resolution galaxy formation simulation to date produces star cluster properties which are all consistent with observations. The reason could be the still limited capability to properly resolve internal star cluster properties in galaxy evolution simulations. Important caveats here might be:

- limitations for resolving the internal star-forming cloud structure and dynamics on sub-parsec scales
- inability of the $\epsilon_{\rm ff}$ based star formation sub-grid model to capture the accurate distribution and timing of star formation and stellar feedback
- inability of the feedback model to accurately capture gas expulsion from forming star clusters (see e.g. Bastian and Goodwin, 2006)
- missing feedback channels like stellar winds
- limited capabilities of the typically used second order integrators to follow important relaxation effects on cluster scales.

A possible solution might require a turning away from Schmidt (1959)-type star formation models. Additionally, the interactions between the stars themselves are softened within the simulations, reducing the two-body interactions within the clusters. These interactions are essential in both the formation as well as the evolutionary fate of the clusters. Gieles et al. (2010a) show that by 10 Myr, two-body relaxation has had a strong effect on the evolution of globular clusters. Accurately modelling these interactions could therefore be achieved by the use of higher order forward integration schemes (see e.g Rantala et al., 2021), which allow for higher dynamical fidelity in dense stellar systems and a straight forward coupling with hydrodynamics.

3.6 Conclusions

We present high-resolution (sub-parsec, $4\,\mathrm{M}_\odot$) simulations of the evolution of dwarf galaxies. The simulations include non-equilibrium heating and cooling processes and chemistry, an interstellar radiation field varying in space and time, star formation, a simple model for HII regions as well as supernova explosions from individual massive stars. We explore the impact of assumed star formation efficiencies, ϵ_{ff} per free-fall time for a Schmidt (1959)-type formation model on the resulting star formation and outflow rates and the star cluster properties. We find the following results:

- Star formation rates and outflow rates are independent of ϵ_{ff} for the investigated range of $\epsilon_{\mathrm{ff}} = 0.02$ - 0.5 (`SFE02`, `SFE2`, `SFE10`, `SFE20` and `SFE50`) and a model with instantaneous star formation at a high density threshold (`SFE0`). The test model without HII regions (`SFE2noPI`) has a similar star formation rate, but a slightly higher outflow rate resulting in a slightly increased mass loading.

- All simulations form star clusters with power law mass functions similar to observations. With increasing ϵ_{ff}, the slope α increases from -3 to -2. The normalisation of the cluster mass function, i.e. the mass of the most massive cluster formed, decreases with increasing ϵ_{ff}. At higher ϵ_{ff}, clusters are less likely to form as well as survive due to the fact that the stars are formed at lower ambient densities.

- The clusters become less bound and the cluster formation efficiencies decrease from $\Gamma \sim 0.6$ to $\Gamma \sim 0.1$ with increasing ϵ_{ff}. The physical reason for this is due to the fact that changing the ϵ_{ff} controls the densities at which the stars form, as shown in Sec. 3.3.2. Low star formation efficiencies mean more star formation at higher densities resulting in massive, compact, bound clusters. The low formation star efficiency ($\epsilon_{\mathrm{ff}} = 0.02$, `SFE02`) and the instantaneous formation model (`SFE0`) are inconsistent with all available cluster formation efficiency observations.

- None of the models seem to match observed cluster sizes. Clusters in simulations with high efficiencies $\epsilon_{\mathrm{ff}} \gtrsim 0.2$ are too diffuse. While they shown signs for cluster disruption these models are disfavoured as no internal rapid cluster evolution process can make cluster more compact. Clusters in low ϵ_{ff} simulations are too compact and do not disrupt. A more accurate modelling of internal evolutionary processes might be able to alleviate this problem.

The failure of the current highest resolution galaxy evolution models to capture all fundamental star cluster properties poses a challenge for all future numerical studies on galactic star cluster populations.

"No matter what I do, no matter how predictable I try to make my life,
it will not be any more predictable that the rest of the world.
Which is chaotic."

Elizabeth Moon, The Speed of Dark

4 Physically motivated alterations to star formation

We present a suite of solar-mass and sub parsec resolution simulations with individual massive stars, where we explore the effect of physically motivated alterations to the sub-grid star formation prescription in order to understand their impact on galactic properties such as the star formation rates and outflow rates, as well as the smaller scale properties of star clusters. We test two primary processes: kicking newly formed stars with a small velocity kick, and delaying the realisation of a star-forming gas particle into a star by the typical free-fall time. We find that applying the velocity kick to the stars has the effect of producing fewer, more extended and less-dense clusters, making these clusters more susceptible to disruption mechanisms. Delaying star formation resulted in a minor enhancement in the fraction of stars born in clusters. Even a small delay time of 10^4 yrs is enough to make the clusters produced more extended and diffuse in comparison to the run with no delay time, but increasing the delay time beyond this did not have much effect. For both alterations to the star formation model, the global properties such as the star formation rate and outflow rates were largely unaffected. The results presented in this chapter will be submitted for peer-review in the near future.

4.1 Introduction

Galaxy scale simulations are continuously pushing their limitations in order to explore new and unknown effects of physical processes on ever larger and smaller scales. Cosmological simulations are expanding to larger volumes to understand structure formation and the assembly of galaxies self-consistently in a fully cosmological context (Somerville and Davé, 2015; Vogelsberger et al., 2020) as well as gaining higher numbers of galaxies in these large boxes to enable the sampling of the most rare objects in the Universe (Power and Knebe, 2006). Whilst recent simulations are now working to resolve the smaller scales of internal structure formation such as recovering the initial mass function (IMF, see reviews from Krumholz (2014) and Klessen and Glover (2016) for a comprehensive discussion on reproducing the IMF) in simulations of giant molecular clouds (e.g. Nordlund and Padoan, 2003; Grudić et al., 2021; Mathew and Federrath, 2021) and producing populations of individual stars and star clusters in isolated galaxies. Linking these small scale simulations to the largest scales is non-trivial due to the dynamic range required, making it also difficult to comprehend at what scales the small-scale physics becomes relevant at larger scales and vice versa, especially when considering the differences in the assumptions made. Nevertheless, approaching galaxy formation from both large and small scales can hope to build a consistent picture of galaxy formation and evolution from the scales of individual resolved gas clouds up to statistical populations representing extremely large volumes of the Universe.

The motivation behind numerical simulations is arguably to gain a deep understanding of the physical processes dictating the formation and evolution of stars, clouds, star clusters, galaxies, galaxy clusters, or the entire Universe. But typically the approach is that if a result does not match what is observed in the Universe, it is discarded as a model that does not represents nature. Given that galaxy scale simulations rely on a plethora of parameterised sub-resolution models (see Benson, 2010, for a review), it becomes dangerous territory when trying to find some combination of parameters in order to reproduce observations. Many cosmological scale simulations impressively well reproduce vast populations of galaxies (Dubois et al., 2014; Vogelsberger et al., 2014; Schaye et al., 2015; Springel et al., 2018; Davé et al., 2019), but manage to do so with very different physical models, bringing into question whether the primary goal of understanding the physics is really being prioritised (see Naab and Ostriker, 2017, for a review). With that being said, reproducing galaxies in agreement with what is observed is naturally desirable. A physically well-motivated model that produces galaxies that do not match our observations is an important result in terms of motivating exploration of missing physical processes. This can be addressed by including genuinely missing physics (e.g. magnetic fields or cosmic rays (Hopkins et al., 2020a)) but it is also important to turn to the sub-grid models used and address if they are really appropriate for the question being answered and the scales considered.

In galaxy formation simulations that resolve individual stars, it has so far proven somewhat difficult to reproduce star clusters with sizes and densities consistent with observations, as well as producing star clusters which are susceptible to being disrupted. The fraction of stars born in clusters is observationally well studied (Bastian, 2008) but the substantial scatter in the observations gives hints at not only the difficulties in consistently measuring star cluster properties, but also highly likely an intrinsic scatter due to various different environmental effects, both internal and external to the host galaxies (Adamo et al., 2015; Adamo and Bastian, 2018; Adamo et al., 2020a). The clustering of stars as well as their kinematics is not only a desirable observation to recover, but the cluster nature of star formation matters for feedback and its regulatory role on the star formation cycle at galactic scales. The formation of star clusters and reliably predicting which masses of stars will form within giant molecular clouds is also non trivial. Once able to form a population of star clusters consistent with observations, following their evolution and understanding the disruption mechanisms is the next challenge. The process of formation and destruction are naturally heavily interlinked, as the formation mechanism and the spatial and energetic properties of the stars within a cluster heavily dictate their future evolution in a galactic environment.

Another important observable is the initial cluster mass function. Numerous observations have found that the distribution of clusters is well described by a truncated power-law mass function $dN/dM \propto M^{\alpha}$, with index $\alpha \sim -2$ (e.g. Zhang and Fall, 1999; Bik et al., 2003; Hunter et al., 2003; de Grijs et al., 2003). The truncation mass, or maximum cluster mass appears to be a function of environment, such that the most massive galaxies can grow the most massive clusters (Larsen, 2009; Portegies Zwart et al., 2010; Bastian et al., 2012). Typical truncation masses for spirals are observed to be of the order of 10^5 $M_\odot$ (Larsen, 2009).

As well as the overall population properties, we also have to consider the spatial properties of the clusters, such as their sizes and surface densities. Brown and Gnedin (2021) did a recent study on over 6000 identified young star clusters in 31 nearby galaxies and found a peak cluster radius of around 3 pc, but with a range of 0.1 pc up to 20 pc. They identify a scaling relation between the mass and radius to be $R_{\text{eff}} \propto M^{0.25}$ (this data is shown in Fig. 4.7 and Fig. 4.23). The surface densities of the clusters peaks around 10^2 $M_\odot$/pc^2, with a range from 10^0 $M_\odot$/pc^2 and exceeding 10^4 $M_\odot$/pc^2.

Star clusters embedded within a galaxy are expected to disrupt on timescales of a few Myr (Bastian et al., 2005; Gieles, 2010; Bastian, 2011; Goodwin, 2011). The disruption mechanisms can heavily depend on the mass and spatial properties of the star cluster as well as their environmental properties such as their proximity to the galactic centre and the scale height (see Bastian and Gieles, 2008, for a review). Starting in chronological order, the first disruption mechanism, which depending on the chosen definition of a star cluster can actually prevent star cluster formation altogether is gas expulsion (Geyer and Burkert, 2001; Kroupa and Boily, 2002). Gravitationally bound collapsing molecular clouds begin to form stars within them, and this system of gas and stars together can be bound. Stellar feedback from the newly formed stars however will heat and push out the gas. If the stars alone are not bound in the absence of the gas, this is a quick and effective way of destroying the forming star cluster. Any future tidal interactions with passing gas or even other star clusters will therefore have no difficulties in stripping off the remaining stars and erasing the group of stars. Once the gas has been removed from the cluster, two mechanisms appear to be dominant in their future evolution: mass loss due to stellar evolution, and mass loss due to relaxation (Krumholz et al., 2019). 3-40 Myr after star formation, a cluster will typically expel around 20 per cent of their mass in supernovae, producing high-speed gas that very likely escapes from the cluster. Additionally, left behind from the supernovae are neutron stars or black holes, which receive kicks of several hundred km/s meaning they also likely escape from the cluster (e.g. Faucher-Giguère and Kaspi, 2006). Following the supernova phase (after 40 Myr), the mass loss becomes dominated by the shedding of the envelopes of asymptotic giant branch (AGB) stars. This is a less aggressive process than the supernovae, such that a cluster can expel up to 40 per cent of its mass but over the timescale of a Gyr. The velocities of AGB winds are typically lower than those powered by core-collapse supernovae (CCSN), on the order of a few tens of km/s. This still can be enough to escape from particularly lower mass clusters, but the mass loss is further decreased due to the fact the white dwarf remnants of AGB stars receive substantially smaller kicks, and are much more likely to remain in their parent cluster (Kruijssen, 2009). These mass loss processes are naturally enhanced by the cluster being embedded in a tidal field. Adiabatic mass losses cause the cluster to expand overall whilst the tidal radius decreases. The stars now outside this tidal radius are therefore stripped from the cluster. This can have quite devastating effects on clusters, by roughly doubling the mass-loss in comparison to stellar evolution alone (Takahashi and Portegies Zwart, 2000; Baumgardt and Makino, 2003; Lamers et al., 2010). In the presence of this tidal field, there is a maximum ratio of half-mass radius to tidal radius beyond which virial equilibrium is impossible and the cluster completely disrupts (Chernoff and Weinberg, 1990; Fukushige and Heggie, 1995). The effect of all the previously described disruption mechanisms are enhanced when considering a cluster which has undergone mass segregation, where the most massive stars have migrated toward the centre. In simulations which do not resolve individual star formation but model star clusters in a sub-grid prescription, this tidal field and its effect on cluster disruption is modelled explicitly (e.g. Reina-Campos et al., 2022)

At the resolutions at which we resolve individual stars, it is debatable as to what extent each of the processes leading to cluster disruption is really captured. Due to the gravitational softening between the stars and the lack of multiplicity, it is clear that the stellar kicks mentioned previously able to remove stellar remnants are not captured. Instead, the feedback processes primarily have an extremely effective impact on the gas surrounding star formation. Improving the modelling of the effect of stellar evolution and its impact on the stars themselves is clearly an important future feature required to further understand and capture star cluster disruption in these simulations. We can however make some steps toward understanding the impact of the unresolved stellar kicks by implementing small velocity kicks to the stars at birth. The physical justification for this can be explained by several processes. As well as multiplicity and the effect of stellar evolution as described above, an additional justification is that we do not resolve the smaller-scale turbulence present in the ISM at the time of star formation (Larson, 1981; Hopkins, 2013; Williams et al., 2000; Bonnell and Bate, 2006; Hopkins, 2013; Ejdetjärn et al., 2022), which is likely to alter the dynamical properties of a star in comparison to the gas from which it formed. For simplicity, we can choose to not differentiate between these processes for now (which can be reserved for much higher resolution studies resolving star formation (e.g. Guszejnov et al., 2022; Hu et al., 2022c) and instead explore the overall effect, as opposed to the origin. To do this, we implement a small, randomly orientated kick to each star particle and explore the effect on the star cluster populations.

In Chapter 3, we found that we formed star clusters with good agreement to observables such as the cluster mass function and the cluster formation efficiency, but noted that the structural properties of the clusters were highly influenced by the density at which stars formed. In the models with a lower star formation efficiency, stars were formed at higher densities and subsequently the star clusters themselves also had higher densities. Star clusters can be disrupted from either external factors or internal processes. The external processes primarily involve interactions with molecular clouds or other star clusters which can pull unbound stars away from the clusters and/or exert tidal forces. Internally, star clusters can become unbound from gas loss due to stellar feedback, losing stars from stellar interactions and on longer timescales by mass segregation (Guszejnov et al., 2022). In our simulations, due to the softened interactions between the stars, the interactions between stars are not captured. In the same way, the gas turbulence is not captured and translated to the stars. In order to reconcile this, and in an attempt to build a model of star cluster formation that not only reproduces properties such as the cluster mass function and cluster formation efficiency, but also reproduces the expected observed properties of individual star clusters such as the sizes and densities, as well as the disruption timescales and ages.

It was found in Dobbs et al. (2022) that in the highest density regions, star formation has already occurred too quickly before photoionisation or any other pre-supernova feedback has had a chance to disperse or ionise the gas. This is also what is observed in Chapter 3, where photoionisation does not have enough time to disperse the gas in the models where we form stars at very high densities, as these stars typically form in a very small time window. To further understand this effect, it is also important to consider the effect of the timings of the feedback, both pre-supernova feedback and supernova explosions. Hu et al. (2016, 2017), as well as a recent paper by Keller and Kruijssen (2022) explored the effect of the timing of supernova feedback and found that even if the supernovae energy budget is kept constant, changing the delay between star formation and the first supernova, or the duration of supernovae can have significant effects on the ability of supernovae to regulate star formation and drive outflows. They also note that long delays (>20 Myr) increases the clustering of stars and increases the ability of supernovae to drive outflows. Missing from these simulations however, and likely to have a larger impact on star formation than the supernova feedback is the photoionising feedback, which acts on timescales comparable to that of star formation in contrast to supernovae, the majority of which explode on timescales long after star formation has finished. Photoionisation is shown to be the most dominant component of pre-supernova feedback in its role in dispersing star forming regions. This is shown in zoom-in simulations on Milky Way-like spiral arm simulations by Bending et al. (2020). Using these simulations, Ali et al. (2022) explored the effect of different feedback prescriptions on dispersing spiral arm structure. They also found that photoionisation was of high importance, but that stellar winds do not appear to make that much difference on these scales (Dale and Bonnell, 2008; Gallegos-Garcia et al., 2020; Rosen et al., 2021; Lancaster et al., 2021; Franeck et al., 2022).

In our simulations, when a gas particle becomes star forming, it is typically immediately turned into a star particle and begins its feedback cycle. This does not account however for the time it takes for a cloud core at some density to collapse into a star. We therefore exploring delaying this star particle by a typical free-fall time, in order to try to quantify the impact of primarily delaying the early stellar feedback on both the galactic properties as well as the local densities of star formation and supernovae and the clustering of stars. Delaying the star formation in this setup has a physical origin in that the star forming gas particles have typical densities of around $n_H \sim 10^{3-5}$ cm^{-3} corresponding to free-fall times on the order of a Myr. Delaying star formation and the subsequent photoionising feedback has a substantial impact on the surrounding gas that may be eligible for star formation, and therefore may be a key consideration when understanding the impact of feedback on star cluster formation.

This paper is organised in four main sections. Sec. 4.2 introduces the simulations used in this study and highlights particularly the most relevant sub-grid models employed in these simulations and the alterations that we explore along with the physical motivation. We then split the analysis into two sections: Sec. 4.3 and 4.4 show the results on the global and star cluster properties from implementing a small velocity kick to star particles after they have formed. Then Sec. 4.5

and 4.6 show the results of accounting for the cloud core collapse free-fall times on the global and small-scale properties of the galaxies. We discuss the implications of these alterations to the star formation models and compare to similar studies in Sec. 4.7 before making our concluding remarks in Sec. 4.8.

4.2 Simulation setup

The simulations used in this study follow that of Chapter 3. We use SPHGal (Hu et al., 2014, 2016, 2017) as part of the GRIFFIN project[1] (Galaxy Realizations Including Feedback From INdividual massive stars) (Lahén et al., 2019, 2020; Hislop et al., 2022). This is an updated version of the GADGET-3 code (Springel, 2005) with detailed non-equilibrium cooling and heating processes using a chemical network for gas below 3×10^4 K. We omit the full description of the simulations here and refer the reader to Chapter 3 and Chapter 5, and instead just highlight the most relevant details of the simulations.

4.2.1 Star Formation

Gas particles have an associated Jeans mass, defined as

$$M_J = \frac{\pi^{5/2} c_s^3}{6 G^{3/2} \rho^{1/2}}, \tag{4.1}$$

where c_s is the local sound speed of the gas, G is the gravitational constant, and ρ is the gas density. A gas particle is flagged as star forming when $M_J < N_{\rm thres} M_{\rm ker}$, where $M_{\rm ker} = N_{\rm ngb} m_{\rm gas}$ is the SPH kernel mass and $N_{\rm thres}$ is a free parameter. In line with Hu et al. (2016), we use $N_{\rm thres} = 8$ to properly resolve the Jeans mass for the star-forming gas.

In contrast with Chapter 3 where we used a Schmidt (1959)-type star formation model with an efficiency parameter, here we only use the threshold at $M_J = 0.5 M_{\rm ker}$. When a gas particle passes below this threshold, which is dependent on density and temperature, we instantaneously form a star particle. When forming a star particle, we sample from a Kroupa (2001) IMF. We sample stellar masses with a upper limit of 50 M$_\odot$, and sampled stellar masses above the gas particle mass of 4 M$_\odot$ are realised as individual stellar particles. For sampled stellar masses below this threshold, we keep drawing from the IMF until we have at least 4 M$_\odot$ (see Hu et al., 2016).

When a star particle is realised, the dynamical properties of the star are adopted directly from the gas, such that the position and velocity are the same. In simulations at this resolution, this is a reasonable assumption, however there is likely to be changes in the velocities of the formed stars from unresolved turbulence in the gas forming the stars, as well as stellar interactions. Simulations of clusters (e.g. Oh and Kroupa, 2016) show that velocity kicks of stars typically originate from gravitational interactions (Poveda et al., 1967), including the disruption of binaries through supernovae explosions (Blaauw, 1961). This is not something considered in these simulations, but multiplicity of stars (e.g. binaries) is likely to have a strong dynamical effect on the dynamic

[1]https://wwwmpa.mpa-garching.mpg.de/~naab/griffin-project

properties of stars (e.g. runaway stars as explored in Andersson et al., 2020; Steinwandel et al., 2022a). For this reason, we explore this assumption and its effects by implementing small kicks to newly formed star particles as discussed in Sec. 4.2.2.

4.2.2 Kicks Model

Once a star particle is realised in the simulations, we apply a small isotropic velocity kick. We implement a fixed kick for all particles. This mimics a velocity kick that a star would inherit from the turbulent star-forming ISM but that is not captured within the star-formation prescription due to resolution. We here compare including no kick (`kick_0km/s`), a 1 km/s kick (`kick_1km/s`) and a 3 km/s kick (`kick_3km/s`). These values are motivated by typical velocity dispersions in star clusters (e.g. Gieles et al., 2010b; Kuhn et al., 2019).

Newly formed stellar particles inherit their velocities from their progenitor gas particle, which is then altered by this velocity kick to each newly formed stellar particle. The magnitude is fixed but the direction is randomly generated such that the new velocity of each particle $v_{i,j}$ is

$$v_{i,\hat{j}=\hat{x},\hat{y},\hat{z}} = v_{0_{i,\hat{j}=\hat{x},\hat{y},\hat{z}}} + (\mathrm{M}_{\mathrm{kick}} \times \Delta v_{i,\hat{j}=\hat{x},\hat{y},\hat{z}}), \tag{4.2}$$

where $\hat{j}$ is the x, y or z component of the velocity, $v_{0_{i,\hat{j}=\hat{x},\hat{y},\hat{z}}}$ is the initial velocity of the ith particle, $\mathrm{M}_{\mathrm{kick}}$ is the magnitude of the kick and $\Delta v_{i,\hat{j}=\hat{x},\hat{y},\hat{z}}$.

$$dv_{\hat{x}} = \sin(\theta_{\mathrm{rand}}) * \cos(\phi_{\mathrm{rand}}), \tag{4.3}$$
$$dv_{\hat{y}} = \sin(\theta_{\mathrm{rand}}) * \sin(\phi_{\mathrm{rand}}), \tag{4.4}$$
$$dv_{\hat{z}} = \cos(\theta_{\mathrm{rand}}) \tag{4.5}$$

such that θ_{rand} and ϕ_{rand} are randomly sampled angles between 0 and π. This has the effect of either increasing or decreasing the velocity of the particle.

4.2.3 Stellar Feedback

Photoionisation is implemented using a Strömgren (1939)-sphere approximation which assumes that the recombination rates equals the photon production rates. This approximation well reproduces the evolution of D-type fronts in good agreement with the Starbench results for different numerical implementations (Hu et al., 2016, 2017). This model is a good approximation for the local impact of hydrogen ionising radiation, however it does not capture the full radiation field on larger scales.

Type II supernovae are included in these simulations for individual stars above 8 $\mathrm{M}_{\odot}$. As all stars above 4 $\mathrm{M}_{\odot}$ are realised individually, all feedback from stars above this mass range can be modelled individually. Every star above 8 $\mathrm{M}_{\odot}$ ends its life as a CCSN and releases a canonical 10^{51} erg of energy into the surrounding gas as thermal energy. The stellar lifetimes dictating the time between the realisation of a star particle and exploding as a CCSN are calculated from stellar models of Georgy et al. (2013). For simulations without sufficient resolution (baryonic particle masses » 1 $M_{\odot}$), thermal energy released by a single CCSN is radiated away too quickly resulting in artificial over-cooling. Hence in lower resolution studies, the energy released from CCSN is typically modelled using a radially varying fraction of kinetic or thermal energy. At the baryonic mass resolution of the simulations presented here however, it has been shown in Hu et al. (2016) that CCSN can be considered fully resolved. We therefore employ purely thermal energy injection and resolve the Sedov-Taylor phase naturally by self consistently building up the hot mass and the momentum in a subsequent pressure driven snow plough phase (Kim and Ostriker, 2015; Steinwandel et al., 2020).

4.2.4 Accounting for cloud core collapse timescales

As a gas cloud is collapsing and increasing in density, once it has passed the star formation threshold in our simulations, it is normally turned into a star immediately and it begins its feedback. The cloud core however that has formed still has some time delay before it would form a star, and so we also explore the effect of accounting for this cloud core collapse timescale on the cluster structure as well as its effect on outflows. When a gas particle becomes star forming, we realise this particle as an inactive star particle, until a typical free-fall time has passed and then the particle becomes active and begins its feedback. In practise therefore we are effectively delaying the photoionising feedback. We explore a lot more the effect of the feedback prescriptions on the outflow properties and the ISM densities in Chapter 5, but for the purposes of this study, we explore the effect of this delay on the structural properties of the formed star clusters. Changing the star formation efficiency (as explored in Li et al., 2020; Hislop et al., 2022) as well as employing the kicks model as discussed in Section 4.2.2 both change the birth densities of the stars formed and so is expected to have a strong impact on the initial structural properties of the star clusters. Accounting for the cloud core collapse free-fall time has a less predictable impact, but would naturally be expected to have a strong effect as star formation is primarily regulated by pre-supernova feedback, particularly photoionisation. However, its impact will have a strong dependence on how quickly the gas is collapsing balanced with how quickly the photoionising feedback can act on the surrounding gas to prevent further star formation. If a large collection of gas particles in a collapsing gas cloud are increasing in density and pass the threshold for star formation on the same, or a very similar timescale, photoionisation will not have enough time to act on the gas immediately surrounding the first stars. For this reason, one might still expect to produce dense and compact star clusters with this model. This photoionisation undoubtedly still has an impact on further star formation however, in terms of pre-processing the surrounding ISM and regulating the densities at which CCSN explode some Myr later, having a strong impact on the outflow properties of the galaxy.

4.3 Effect of kicks on global galaxy properties

Fig. 4.1 shows the surface density maps of gas and stars for each of the simulations `kick_0km/s`, `kick_1km/s` and `kick_3km/s`. We can take a qualitative look at the stellar distributions and find that even by eye this small velocity kick has an impact on the stellar surface densities.

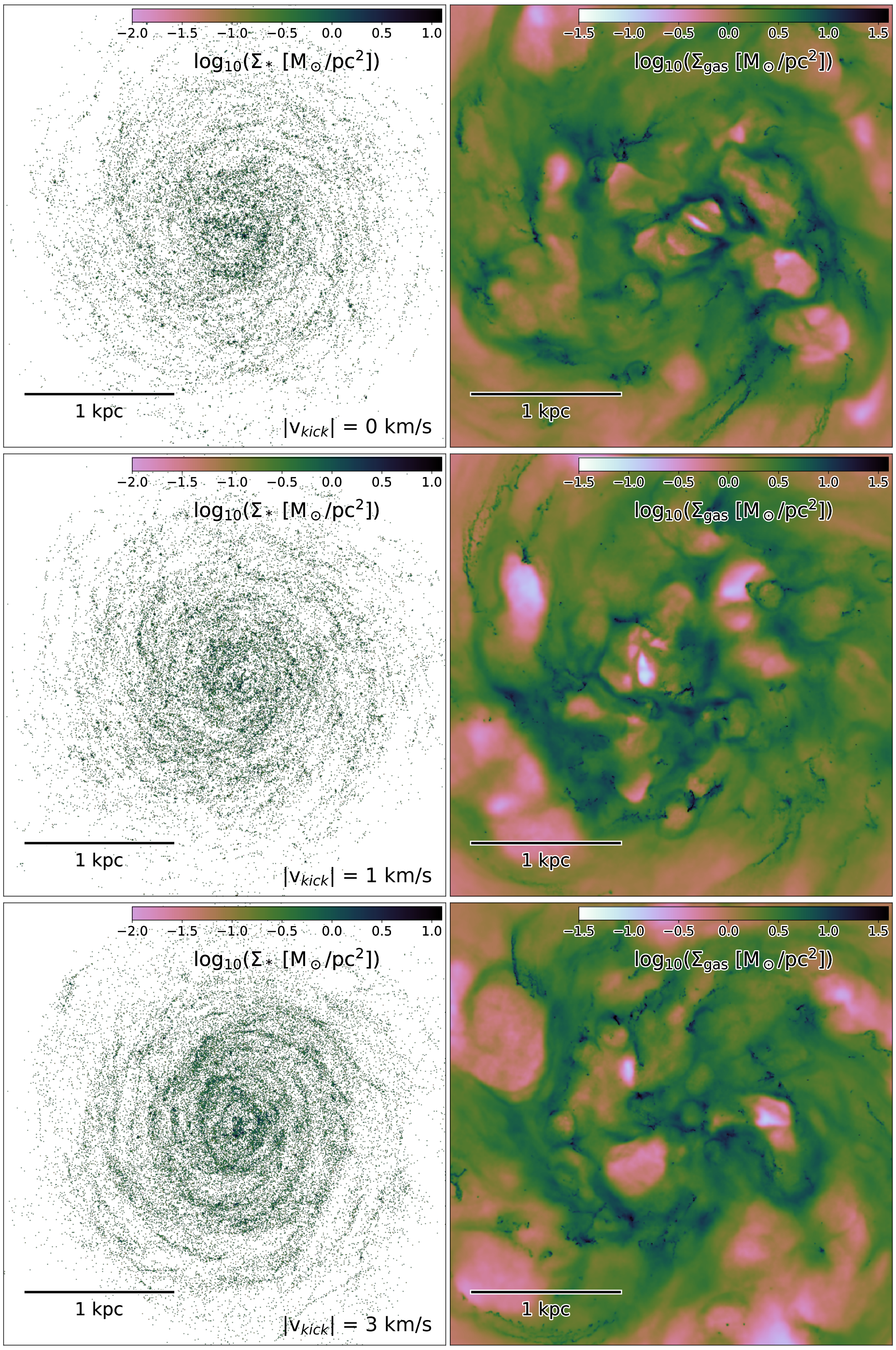

Figure 4.1: Stellar surface density (left column) and gas surface density (right column) shown for all of the simulations at 500 Myr. The top row shows the `kick_0km/s` model, the middle row shows `kick_1km/s`, and the bottom row shows `kick_3km/s`.

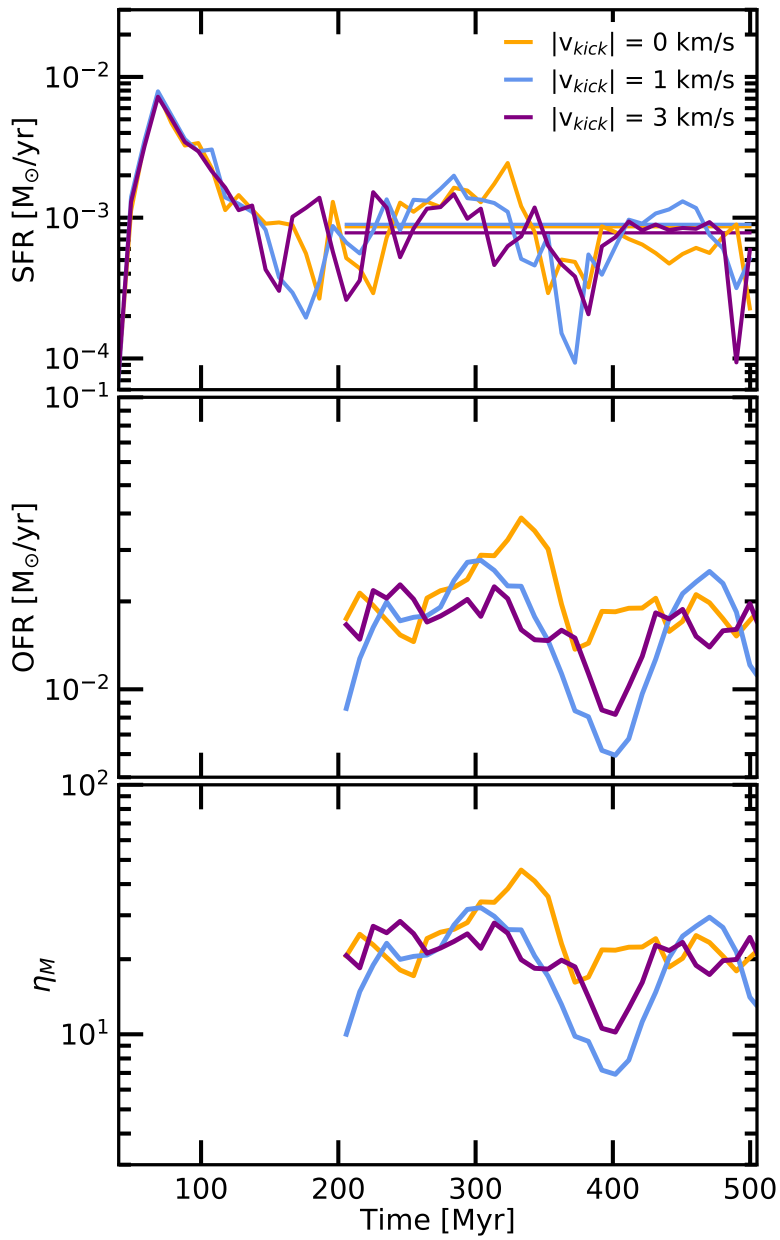

Figure 4.2: *Top panel*: The star formation rate as a function of time for the simulations without kicks (0 km/s, orange line), with a 1 km/s kick (blue line) and with a 3 km/s kick (purple line). The horizontal lines show the average star formation rates calculated between 200-500 Myr excluding the initial burst of star formation. This is the average star formation used to calculate the mass loading. The star formation histories show very little difference overall, with only some variation in the scatter. *Middle panel*: Outflow rates for each of the simulations shown for 200 Myr onward such that we exclude the initial starburst, measured at 1 kpc above and below the disk. *Bottom panel*: The mass loading, defined as the outflow rate divided by the average star formation rate calculated between 200-500 Myr.

Model	$\lvert\vec{v}_{\rm kick}\rvert$ [km/s]	$N_{\rm cl}$	$M_{\rm cl,min}$ [$M_\odot$]	$M_{\rm cl,max}$ [$M_\odot$]	$\Sigma M_{\rm 5MMC}$ [$M_\odot$]	$M_{*,\rm final}$ [10^5 $M_\odot$]	$N_{\rm CCSN}$
`kick_0km/s`	0	816	115	4177	277487	5.99	8228
`kick_1km/s`	1	727	121	2049	237300	6.11	8384
`kick_3km/s`	3	97	124	7414	51779	5.73	7889

Table 4.1: Properties of the clusters present at 500 Myr in the simulations. The columns here describe the model name, $\lvert\vec{v}_{\rm kick}\rvert$ shows the magnitude of the fixed kick given to the stellar particle at birth, $N_{\rm cl}$ is the total number of clusters present in the simulation at 500 Myr, $M_{\rm cl,min}$ and $M_{\rm cl,max}$ show the lowest and highest mass of these identified FoF groups, respectively and $\Sigma M_{\rm 5MMC}$ gives the sum of the mass of the 5 most massive clusters at 500 Myr. We also show the final stellar masses at 500 Myr, $M_{*,\rm final}$ as well as the total number of supernovae $N_{\rm CCSN}$. There is a significant contrast between the number of clusters, with the highest kick `kick_3km/s` resulting in an order of magnitude less clusters in total number. The smallest mass does not vary much, but is primarily sensitive to the parameters of FoF as opposed to being some kind of physical limit. The most massive cluster also varies a lot and is not a linear relation with the magnitude of the kick.

For the `kick_0km/s` model (top row), the stars appear to form in a clustered way with many visible compact and spherical star clusters over the whole galaxy including the outskirts. For the `kick_1km/s` model (middle row), we still see many star clusters, but additionally also a smoother component of the galaxy showing signs of a spiral pattern. The `kick_3km/s` model (bottom row) then shows this smoother component even more. Some star clusters are visible, particularly near the centre, but the majority of stars appear much smoother with a smaller fraction of stars in visible compact clusters.

For the gas component of each of the models in Fig. 4.1, there appears to be relatively little difference. In all cases we see dense filamentary structures showing dense, potentially star-forming gas as well as large bubbles carved out by multiple CCSN explosions. At this particular snapshot, one can pick out more specific differences but the structure of the ISM changes quite drastically over time dependent on where and when the CCSN are exploding. Averaged over time, the gas distributions of each of the models demonstrate no distinct differences.

Fig. 4.2 shows the star formation rate for the 3 kicks model runs, the outflow rates and the mass loading. The overall star formation rates and outflow rates show very little difference between the runs as can also be seen by the average star formation rates shown as horizontal lines in the upper panel. We would not expect the kicks model to have a substantial effect on the star formation rate, other than the fact that stars formed in previous times produce feedback which can prevent (also in some cases trigger) further star formation. We do not see any evidence here that this small velocity kick has any impact however. The outflow rates and mass loading however could potentially be impacted by the kicks. Kicking the stars reduces the clustering as will be discussed in Section 4.4, and this can be motivated to have an impact on outflow rates. When stars are less clustered, the supernova explosions are typically assumed to subsequently also be less clustered. Whether this is a reasonable assumption however is explored in much more detail in Chapter 5. As has been explored in previous studies (e.g. Smith et al., 2021; Keller and Kruijssen, 2022), increased clustering can be linked to enhanced outflow rates and increased mass loading. This is not however seen in the simulations presented here. The reasoning behind this lies in examining the distribution of the ambient density of the CCSN in these simulations, as discussed in Sec. 4.3.1. Understanding why we do not reproduce the results found by e.g. Smith et al. (2021) and Keller and Kruijssen (2022) is not trivial to disentangle, however both of the studies mentioned are for higher mass galaxies with higher mass clusters. There is therefore perhaps a resolution dependence here, but also maybe a cluster mass cutoff. Larger galaxies produce larger clusters with more correlated CCSN. This is the topic of further work in order to understand if there is a threshold mass by which you need a certain number of temporally and spatially clustered CCSN to really enhance outflows.

4.3.1 Ambient density of CCSN

Fig. 4.3 shows the distribution of CCSN ambient densities in each of the simulations. The overall distribution of ambient densities of CCSN does not change in any significant way with the inclusion of the kicks, however the fraction of explosions in FoF groups and the field does change drastically. This is a natural consequence of the fact that the clustering is lower in the `kick_3km/s` model, however it is somewhat interesting to see which ambient densities this affects. The CCSN ambient densities are distributed in two peaks, at low densities ($\sim 10^{-3}$ cm^{-3}) and at high densities ($\sim 10^{-1}$ cm^{-3}), with the peak at lower densities containing more of the CCSN. For all of the simulations, the contribution from field CCSN to each of the peaks appears to be roughly similar. Within FoF groups however, most CCSN explode in the lower density peak. This is particularly noticeable when the clustering is reduced in the `kick_3km/s` run as we see almost no CCSN exploding in the higher density peak. Similarly in the `kick_0km/s` and `kick_1km/s` runs, there is a factor of ~ 3 more CCSN in the lower density peak than in the higher density peak within the identified FoF groups. The high density peak contains the CCSN that explode within an environment not yet impacted by previous CCSN, whilst the lower density peak are CCSN that explode in an environment that has already been impacted by the generation of CCSN beforehand. As discussed in Chapter 5, for a given cluster containing some 10 CCSN or so, there is typically only one SN explosion at high densities followed by the rest at lower densities. This explains why the lower density peak also contributes more to the overall fraction.

The fact that the outflow properties between each of these runs does not change even when the clustering is altered can also be explained by the overall distribution of the ambient densities of the CCSN. Considering that CCSN are the main driver of outflows, the fact that the distributions are highly similar can explain the similar outflow rates. The absolute number of supernova is also similar but not identical, which can also have some impact. However, the ambient density of CCSN only captures the spatial properties of where these CCSN explode, and does not give full temporal information. The fact that we have very different fractions of CCSN in FoF groups and field and there appears to be no impact on the outflow rates would imply that the density of the CCSN explosions is the primary component dictating the outflow rates and mass loading. As hinted at already however, although this argument holds in this particular setup, there may be a cluster mass above which this does not hold. In higher mass systems with higher mass clusters, this justification may break down.

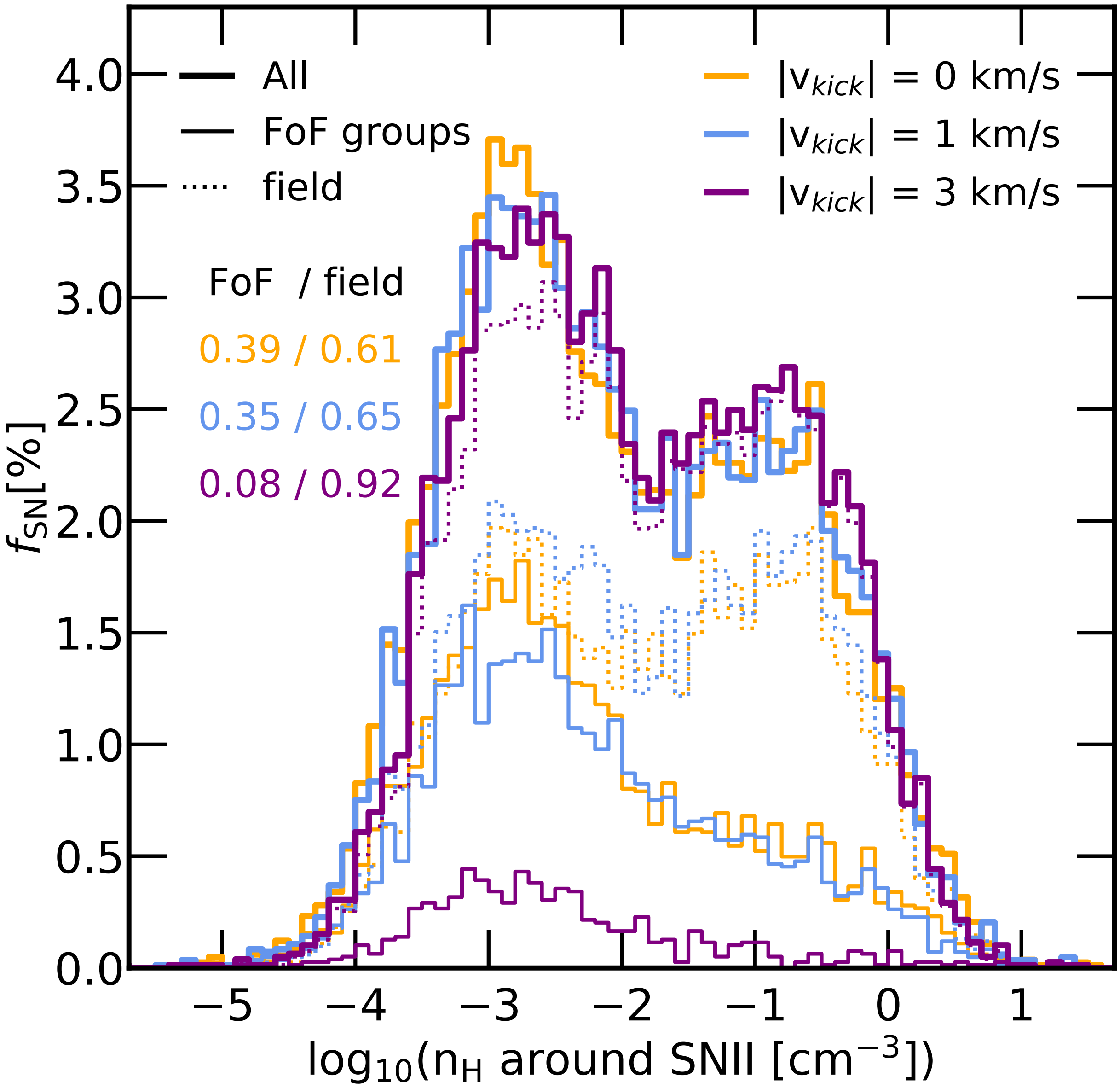

Figure 4.3: Histogram of the ambient density of CCSN normalised by the total number of CCSN in each of the simulations. The bolder lines show the overall distribution of all CCSN explosions, whilst the thinner solid lines and dotted lines show this distribution split into FoF group and field CCSN explosions. Here FoF groups describes all CCSN that exploded whilst belonging to an identified FoF group, whilst field is simply stars that exploded as CCSN not belonging to a FoF group. The fraction of stars belonging in FoF/field is also displayed on the plot for each of the models.

4.4 Effect of kicks on star cluster properties

In Sec. 4.3, we saw that there was very little impact on the global properties of the resultant galaxies with each of the values for the kick velocity. In this section, we explore the the star cluster properties of the resulting models with different kick magnitudes.

4.4.1 Cluster mass function

The effect of the kicks can be seen in the cluster mass function (CMF) shown in Fig. 4.4 where we show the CMF for FoF groups of all ages (left column), the young newly formed FoF groups (middle column) and also the oldest FoF groups (right column). Concentrating initially on the left-hand column showing FoF groups of all ages, when increasing the magnitude of the kick, we can see a flattening of the CMF. For the `kick_0km/s` kick model, we see a slow build up of low mass FoF groups over time. At higher masses, the CMF slope and normalisation appears to stay relatively constant. As the kick magnitude is increased, the build up of low mass FoF groups observed in the `kick_0km/s` run is reduced. For the `kick_1km/s` simulation, some build up at lower masses is seen, but then some turnover seems to occur at later times after around 400 Myr in the simulation. For the `kick_3km/s` simulation, there appears to be no sign of cluster build up for any of the masses. The normalisation overall is also lower at all times for the low mass FoF groups, reflected in the order of magnitude lower number of FoF groups as shown in Table 4.1. For the newly formed FoF groups (<20 Myr) shown in the middle column of Fig. 4.4, for the `kick_0km/s` and `kick_1km/s` runs, the newly formed CMFs look similar. The right-hand column shows the FoF groups with ages greater than 100 Myr. We would expect to see some signatures of cluster disruption, as star clusters embedded in a galaxy would be subjected to disruption processes such as tidal interactions with other star clusters or passing molecular clouds (Portegies Zwart et al., 2010). In these simulations however we do see a build up, as discussed at some length in Chapter 3. The build up does however seem to be reduced by increasing the magnitude of the kick. When forming star clusters in these simulations, as can be hinted at by the discussion of the structural properties in 4.4.3, the inter-stellar separations within the formed star clusters are typically below 0.1 pc, which is the softening length used. This means that once the star clusters have formed, the interactions between the stars themselves are almost completely softened, meaning that important internal processes within star clusters able to make them disrupt, or at least more susceptible to disruption are unresolved. Naturally increasing the distance between the stars reduces the effect of the over-softened interactions and also makes the clusters less bound, meaning that tidal interactions are more likely to unbind the clusters. This is potentially what we observe here for the `kick_3km/s` run. This simulation produces fewer, less bound star clusters which are more extended and diffuse. We therefore likely see evidence of cluster disruption in this simulation, but further investigation of this will require fully tracking the clusters which is the topic of future work. For the analysis of these FoF groups, we use a fixed linking length of 5 pc, however this may miss some of the very diffuse clusters produced in particularly the `kick_3km/s` simulation. It appears to not make a substantial difference to the overall distribution however. Decreasing the linking length naturally increases the number of smaller FoF groups identified, whilst a larger linking length means that the maximum cluster

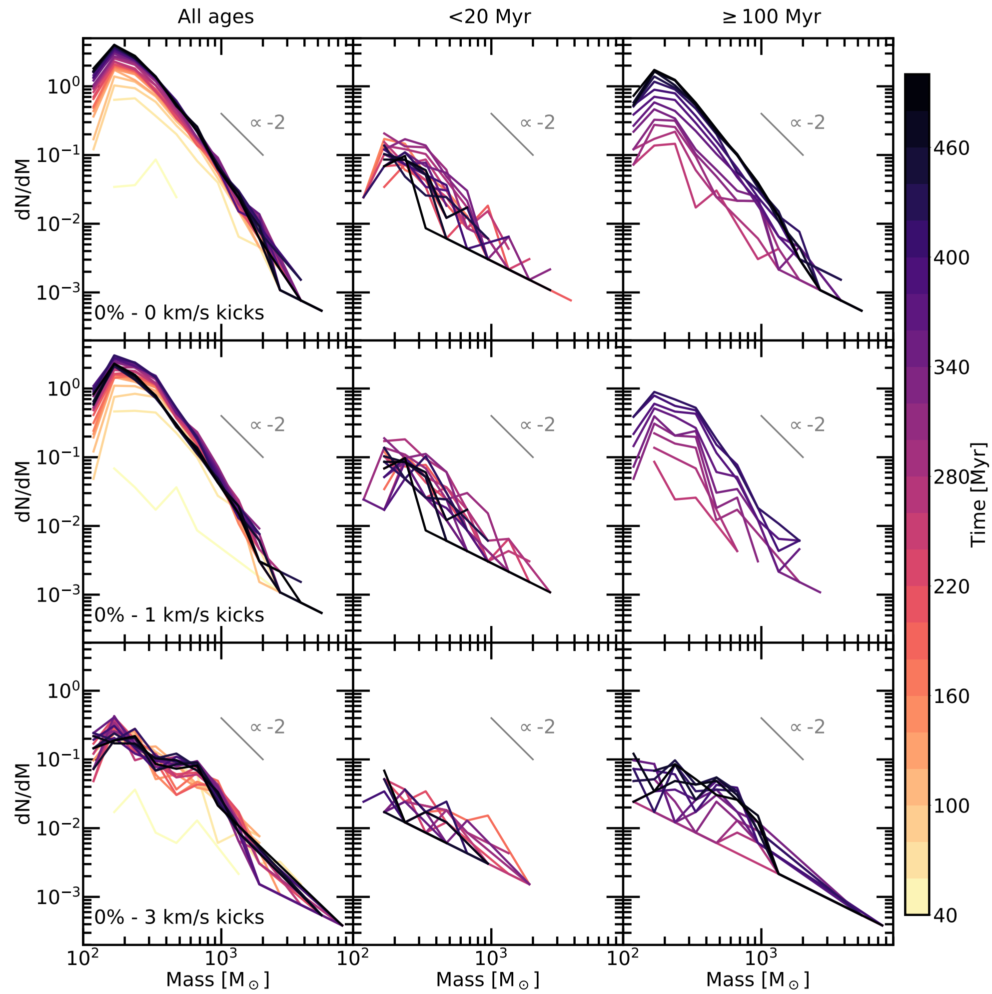

Figure 4.4: Cluster mass function for the no kicks run (`kick_0km/s`, upper three panels), the 1 km/s kick run (`kick_1km/s`, middle three panels) and the 3 km/s kicks run (`kick_3km/s`, lower three panels). We show all FoF groups of all ages in the left column, FoF groups with average ages of less than 20 Myr in the middle column and FoF groups with average ages of greater than 20 Myr in the right column. The cluster mass function is shown here as a function of time as shown by the colour bar. For the simulation without kicks (top row), we see that whilst the cluster mass function of newly formed clusters actually decreases with time, the total number of clusters continues to increase as shown by the increase in normalisation in the top-left panel. The reason for this can be seen in the top-right plot, as we see the pile-up of older clusters which are not destroyed with time. For the simulation with a 3 km/s kick (bottom row), we do not see the same increasing in normalisation in the bottom-left panel. Instead, we can see that the number of old clusters (bottom-right panel) after some time stops increasing in normalisation and instead stays constant. This is a clear indication that some of these older clusters are being destroyed in order for this normalisation to stay constant.

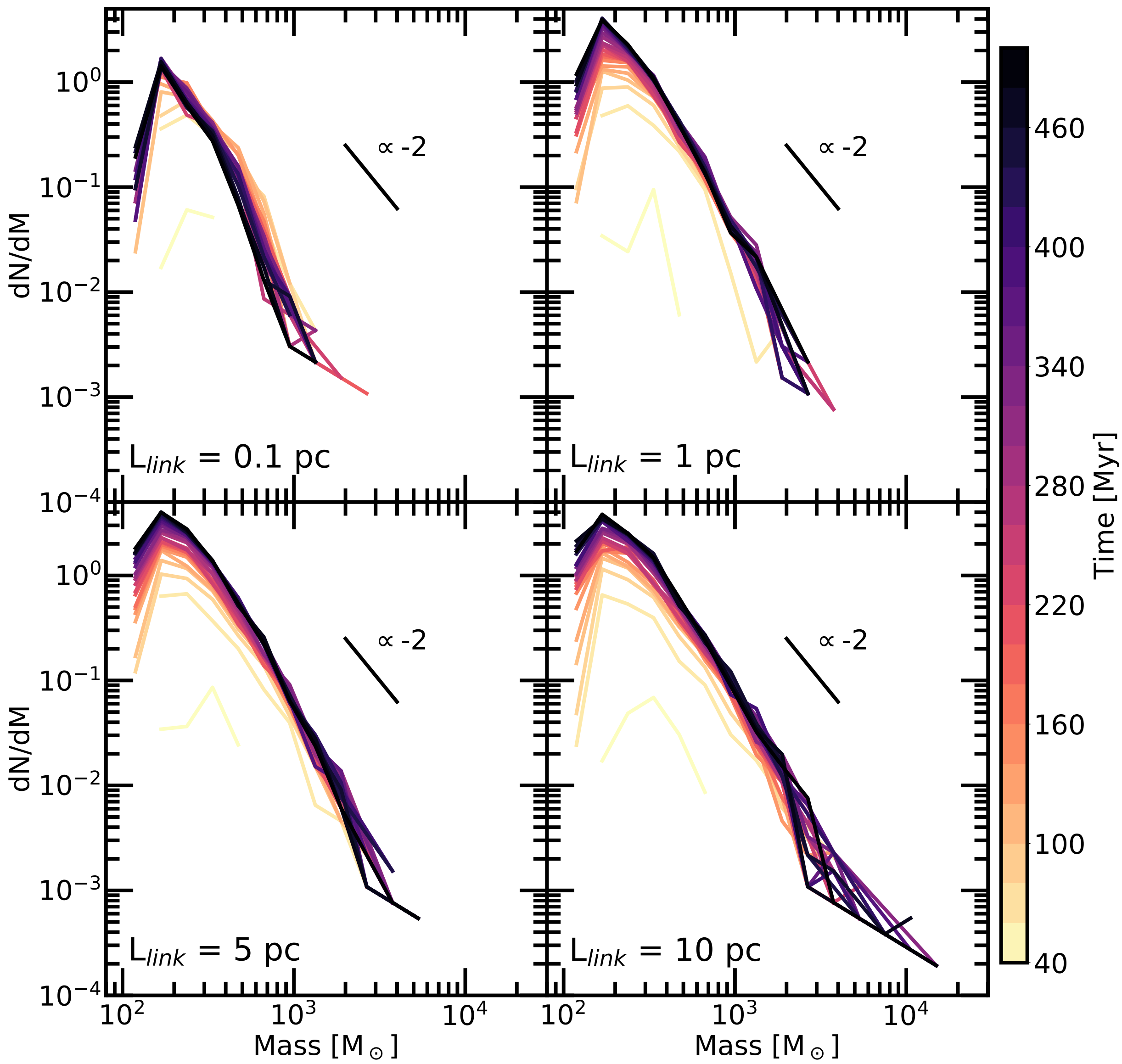

Figure 4.5: Comparison of FoF linking lengths for the `kick_0km/s` model. Here the linking length is varied from 0.1 pc to 10 pc to explore the effect of the linking length on the measured distribution of clusters. The FoF groups measured with smaller linking lengths do not extend to the same higher masses as measured with a larger linking length.

mass is increased, as it begins to link together multiple FoF groups. We show tests for the effect of varying the FoF linking length in Fig. 4.5.

4.4.2 Cluster positions

Fig. 4.6 shows the distribution of identified FoF groups at 500 Myr in the simulations. As could also be seen from the surface density maps in Fig. 4.1, it is clear that the number of clusters is substantially affected by the implementation of the kick. The `kick_0km/s` model (top panel) shows many clusters distributed over the whole galaxy, also with a wide mass range. We see several higher mass clusters (darker coloured), along with a few that seem to be centrally concentrated. On the outskirts of the galaxy, there are also several clusters but generally of lower masses. To contrast, the `kick_3km/s` (bottom panel) shows far fewer clusters. These clusters appear to generally be larger in size and only occupy the galaxy out to a radius of around 500 pc, showing that the clustering on the outskirts is significantly reduced. There does appear to be some central concentration in this model, with the largest cluster residing near the centre. For the intermediate kick model, `kick_1km/s`, we see the same spatial distribution of clusters as in the `kick_0km/s` model, but this time the clusters appear to be more smoothly distributed over the galaxy and it also lacks any kind of centrally concentrated cluster. Of course, this can be a random consequence of looking at this galaxy at this particular timestep, but given that the clusters are long-lived, it appears that in this particular simulation, there is no central build up. The mass ranges and sizes of the clusters are discussed in more detail in Sec. 4.4.3.

4.4.3 Cluster masses & densities

Fig. 4.7 shows the effect of the kick on the spatial properties of the identified FoF groups. When increasing the magnitude of the kick from 0 km/s to 3 km/s, the half-mass radii of the identified clusters increases by almost an order of magnitude and subsequently the half-mass surface density and total surface density decreases substantially. Decreasing the surface densities of clusters makes them easier to be disrupted as it lowers the virial parameter as shown in Fig. 4.8. We can also see the number as well as the distribution of masses of clusters well in Fig. 4.7. The overall number of clusters is reduced by roughly an order of magnitude between the `kick_0km/s` and `kick_3km/s` model (exact numbers shown in Table 4.1) but in general the mass range sampled between the models is quite similar. The majority of clusters sit in the range from 10^2 to 2×10^3 $M_\odot$, with a couple of clusters scattered at higher masses up to a few $\times 10^3$ $M_\odot$. In this particular snapshot, the most massive cluster actually comes from the `kick_3km/s` model, with a cluster at 7414 $M_\odot$ which sits in the centre of the galaxy as seen in Fig. 4.6, but this should not be over-interpreted as a feature of the model, more that this is a somewhat fortunate outcome of the simulation at this particular time for this particular setup.

This small velocity kick implemented here has a very similar effect to the star formation efficiency as shown in Chapter 3. An increasing kick magnitude has the same impact as an increasing star formation efficiency. Increasing the star formation efficiency parameter caused star formation to happen at lower densities as we did not let the gas collapse to such high densities before forming stars, whilst the kick alters the density of the stars following their realisation as a

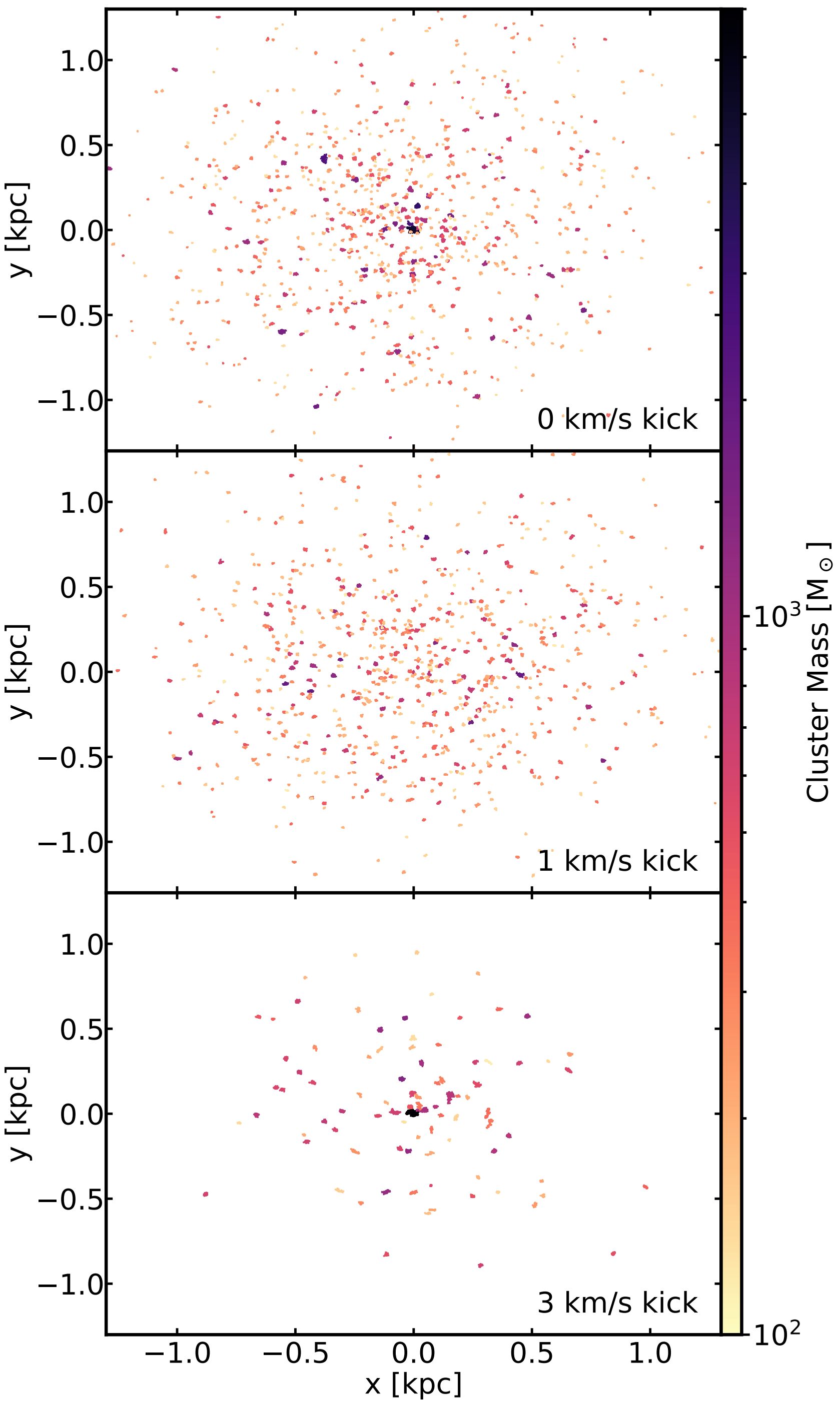

Figure 4.6: The identified FoF groups in each of the runs at 500 Myr, colour coded by cluster mass in $M_\odot$. The top panel shows the `kick_0km/s` run, middle panel shows `kick_1km/s` and the bottom panel shows `kick_3km/s`. Visually, immediately we can see how the spatial distribution of clusters changes as the magnitude of the kick is increased.

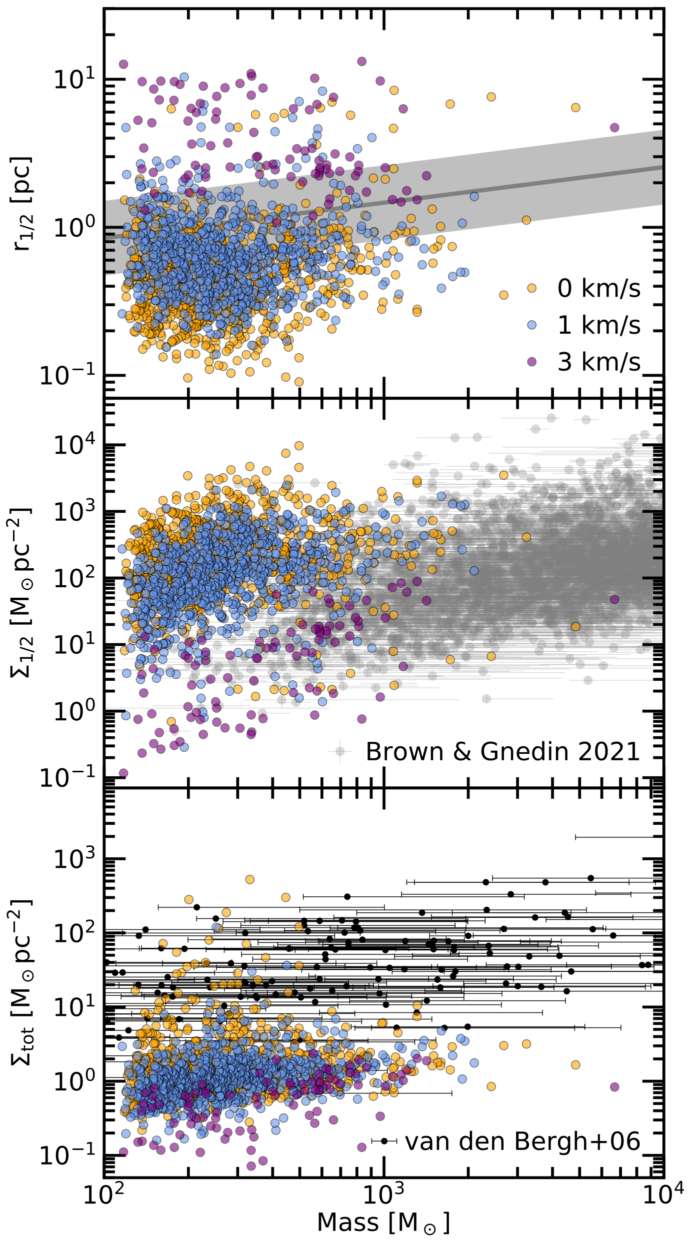

Figure 4.7: *Top*: The half-mass radius as a function of mass. *Middle*: The half-mass surface density as a function of mass. *Bottom*: The total surface density as a function of mass, described as the surface density enclosing 90 per cent of the FoF group mass. All panels show star clusters of all ages identified at 360 Myr. We compare to observational data from Brown and Gnedin (2021) shown in the top and middle panels, which is a sample of 6097 young star clusters collected from 31 local galaxies, whilst the van den Bergh (2006) sample shows a population of open clusters in the Milky Way.

star particle. The direction of the kick is random, and therefore can either increase or decrease the velocity of each star.

4.4.4 Virial parameter

The effect of the kick on the virial parameter of the formed FoF groups can be seen in Fig. 4.8. The virial parameter here is defined as the ratio of twice the kinetic energy E_{k} to the gravitational energy E_{g} of the identified FoF group assuming a uniform density sphere (Bertoldi and McKee, 1992), such that

$$\alpha_{\mathrm{vir}} = \frac{2E_{\mathrm{k}}}{E_{\mathrm{g}}} = \frac{5\sigma_v^2 R}{GM}, \tag{4.6}$$

where G is the gravitational constant, σ_v^2 is the average one-dimensional velocity dispersion along the line of sight, R is the characteristic radius of the cluster, and M is its mass. This virial parameter naturally holds not only for star clusters but also for molecular clouds. In the `kick_0km/s` model for example, the virial parameter of the star clusters should be relatively similar to their parent cloud, but this transition is not straightforward and this is an interesting study for future work to examine the link between the dynamical properties of molecular clouds and the resultant star clusters. We include some observational values for molecular clouds as well as star clusters in Fig. 4.12 to give some hints toward this.

We take the definition of a FoF group with a virial parameter of $\alpha_{\mathrm{vir}} \leq 1$ to be bound. It should be noted that this excludes the effect of the background potential of the galaxy, as well as the impact of high velocity star particles which are just spatially incident with the star cluster at this particular snapshot, but this effect on the virial parameter is small. The trend with the kick velocity can be seen such that with increasing kick magnitude, more FoF groups move above the $\alpha_{\mathrm{vir}} = 1$ line, showing that more FoF groups are unbound. Additionally one can see that the number of identified FoF groups is reduced when increasing the kick velocity. In the `kick_0km/s` simulation without any velocity kick, the gas is allowed to collapse substantially before forming stars. The gas particles close to the star formation threshold are also highly likely to be bound to one another and the gas in a particular region highly likely satisfies the star formation criterion at the same or very close timesteps. These highly bound gas particles are therefore transformed into a highly clustered and bound collection of stars. Feedback naturally has an impact on future star formation and evacuating the gas surrounding this group of stars preventing further star formation, but the star cluster formation has actually already happened by this point. For this reason, this simulation produces many tightly bound star FoF groups with virial parameters substantially below 1. For the runs with the kicks, the star formation criteria is naturally the same and the effect is the same in the sense that the star forming gas particles will be converted into stars on similar timesteps, but the kick has the effect of puffing out the cluster and affecting the boundedness of the FoF groups, as the virial parameter of the star particles will be substantially altered from that of the star forming gas particles. The effect is seen clearly for the `kick_3km/s` simulation, where fewer FoF groups are formed overall and a much larger fraction have virial parameters greater than 1.

Considering the dependencies of the virial parameter, for the virial parameter to increase following the inclusion of the kick, this means either the velocity dispersion increases, the radius increases, or the mass decreases. We can see in the upper panel of Fig. 4.7 that the masses overall are relatively similar, but the radius substantially increases. Assuming a fixed velocity dispersion for this argument (which is looked at in more detail in Sec. 4.4.6), then we can attribute the higher virial parameters purely to the expansion of the radius of these clusters.

4.4.5 Velocity distributions

Fig. 4.9 shows the distribution of stellar velocities for the three runs for stars identified to be in FoF groups (solid lines) and stars not associated with FoF groups (field stars, dashed lines) for all stars (top panel) and then shown normalised by the total number of stars (bottom panel). The number of stars produced in each of these simulations is comparable, ranging from 5.7 to 6.1 $\times 10^5$ $M_\odot$ (see Table. 4.1. For the field stars, the overall distribution appears to be relatively similar. One might expect a shift towards higher and lower velocities as the kick is increased, but it is important to note that a velocity kick of 1 or 3 km/s is small in comparison to the velocities of the stars. Additionally, this kick can be constructive (increasing the velocity) or destructive (decreasing the velocity of the particle) as discussed in Sec. 4.2.2, and is only maximally effective a small fraction of the time. Therefore, for the overall distribution of velocities, we do not see the effect. When looking at the distribution of velocities in FoF groups however, we do start to see the impact of the kick. For the `kick_1km/s` run, the effect is not particularly visible, but for the `kick_3km/s` run, the number of FoF groups is substantially reduced and also the distribution of velocities in the bottom panel of Fig. 4.9 shows hints that the FoF groups have lower overall velocities in comparison to the field stars. Perhaps in this model, the stars that are given a destructive kick preferentially end up in FoF groups.

4.4.6 Velocity dispersion

In order to understand the effect of the kick on the properties of the resultant clusters and to disentangle the reasoning behind the increasing virial parameters when including the kicks, we can look also at the velocity dispersion and the relation to the mass and radius.

Fig. 4.10 shows the 1-D velocity dispersion in the x, y and z directions for each of the simulations. The first thing to note is that there is very little difference between the dispersions in the different directions. These star clusters are roughly spherical, and so measuring the dispersion only in the x-direction as we have done for Figs. 4.11 and 4.12 is perfectly appropriate in this case. The velocity dispersion for all kick magnitudes increases with the mass of the FoF group, with the range of dispersions varying from 0.1 km/s up to 7 km/s. Interestingly all models show very similar velocity dispersions. Understanding how these velocity dispersions can stay constant is explored in more detail below.

Fig. 4.11 shows the half-mass radius and velocity dispersion properties of the FoF groups as a function of mass. We split by age in order to see if there is some distinguishable difference between FoF groups of different ages. The upper panel we have already seen in Fig. 4.7, but this time we distinguish between ages which is useful to capture the properties of the newly formed

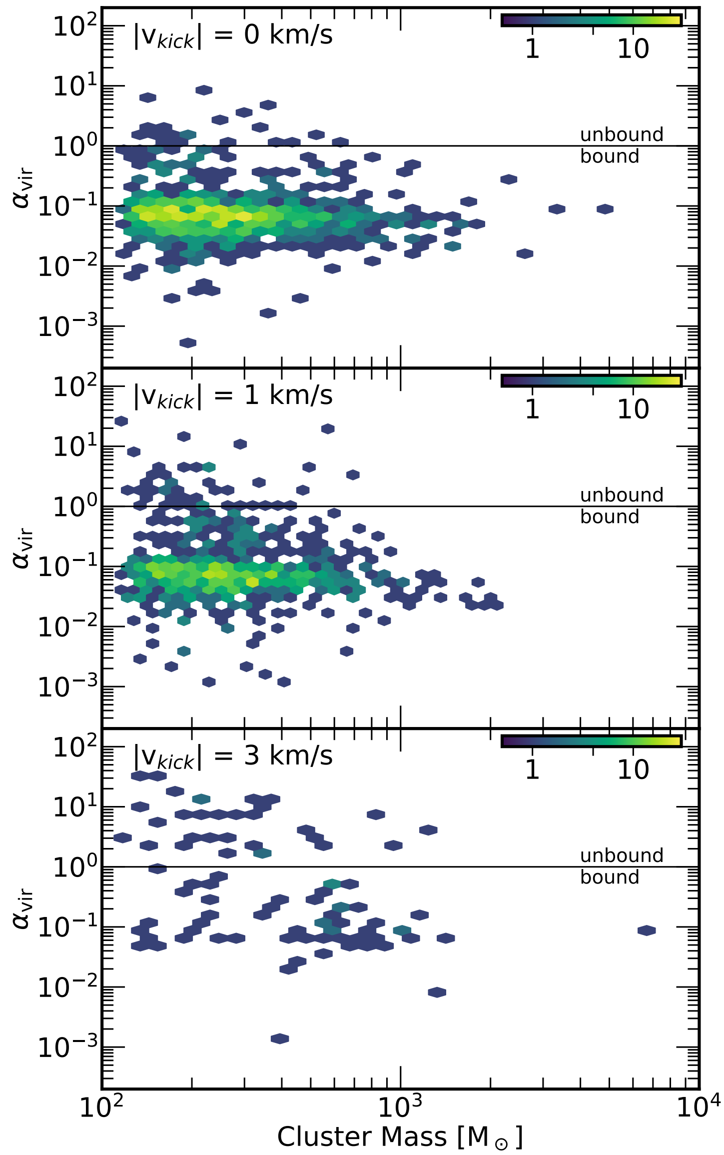

Figure 4.8: The virial parameter for the FoF groups identified at 500 Myr in the simulations. The three panels show the result for the different simulations with the magnitude of kick shown in the top left corner. The colour indicates the number of FoF groups. The solid line at $\alpha_{\rm vir}$=1 indicates the threshold at which FoF groups are considered bound ($\alpha_{\rm vir} eq 1$) or unbound ($\alpha_{\rm vir}$>1). In the upper panel, we can see that in the absence of a kick, nearly all (98 per cent) of the FoF groups lie below the $\alpha_{\rm vir}$=1 line. Moreover, 83 per cent of these FoF groups have virial parameters below 0.1, indicating these FoF groups are highly bound. Conversely, when stars are given a 3 km/s kick, we can see in the lower panel that there is a much wider spread of virial parameters. Whilst 68 per cent still lie below the $\alpha_{\rm vir}$=1 line, only 33 per cent have virial parameters below 0.1. Additionally, 32 per cent of FoF groups lie above this $\alpha_{\rm vir}$=1 line, indicating that these FoF groups are unbound associations.

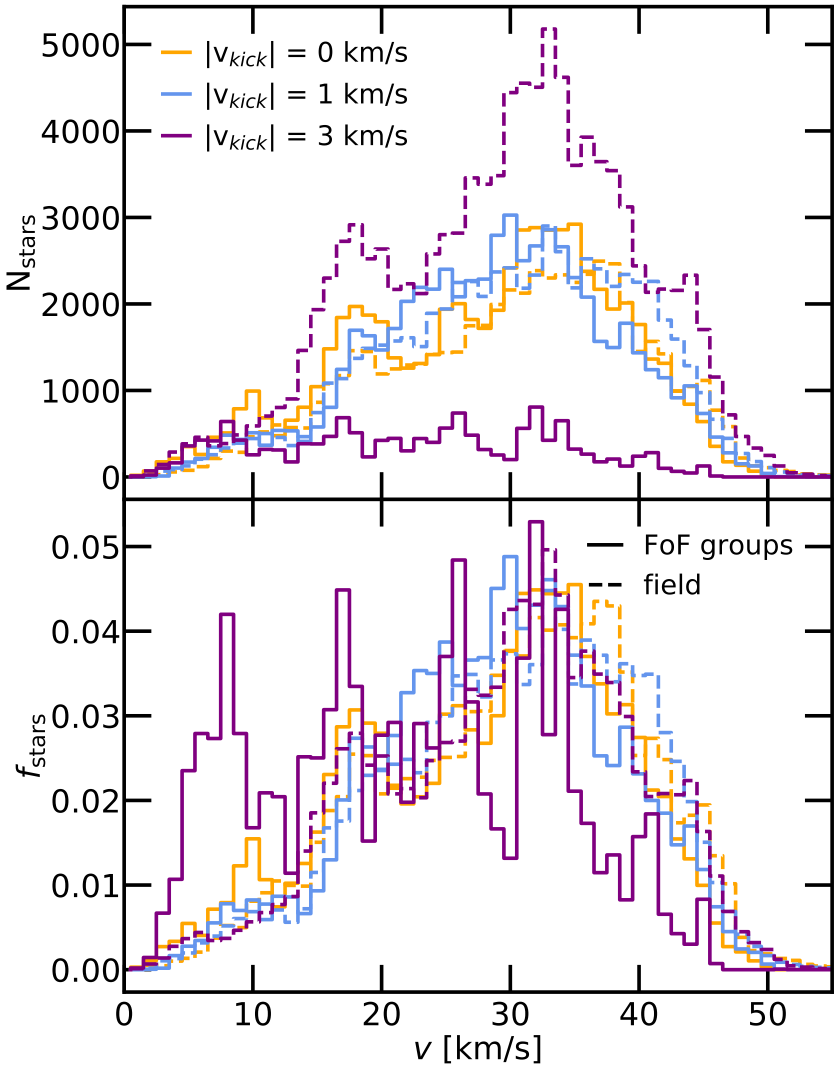

Figure 4.9: Histogram of stellar velocities in FoF groups and in the field. We show the total number in the top panel as well as the fraction of the total number in either the FoF groups or field stars. In the top panel, one can see that the number of stars in FoF groups and in field for the `kick_0km/s` and `kick_1km/s` runs is relatively equal, and the distributions of velocities is also very similar between FoF group and field stars. For the `kick_3km/s` model however, the initial observation is that there is a substantially lower number of stars in FoF groups in comparison to field stars. The distribution of velocities in the field stars appears to be consistent with that found in the `kick_0km/s` and `kick_1km/s` run. This is further illustrated in the bottom panel where we normalise by the total number of stars in FoF groups or field stars. The overall velocity distribution appears to be very similar for all field stars, despite the velocity kick, but the `kick_3km/s` run shows a significantly different distribution of velocities for the stars in FoF groups. Furthermore this distribution appears to be shifted towards lower velocities.

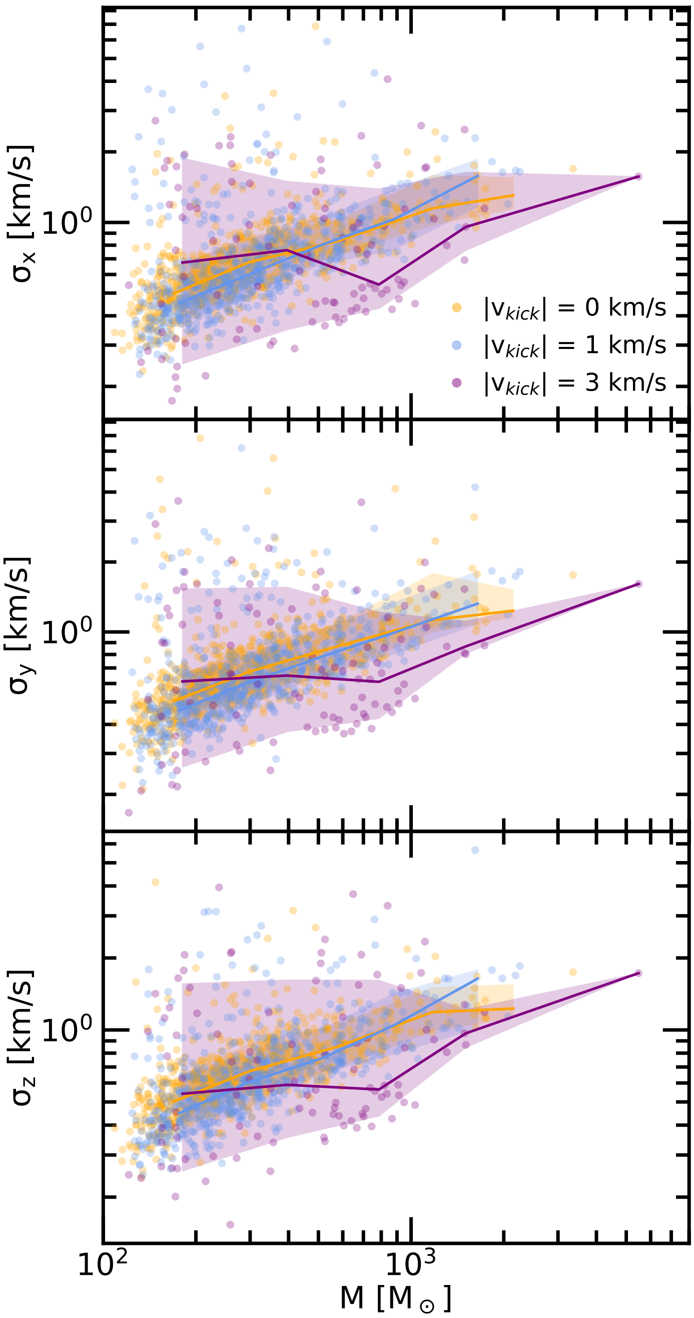

Figure 4.10: The 1D velocity dispersion for all FoF groups in the `kick_0km/s` (orange), `kick_1km/s` (blue) and `kick_3km/s` runs (purple) simulations at 300 Myr. The solid coloured lines show the respective medians and the shaded region show the upper and lower 1 sigma of the fit. The `kick_0km/s` and `kick_1km/s` show a relatively more narrow scatter with many of the FoF groups having dispersions very close to the median. The 3 km/s simulation however produces FoF groups with a substantially wider range of velocity dispersion. In all cases, the velocity dispersion increases as a function of mass.

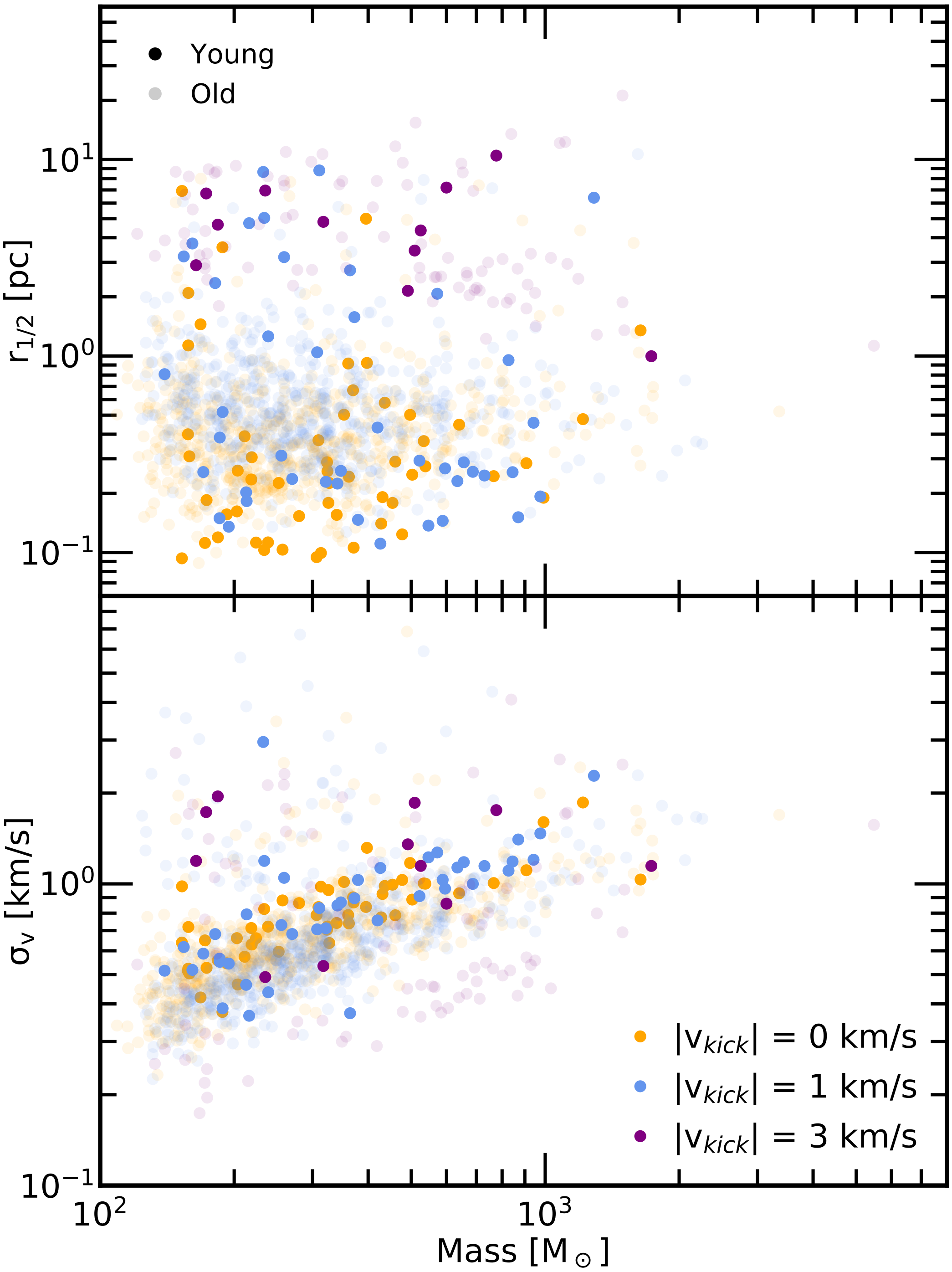

Figure 4.11: *Top*: Mass-radius relation as shown in Fig. 4.7 but now distinguishing between young (≤20 Myr) and old (>20 Myr) FoF groups at 300 Myr. *Bottom*: The 1-D velocity dispersion of FoF groups as a function of mass. The points are separated by age, with bold points showing FoF groups with ages ≤ 20 Myr and faded point showing FoF groups with ages > 20 Myr.

clusters. We choose to analyse the clusters here at 300 Myr as this is about the moment at which the star formation rate has settled (see Fig. 4.2), meaning we are sampling newly formed FoF groups at this steady star formation rate as well as seeing the FoF groups formed during the slightly more bursty star formation episode, peaking around 200 Myr in the simulation. For the `kick_0km/s` and `kick_1km/s` models, the newly formed FoF groups shown in Fig. 4.7 appear to lay at the more compact end of the distribution of FoF groups. The sampled FoF group masses are similar to the overall population, but the radii are smaller, particularly for the `kick_0km/s` model. For the `kick_1km/s` model, they also are on the compact side for some FoF groups, but we also see a significant population of much more extended FoF groups, with half-mass radii out to 10 pc. For the `kick_3km/s` model, the FoF groups overall are much more extended, with no FoF groups having half-mass radii below 1 pc, and the newly formed FoF groups appear to sample the same space in mass and radii as the previously formed FoF groups.

It has been shown in observations of clusters from Ramírez-Tannus et al. (2021) that there is a correlation between velocity dispersion of clusters and cluster age, indicating an evolution of the velocity dispersion of star clusters as they age. Looking at the bottom panel of Fig. 4.11, we do not see signatures of the evolution of the velocity dispersion with ages, as the velocity dispersions shown for the youngest clusters look consistent and maybe a little bit higher than the dispersions for the older clusters, but it should be mentioned that the timescales considered in Ramírez-Tannus et al. (2021) are shorter than 20 Myr, and so it is possible that the evolution with age is somewhat shorter lived than considered in our comparison. The velocity dispersions of the newly formed clusters in Fig. 4.11 show a relatively tight correlation for all models. The scatter is certainly larger for the `kick_3km/s` model, but otherwise the distributions look very similar. This is demonstrated further in Fig. 4.10.

In line with the review from Heyer and Dame (2015), Fig. 4.12 shows the relationship between velocity dispersion and half-mass radius (left panel) as well as with the product of the half-mass radius and the half-mass surface density (right panel). It must be noted that Heyer and Dame (2015) discuss exclusively molecular clouds identified in the Milky Way, as opposed to star clusters, but the relationship is expected to be somewhat related. We therefore find it useful to compare the results for star clusters to these molecular clouds. As an additional piece of information, we now also distinguish between bound and unbound clusters in order to note any differences. It is important to consider the definition we use here for something being bound. This analysis does not include the full unbinding procedure considered in Chapter 3 for example, and so high velocity stars incident with the FoF group at some particular time can have an effect on being considered bound or unbound, but this effect is most certainly small. Additionally, calling clusters with virial parameters above 1 may be too harsh of a criteria. This is one of the reasons why we still include ‘unbound’ FoF groups in the analysis. Nevertheless, focusing on the newly formed bound FoF groups (bold filled circles) in Fig. 4.12, the velocity dispersion and half-mass radius relation shows some interesting behaviour. There even appears to be an anti-correlation between these two variables, with the velocity dispersion decreasing with increasing with half-mass radius for the FoF groups identified in the `kick_0km/s` and `kick_1km/s` models. Should the radius increase by a factor of 2, for a constant density the mass would increase by a factor of approximately 8. To keep a constant virial parameter, from Eq. 4.6, the velocity dispersion would therefore increase by a factor of 2. This decrease in velocity dispersion with radius therefore

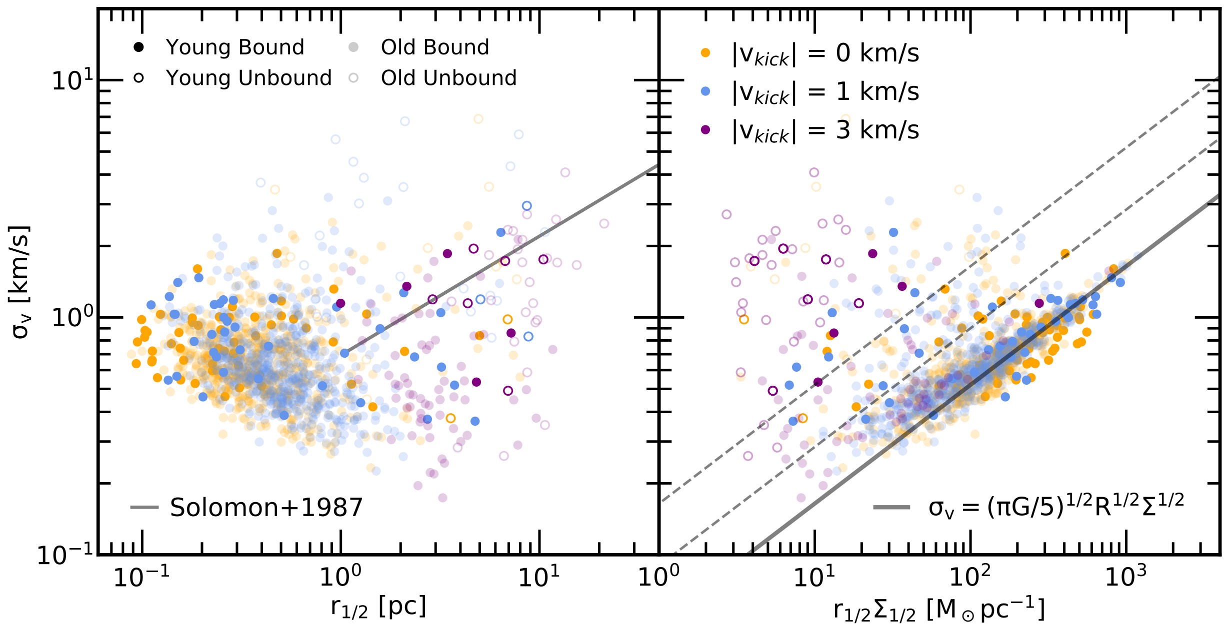

Figure 4.12: *Left*: Velocity dispersion as a function of half mass radius for the simulations at 300 Myr. Again we distinguish between FoF groups which are young (≤20 Myr, bold colours) and old (>20 Myr, faded colours), but additionally also between bound ($\alpha_{\rm vir} \leq 1$, solid symbols) or unbound ($\alpha_{\rm vir} > 1$, open symbols). The grey line shows the best fit of data presented by Solomon et al. (1987) for molecular clouds as summarised in the review by Heyer and Dame (2015). *Right*: Velocity dispersion as a function of the product of the half-mass radius and half-mass surface density. Colours and symbols are identical to the left plot. The solid grey line shows the Larson relation and the dashed lines are for a virial parameter $\alpha_{\rm vir}$ = 3 (lower line) and $\alpha_{\rm vir}$ = 10 (upper line).

implies potentially that the surface density assumption is not valid. We can see this more by now looking at the right hand panel of Fig. 4.12, which shows the velocity dispersion as a function of the product of the half-mass radius and the half-mass surface density. Combining the scaling relationships for molecular clouds derived by Larson (1981) and equating the virial mass to the mass of the cloud gives

$$\sigma_v = (\pi G/5)^{1/2} R^{1/2} \Sigma^{1/2}, \tag{4.7}$$

where σ_v is again the velocity dispersion, and R and Σ are the half-mass radii and surface density, respectively. Molecular clouds within the galactic disk are shown to follow this relationship, and so we can also compare this property to that of the identified FoF groups in our simulations in order to understand the effect of the kick on the dynamical properties. This is appropriate given that the kick is introduced in order to modify the kinematic properties of the gas that are transferred to the FoF groups. For the `kick_0km/s` model (orange), all points sit tightly in agreement with Eq. 4.7. There is some scatter upwards for the older bound clusters, and we can also see that the couple of young unbound FoF groups identified (bold open circles) also sit well above this relationship. With the introduction of the kick, the results from the `kick_1km/s` model (blue) again shows a relatively tight relationship with Eq. 4.7 but with a little bit more scatter upwards to higher velocity dispersions on the lower cluster mass end. It is difficult to distinguish from this model if it is the velocity dispersions which are higher, or the product of the half-mass radius and surface density is lower, but we can see this much more clearly when looking at the `kick_3km/s` model. One might expect that the introduction of the kick to increase the velocity dispersion of a given cluster mass, which would keep the points within the same mass range but scatter them upwards, but this does not appear to be what happens following the kick. Instead, the FoF groups that have received the 3 km/s kick have roughly similar velocity dispersions (as was also seen in Fig. 4.10 but the product of their half-mass radii and surface densities have decreased. Looking again at the right panel of Fig. 4.12, we can see these clusters have larger half-mass radii than those from the `kick_0km/s` and `kick_1km/s` models, therefore we can conclude it is the surface density of these FoF groups which has been significantly reduced. To understand what is really happening to the structural properties, we can compare three similar mass FoF groups from each of the simulations and observe how the kick affects them.

Fig. 4.13 allows for further understanding of the structural properties of the star clusters formed in the simulations. Presented here is a FoF group from each of the simulations with different kick magnitudes. Each FoF group is identified to have the same mass ($\sim 1.3 \times 10^3$ M$_\odot$) and we can now examine the spatial distribution of the stars and differences in the velocities. Contrasting the `kick_0km/s` model (left panel) and the `kick_3km/s` model (right panel), we can see the radius of the FoF group is significantly different. The half-mass radii for the `kick_0km/s`, `kick_1km/s`, and `kick_3km/s` models are 0.28 pc, 0.81 pc and 1.54 pc, respectively. Despite the very different radii, they have similar velocity dispersions of 1.22 km/s, 1.20 km/s and 0.96 km/s. Coming back to the discussion in Sec. 4.4.4, we can see for a cluster of fixed mass, the velocity dispersions are fairly similar, but it is the radii which are the most different which is driving the differences in virial parameters observed between the different models.

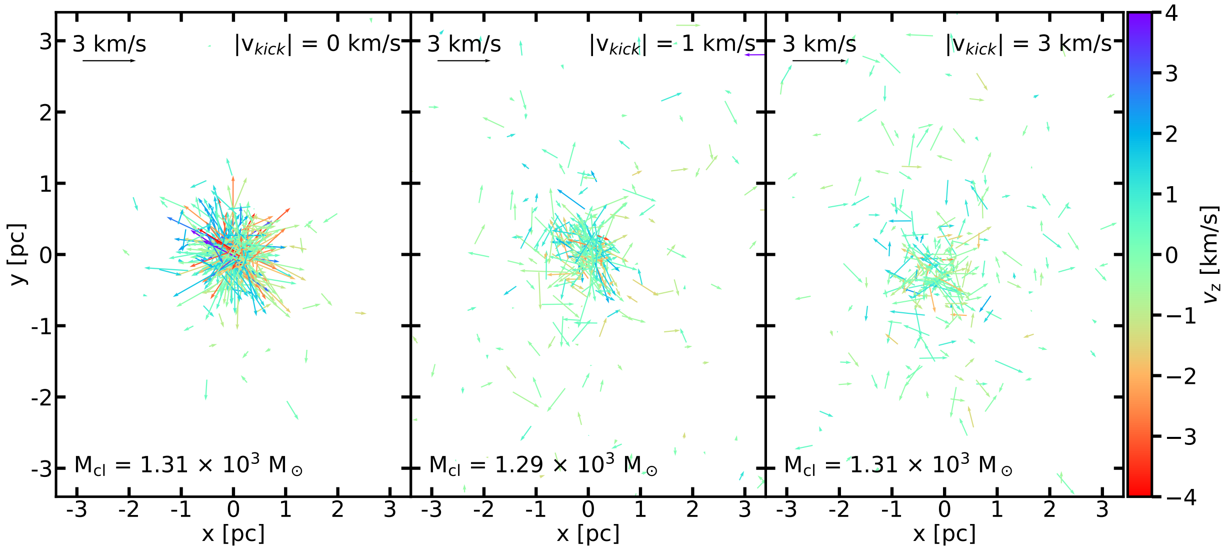

Figure 4.13: Velocities of stars in 3 example comparable stellar FoF groups in each of the simulations. All of the FoF groups were randomly selected for having similar masses of $\sim 1.3 \times 10^3$ $M_\odot$. Every star is plotted individually by an arrow, with the base of the arrow showing the star's current position, direction of the arrow shows the velocity in the x-y plane (6×6 pc^2) where the length shows the magnitude of the velocity in the x-y plane. The colour shows the magnitude and direction of the velocity in the z-direction. The key in the top left corner of each plot shows a vector with a magnitude of 3 km/s. Spatially, we can see what is also apparently from Fig. 4.7 in that the stars in the `kick_0km/s` run are much more compact and clustered together. Increasing the kick results in less dense FoF groups. Additionally, the velocities appear to decrease as the magnitude of the kick is increased.

4.5 Effect of accounting for cloud core collapse timescales on global galaxy properties

As shown in Chapter 5, where we explore the effect of different feedback prescriptions on the star cluster properties, photoionising feedback has a substantial impact on the structural properties of the star FoF groups formed in our simulations. Photoionising feedback heats the gas surrounding the star forming regions, preventing further star formation. This self-regulated process is far more important in setting the properties of the stars and their clustering in comparison to CCSN, as CCSN explode on timescales longer than the typical episodes of star formation. In our very high resolution simulations, gas particles are allowed to collapse to densities of $\sim 10^2 - 10^5$ cm^{-3} dependent on the densities, as described in Sec. 4.2.1 and shown in the phase diagram in Fig. 4.14. Star formation is enforced instantaneously once gas particles pass below this M_J = 0.5 threshold, but we can question whether instantaneously turning this gas particle into a star and beginning its feedback processes is appropriate and if there is an substantial effect on the subsequent star formation should we alter the time delay between a gas particle being labelled as 'star forming' and actually being realised as a star.

We explore the effect of delaying the realisation of gas particles into star particles on the resultant star FoF groups to try and quantify its effect. In our simulations presented first in Chapter 3, photoionising feedback begins for stars immediately after star formation. For the densities at which we form stars see in Fig. 4.14, the typical free fall times are shown in Fig. 4.15. By beginning the photoionising feedback immediately, we are therefore 'not resolving' this time where the cloud would fully collapse to become a star. Of course, at our resolutions, this is not currently possible to allow the gas to collapse down to the typical physical densities at which stars form in the Universe, but we can test this approximation and its effect by delaying the star formation by a typical free-fall time to quantify if this may have a significant effect and be a contributing limitation to our modelling of star cluster formation.

The free-fall time within the simulation is calculated from the density at which the gas particle is realised into a star,

$$\mathrm{t_{ff}} = \left(\frac{3\pi}{32\mathrm{G}\rho}\right)^{\frac{1}{2}}, \tag{4.8}$$

where $\mathrm{t_{ff}}$ is the local free-fall time in units of 9.8×10^8 yr, G is the gravitational constant in Gadget units, such that G = 43007.1 kpc $(10^{10}\mathrm{M}_\odot)^{-1}(\mathrm{km/s})^2$ and ρ is the gas density in units of 10^{10} $\mathrm{M}_\odot/\mathrm{cm}^{-3}$. The range of typical free-fall times calculated from the ambient density of the realised star forming gas particles is shown in Fig. 4.15. We test the effect of delaying the feedback by free-fall times of 0.01 Myr, 0.1 Myr and 1 Myr (see also Chapter 3 and Chapter 5 for the effects of excluding photoionisation altogether).

The stellar and gas surface densities of each of the simulations with the delay in star formation are shown in Fig. 4.16 and Fig. 4.17 at 360 Myr in the simulations. All galaxies look similar in terms of their distributions of stars and gas, however the shorter delay times appear to produce a slightly smoother distribution of stars. All simulations show clear clustering, with visible clumps of stars at all radii, but the increase in delay has some more elongated stellar structures,

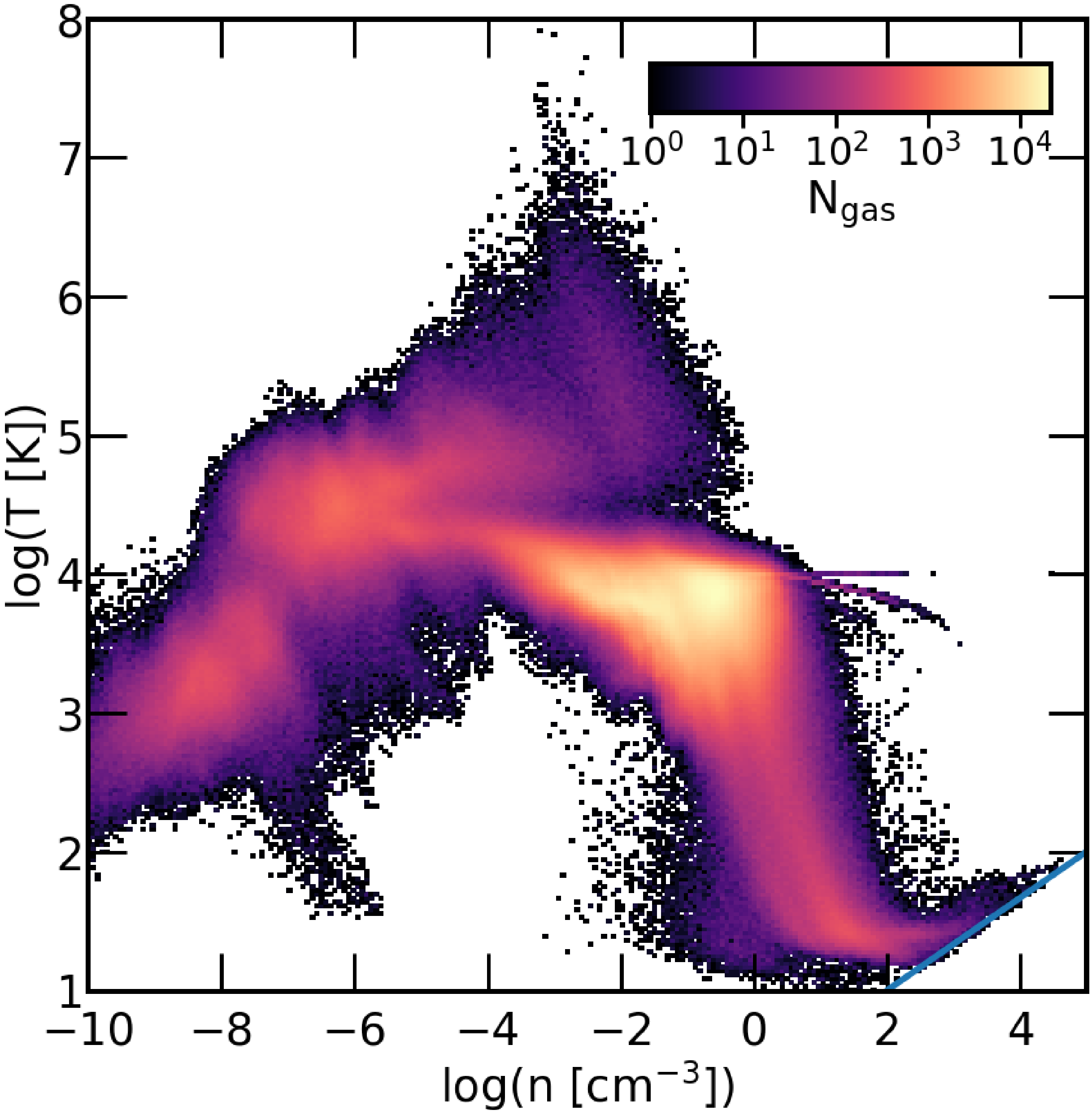

Figure 4.14: Phase diagram for the run with 0% star formation efficiency with no delay time. The star formation threshold of $M_J = 0.5$ is shown by the blue line. Gas particles which pass beyond this line are instantaneously formed into star particles by sampling from a Kroupa (2001) IMF.

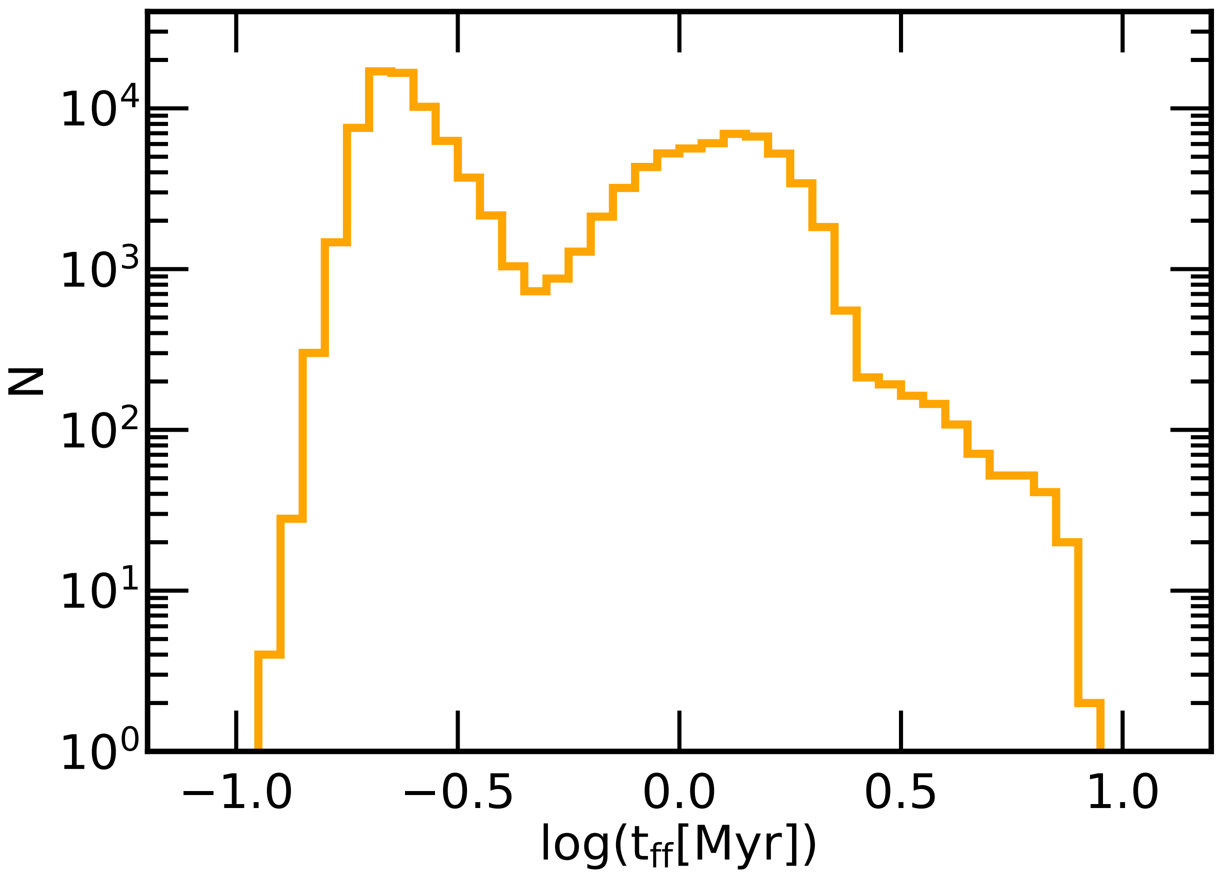

Figure 4.15: Distribution of free-fall times for newly formed stars. This distribution is shown for the run with 0 per cent efficiency and zero magnitude kick, `kick_0km/s`. The free fall time is calculated from the ambient density at which the star is realised. We can see a distribution ranging from 0.1 Myr up to 10 Myr.

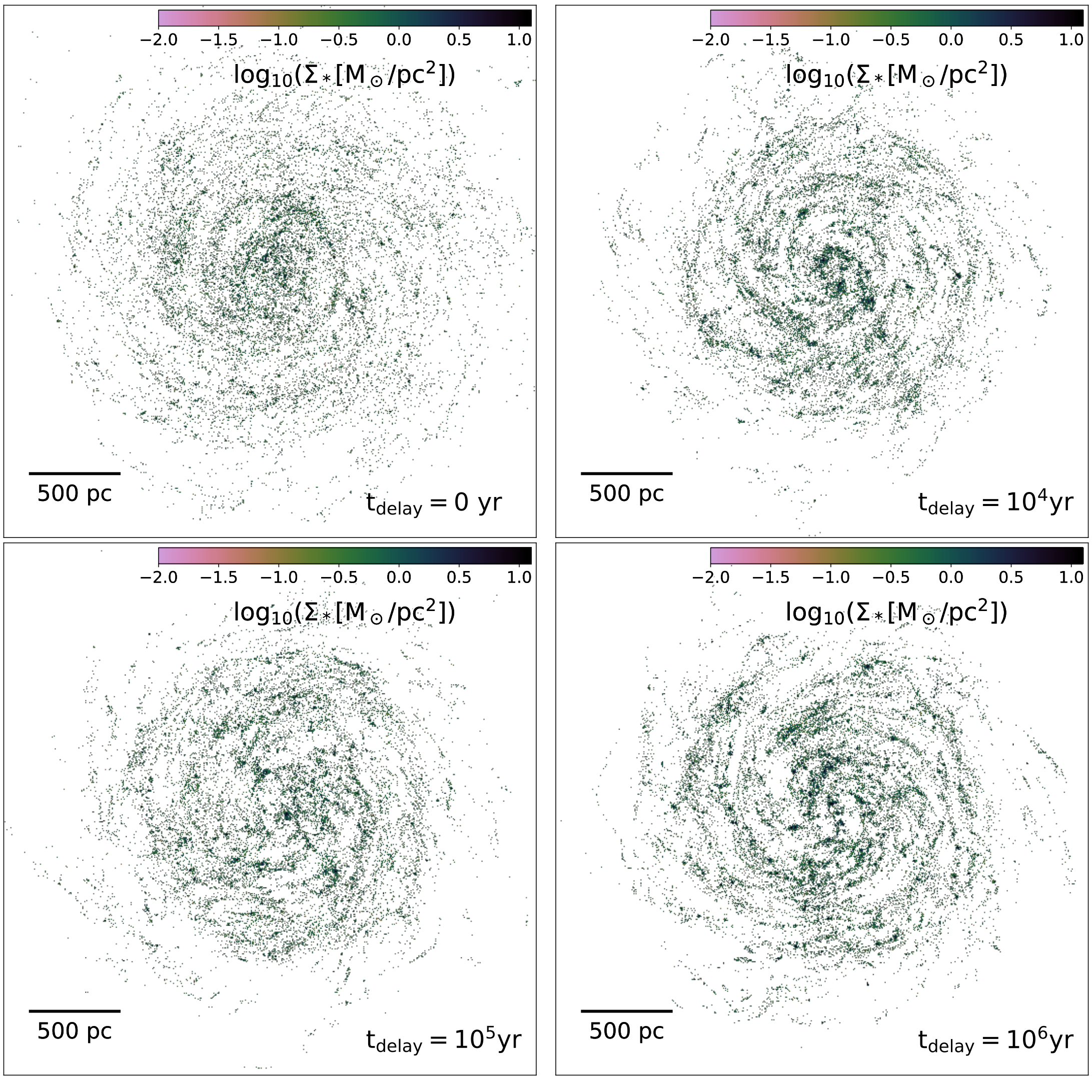

Figure 4.16: Stellar surface density maps for the runs with differing delay times, including the fiducial model with no delay time (`delay_0`). All simulations are shown at 360 Myr for a 3 kpc $\times$ 3 kpc region represented by 1024 $\times$ 1024 pixels. This makes each pixel represent $\sim$ 3 pc. Some of the surface densities of individual clusters are much higher than this (up to 10^4 $M_\odot/pc^2$, see Fig. 4.23), but these densities are artificially lowered in this plot due to the averaging effect in each pixel. Comparing no delay time (`delay_0`) with the runs with a delay time (`delay_1e4`, `delay_1e5` and `delay_1e6`), the stellar distributions appear to be a bit more smooth when including a delay before realising a star forming gas particle as a star. There are also some subtle differences between the runs with different delay times, for example some larger and perhaps more diffuse clusters are visible near the centre of `delay_1e4` with not much clustering on the outskirts of the galaxy in comparison to `delay_1e6`, where several dense clusters are visible all over the galaxy, including at larger radii.

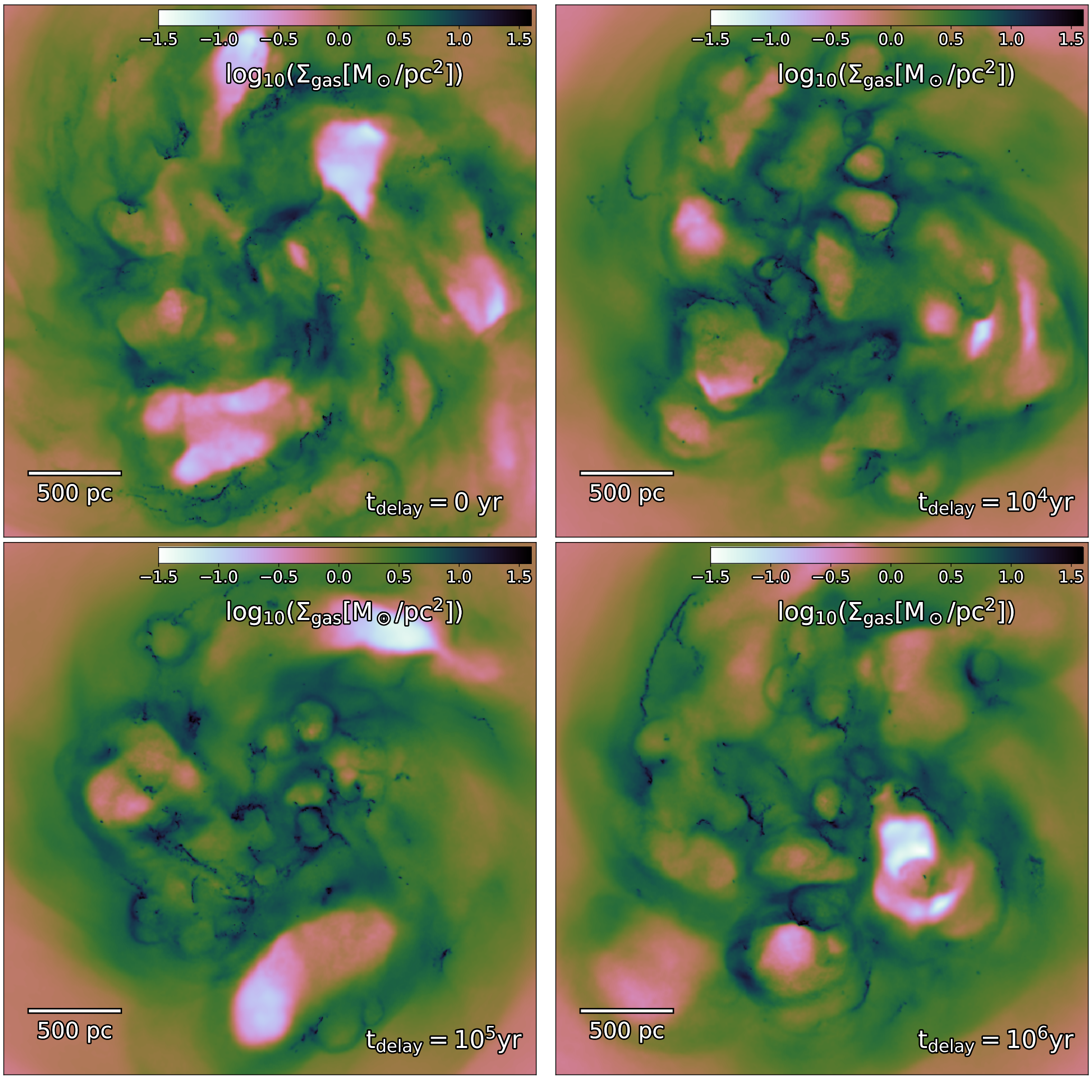

Figure 4.17: Gas surface density maps, as in Fig. 4.16 at 360 Myr in the simulations. This again shows a 3×3 kpc^2 region represented by 1024×1024 pixels. One can notice the areas of dense gas, here shown only up to $\Sigma_{gas} = 1.5$ M$_\odot$/pc^2, but the gas naturally reaches much higher densities at the sites of star formation, but on much smaller scales than the pixel size of 3 pc.

potentially from disrupted clusters. For the gas in Fig. 4.17, clear supernova bubbles are seen in all panels. We can also observe the dense regions surrounding the supernova bubbles where star formation is also then triggered. The upper right panel showing the `delay_1e5` simulation shows a particularly attractive example of this in the centre. Given that this is a single snapshot, any noticeable differences in the gas distribution are likely to be simply random moments in the simulations with the ever changing ISM as the gas is constantly compressed, converted into stars, heated and blown out in bubbles.

In agreement with the very similar distributions of stars and gas for each of the models, the star formation histories shown in Fig. 4.18 are also very similar amongst the models. There is an initial period of higher star formation rates around 50-100 Myr as the gas collapses and forms many stars rapidly. All simulations then settle to a steady average star formation rate of $\sim 10^{-3}$ $M_{\odot}$/yr for the remainder of the simulations, but with some range in burstiness. The longer delay times result in more bursty star formation rates. This is in agreement with Chapter 3 where we explored the effect of completely excluding photoionisation. Excluding photoionisation still resulted in a similar average star formation rate of $\sim 10^{-3}$ $M_{\odot}$/yr (but with a much larger burst of star formation at earlier times) but the star formation rate was substantially more bursty than the runs that included photoionisation.

The final stellar masses at 360 Myr are M_*[`delay_0`] = 5.17×10^5 $M_{\odot}$, M_*[`delay_1e4`] = 4.44×10^5 $M_{\odot}$, M_*[`delay_1e5`] = $4.64 \times 10^{\,5}$ $M_{\odot}$ and M_*[`delay_1e6`] = 5.82×10^5 $M_{\odot}$. Interestingly it appears that the short delay time (`delay_1e4`) reduces the total stellar mass formed by 360 Myr in comparison to the `delay_0` run with no star formation delay, but the increasing of this time delay then increases the stellar mass formed. The stellar mass formed in the `delay_1e6` run exceeds that of the `delay_0` by a non-negligible amount. Understanding why this happens involves consideration of local areas of star formation. If we consider a small area of a few hundred solar masses for example, with no delay, in a given timestep, a couple of stars form and immediately begin to heat the surrounding gas to 10^4 K halting star formation immediately. When delaying the star formation process, in practise we are delaying the onset of photoionising feedback. Taking the example of this small region, the longer the delay time, the more stars are able to form in that given region before photoionisation begins and halts star formation (followed by CCSN explosions which completely destroy star formation in that region). This effectively explains why we see an increase in stellar mass formed between the `delay_1e4` and `delay_1e6` runs, but it does not explain the decrease in stellar mass between the `delay_0` and `delay_1e4` runs. When considering the way that the feedback processes influence star formations, one cannot only consider a small region and extrapolate to larger regions, hence why we cannot answer galaxy formation by only simulating very small regions. Speculatively, the reasoning behind the stellar mass formed decreasing with the 10^4 km/s kick in comparison to no kick is that gas in the `delay_1e4` run is allowed to collapse sufficiently more to let more stars form, but their collective feedback, both photoionisation but also supernovae is highly destructive to gas surrounding these regions. Waiting for longer delay times, in the case of `delay_1e5` and `delay_1e6` will form more and more stars before this collective feedback kicks in. Forming more and more stars means that more gas is converted into stars and are subsequently immune from the feedback effects of the stars. This is speculation, and it is not possible to fully justify this assumption, but we leave this suggestion as a topic of future investigation.

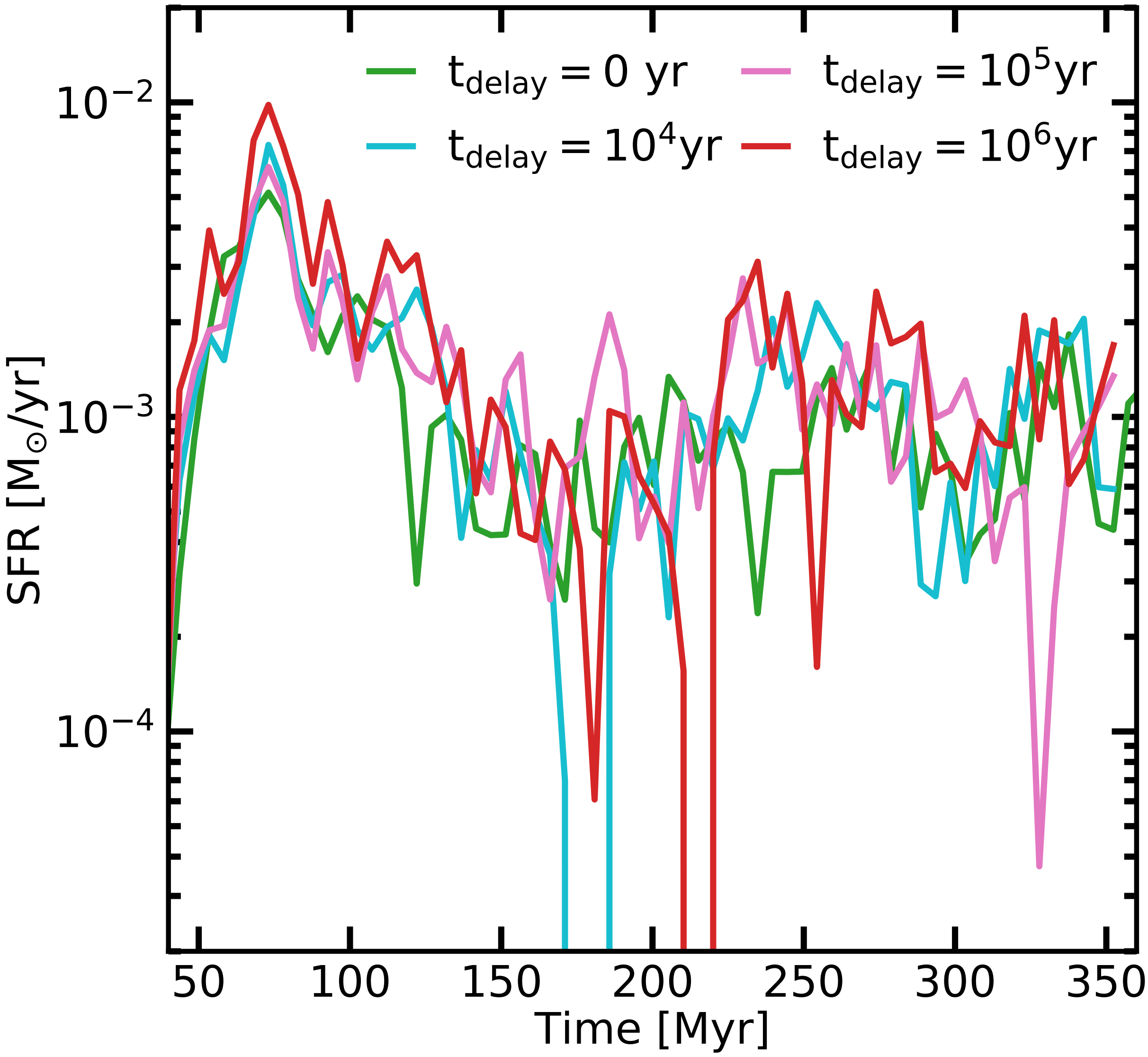

Figure 4.18: Star formation histories for the runs with different delay times. The star formation rates look very similar for all of the models, however the total mass in stars formed is slightly increased when increasing the delay in the photoionising feedback. This is due to the gas being able to collapse more and form more stars in the absence of photoionisation.

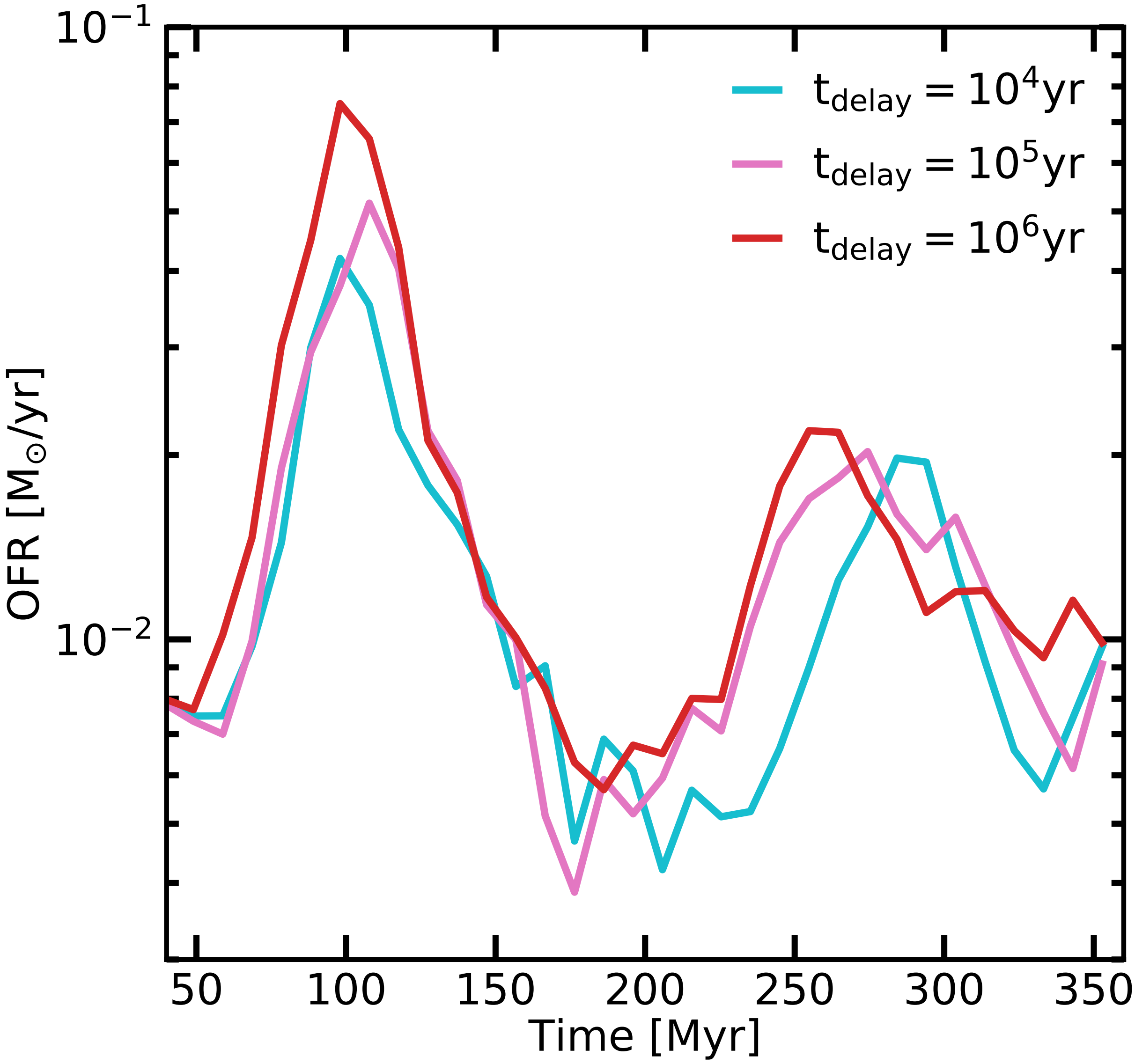

Figure 4.19: Outflow rates for the runs with different delay times. Early on in the simulation, there is an enhanced burst of star formation between 50-100 Myr as seen in Fig. 4.18. This is echoed in the burst in outflows just after 100 Myr. There is a minor trend with the delay time, such that the longer delay times result a slightly more enhanced outflow due to the fact that more gas is allowed to collapse into stars at this stage, and so more tightly packed CCSN slightly enhance the outflow rate.

The outflow rates as seen in Fig. 4.19 show the effect of the initial collapse and burst of star formation seen between 50-100 Myr in Fig. 4.18. This is also reflected in the stellar mass formed by 100 Myr, where the `delay_1e4` and `delay_1e5` runs have formed 1.74×10^5 $M_\odot$ and 1.72×10^5 $M_\odot$, respectively. The `delay_1e6` run however has produced 2.59×10^5 $M_\odot$. The formation of more stars means more CCSN and higher outflow rates. The effect of clustering and CCSN rates on outflows is explored in a lot more detail in Chapter 5, but here at least we see no substantial differences between the outflow rates when introducing this kicks model. We can however see a systematic increase in the outflow rate when increasing the delay time at around 100 Myr. This correlates with the increased stellar mass formed by this time as already mentioned. Another interesting feature is the slight time shift in the peak in the outflow rates after the initial starburst at 250-300 Myr. The outflow rates peak at around 250 Myr for the `delay_1e6` run, but at around 300 Myr for the `delay_1e4` run, but they peak at the same heights ($\sim 2 \times 10^{-2}$ $M_\odot$/yr. This could just be a consequence the delay in forming enough stars to produce enough CCSN to drive outflows, but the absolute number of CCSN is not the only thing that dictates the outflow rates, as discussed heavily in Chapter 5. The clustering of stars and densities at which the CCSN actually explode can be a dominant factor in dictating outflows. We examine the clustering of the stars and of CCSN to see if we can explain these similar outflow rates.

To try to gauge further what effect the delay on the feedback has on the galactic properties, both globally and on small scales, Fig. 4.20 shows the cluster formation efficiency as a function of time. The cluster formation efficiency quantifies the fraction of stars that are born in FoF groups or bound clusters. Observationally, this number is somewhat debated. In Chapter 3, we showed how this cluster formation efficiency changed drastically as we varied the density at which stars formed, producing cluster formation efficiencies from as little as 1-2 per cent for bound clusters up ($\sim$ 10 per cent for FoF groups) up to the cluster formation efficiencies we see here of $\sim$ 60 per cent for both bound clusters and FoF groups. Completely excluding photoionisation resulted in cluster formation efficiencies of around 65 per cent, and produced many more tightly bound clusters than the corresponding run that included photoionisation. The delay in star formation and its subsequent photoionising feedback therefore allows us to understand the contribution of pre-supernova feedback on reducing the fraction of stars in clusters. All models produce high cluster formation efficiencies. For `delay_1e4`, `delay_1e5` and `delay_1e6`, the cluster formation efficiencies for FoF groups are 0.58, 0.60 and 0.66, respectively. For bound clusters, the cluster formation efficiencies are 0.44, 0.46 and 0.54 for the three models in order of increasing delay time. There is therefore an albeit subtle trend with the delay time, showing that delaying photoionising feedback results in increased clustering, but the effect is much more subtle than that shown in Chapter 3.

We know that there is an increase in the number of stars formed in identified FoF groups and bound clusters, but we can also try to explore the overall clustering of the stars by looking at the 2-point correlation function. This does not rely on any models of what is a cluster or discriminate on being bound or not, instead it just explores how clustered are the stars overall. This is an important distinction which is often not considered and can have a substantial effect on the conclusions drawn. We discuss this more in Sec. 4.7.2. We also look at the clustering of the CCSN as well to see if this could have an impact on the slightly enhanced outflows we observe with increasing delay time. In the upper panel of Fig. 4.21, we show the 2-point correlation

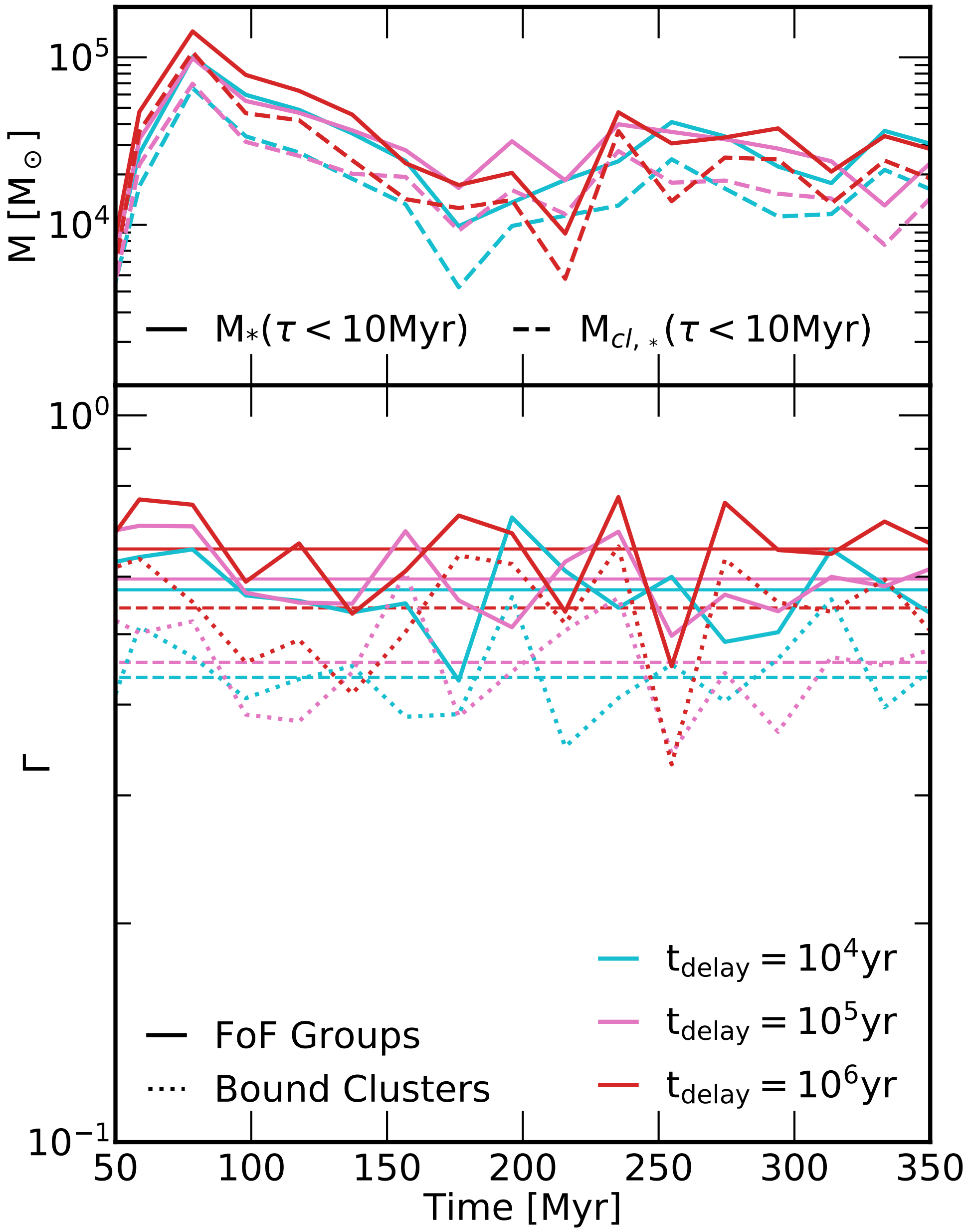

Figure 4.20: The cluster formation efficiency, defined as the fraction of stars in FoF groups or bound clusters as a function of time for each of the delay runs. The upper panel shows the mass in all newly formed stars (solid lines) as well as the mass in FoF groups (dashed lines) as a function of time. The lower panel shows the fraction of all stars in FoF groups (solid lines) and in bound clusters (dotted lines). The horizontal solid lines in the lower panel show the average cluster formation efficiency for FoF groups over the whole simulation whilst the horizontal dashed lines show the average cluster formation efficiency for bound clusters. A subtle but clear trend can be seen with the delay time, such that cluster formation is enhanced when increasing the delay between star formation and photoionising feedback.

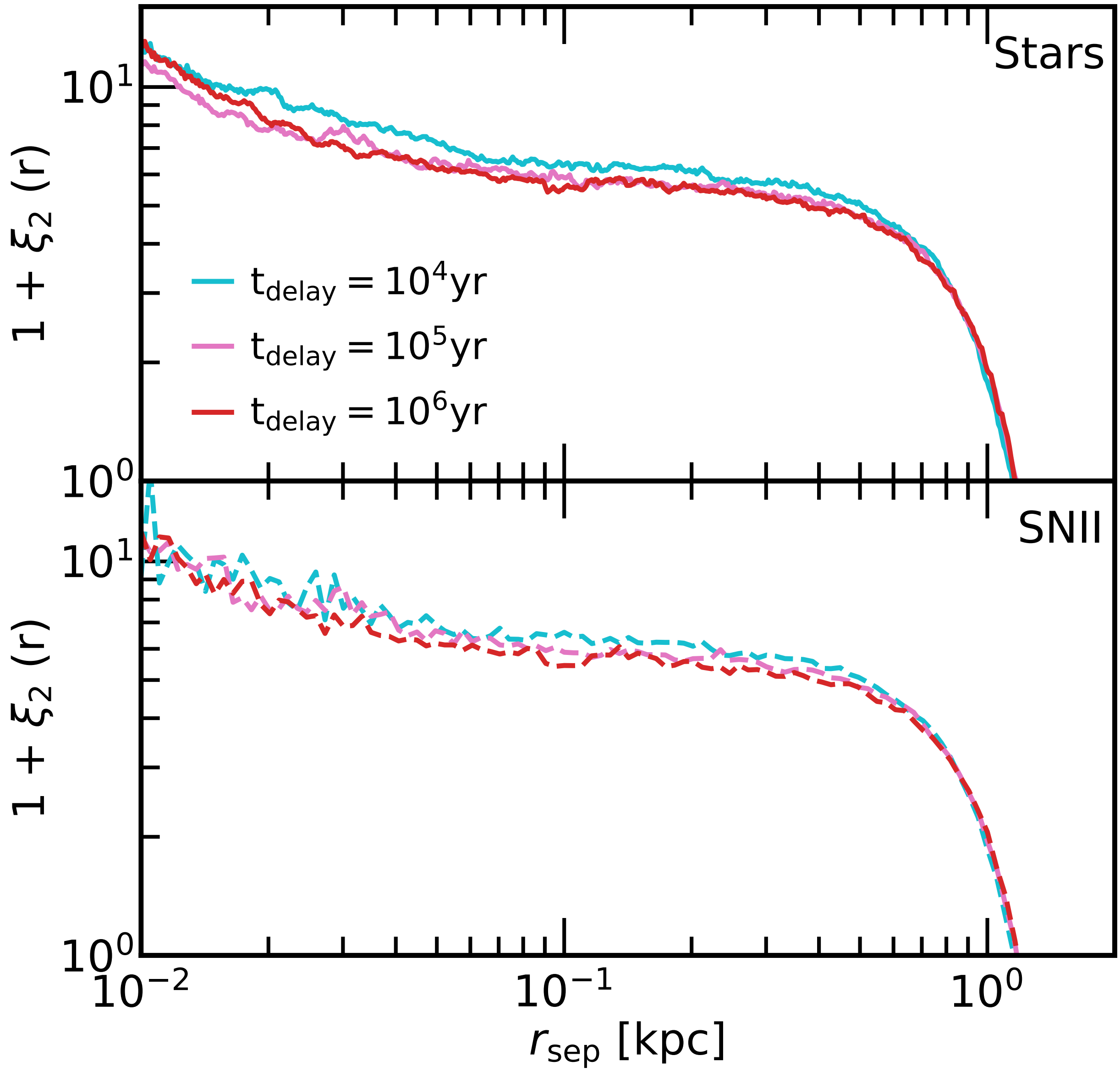

Figure 4.21: 2 point correlation function for the positions of the stars (upper panel) and the positions of the supernova explosions (lower panel). The correlation of the CCSN directly follow the correlation of the stars.

function for the stars. The 2-point correlation function here is the normal two-point correlation function of number counts calculated using the Landy and Szalay (1993) estimator,

$$\xi_2(r) = (\mathrm{DD}(r) - 2\mathrm{DR}(r) + \mathrm{RR}(r))/\mathrm{RR}(r), \tag{4.9}$$

where DD(r) describes the number of true pairs within a separation r, RR(r) is the number of random pairs with the same mean density and DR(r) is the cross-correlated data-random pairs. There appears to be no substantial differences in the clustering of either stars or CCSN. If anything, the clustering of the stars for the `delay_1e4` run actually appears to be a little bit higher than that of the `delay_1e5` and `delay_1e6` run. This perhaps sheds some light on the importance of the definition of the clustering, as well as the classification of a FoF group or cluster. The clustering of the CCSN appears to tightly follow the clustering of the stars. This relationship between the distribution of the ambient density of CCSN and the ambient density of the ISM is explored in much more detail in Chapter 5, but this would seem to imply that the distribution of CCSN is well represented by the overall density distribution of the stars. Despite a slightly enhanced fraction of stars in identified FoF groups and bound clusters shown in Fig. 4.20 for the `delay_1e6` run in comparison to that of the `delay_1e4` run, this is not reflected in the overall spatial clustering of neither the stars, nor the CCSN.

4.6 Effect of account for cloud core collapse timescales on star cluster structure

We have explored in some detail about the overall galaxy properties as well as the overall population of the star clusters identified in each of the simulations, but we can also look at the spatial and kinematic properties of the star clusters produced in each of the simulations.

4.6.1 Cluster mass function

Following on from the first look at the clustering of the stars shown in Fig. 4.21, we can look further now into the properties of the star clusters formed in the simulations. Fig. 4.22 shows the different cluster mass functions for each of the delay times. Overall, the distributions of clusters are extremely similar. All have a very similar normalisation and maximum cluster masses. The slopes are consistent with -2, with a slight steepening of the slope as the age increases. There is a build up of low mass clusters, as can be seen from the increased normalisation particularly at the low mass end. This is a sign of a lack of cluster disruption. We saw in Sec. 4.4.1 that increasing the velocity kick could prevent this build up of lower mass FoF groups, and so we can suggest that the kinematics of the forming star clusters is a more dominant factor in the disruption of star clusters in comparison to the onset of feedback.

4.6.2 Cluster masses & densities

As well as the cluster population as a whole, Fig. 4.23 shows the structural properties of the bound clusters produced in the simulations with differing time delays. For the `delay_1e4`, `delay_1e5`

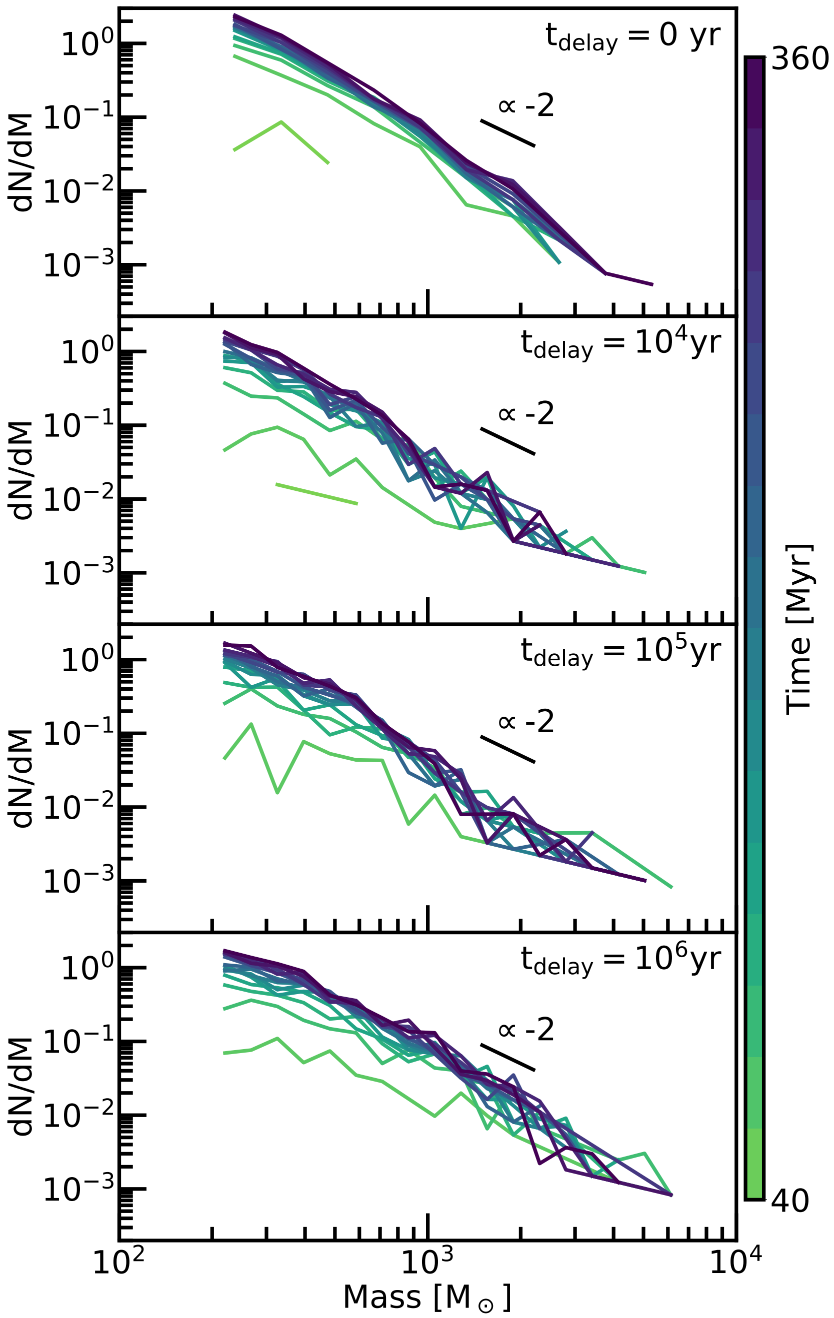

Figure 4.22: Cluster mass function for the simulations with different delay times as indicated in the top right-hand corner of each panel. Each line shows the cluster mass function for all FoF groups identified in the simulations in 20 Myr intervals between 40 and 360 Myr. The typical observed slope of -2 is also shown to guide the eye. We see that all cluster mass functions agree with a slope of -2 and we observe relatively little difference between the different runs. In all models we observe an accumulation of low mass clusters around 200 $M_\odot$ and all models have similar maximum cluster masses around 5-6 × 10^3 $M_\odot$.

and `delay_1e6`runs, the distribution of cluster sizes and densities shows no trend with the delay time, with very similar clusters being produced in all of the runs. Contrasting this to the `delay_0` run however, we see that the clusters produced are much more compact and have higher surface densities. Including a star formation delay puts these spatial properties more inline with the observations of Brown and Gnedin (2021), motivating the inclusion of a star formation delay being included in future star formation models in order to produce star clusters with radii and surface densities in line with observations. However, as has been shown in Chapter 3 and also here in Sec. 4.4, there are other ways to tune the star formation model to change these properties. Deciding which is the most relevant is non-trivial as all can be physically justified. It requires future work to explore perhaps a combination of the models employed so far to capture the observed properties. Instead for now, rather than trying to reproduce these properties by tuning these parameters, our aim is instead to understand the physical processes dictating star cluster formation in our models.

4.6.3 Kinematic properties

Another important feature we can compare between these models is understanding if the delaying of star formation has any impact on the kinematic properties of the FoF groups formed. We show the virial parameter in Fig. 4.24, and find that all models produce FoF groups with a majority that are bound. The bound fraction for the `delay_0` run is almost 100 per cent and none of the clusters have virial parameters much below 10. Contrast this to the `delay_1e6` run, and we find still many bound FoF groups (91 per cent) but much more scatter about this region and also a larger scatter above the $\alpha_{\rm vir} = 1$ line, with virial parameters up to 100. The increase in maximum cluster mass with delay time is also nicely demonstrated in this plot.

To tie in this analysis with that presented in Sec. 4.4, we also examine how the velocity dispersions of the clusters are effected by the delay in star formation. We can already make a prediction for this given what has been shown previously. Remembering Eq. 4.6, for similar virial parameters and masses shown in Fig. 4.24 and the smaller radii from Fig. 4.23, the velocity dispersion must increase to compensate. This is exactly what we see in Fig. 4.25, where we see an offset of the median velocity dispersion for the `delay_0` run from the runs including the delay time. All runs with similar delay times have very similar distributions of velocity dispersions, but with significant scatter to much higher velocity dispersions for all runs. Some contribution to these is highly likely the scatter of FoF groups above the $\alpha_{\rm vir} = 1$ line seen in Fig. 4.24.

4.7 Discussion

Making adjustments to the sub-grid star formation model undoubtedly have an impact on particularly the clustering properties of the stars, but also to the global properties, albeit much more subtle. Understanding which of the processes is driving the differences and disentangling the degeneracies between the different physical processes still requires some investigation. A wealth of literature has explored how the different stellar feedback prescriptions interact with one another

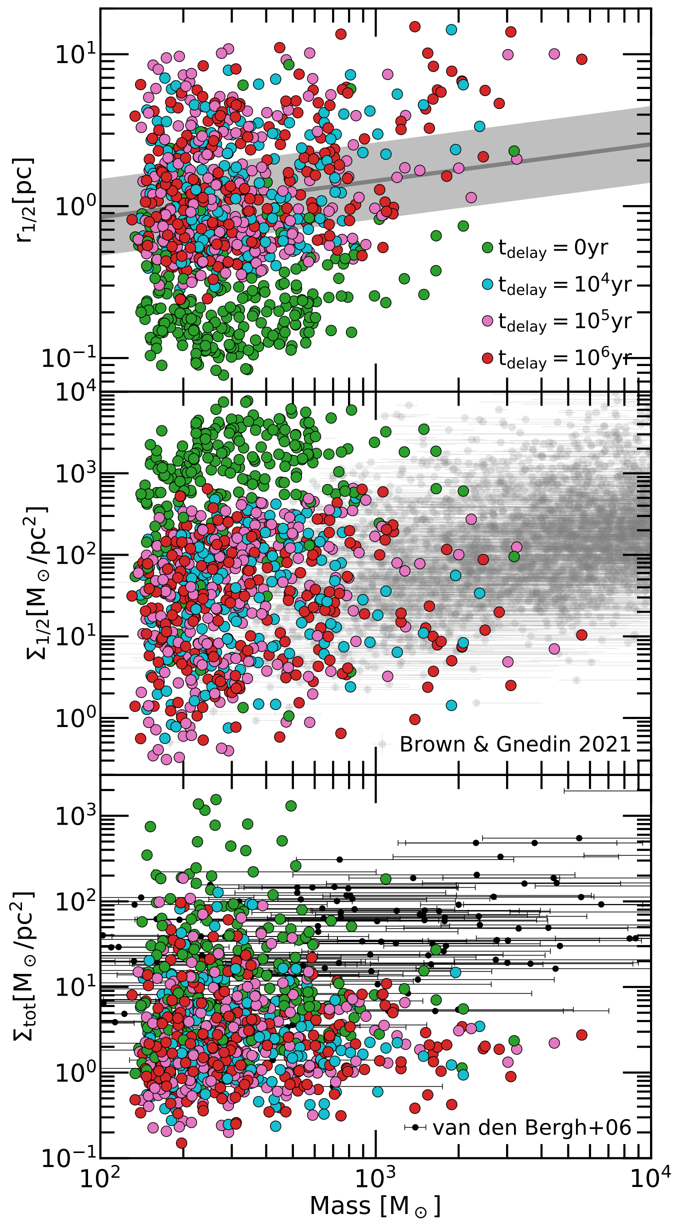

Figure 4.23: The effect of delaying the photoionising feedback on the structural properties of the bound star clusters formed in the simulations. We show this for clusters younger than 40 Myr, formed between 200 and 360 Myr in 40 Myr intervals in order to increase the number of clusters without duplicating. We show the half-mass radius (top panel), half-mass surface density (middle panel) and the total surface density (bottom panel) defined as the surface density containing 90 per cent of the cluster mass. We compare to the same observational data as shown in Fig. 4.7. The delaying of photoionising feedback effectively reduces the surface densities and makes clusters more extended. This effect is seen by delaying feedback by as little as 10^4 yr and does not seem to make much difference when increasing this delay further. Delaying the photoionisation also increases the masses of the clusters, as we see more clusters with masses above 10^3 $M_\odot$.

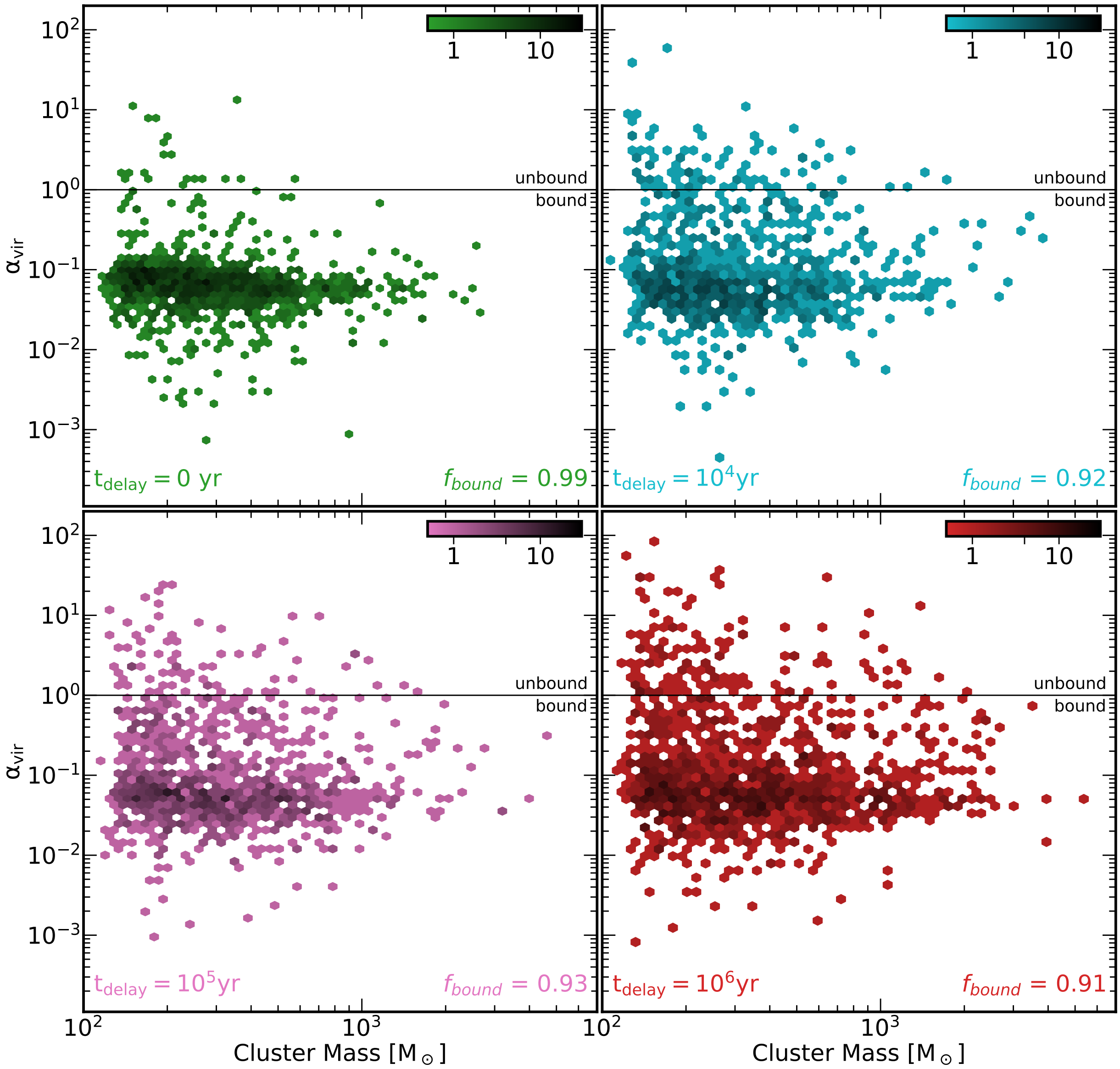

Figure 4.24: The virial parameter, $\alpha_{\rm vir}$ defined as the ratio of the kinetic energy to potential energy (described in detail in Sec. 4.4.4). A virial parameter of 1 is marked as a horizontal line in all panels indicating the distinction between bound and unbound FoF groups. The colourbar indicates the number of clusters in each hexbin. The fraction of FoF groups considered bound ($\alpha_{\rm vir} \leq 1$) is shown in the bottom right corner of each panel. Increasing the delay time results in FoF groups extended to a slightly higher mass range, as well as more scatter above the $\alpha_{\rm vir} = 1$ line. This is reflected in the bound fraction shown. For all models however, the majority (>90 per cent) of FoF groups are bound and sit quite substantially below the $\alpha_{\rm vir} = 1$ line, with most sitting between $\alpha_{\rm vir} = 10^{-2} - 10^{-1}$.

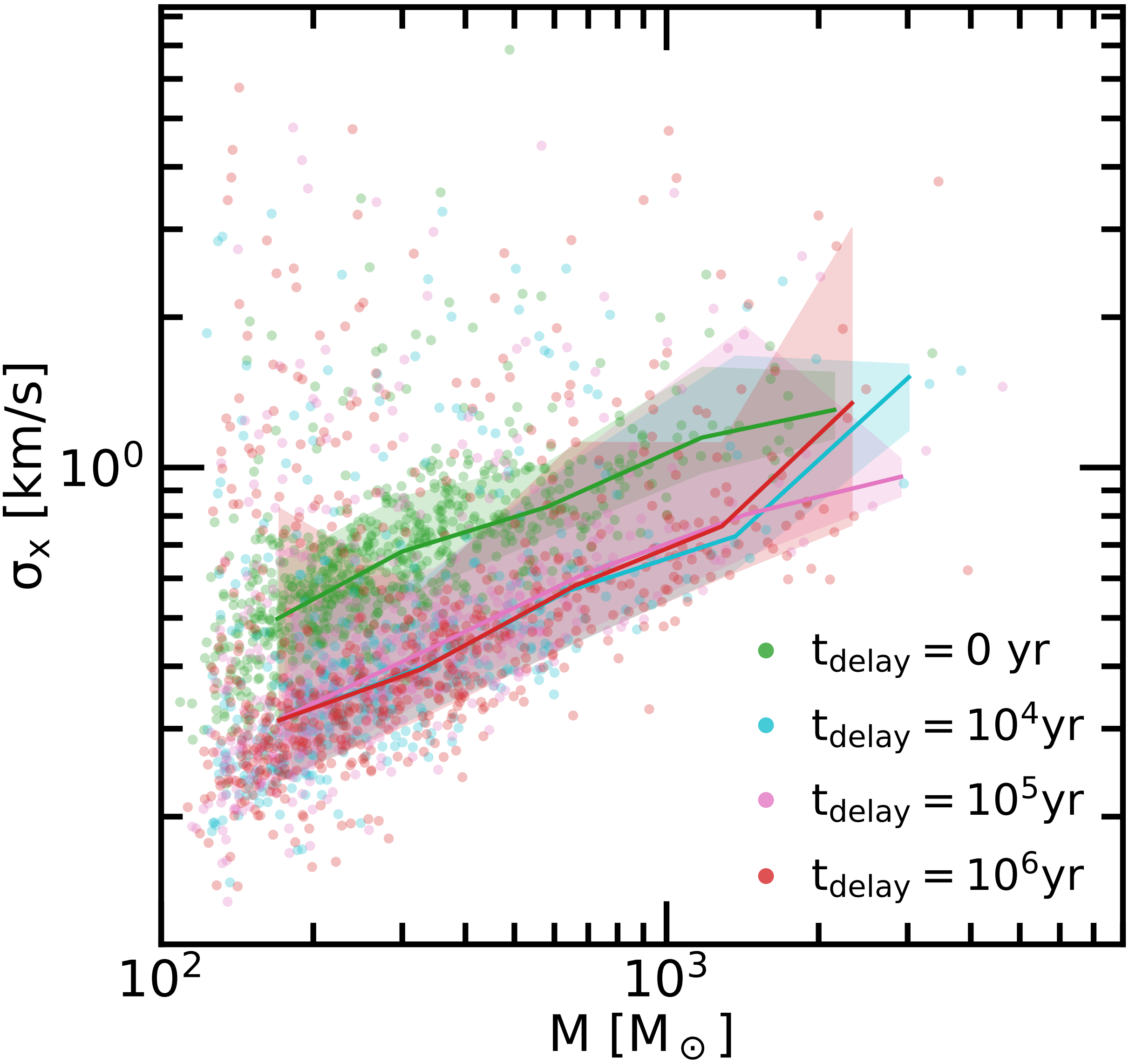

Figure 4.25: 1D Velocity dispersion of all identified FoF groups in the simulations at 300 Myr. The solid lines show the median of the distribution and the shaded area shows the 1 sigma scatter around the median. The distribution of masses is similar for all delay times, whilst the spread in 1D velocity dispersion is increased quite substantially when increasing the star formation delay time. For the `delay_0` run with no delay time, all clusters follow a quite tight distribution of dispersions. The median of the dispersion for all of the runs with a non-zero delay time is lowered by a factor of around 2, but with much more scatter to higher velocity dispersions also.

and influence star formation and outflows for example. But there are hints in this literature that this picture can change as we push our simulations to different resolution regimes.

4.7.1 Modelling star formation

One of the most important processes is star formation. In our simulations, as well as many others, the Schmidt (1959)-type star formation is used. When applied to a stellar particle representing a large population of stars, it appears to be reasonable. In Chapter 3 however, we provided some motivation that using this star formation prescription at these resolutions may become inappropriate, as we are 'averaging out' a quantity which is no longer appropriate to be averaged on the scales we resolve. This has already been addressed in several studies. Hopkins et al. (2013a) did an extensive study where they compare various different star formation criteria, and find that the most favoured scenario is a self-gravity criterion, based on the local virial parameter and the assumption that self-gravitating gas collapses to high density in a single free-fall time.

4.7.2 What do we mean by 'clustering'?

There is no general consensus in the literature, neither observationally nor in simulations as to how to correctly or consistently define a cluster, partially oweing to the fact that simulators have a much easier time of gaining any reliable measurements of the kinematic properties of their star clusters. This is why we present results for both bound star clusters but also for all spatially identified FoF groups in our simulations. Another difficulty comes however when trying to attribute galactic properties from the stellar properties, and that is talking about 'clustering'. A recent study from Keller and Kruijssen (2022) for example find that in the absence of pre-supernova feedback, the clustering is enhanced. This clustering is quantified by the two-point correlation function in an identical fashion to Fig. 4.21. However, one can argue that the picture is not that simple. We discuss this in more detail in relation to the outflows in Chapter 5, but it is possible to produce the same 2-point correlation function, as well as the same cluster formation efficiencies with different populations of clusters which can produce substantially different results. Many of the studies, including Keller and Kruijssen (2022) do not show cluster mass functions for example. A constant cluster formation efficiency (so a fixed number of stars born in clusters) but with a more shallow cluster mass function means that you have fewer overall clusters, but these clusters are more massive. More massive clusters contain more stars and so have more CCSN. Assuming the formation time of these clusters is relatively short, the spatial and temporal distribution of these CCSN in this high mass cluster will be very close, and therefore able to drive substantial outflows. In contrast, a steeper cluster mass function will contain many more clusters of lower mass. For the same fraction of stars in clusters, the number of spatially and temporally incident CCSN will be significantly reduced, and these clusters are unlikely to be able to drive significant outflows. It is important to be careful when one labels star formation to be 'clustered', as the different definitions can have a high impact on the interpretation, particularly when comparing to other studies.

4.7.3 Runaway and walkaway stars

In a similar style to how the kicks were implemented in this study, Gutcke et al. (2022) also implemented a small kick of 3 km/s to all newly formed stellar particles in high-resolution cosmological zoom-in simulations of dwarf galaxies, and found that whilst there is little impact on the star formation rate, the mass and metal mass loading factors increased by around 0.5 dex.

Another useful comparison to the implementation of this small velocity kick is the inclusion of runaway stars. This was explored in Milky Way mass galaxies in Andersson et al. (2020) as well as in dwarf galaxies in Steinwandel et al. (2022a). The study by Steinwandel et al. (2022a) also uses the Griffin framework, and so is highly similar to the set up we use here with the exception that they use an MFM implementation as opposed to SPH. Both studies set out to explore the effect of runaway stars on the outflow properties of galaxies. The velocities of the runaway stars model used in both of these studies employed a power-law distribution function of velocities from 3 km/s up to 385 km/s, however only 14 per cent of these runaways had velocities above 30 km/s. This is therefore a rather extreme version of what we present here, and its purpose is most certainly different. Nevertheless it is interesting to compare the results. Usefully Steinwandel et al. (2022a) also looked at a 'walkaway stars' model, which employed velocity kicks sampled from a Maxwellian distribution with a width of only 32 km/s, resulting in much lower velocity kicks. This is more comparable to our results, but still much higher than what we employ. Neither studies looked at the properties of the star clusters formed, but instead focussed on the impact of outflows, as the motivation is such that massive stars that are kicked from their birth places and then explode as CCSN will have a substantial effect on outflows as they explode in a lower ambient density medium. When including runaways, Andersson et al. (2020) notice more stars in the interarm region of their Milky Way-like disk in agreement with what we also find but they also find a less-distrurbed ISM due to the reduction of supernovae exploding in star forming regions, predominantly the cold ISM. For the outflows, they found a substantial impact when including runaway stars, with outflow rates enhanced by a factor of a few. Andersson et al. (2020) however do hint towards the end of their study at the effect they see when they look at dwarf galaxies, which in agreement with the further study from Steinwandel et al. (2022a), shows that runaway stars have little effect on the outflows observed in dwarf galaxies, demonstrating there is some mass dependence on which galaxy masses the effect of runaways is significant.

4.8 Conclusions

Recent simulations trying to understand the small scale dynamics of galaxy formation still heavily rely on sub-resolution models for star formation and feedback, and understanding the implications of these models is imperative to the conclusions drawn from these studies. In Chapter 3 we explore the effect of the star formation prescription, particularly the star formation efficiency parameter, and found that it had very minimal impact on the global properties of galaxies but substantial impact on the star cluster properties. Other particular assumptions made in most models of galaxy formation of this type are that star particles inherit their dynamical properties directly from their parent gas particle and that star formation and its subsequent feedback process are instantaneous.

We explore the consequences of these assumptions on the global properties of the galaxies, as well as on the small scale properties of the stars.

The first section of this study looked at implementing a kick model, which introduces a small, randomly orientated kick to the stellar particles when they are realised as stars. As discussed in Sec. 4.2.2, the origin of this kick is not necessarily from a singular process, but it is physically motivated should one consider small-scale unresolved turbulence of the gas which is not captured in our model, as well as binary star evolution. We do not attempt to differentiate between the various origins of this kick, and instead simply employ this kick as a sub-grid model and explore its effect. The main conclusions are as follows:

- Applying a small velocity kick to newly formed star particles does not drastically affect the global properties of the galaxy, such as the star formation rate or outflow rates, shown in Fig. 4.2. Subsequently, the mass loading for each of the simulations is unaffected by the implementation of this kick model.
- With increasing kick magnitude, fewer FoF groups are formed overall. Fig. 4.7 shows how the formed FoF groups have larger radii and lower surface densities. All models produce FoF groups in the mass range of 10^2 to $\sim 5 \times 10^3$ $M_\odot$, with the majority of the distribution between 10^2 and 10^3 $M_\odot$. The `kick_3km/s` model produces FoF groups with half-mass radii approximately an order of magnitude higher than those of the `kick_0km/s` model, and surface densities around 2 orders of magnitude lower.
- The cluster mass function becomes slightly more shallow when including velocity kicks, as seen in Fig. 4.4. With no kick, a pile up low mass FoF groups occurs, indicating there is no (or minimal) cluster disruption with time of these low mass FoF groups. When including a 3 km/s, this pile up does not occur as much, and the number of low mass clusters stays roughly constant with time.
- Fig. 4.10 shows that the velocity dispersions of the FoF groups in each of the models stays roughly similar. The kick primarily has the effect of increasing the radius of the cluster (as shown in Fig. 4.13), subsequently increasing the virial parameter for a fixed velocity dispersion.

The second section explored the effect of account for the cloud core collapse timescales by delaying the photoionising feedback. The motivation for this being that the free-fall times of the gas calculated at star formation are on the order of a Myr, meaning that in nature, gas would still have quite some time to collapse before turning into a star. If the effect were purely gravitational, distinguishing between a star and a gas particle would be unnecessary, but star particles behave differently in the simulations due to the fact that they emit photoionising radiation, which has a strong effect on regulating further star formation in the surrounding gas particles by heating them away from the star-forming regime. Delaying the feedback by 10^4, 10^5 and 10^6 years and comparing with no delay, we can understand if this delay has any substantial impact on the properties of the galaxies formed and if this is an important ingredient that needs to be considered in the sub-resolution models for star formation in simulations of this kind. The impact of the delay in star formation is:

- Employing a delay time, thus delaying the onset of photoionising feedback made little difference to the star formation rate (Fig. 4.18), nor the outflow rates (Fig. 4.19).
- Fig. 4.20 shows that the increased delay time showed slightly enhanced fractions of stars being born in identified FoF groups, whilst the 2-point correlation function (Fig. 4.21) showed very little difference between each of the models in terms of the overall clustering of the stars or the supernovae. This was also reflected in the similar cluster mass functions in Fig. 4.22.
- Whilst the overall number of clusters in the simulations were very similar, even a small delay time of 10^4 yrs had the impact of making the clusters more extended and less dense, as shown in Fig. 4.23. Increasing the delay time further up to 10^6 yrs did not enhance this effect however, with all of the delay times tested producing FoF groups with similar spatial properties, including their virial parameters, seen in Fig. 4.24. The median velocity dispersion (Fig. 4.25) of the formed FoF groups however was decreased by the delay of star formation, but with substantial scatter in all models.

Sub-grid models are here to stay for modelling star formation in a galactic context. Further work needs to be done towards understanding the assumptions made and physically motivating adjustments to all sub-grid models, not just star formation, in order to capture processes vital to the evolution of galaxies on global, but also local scales.

"For those who want some proof that physicists are human, the proof is in the idiocy of all the different units which they use for measuring energy."

Richard P. Feynmann

5

The effect of stellar clustering on supernova clustering, interstellar medium and outflows

In low mass galaxies, supernovae are the primary drivers of galactic scale outflows, and stellar feedback and clustering play an important role in shaping the distributions of supernova explosions, in space, time and density. To explore this in detail, we ran two suites distinct suits of simulations: the first with different combinations of photoionisation and/or supernovae feedback, and the second with different clustering properties (indirectly regulated by altering the star formation efficiency). Comparing these two suites in parallel allows us to disentangle the dependencies of the outflow properties on different feedback modes and on stellar clustering, respectively. We find that enhancing the clustering of the stars results in increased outflows by a factor of ~ 2, and consequentially higher hot gas volume filling fractions and more than double the cold gas mass fraction in the interstellar medium. However, the effect of clustering is minor in comparison to the effect of excluding photoionisation, since photoionisation does not simply change the clustering of the stars but it drastically changes the ambient densities of the interstellar medium. Excluding photoionisation increases the volume filling fraction of hot gas by almost a factor of 3 and results in supernova explosions at orders of magnitude higher and lower ambient densities. We therefore conclude that whilst stellar clustering undoubtedly plays a minor role in setting the outflow properties, the role of the different stellar feedback channels is far more significant as it changes the overall properties of the interstellar medium and densities at which the supernovae explode. The results presented in this chapter will be submitted for peer-review in the near future.

5.1 Introduction

It has long been established that feedback is a vital component for reproducing observed galaxy properties (e.g. Governato et al., 2010; Brook et al., 2012; Agertz et al., 2013; Hopkins, 2013; Hopkins et al., 2014; Stinson et al., 2013; Agertz and Kravtsov, 2015, 2016; Koudmani et al., 2022). This is particularly relevant on the scales of dwarf galaxies, which are particularly susceptible to these processes due to their shallow potential (Collins and Read, 2022). These low-mass galaxies are also a useful test bed for understanding feedback processes, particularly outflows, as they typically remain undisturbed by significant feedback from active galactic nuclei (Neumayer et al., 2020). As galaxy simulations have become more sophisticated in the sub-resolution modelling for star formation, feedback and the thermodynamics and chemical evolution of the interstellar medium (ISM) (e.g. Hopkins et al., 2011, 2012; Kannan et al., 2014; Hu et al., 2014, 2016, 2017; Smith et al., 2021; Lahén et al., 2019), observations have been concentrating on studying the distribution of young stars and dense molecular clouds on scales of parsecs (e.g. Meidt et al., 2013, 2020; Faesi et al., 2014, 2016, 2018; Leroy et al., 2016, 2017; Schruba et al., 2017; Sun et al., 2018, 2020; Schinnerer et al., 2019; Lee et al., 2021). In order to understand the interaction between star formation and feedback, observations mapping of Hα and CO, tracing young massive stars and peaks in molecular gas, respectively can probe the effect of stellar feedback on their surrounding birth environments (e.g. Kreckel et al., 2018; Kruijssen et al., 2019; Schinnerer et al., 2019; Chevance et al., 2020, 2022).

As well as examining the local sites of star formation, substantial outflows are also seen in low-mass galaxies (Rhode et al., 1999). Highly resolved observations, coupled with simulations with sufficient resolution to probe star formation and stellar feedback processes allow us to explore which processes are relevant for not only driving the outflows, but also how this links with the smaller scale features of the galaxy, such as how clustered the stars are in the galaxy and the ambient densities of the ISM.

Metal enrichment is also observed outside the galaxy, and therefore some mechanism is required to explain this mass ejection (Emerick et al., 2020; Richings et al., 2022). This mass ejection is observed as outflows with velocities of the order of hundreds of km/s. Galaxies are typically expelling gas at the same, if not a higher rate, than turning that gas into stars. Some of this gas is expected to fall back in to the galaxy, such that galaxies in a populated environment often have a fresh resource of gas to sustain or enhance their star formation episode. But there is a clear correlation between the star formation rate (SFR) and the outflow rates. The more gas supplied, the higher the SFR and the more gas is expelled by outflows. The origin of these outflows are feedback processes from stars and naturally also in galaxies with central black holes, from active galactic nuclei (AGN) (e.g. Koudmani et al., 2019, 2021).

The structure of the ISM is complex and multi-phase due to constant heating and cooling. Feedback from stars directly impacts the surrounding ISM through various processes, such as ionising radiation and stellar winds, and from supernova (SN) explosions from massive stars at the end of their lives. Particularly lower mass galaxies are additionally impacted by ionising photons from the first stars and galaxies in the Universe, which can completely prevent future star formation (Efstathiou, 1992). Feedback is often thought to be negative, such that feedback from star formation heats the ISM preventing further star formation and is thus self-regulating.

Positive feedback however also occurs, for example stellar winds can compress the ISM creating dense regions triggering star formation (e.g. Walch et al., 2015). But negative feedback must exceed positive feedback on galactic scales in order to explain the observed inefficiency of star formation (Collins and Read, 2022).

In dwarf galaxies, the topic of feedback is particularly interesting. Many dwarf galaxies do not appear to host (active) black holes, and so the role of stellar feedback can be studied in isolation without the influence of AGN feedback. Additionally, the lower galaxy mass means a more shallow potential making them more susceptible to feedback processes. This makes dwarf galaxies an ideal site to study the complex process of stellar feedback.

In simulations, we have the luxury of following the evolution of the ISM densities during the events of star formation, pre-SN feedback, and SN feedback. SNe do not explode at the same densities at which they were born. It was shown in Chapter 3 that there is a decoupling between the process of star formation and SNe explosions, as very different star formation ambient densities resulted in remarkably similar SN ambient densities. Pre-SN feedback in the form of photoionisation (PI), photoelectric heating and radiation pressure from massive stars acts to 'pre-process' the ISM following the formation of the first stars (Walch et al., 2012). The heating of the surrounding gas disrupts the giant molecular clouds and lowers the overall densities before the first SNe some few Myr later by clearing out gas from star forming regions (Vázquez-Semadeni et al., 2010; Walch et al., 2012; Dale et al., 2014; Sales et al., 2014).

Hu (2019), using a very similar simulation setup as presented here, investigated the properties of SN-driven winds and found that around 60 per cent of SNe occur in hot bubbles generated by previous SNe, leading to the formation of superbubbles and venting out hot and highly pressured gas able to drive galactic scale winds. They also test the resolution adopted, and find that wind properties converge at gas particle masses of 5 $M_{\odot}$, which is where the cooling mass of individual SNe can be resolved.

Smith et al. (2021) studied the non-linear coupling of different feedback channels in isolated dwarf galaxies and found that PI and SN feedback are both independently capable of regulating star formation to the same level, whilst photoelectric heating is inefficient. They found that the inclusion of PI results in smoother star formation histories than with SNe. When studying the outflows, they find that including both SNe and PI resulted in substantially reduced outflow rates in comparison to SNe alone, which they attribute to the fact that PI reduces the clustering of SNe, as PI disrupts the star forming clouds prior to the first SNe. Keller et al. (2022) similarly looked at the effect of neglecting PI, and again attributed the enhanced outflows to the enhanced clustering of SNe. In Chapter 3, we also noted that without PI, the simulations produced many more tightly bound star clusters (so clustering was increased) resulting in higher outflow rates. The simplistic conclusion can be that increasing the clustering of stars increases the clustering of SNe which drives more outflows. This is however not entirely trivial, as outflows rely on the spatial and temporal clustering of SNe as well as the ambient densities at which the SNe actually explode. So both pre-SN and SN feedback are responsible for the outflow properties in a non-linear way.

When considering the role of different forms of feedback in disrupting forming star clusters, we must consider the timescales on which the feedback happens. All stars begin to photoionise the surrounding gas immediately after being formed, whilst there is a delay between star formation and SN explosions. The stellar lifetimes from Georgy et al. (2013) used in our simulations are shown in Fig. 5.1. Stars more massive than 8 $M_{\odot}$ explode as SNe, and the time can be as short as 3 Myr for the most massive stars and as long as $\sim$ 32 Myr for 8 $M_{\odot}$ stars. In forming star clusters in the Milky Way, a typical stellar age spread is found to be 5 Myr or less. This means that only the SNe explosion of the most massive stars have likely any kind of influence on a currently forming star cluster. Considering the rarity of these very massive stars, it brings into question the impact SNe really have on their host star cluster as it forms. The feedback that regulates star formation in an isolated collapsing molecular cloud is the pre-SN feedback such as stellar winds and PI. One can also imagine of course that SNe that just happen to be close by to a molecular cloud would have an impact in disrupting and heating that gas, and this would be more likely in a starburst scenario or where the star formation is very spatially concentrated (Hennebelle and Audit, 2007; Hennebelle et al., 2007).

The relative importance of different forms of pre-SN feedback is still in the process of being explored and understood in both observations and simulations. Recent studies (e.g. Barnes et al., 2022) try to quantify the contribution of the different pressure terms measured from HII regions and associated stellar clusters and find in most cases that thermal and wind ram pressure are mildly dominant, with radiation pressure having less of a contribution. Many of these studies however do not resolve the HII regions, making observations challenging. In simulations, Ali et al. (2022) look at the relative importance of PI and stellar winds in a zoom-in region of a spiral arm of a Milky Way-type galaxy and found that the effect of PI was highly dominant over the impact of stellar winds. Winds did not appear to affect the cloud statistics or star formation properties. With their sink-based star formation prescription, they did find that the winds distributed star formation over more low-mass sink particles and produced fewer high-mass sink particles, but still overall had a negligible impact in comparison to PI, which is effective in disrupting the spiral arm and producing many more stars, high density clouds and results in higher velocity dispersions. Geen et al. (2021) also find the same for stars within a stellar cluster, whilst Haid et al. (2018) find that for stars outside the stellar cluster (so for a flat density profile of the surrounding gas) that stellar winds can have a bigger effect.

In a cosmological setting, the FIRE simulations of dwarf galaxies (Muratov et al., 2015) find very high mass loading factors (defined as the ratio of outflow rates to the average SFR), on the order of 100-1000. Idealised dwarf galaxies with a more detailed treatment of the physical processes however find more modest values (e.g. Hu et al., 2016, 2017; Andersson et al., 2020; Hislop et al., 2022). This does however motivate the interest in studying these processes additionally in a cosmological setting to identify the impact on galactic evolution and outflows on these scales.

There are still some key open questions which are still yet to be fully understood that we address in this study, such as how the star formation efficiency (indirectly the SF densities & clustering) affect the properties of the outflows. This is linked, but not exclusively, to how the clustering of the stars affects the clustering of the SNe, both in space and time. Additionally, the different clustering is linked to the densities at which the stars are formed, and whether or not this has a clear imprint on the properties of the ISM such as the temperature and ambient densities. The ISM properties set the ambient densities of the SNe, which is also highly relevant to how efficiently SNe can drive outflows. It is a complicated picture, with highly degenerate processes and with various different circular dependencies.

Simulation	ϵ_{ff} [%]	PI feedback	SN feedback	E_{SN} [erg]	$M_{*,200\ Myr}$ [10^5 $M_\odot$]	$N_{SN,200\ Myr}$
`PI_SN_0%`	0	✓	✓	10^{51}	2.57	3090
`PI_SN`	2	✓	✓	10^{51}	2.08	2500
`PI_SN_20%`	20	✓	✓	10^{51}	1.89	2241
`PI_noSN`	2	✓	✗	-	3.57	0
`noPI_SN`	2	✗	✓	10^{51}	10.8	14193
`noPI_01SN`	2	✗	✓	10^{50}	22.5	28533
`noPI_noSN`	2	✗	✗	-	57.6	0

Table 5.1: Description of the different runs presented. The first column shows the model name used throughout the text. ϵ_{ff} describes the star formation efficiency. Most models use the fiducial value of 2 per cent but we also present the effects of increasing and decreasing this efficiency. This parameter is described in more detail in Sec. 5.2.1. The third and fourth columns summarise which of the feedback prescriptions are implemented in order to explore their effects on galactic and cluster properties. E_{SN} shows the energy per SN. All models including SN feedback use 10^{51} erg with the exception of `noPI_01SN` which uses 10 per cent of this value.

In this study, we attempt to split the analysis to disentangle the difference between clustering and feedback. When considering what drives outflows, the simplistic answer is simply just supernovae. But we can delve further into this by considering the following topics:

- Are the outflow rates dependent on only stellar clustering, and is this equivalent to SN clustering?
- How do the ambient densities at which the SNe explode impact the ISM and the outflows?
- Are outflow rates simply set by the number of SNe and/or the total energy injected by SNe?
- Is the only impact of changing the feedback that it changes the clustering properties?
- How does changing the feedback used impact the radial and height distribution of SNe, and what is the effect on outflows?

We briefly introduce the model used in Sec. 5.2, where we particularly highlight the details of the star formation and feedback models used (see Chapter 2 for a much more detailed introduction). Sec. 5.3 describes the overall properties of the galaxies formed in the different simulations. We then focus on the specific properties of the stellar and SN clustering in Sec. 5.4, the ISM in Sec. 5.5 and the outflows in Sec. 5.6. We provide some discussion of some of the feedback implementations and potential caveats in Sec. 5.7, before summarising our findings in Sec. 5.8.

5.2 Simulation Setup

The simulations used here are a subset of those presented in Chapter 3, with the inclusion of three new simulations with varied feedback prescriptions. The model used is SPHGal, a modified version of the Gadget-3 code (Springel, 2005). More detailed explanations of the model can be found in Hu et al. (2014, 2016, 2017); Lahén et al. (2019, 2020); Hislop et al. (2022). Here we focus on the most relevant details of the model for this study, particularly the star formation criteria as well as the different stellar feedback prescriptions.

5.2.1 Star formation

Every gas particle has an associated Jeans mass, defined as

$$M_{\mathrm{J}} = \frac{\pi^{5/2} c_s^3}{6 G^{3/2} \rho_{\mathrm{gas}}^{1/2}}, \tag{5.1}$$

where c_s is the local sound speed of the gas, G is the gravitational constant and ρ_{gas} is the gas density.

A particle satisfies the star formation criteria when $M_{\mathrm{J}} < N_{\mathrm{thres}} M_{\mathrm{ker}}$, where $M_{\mathrm{ker}} = N_{\mathrm{ngb}} m_{\mathrm{gas}}$ is the SPH Kernel mass. N_{thres} is a free parameter which we adopt to be 8, consistent with Hu et al. (2017) to properly resolve the Jeans mass for the star-forming gas. We therefore define gas particles with Jeans masses between 0.5 M_{ker} and 8 M_{ker} as 'star-forming'.

We use a Schmidt (1959)-type criteria for the local SFR:

$$\frac{\mathrm{d}\rho_*}{\mathrm{d}t} = \epsilon_{\mathrm{ff}} \frac{\rho_{\mathrm{gas}}}{t_{\mathrm{ff}}}, \tag{5.2}$$

where ρ_* and ρ_{gas} are the stellar and gas volume densities respectively, ϵ_{ff} is the star formation efficiency per free-fall time and $t_{\mathrm{ff}} = \sqrt{3\,\pi/(32\,G\,\rho_{\mathrm{gas}})}$ is the free-fall timescale of the gas (Binney and Tremaine, 2008).

The star formation efficiency ϵ_{ff}, describes the fraction of gas particles which satisfy the star formation criteria ($0.5 M_{\mathrm{ker}} < M_{\mathrm{J}} \le 8 M_{\mathrm{ker}}$) that are realised into star particles in a stochastic manner. Effectively, a lower star formation efficiency means that more star formation occurs at lower Jeans masses (i.e. higher densities and lower temperatures). In Chapter 3, we explored this parameter in detail, and found it an effective way to alter the clustering properties of the stars (see also e.g. Li et al., 2019; Semenov et al., 2021). Gas particles with $M_{\mathrm{J}} \le 0.5 M_{\mathrm{ker}}$ are immediately realised into stellar particle at 100 per cent efficiency (Lahén et al., 2019). In this study, we explore three different values of ϵ_{ff} (also summarised in Tab. 5.1). For testing the different feedback prescriptions, we use the fiducial value of 2 per cent, which is a typically adopted value in many Schmidt (1959)-type star formation based simulations (Hu et al., 2016, 2017; Lahén et al., 2019, 2020). We then also present results using a ϵ_{ff} of 0 per cent, meaning there is no star formation in the $0.5 M_{\mathrm{ker}} < M_{\mathrm{J}} \le 8 M_{\mathrm{ker}}$ regime, and only star formation in gas particles where $M_{\mathrm{J}} \le 0.5 M_{\mathrm{ker}}$. This setup has been shown to increase the clustering of stars, as shown in Chapter 3. We also present an ϵ_{ff} of 20 per cent, which increases the amount of star formation able to occur at higher Jeans masses, meaning lower densities and higher temperatures, resulting in less clustered star formation.

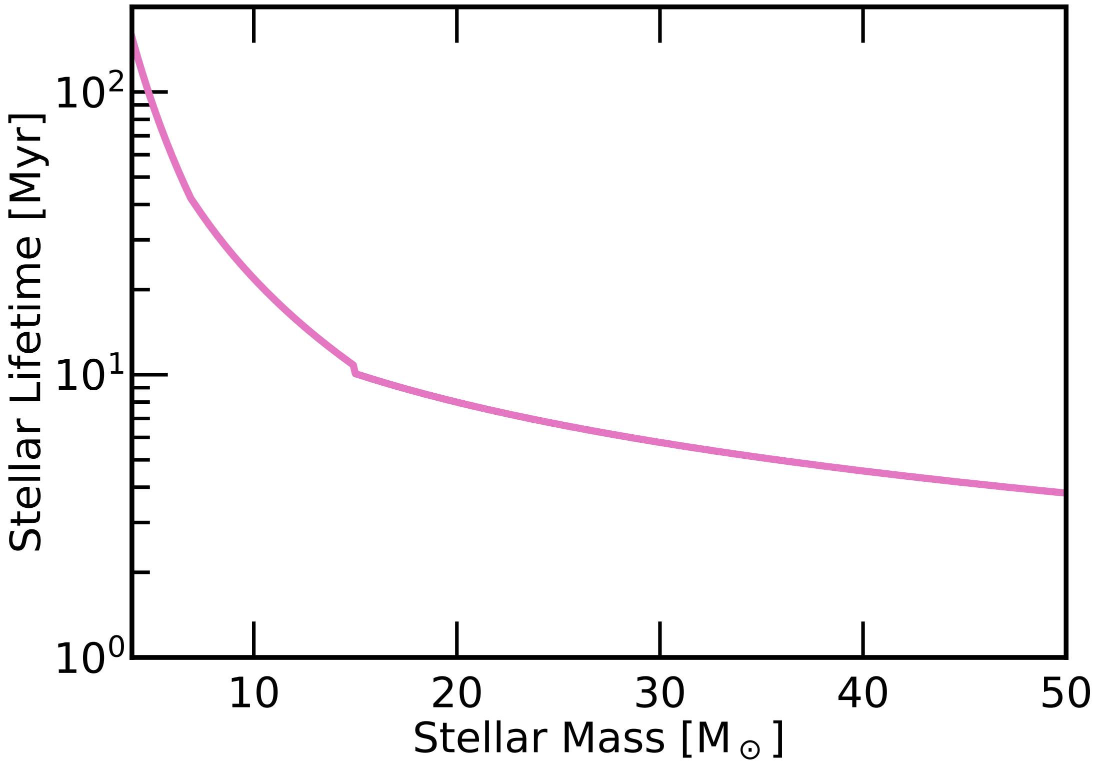

Figure 5.1: The stellar lifetimes from Georgy et al. (2013) as a function of stellar mass used in the simulations. Massive stars (>8 $M_{\odot}$) explode as SNe at the end of their lifetimes. The most massive stars explode after ~ 3 Myr whilst 10 $M_{\odot}$ stars explode as SNe after around 20 Myr.

5.2.2 Pre-supernova feedback

We follow feedback for the stars that form within the simulations in the form of photoelectric heating, UV-radiation and PI, as well as the metal enrichment from asymptotic giant branch (AGB) stars and stellar winds. The UV radiation of single stars follows the implementation from Hu et al. (2017), assuming a locally optically thin medium which is a reasonable assumption for dwarf galaxies. This allows to sum over the radiation field for each star using an inverse square law. The lifetimes of the stars (shown in Fig. 5.1) as well as the stellar effective surface temperatures are taken from Georgy et al. (2013). The UV luminosity of each star is taken from the BaSeL stellar library (Lejeune et al., 1997; Westera et al., 2002) in the energy band 6-13.6 eV, which is the dominant region of photo-electric heating in the ISM. We trace the UV radiation for all stars above 2 $M_{\odot}$, which is just below our mass resolution above which every particle represents an individual star. The radiation contributions from all stars are then integrated during the tree-walking procedure. This makes this method effectively a ray-tracing approach, dependent on the angular resolution of the tree. It is possible to improve this implementation in future works by including higher order moments in the tree or modifying the opening angle (see e.g. Grond et al., 2019, for an approach).

The photoelectric heating rates are taken from Bakes and Tielens (1994), Wolfire et al. (2003)

and Bergin et al. (2004), given by

$$\Gamma_{\rm pe} = 1.3 \times 10^{-24} \epsilon D G_{\rm eff} n \; {\rm ergs^{-1} cm^{-3}}, \tag{5.3}$$

where n is the number density of hydrogen, $G_{\rm eff} = G_0 {\rm e}^{-1.33} D N_{\rm H,tot}$ is the effective attenuation ration field, D is the dust-to-gas ratio, $N_{\rm H,tot}$ is the total hydrogen column density and ϵ which is the photoelectric heating rate given by

$$\epsilon = \frac{0.049}{1 + 0.04\psi^{0.73}} + \frac{0.037(T/10^4)^{0.7}}{1 + (2 \times 10^{-4}\psi)}, \tag{5.4}$$

with $\psi = G_{\rm eff}\sqrt{T}/n^-$, where T is the temperature of the gas and n^- is the electron number density.

PI is included in the form of a Strömgren (1939)-sphere approximation, such that every star particle with a mass greater than 8 $M_\odot$ is treated as a photoionising source. Within a Strömgren radius R_S, all gas particles are immediately labelled as photoionised. The molecular and neutral hydrogen in these particles are destroyed and converted to H^+ and this gas is heated to 10^4 K, which is the temperature of HII regions. In a region of constant density gas, calculating R_S is straightforward, however in practise this assumption doesn't really hold. We obtain R_S iteratively and use the classic Strömgren radius as an educated guess (for a more detailed explanation see Hu et al., 2016).

5.2.3 Core-collapse SNe

We employ the resolved SN feedback mechanism developed by Hu et al. (2017) and Steinwandel et al. (2020), which allows for a self consistent build up of the hot phase and the momentum of individual SN events in a resolved Sedov-Taylor phase (Hu et al., 2021, 2022a). This means that all of the outflow properties presented from these simulations are self-consistently driven from the hot phase of the ISM with no requirements for tuning the mass loading factors that have shown to be necessary to adopt in lower resolution simulations of galaxy formation. The SN feedback modelled in our simulations is from core-collapse SNe. Each SN injects 10^{51} erg into the nearest 100 neighbours. We follow chemical enrichment from these SNe using yields from Chieffi and Limongi (2004), which are given for progenitors from 13 $M_\odot$ to 35 $M_\odot$ for zero up to solar metallicity, which we then interpolate in our metal enrichment routine. When a star explodes as a SN, its mass is distributed within the kernel to the 100 neighbouring gas particles along with the respective chemical enrichment. The metal enrichment of the particles is a key component to our model as it has a substantial impact on the cooling timescales. The purely thermal injection of feedback in lower resolution simulations has resulted in the 'overcooling problem', where too little energy is injected into too much mass, such that the affected region only reaches temperatures $\leq 10^5$ K, as opposed to T > 10^7 or so, resulting in galaxies producing far too many stars (Wise et al., 2012; Emerick et al., 2018). This is however not an issue in these simulations as has been shown in Hu et al. (2017); Hu (2019) and Steinwandel et al. (2020) when the Sedov-Taylor phase is resolved and the SN blast wave behaves as expected.

5.2.4 Initial Conditions

The initial conditions for these simulations are generated using the code `MakeDiskGal` presented in Springel (2005). We construct an isolated dwarf galaxy with a baryonic mass of 6×10^7 $M_\odot$ and a dark matter mass of 2×10^{10} $M_\odot$. The baryonic mass resolution used, and subsequently the mass of the gas particles is 4 $M_\odot$ with 0.1 pc force softening. Dark matter particles have masses of 6.8×10^3 $M_\odot$ with a force softening of 62 pc. We present 7 different setups in this study, all starting from the same initial condition. The differences of the simulations are summarised in Table 5.1. The result from the initial conditions generator is a smooth distribution of gas, which when allowed to then cool and form stars, collapses violently, forming many stars and results in a hole in the central part of the galaxy (see Hu et al., 2016). In order to avoid this, we run turbulent driving in the disk, where we disable star formation, and instead inject 10^{51} erg of thermal energy into the overdense gas particles (with $n_{\rm gas} > 0.1$ cm^{-3} and T>10^4 K) with an efficiency of 2 per cent per free-fall time (in a very similar fashion to the star formation criteria described in Sec. 5.2.1). We run this for 30 Myr, and the result is a turbulent gas disk with pre-existing ISM structure, shown to prevent the star burst from the initial collapse of the disk, allowing the system to setting into a steady state more quickly (see also Hu et al., 2017).

5.3 Global properties

Fig. 5.2 shows the SFR, outflow rate and mass loading for the runs with a fixed feedback prescription (including SNe and PI), but varying the star formation efficiency. The overall results for the different star formation efficiencies have already been presented in Chapter 3, but we present them again in order to compare the effect of the star formation efficiency (indirectly the impact of different stellar clustering) with the effects of the feedback. Whilst the star formation efficiency parameter is what has been varied, it is more useful to think of its impact on the densities at which stars form in order to understand the physical impact. The lowest star formation efficiency, `PI_SN_0%` means that star particles are only formed once they reach the $M_J = 0.5$ threshold. Increasing the star formation efficiency increases the amount of star formation that is allowed to happen at lower densities and higher temperatures. Low star formation efficiency means stars form at the highest gas densities, whilst higher star formation efficiency means stars are allowed to form at lower gas densities.

As shown in Chapter 3, the differences in the peak densities at which stars form is not a conservative change. For the `PI_SN_0%` run, star formation ambient densities start at 10^2 cm^{-3} and peak between 10^4-10^5 cm^{-3}. For the `PI_SN` run (with 2 per cent star formation efficiency), the ambient densities range from $\sim 10^1$ - 10^5 cm^{-3} with a flat maximum distribution between $\sim 10^2$ - $10^{4.5}$ cm^{-3}. For the `PI_SN_20%` run, the ambient densities peak at $\sim 10^2$ cm^{-3}, steeply declining up to $\sim 10^{4.5}$ cm^{-3}. All of this being said, despite these very different star formation ambient densities, the global properties have some subtle differences but overall are very similar, as seen in Fig. 5.2. The SFR being similar is perhaps somewhat expected, but the outflow rates are interesting as these are dictated quite strongly by SNe, and the densities at which the SNe explode influences their ability to drive outflows. What we conclude (and was stated in quite

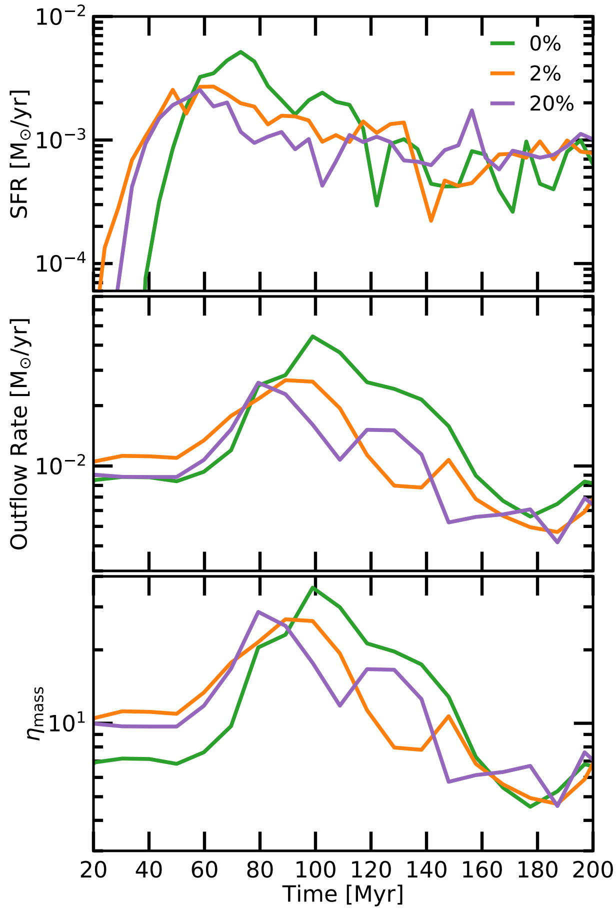

Figure 5.2: SFR, outflow rates and mass loading for the different star formation efficiencies, 0 per cent (0%, `PI_SN_0%`), 2 per cent (2%, `PI_SN`) and 20 per cent (20%, `PI_SN_20%`). *Top panel*: The SFR, where we can see that the onset of star formation is affected by the star formation efficiency, such that the lower star formation efficiency run (`PI_SN_0%`) has an onset of star formation around 10-20 Myr later than the runs with a non-zero star formation efficiency. This is then reflected in a slight overshoot of the SFR for the `PI_SN_0%` model at around 80 Myr. By $\sim$ 140 Myr, the SFR of all runs has flattened to a consistent rate of $\sim 10^{-3}$ M$_\odot$/yr. *Middle panel*: The outflow rates for the `PI_SN` and `PI_SN_20%` runs are very similar, but the `PI_SN_0%` run has an increased outflow (by a factor of only a few) at around 100 Myr, owing to the increased SFR previously. *Bottom panel*: The mass loading, defined as the ratio of the outflow rate to the SFR. We use the average SFR in the denominator of this ratio. The overall shape of the mass loading therefore follows that of the outflow rates. The overall mass loadings are not substantially different, and settle to very similar values by 200 Myr.

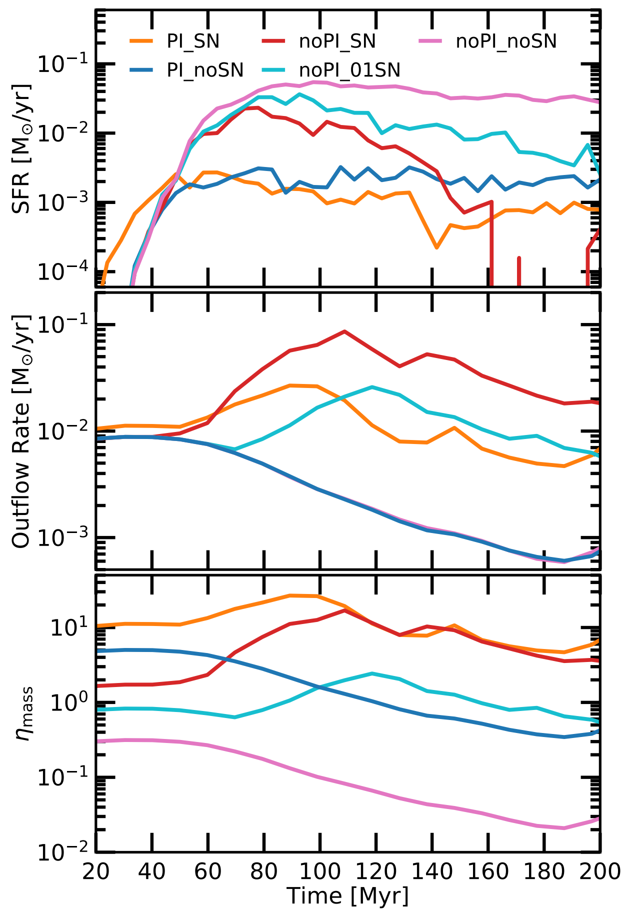

Figure 5.3: Star formation history, outflow rates and mass loading for the fiducial 2 per cent star formation efficiency but now looking at the effect of the different feedback combinations (see Table 5.1). *Top panel*: The SFR. The `PI_SN` run (orange line) shows the fiducial run with both feedback processes included. Both SNe alone and PI alone are effective at regulating star formation, with some delay for the SNe only run (`noPI_SN`, red) due to the time delay between star formation and the SNe explosions. No feedback (`noPI_noSN`, pink) has a substantially increased SFR by 200 Myr in comparison to the run including both PI and SNe (`PI_SN`). *Middle panel*: The outflow rate, measured at 1 kpc above and below the disk. The outflow rates start at the same value due to the fact that some turbulent driving is applied to the initial conditions, and thus these outflows are 'left over' from this. Following the evolution of these outflows however, we see in the absence of SNe (`PI_noSN`, blue and `noPI_noSN`, pink) both have identical outflow rates which decrease steadily from the initial driving applied due to the fact that no SNe are present to drive any outflows. *Bottom panel*: The mass loading, defined as the outflow rates divided by the average SFR. With no feedback (`noPI_noSN`, pink), the low outflow rates and high SFR result in very low mass loadings. PI alone (`PI_noSN`, blue) results in mass loadings around an order of magnitude higher. The highest mass loadings come from the fiducial model, including both PI and SNe (`PI_SN`, orange).

some detail in Chapter 3) is that despite the very different star formation ambient densities, the densities in the ISM are regulated by feedback processes, both before the SNe explode, but also by SNe themselves.

Fig. 5.3 shows the effect of the different feedback prescriptions on the SFR, outflow rates and mass loading. Looking firstly at the SFR, excluding SNe (`PI_noSN`) results in a small increase in the SFR by a factor of around 2. Excluding PI now, but including SNe (`noPI_SN`) results in an increased SFR at early times, as not enough SNe have not had a chance to explode by this point, but the SFR is drastically reduced by $\sim$ 150 Myr by SNe alone. In the absence of PI, decreasing the SNe energy (`noPI_01SN`) or excluding it entirely (`noPI_noSN`) increases the SFR substantially. In the `noPI_noSN` run with no feedback at all, the SFR is increased by a factor of $\sim$ 30 in comparison to the run including both feedback processes (`PI_SN`) by 200 Myr.

As part of the generation of the initial conditions, we drive turbulence in the gas disk for around 30 Myr, by injecting SN feedback in the dense regions of the disk (without any cooling or star formation). Subsequently when we look at the outflow rates, all models show outflows at around 10^{-2} $M_{\odot}$/yr from the beginning of the simulation. For the runs excluding SNe, we would expect no outflows as SNe are necessary to drive this process, at least on a galactic scale. For this reason, in the absence of SN feedback we see a substantial decrease in the outflow rates (actually at identical rates for both the `PI_noSN` and `noPI_noSN`runs). The highest outflow rate comes from the `noPI_SN` run. The reasoning behind this is due to the increased number of SNe in the absence of PI, as well as the densities at which these SNe explode, as explained in Sec. 5.4.1. The `PI_SN` and `noPI_01SN` runs both have similar outflow rates. In comparison to the `PI_SN` run, the `noPI_01SN` has substantially more SNe explosions (see Fig. 5.7), but these SNe only carry 10 per cent of the canonical 10^{51} erg, so the total energy injected into the ISM is similar (see Sec. 5.4.3).

Fig. 5.4 shows the stellar surface densities for each of the runs with different feedback prescriptions. For the differences in the stellar distributions for the different $\epsilon_{\rm ff}$ simulations, please see Chapter 3. Contrasting firstly the effect of excluding SNe only, from the x-y projection, the size of the disk is similar between the `PI_SN` and `PI_noSN` runs, but the z-projection for the `PI_noSN` run shows a much thinner disk. The x-y projection also appears to show much less spiral-like structure but instead more of a circular structure. Comparing now to excluding PI but including SNe (`noPI_SN`), the disk is much more puffed out in all directions. There is no distinguishable spiral-like structure anymore and the stars are at noticeably larger radii from the centre of the disk. The z-projection however is the most substantially different here, with many stars extended more than 1 kpc above and below the plane of the disk. For the same feedback combination, but just decreasing the SN energy to 10 per cent of the canonical value (`noPI_01SN`), the effect is not as significant. The distribution of the stars perpendicular to the disk is much more similar to the fiducial `PI_SN` run, whilst the structure of the disk looks quite similar to the run without SNe (`PI_noSN`). When turning off both forms of feedback (`noPI_noSN`) we see a very thin disk, with a lot of very dense clumps of star formation and a very compact disk in all dimensions.

Fig. 5.5 shows the same as Fig. 5.4 but now for the gas. Without SNe, as in `PI_noSN` and `noPI_noSN`, we see no low density gas in the x-y projection and no indications of any kind of outflows in the z-projection, as expected, as we know that we need SNe in order to drive

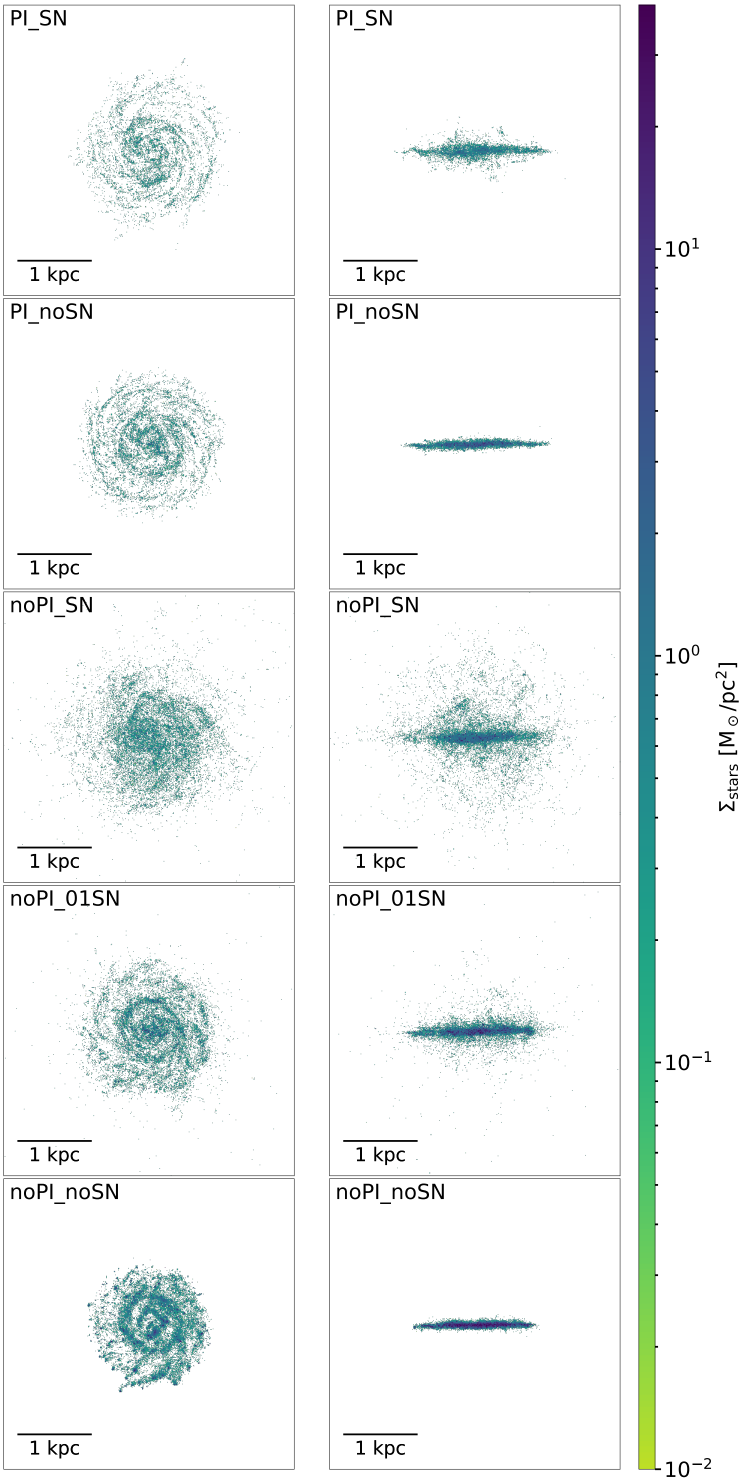

Figure 5.4: Surface density of stars in each of the simulations at 200 Myr with the varied feedback prescriptions. The left column shows the x-y projection and the right column shows the x-z projection to show the edge on distribution of the stars. All panels are 4×4 kpc^2.

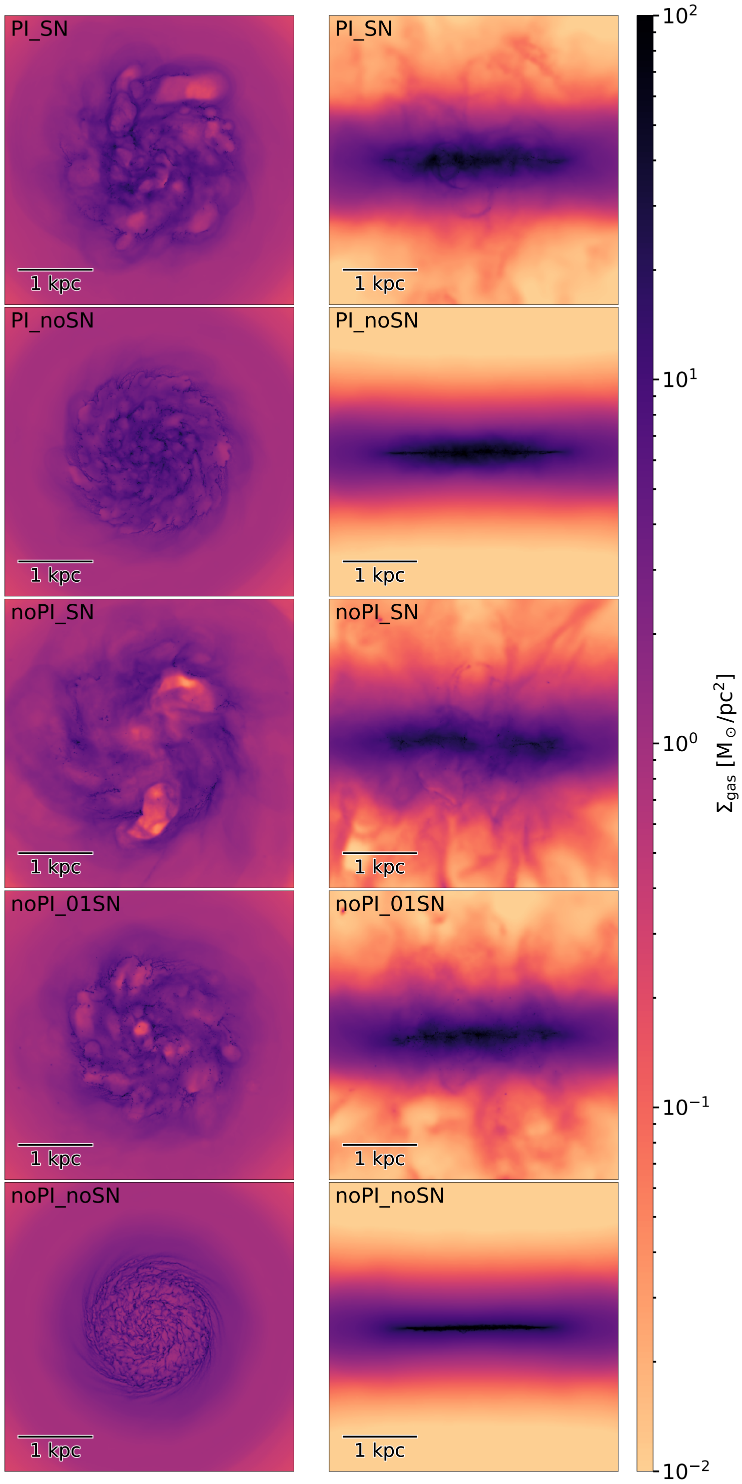

Figure 5.5: Gas distribution for the different models with varying feedback prescriptions.

outflows on these scales. Excluding PI enhances outflows, as we see large structures of dense gas perpendicular to the plane of the disk being driven by correlated SNe explosions in the `noPI_SN` run. This effect is naturally reduced when lowering the SN energy injected in `noPI_01SN` where we see similar gas structure to the fiducial `PI_SN` run.

5.4 Stellar and SN clustering

5.4.1 Ambient density of SNe

In Chapter 3, we showed that even with very different clustering and ambient density of star formation, the ambient density of SNe ended up being extremely similar in their distributions. We concluded in that study that there is a decoupling between the densities at which these two processes occur, but we aim here to explore further into this topic to see what is regulating these densities. Naturally, there is a delay of some Myr between star formation and when the SNe explode, but how does the ISM regulate its density? By turning off PI, we saw some key differences in the ambient density distribution of SNe. Firstly, the density distribution becomes wider, meaning we have a tail of very high density SNe as well as an extension down to lower densities than in the corresponding run that includes PI. Additionally, there is a suppression of the peak in the ambient density at $\sim 10^0$ cm^{-3}. Whilst excluding PI is not what happens in nature, it is an extreme way of enhancing clustering and producing SNe at more extreme ambient densities, both low and high. To add complication to this topic however, it is not immediately obvious which of the SNe at which ambient densities actually contribute to driving outflows. Also, outflows are not typically produced by single SNe, it is the combination of multiple SNe. Numerous SNe need to be close enough, both spatially and temporally in order to drive outflows, and understanding what is the minimum requirement for outflows is a challenging task.

Fig. 5.6 shows the ambient density of SNe for the different star formation efficiency runs. The densities are distributed in approximately in two peaks. In the higher density peak ($\sim 10^0$ cm^{-3}), the majority of these SNe explode in the field (outside of identified FoF groups). The height of this peak shows a trend with the star formation efficiency, with an increasing fraction of SNe exploding in the field and less SNe in FoF groups with increasing star formation efficiency (resulting from decreasing clustering). Equally there is the same trend for the lower density peak at around 10^{-3} cm^{-3}. More SNe explode in the lower density peak with decreasing star formation efficiency (higher clustering). For all of the runs including PI, the high density peak is dominated by SNe exploding in the field. For the lower density peak, there is an increase in the number of SNe in FoF groups with increased clustering (decreasing star formation efficiency).

Fig. 5.7 shows the ambient density of the SNe for the runs with different feedback implementations that include SNe. There are substantially more SNe exploding in the runs without PI, particularly at lower densities. There is also a prominent tail towards higher densities without PI. In the interest of understanding the contribution of SNe at different densities, we can more fairly compare the models by the bottom panel, which shows the fraction of SNe for each simulation. For the simulations excluding PI, the higher density peak at around 10^0 cm^{-3} doesn't really exist, and an equal number of SNe appear to explode at these densities in FoF groups and in the

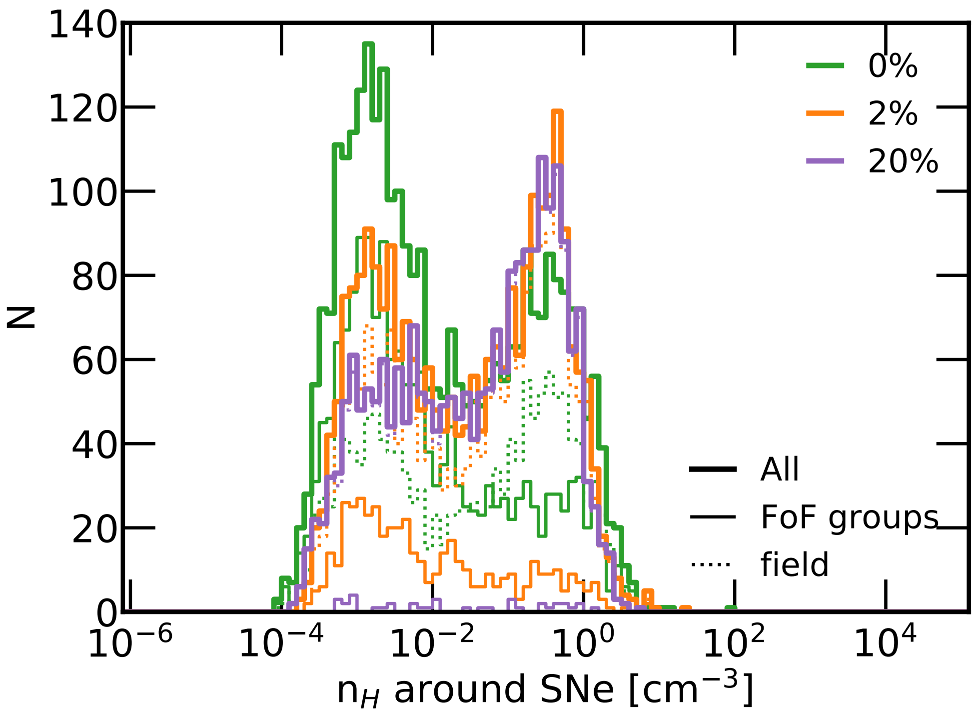

Figure 5.6: The ambient density of SN explosions shown for the three simulations at 200 Myr employing both SN feedback and PI. We show here the contrast between the three star formation efficiencies, 0 per cent (0%, `PI_SN_0%`), the fiducial 2 per cent (2%, `PI_SN`) and 20 per cent (20%, `PI_SN_20%`). The ambient densities are shown for all SNe (bold lines), as well as split into SNe identified in FoF groups (thinner lines) and not in a FoF group (field, dotted lines). We see two distinct peaks, one at $\sim 10^0$ cm^{-3} and another at $\sim 10^{-3}$ cm^{-3}. Looking at the overall distribution of all SNe, when increasing the star formation efficiency, there is an increase in the number of SNe in the higher density peak and a decrease in the number in the low density peak.

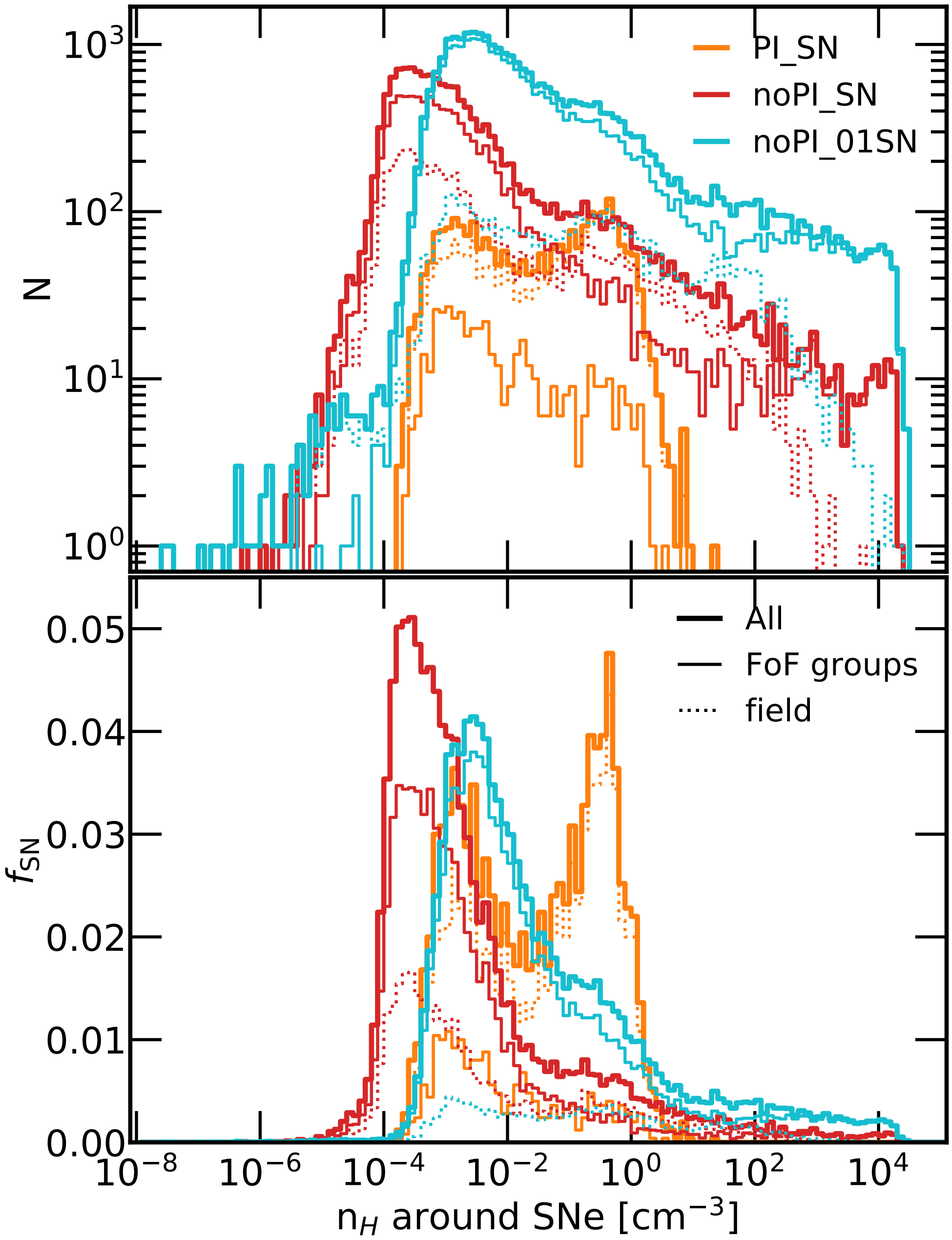

Figure 5.7: The ambient density of SNe at 200 Myr, similar to Fig. 5.6, but now shown for the different feedback runs, `PI_SN`, `noPI_SN` and `noPI_01SN`. For reference, the orange lines for `PI_SN` are the same as the orange lines in Fig. 5.6. We show the absolute number of SNe in the upper panel, but owing to the differences in the number of SNe in the models that exclude PI, we also show the fraction of SNe in the bottom panel, normalised by the total number of SNe.

field. For the lower density peak however, we see an extreme enhancement in the number of SNe exploding in FoF groups at densities slightly lower than the low density peak identified for runs including PI. There are also a non-negligible number of SNe exploding in the field at these densities. Whilst we see a large number of SNe at these densities, there is also a substantial tail to high and low densities, well beyond the distribution of the runs including PI. This broadening of the ambient density distribution of the SNe when excluding PI shows that the overall distribution of the ISM that is sampled by the SNe is altered substantially when excluding PI. The densities at which the SNe explode has a strong impact on the outflow properties.

5.4.2 Individual SNe in clusters

In Fig. 5.8, we show the distribution of the ambient densities of SNe explosions binned by the mass of the identified FoF group. For the `PI_SN_0%` run, the majority of SNe explode in lower mass FoF groups between 200 and 600 $M_\odot$ as shown in the upper panel, however we see from the lower panel that these lower mass FoF groups have a lower number of SNe per cluster on average. Therefore this is simply a direct consequence of the fact that the lower mass FoF group are more numerous. Assuming a cluster would have a stellar population representative by the initial mass function (IMF), it is naturally to be expected that lower mass clusters would have less SNe. We see this in the lower panel with the more massive clusters having more SNe per FoF group overall. We can therefore understand that for a given FoF group of any mass, it will only have around one SN contributing to the high density peak ($\sim 10^0$ cm^{-3}), and that the rest of the SNe explode in the lower density peak ($\sim 10^{-3}$ cm^{-3}). Increasing the mass of the FoF group simply increases the number of SNe in the low density peak. This is in line with what is expected when considering a typical FoF group, which has a half-mass radius on the order of a pc. As star formation happens in that region, the densities decrease as a consequence of PI (as well as consumption of gas by further star formation) down to $\sim 10^0$ cm^{-3} by the time that the first SN explodes. The injection of energy into this region from this first SN then dramatically decreases the gas densities in this region, meaning that the following SNe explode at much lower densities. This helps to build the picture of which feedback processes regulate each density regime of the ISM. PI (when included) is responsible for regulating the highest densities ($> 10^0$ cm^{-3}) whilst SNe are responsible for regulating the densities below this range.

Fig. 5.9 allows us to observe the effect of the SNe in the absence of PI. Firstly, as already seen from Fig. 5.7, the absolute number of SNe is increased substantially when excluding PI. This is enhanced even more when the SN energy is decreased in the `noPI_01SN` run. In the whole simulation (not just in FoF groups), the number of SNe in the `noPI_01SN` run is double that of the `noPI_SN` run. In FoF groups, there are 2.6 times more SNe in the `noPI_01SN` run in comparison to the `noPI_SN` run, showing that there is also an enhancement of SNe in clusters when reducing the SN energy to 10^{50} erg. We can also notice that in contrast with the runs including PI, the majority of SNe explode in the most massive clusters, as the lack of PI results in many more massive FoF groups. Looking at the average number of SNe per cluster in the lower row of Fig. 5.9, we see the same trend as we saw for the `PI_SN_0%` model in Fig. 5.8, such that in a given cluster, there is <1 SN explosions at densities above 10^0 cm^{-3} followed by an increasing number of SNe at lower densities with the mass of the FoF group. The more massive clusters

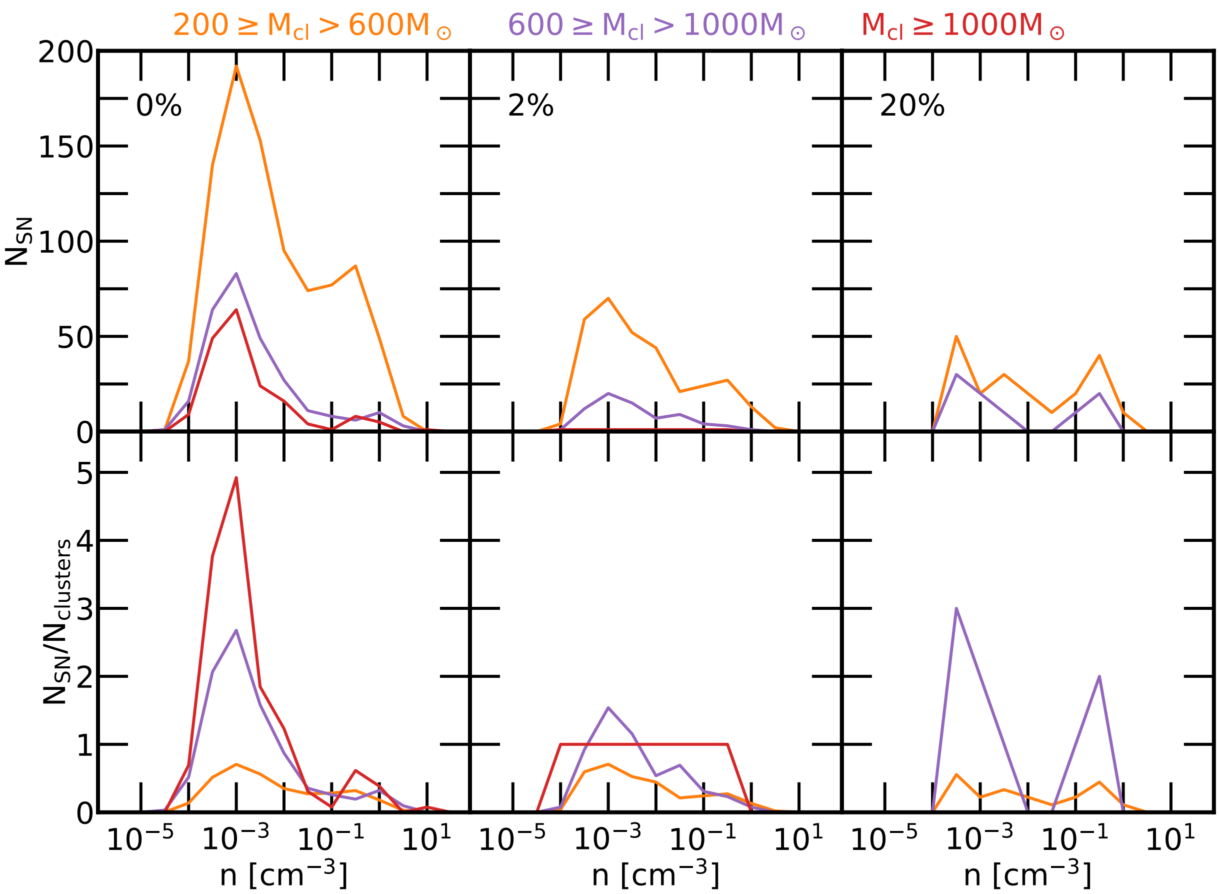

Figure 5.8: Histogram of the ambient densities of SNe exploding in FoF groups binned by mass. The first column shows the `PI_SN_0%` (0%) run, the middle column shows the `PI_SN` (2%) run and the final column shows the `PI_SN_20%` (20%) run. Orange lines show the distribution of ambient densities for identified FoF groups with masses $200 \leq M_{cl} < 600\ M_{\odot}$, purple lines show $600 \leq M_{cl} < 1000\ M_{\odot}$ and red shows $M_{cl} \geq 1000\ M_{\odot}$. *Top row:* absolute number of SNe exploding in clusters of a given mass for each of the simulations with varying star formation efficiency. As there are many more FoF groups identified in the `PI_SN_0%` run, we also naturally see more SNe. For all star formation efficiencies, the majority of the SNe explode in the low mass FoF groups, predominantly because they are much more numerous than the higher mass FoF groups. *Bottom row:* The number of SNe as a fraction of the number of clusters in that given mass range, denoting the average number of SNe exploding per cluster of that mass. The numbers of FoF groups for the `PI_SN` and `PI_SN_20%` runs makes this somewhat difficult to interpret, but we show it here for completeness. From the `PI_SN_0%` run however we can get a nice picture of the way in which the SN ambient densities are distributed in FoF groups, such that all masses of FoF groups have an average of (less than) one SN in the high density peak ($\sim 10^0$ cm^{-3}). As the cluster mass increases, the number of SNe exploding in the lower density peak ($\sim 10^{-3}$ cm^{-3}) also increases.

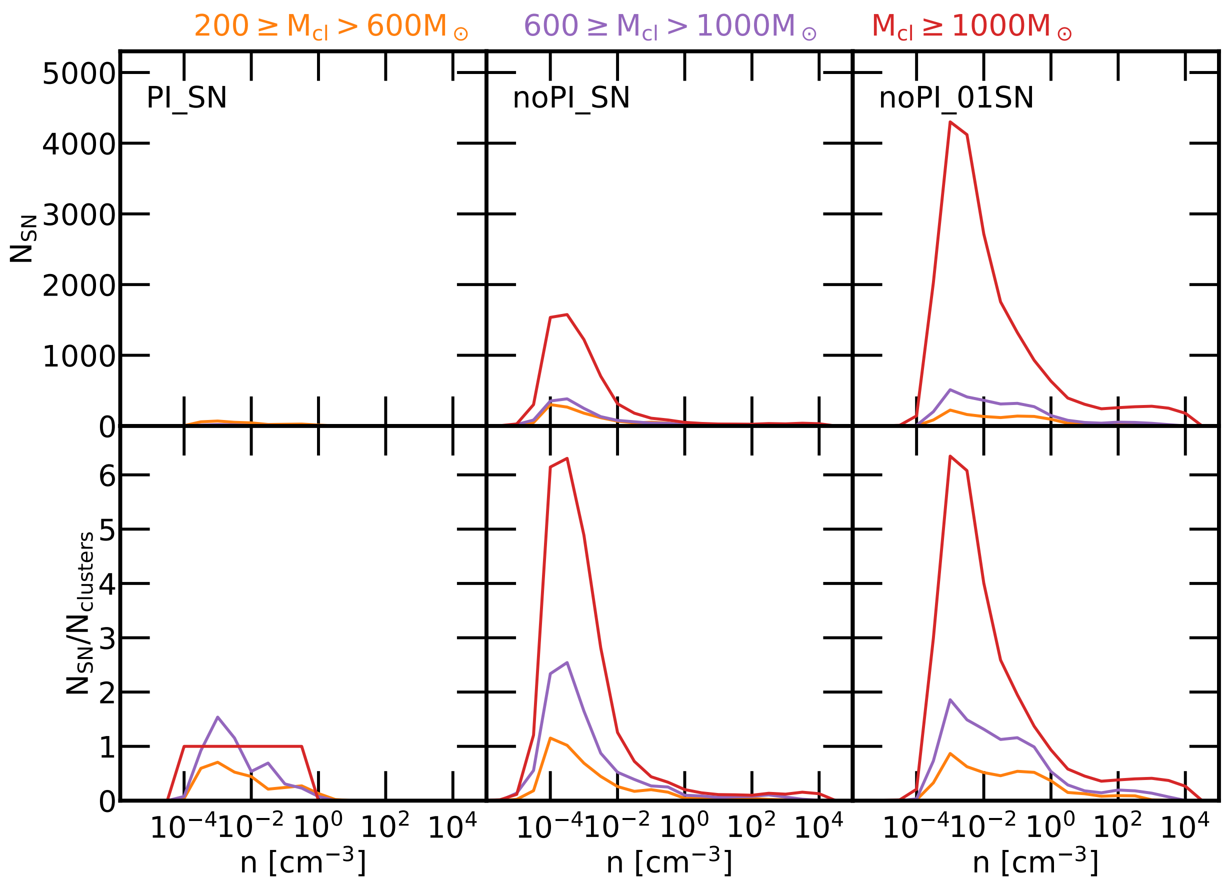

Figure 5.9: Histogram of the ambient densities of SNe exploding in FoF groups, in the same presentation as Fig. 5.8, but now showing the different feedback prescriptions. We show the fiducial run `PI_SN` in the left hand column (identical to that shown in the middle column of Fig. 5.8). The upper panel shows the absolute number of SNe. Immediately we can notice that when the axes are adjusted to accommodate the number of SNe from the `noPI_SN` and `noPI_01SN` runs, the number of SNe in the `PI_SN` run are completely not visible. We include this nonetheless to really highlight the substantial contrast in the number of SNe in the simulations when we have excluded PI. Concentrating on the models without PI, in the bottom panels, we see the same trend as we saw in Fig. 5.8 such that the most massive FoF groups have the highest number of SNe per cluster, but now we can see that the density distribution extends to much higher densities. We still see the trend of <1 SN at densities above 10^0 cm^{-3} and then an increasing number of SNe at lower densities with cluster mass.

produce more spatially incident low density supernovae, and it is these supernovae that are able to drive outflows.

5.4.3 SN energy injected into the ISM

To understand what is really responsible for the differences in the outflow rates, we can look at how much energy is injected into the ISM. Summing up the energies of all the SNe explosions in the simulations by 200 Myr, we find that the `PI_SN` run has injected 2.5×10^{54} erg, the `noPI_SN` run has injected 1.4×10^{55} erg, and the `noPI_01SN` run has injected 2.9×10^{54} erg. Remembering from Fig. 5.3, despite the very different number of SNe between the models, we saw very similar outflow rates for the `PI_SN` and `noPI_01SN` runs, and perhaps the similar values of energy injected into the ISM is the explanation. We can contrast this to the `noPI_SN` run which had the highest outflow rates of all the simulations, and injects more than 5 times the total amount of SN energy in comparison to the run including PI.

5.5 Properties of the ISM

We can see the impact of the clustering as well as the stellar feedback combinations on the properties of the ISM. This process is somewhat circular in that the properties of the ISM are dictated by where and how energy is injected into the ISM by stellar feedback, which in turn impacts future star formation. We can gauge the overall temperature distribution from Fig. 5.10, where we show the impact of the different stellar clustering properties as well as the feedback combinations. Comparing the runs with different $\epsilon_{\rm ff}$ (`PI_SN_0%`, `PI_SN` and `PI_SN_20%`), we see little difference distinguishable by eye between the runs. Cold filamentary structures of gas are visible in all runs, as well as large bubbles generated by SNe. Small red dots are noticeable, which are freshly exploded SNe which are in the processes of heating the surrounding gas. Contrasting these runs to the `noPI_SN` simulation which excludes PI, we can see a loss of the structure in the gas. Some colder gas structure is still visible, but overall the galaxy looks smoother and also slightly more extended, with some large SNe generated holes. The `PI_noSN` run shows the effect of now including PI but excluding SNe. The galaxy is clearly more compact with lots of cold gas structure. We see no gas above 10^5 K due to the lack of heating from SNe as well as of course no large cavities driven by SNe feedback. This is taken to the extreme when then looking at `noPI_noSN` which additionally neglects PI. The galaxy is extremely compact, with a lot of very cold filamentary structure. When comparing `PI_noSN` and `noPI_noSN`, it is clear to see the quite drastic impact of only the PI on the gas structure. SNe naturally have a large effect at pushing gas out of the galaxy and driving large cavities, but PI has an substantial impact on puffing out the galaxy and heating the gas in the vicinity of star formation.

5.5.1 Phase Diagrams

Fig 5.11 shows the phase diagrams for the runs with the different feedback combinations as well as also the `PI_SN_0%` model. The top row shows the runs including both PI and SNe but with

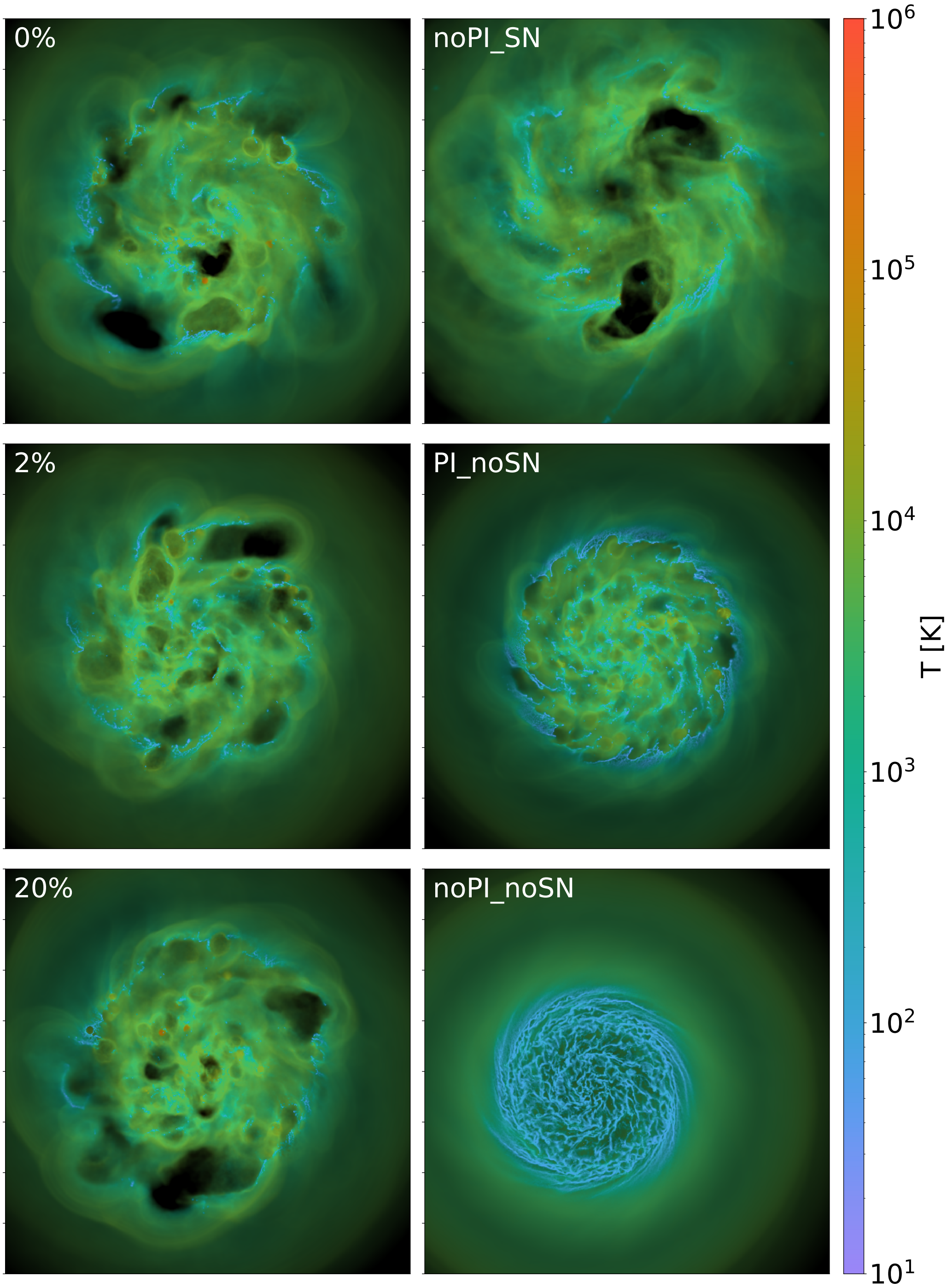

Figure 5.10: Surface density of the gas colour-coded by the gas temperature at 200 Myr. The left column contrasts the same feedback model (including PI and SNe) but with the variation in $\epsilon_{\rm ff}$. The right column shows the contrast between the models with a fixed $\epsilon_{\rm ff}$ of 2 per cent, but now showing the effect of PI and SNe explosions on the gas density and temperature.

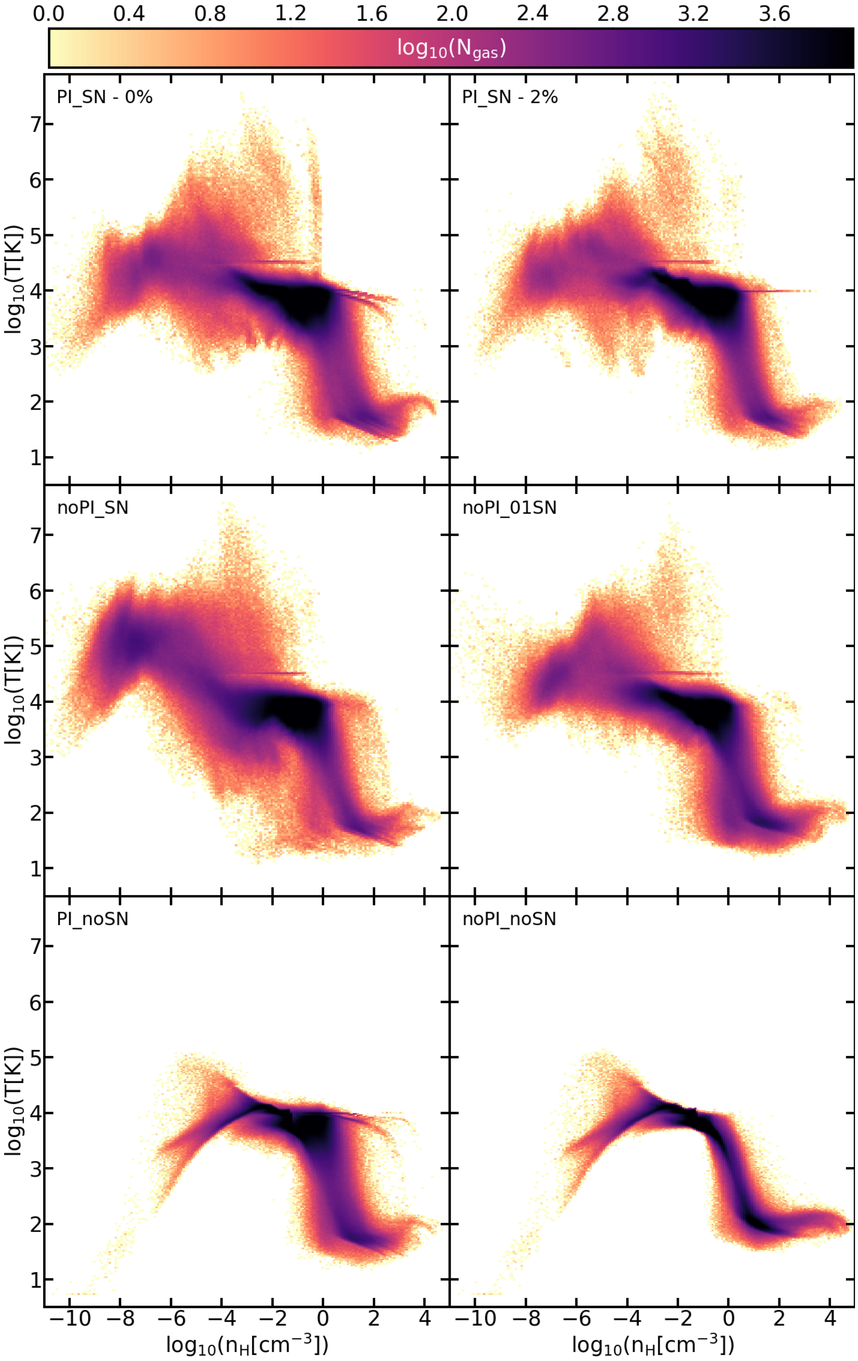

Figure 5.11: Phase diagrams for each of the simulations at 200 Myr with modified feedback as shown in the top left corner of each panel. We show the phase diagram for all gas in the simulation box. Without SNe, we see no gas above 10^5 K, as SNe are the only mechanism able to heat gas up to temperatures of 10^8 K. One key difference to see between `PI_SN` and `noPI_SN` is the effect of PI in producing this strong feature at 10^4 K. This feature comes directly from PI, where gas surrounding photoionising stars is heated directly using the Stromgren approximation.

Gas State	Temperature	Description
Cold	$T \leq 300$ K	Thermally stable cold gas
Warm	300 K $< T \leq 20000$ K	Warm atomic and ionised gas
Warm-hot	20000 K $< T \leq 300000$ K	Highly ionised gas, thermally unstable
Hot	$T > 300000$ K	Very hot gas, mostly in hot SN remnants

Table 5.2: Description of the gas temperature states used for the analysis.

different $\epsilon_{\rm ff}$. The phase diagrams look quite similar, with some differences particularly at densities above 10^0 cm^{-3}, which is to be expected as was described in Sec. 5.3, varying the $\epsilon_{\rm ff}$ parameter had a substantial impact on the distribution of densities at which gas particles were turned into stars. The line at 10^4 K shows gas particles which have been heated to this temperature due to being within the vicinity of photoionising sources. This feature is naturally missing from the simulations which exclude PI. There are also some differences near the star forming regime in the bottom right-hand corner of the plot. We see a small 'arch' feature in the `PI_SN_0%` run which is not present in the `PI_SN` run. The origin of this feature requires further investigation.

The middle two panels show the effect of just changing the SN energy in the absence of PI. When each SN carries 10^{51} erg for the `noPI_SN` simulation, the phase diagram overall is a bit more 'fluffy' in all directions. The temperatures naturally extend higher due to the higher SN energy injected, but there is also a mild extension to lower temperatures. Injecting SN energy makes the system have a larger range of environments in the gas. The `noPI_01SN` model, which excludes PI but only injects 10^{50} erg per SN has a very similar phase diagram structure to that of the `PI_SN`. One may notice a small horizontal feature in the top four panels at a temperature of 3×10^4 K. This is an artificial feature (which has subseqently now been fixed in current version of the model) from the fact that we do not follow non-equilibrium cooling for $T > 3 \times 10^4$ K. The transition between the cooling rate calculations leads to a small discontinuity, which has only a minor impact on the dynamical behaviour of the ISM so long as cooling is rapid in this regime (see Hu et al., 2017, for a more extended discussion).

The two bottom panels show the effect of including/excluding PI in the absence of SNe. Without SNe, we would not expect to see any gas at all above 10^4 K, as there is no mechanism other than SNe that heat gas to temperatures above this. We do however see a small amount of gas above 10^4 K in these phase diagrams, and this is left over from the turbulent driving as discussed in Sec. 5.2.4. Comparing `PI_noSN` and `noPI_noSN`, the inclusion of PI broadens the distribution of gas densities between 10^0 and 10^2 cm^{-3}, in agreement with what was discussed in Sec. 5.4.1, such that PI is the primary mechanism that regulates the ambient densities of the ISM above 10^0 cm^{-3}. This is confirmed by also comparing the phase diagrams for the `PI_SN` and `PI_noSN` runs. The difference between these two runs is just including or excluding SNe, and we can see that the shape of the phase diagram for densities above 10^0 cm^{-3} is very similar. For densities below 10^0 cm^{-3} however, this is strongly regulated by SNe, which is very clear when comparing the bottom two panels excluding supernovae and the upper four panels which have it included.

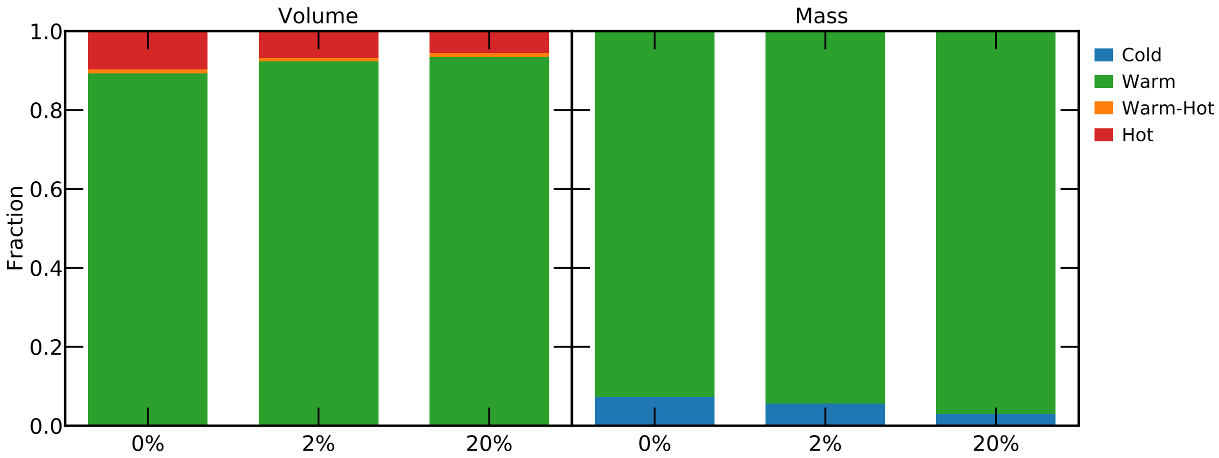

Figure 5.12: Volume and mass filling fractions averaged between 100 and 200 Myr for gas within a radius of 1.5 kpc and a height of 100 pc above and below the plane of the disk for the runs with different ϵ_{ff}. The first bar of both panel shows ϵ_{ff} = 0% (`PI_SN_0%`), the second shows the fiducial value of ϵ_{ff} = 2% (`PI_SN`) and the third shows ϵ_{ff} = 20% (`PI_SN_20%`).

5.5.2 Volume and mass filling fractions

We also look at the volume and mass filling fractions in order to quantity the properties of the ambient density of the ISM on the scales at which most star formation occurs. For this reason we only look at the ISM 100 pc above and below the plane of the disk. We divide our analysis of the gas temperatures into four temperature regimes, summarised in Table 5.2, as traditionally defined in Mihalas and Binney (1981).

As can be seen in Fig. 5.5, this 200 pc region well captures the densest part of the ISM. Fig. 5.12 shows the average volume and mass filling fractions between 100 and 200 Myr for the runs with different ϵ_{ff}. The vast majority of the gas volume is taken up by warm gas (300 K < T ≤ 20000 K). There is then a very small contribution of ~ 1 per cent in all cases for the warm-hot gas (20000 K < T ≤ 300000 K). For the lowest ϵ_{ff} run (`PI_SN_0%`), the clustering is the highest of the three runs. This is the simulation where the gas must collapse to the highest densities and lowest temperatures before forming stars, resulting in the highest cluster formation efficiencies. This is reflected in the increased mass fraction of cold gas. Higher clustering also results in a larger hot volume filling fraction, driven by more clustered supernovae being more efficient in driving large bubbles of hot gas. This will be even more evident outside the plane of the disk, but even in this 200 pc region, we still see an increased hot volume filling fraction for the lowest ϵ_{ff} (`PI_SN_0%`) where 10 per cent of the ISM volume is hot gas, in comparison to the higher ϵ_{ff} (`PI_SN_20%`) with only 6 per cent.

For the mass fraction, it is again highly dominated by the warm gas (300 K < T ≤ 20000 K). A negligible fraction (~ 0.1 per cent) of the mass is taken up by gas above 20000 K. Varying ϵ_{ff} has an impact on the cold gas mass fraction however, such that the lowest ϵ_{ff} run (`PI_SN_0%`) has a 7 per cent mass fraction of cold gas in comparison to the higher ϵ_{ff} (`PI_SN_20%`) which has 3 per cent. In the `PI_SN_0%` run, gas is allowed to collapse to higher densities and cooler

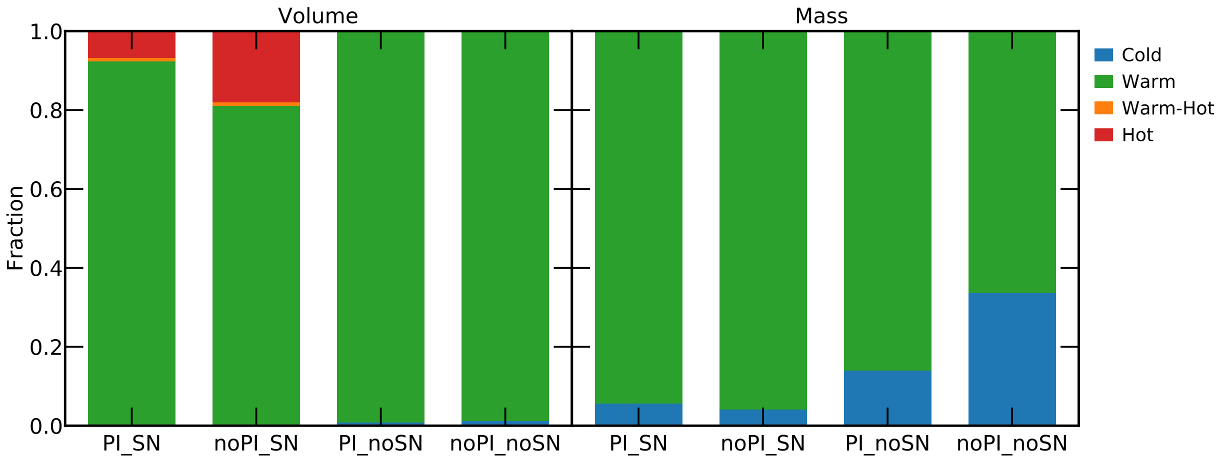

Figure 5.13: The same as Fig. 5.12 but for the runs with different feedbacks. We can see immediately that the simulations excluding SN feedback have no hot gas in the volume or mass filling fractions, as is also reflected in the phase diagrams shown in Fig. 5.11.

temperatures before forming stars, explaining why the gas mass fraction of the ISM is higher for this model as opposed to the PI_SN_20% run, where gas does not have to collapse to such high densities and low temperatures before forming stars.

We can also compare the volume and mass filling fractions for the runs with different feedback combinations in Fig. 5.13. Here we just compare PI_SN (which is the same as the middle column of Fig 5.12), noPI_SN, PI_noSN and noPI_noSN. The runs with no SNe have no volume or mass in gas above 20000 K in the ISM. When discussing the phase diagrams in Fig. 5.11, we saw some gas above 10^4 K which was left over from the turbulent driving, but this gas was well above the plane of the disk and so is not seen here. For the runs that do include SNe however, we can see the impact of including and excluding PI by comparing PI_SN and noPI_SN, where we see that the volume filling fraction of the hot gas is more than doubled (from 7 per cent to 18 per cent) when excluding PI. A significant reason for this is just a higher number of SNe (see Fig. 5.7). The warm-hot gas is the same between the two simulations, and both also show no volume fraction of cold gas, as in Fig. 5.12. For the mass fraction, the fraction of cold gas mass is decreased slightly to 4 percent in the noPI_SN run in comparison to 6 per cent in the fiducial PI_SN run, showing PI does have some small impact on the mass fraction of cold gas. Turning off SNe has a much larger impact however. The PI_noSN run has a 14 per cent cold gas mass fraction, which increases to 34 per cent when excluding both PI and SNe.

5.5.3 Densities of the ISM

As well as the temperatures, we can also understand the impact of the clustering and feedback on the densities of the overall ISM. To link this back to the ambient densities of the SNe shown in Sec. 5.4.1, we can ask if the clustering of the SNe is an important contributor to the outflows, or do the SNe just trace the overall density distribution of the ISM. Of course, SNe undoubtedly play an important role in setting the densities of the ISM in the first place and so we firstly understand how the ISM is impacted by the different clustering and also the different forms of feedback.

Fig. 5.14 shows the volume-weighted densities of the cold, warm, warm-hot and hot medium. In line with the volume filling fractions (Fig. 5.12 and Fig. 5.13), we only look at the ambient densities of the ISM 100 pc above and below the plane of the disk. The volume-weighted densities are computed by binning the region of radius 1.5 kpc from the centre of the disk and 100 pc above and below the disk into cubes of 50 pc on the sides and computing the kernel-weighted volume taken up by gas particles in the respective temperature regimes. The left column of Fig. 5.14 shows the impact on the different clustering by varying $\epsilon_{\rm ff}$ on the ambient densities. The overall distributions (black dashed lines) have similar shapes, with a peak at around 10^{-1} cm^{-3} and another around 10^{-3} cm^{-3}. The majority of the higher density peak ($\sim 10^{-1}$ cm^{-3}) is from the warm ISM, with the rest being from the cold gas. The warm ISM is dominated by photoionised gas, and so in this regime we are looking at the gas which is surrounding regions of star formation, either on its way to forming stars, or dense gas around newly formed stars which has been photoionised. The shape of the cold gas in all cases is quite similar, with a very slightly higher fraction of cold gas in the highest density bins for the `PI_SN_0%` run in comparison with `PI_SN_20%`. The tail off to lower densities of the cold gas is also suppressed quicker in the case of higher $\epsilon_{\rm ff}$. The warm medium has a very similar distribution in all runs, as does the warm-hot and hot medium, other than the fact for the `PI_SN_0%` run, the warm-hot and hot medium occupies from lower ambient densities than for the runs with higher $\epsilon_{\rm ff}$. Overall, the distributions of each of the ambient densities for the different temperatures are very similar when varying the $\epsilon_{\rm ff}$.

The phase diagrams (Fig. 5.11) showed that changing the feedback has a substantial effect on the properties of the ISM. Now focusing on the right column of Fig. 5.14, we can compare excluding PI, excluding SNe and excluding both PI and SNe. Firstly, the `noPI_SN` run, which excludes only PI in comparison the `PI_SN` run has a very similar distribution of ISM densities for all temperatures. This is in agreement with the fact that the phase diagrams for both of these runs also looked extremely similar, with the only difference being the feature of the PI at 10^4 K. This isn't seen however when looking at the ISM density distributions, especially considering that this is only a very small fraction of the warm gas. The `PI_noSN` and `noPI_noSN` runs do show substantial differences in their ISM densities, showing that the effect of SNe on the overall ISM densities is very strong. The distribution of the ISM densities is now a single peak, as opposed to the double peaked distribution we see when including SNe. We still have a warm phase as we saw in Fig. 5.13 (remembering that warm gas is from 300 K to 20000 K), with a very small amount of warm-hot gas when including PI (`PI_noSN`). There is also a distribution of cold gas to lower densities in the run including PI, as PI has the ability to lower the density of gas by heating the gas causing the gas cloud to expand and become less dense. The impact of PI in the absence of SNe is very clear when looking at the high density parts of `PI_noSN` and `noPI_noSN` between 10^0 and 10^1 cm^{-3}. Without PI, the densest part of the gas is cold and becoming more dense before forming stars. There is no mechanism to push this cold gas away from the Jeans Mass threshold, and so the cold gas remains dense until it forms a star particle. When including PI however, the gas that occupies this region between 10^0 and 10^1 cm^{-3} is highly likely to be surrounding newly formed stars. Whilst some of the gas is cold, it becomes quickly dominated by the warm gas, primarily from PI.

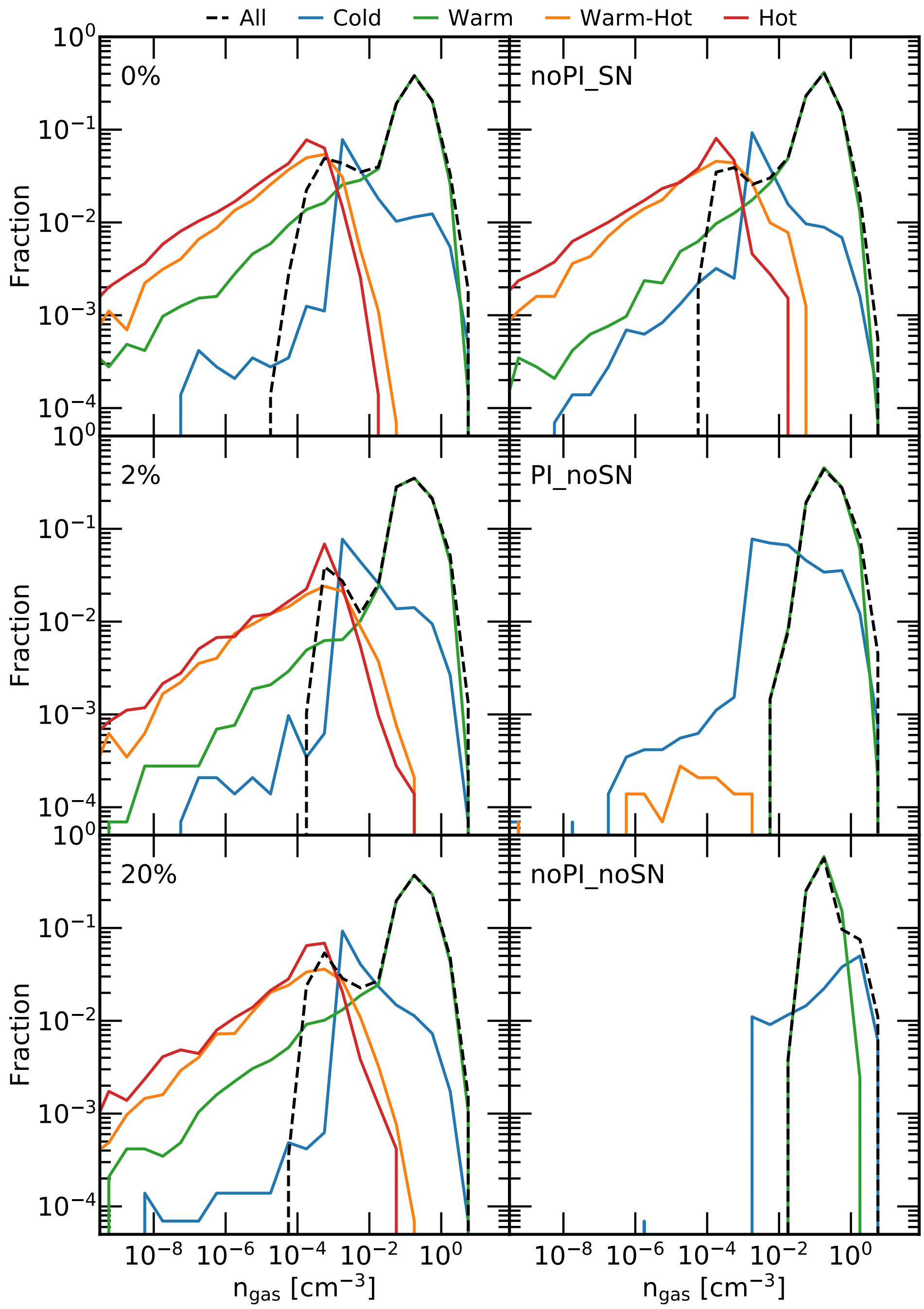

Figure 5.14: Volume-weighted densities of all (black dashed), cold (blue), warm (green), warm-hot (orange) and hot (red) gas in the simulations calculated at a radius of 1.5 kpc in the x-y plane of the galaxy and 100 pc above and below the disk binned in cubes of 50 pc on the side. The distributions are then normalised by the total number of bins. The left column shows the effect of varying the $\epsilon_{\rm ff}$ parameter and the right column shows the effect of the different feedback prescriptions.

Adding into the discussion in Sec. 5.4.1, where we stated that the ambient density of the supernovae were regulated by PI at high densities ($\sim 10^0$ cm^{-3}), we can exactly see this directly by the fact that this regime is dominated by the warm gas, as well as the differences between `PI_noSN` and `noPI_noSN` in the densities just above this. We then argued that the densities in the lower density peak of the SNe ambient densities ($\sim 10^{-3}$ cm^{-3}) were regulated by SNe themselves, which is now supported by the fact that this temperature regime has a substantial contribution from the warm-hot and hot gas.

Leading on from Fig. 5.14, we take the overall volume-weighted density distribution and compare to the ambient densities of the SNe. Firstly we can look at the distributions for the runs with different clustering in Fig. 5.15. As discussed already, the overall volume-weighted density distributions of the ISM are very similar, with a trend for the extension to higher densities with decreasing $\epsilon_{\rm ff}$. Overlaying the ambient densities of the SNe, we see again the two peaks in the distribution as discussed in Sec. 5.4.1. Both distributions have two peaks. For the lower densities, the peaks roughly align for both the ISM and SNe ambient densities at 10^{-3} cm^{-3}. At the higher densities however, there is an offset between the two peaks, with the ISM peak around 10^{-1} cm^{-3} and the peak in the SNe at around 10^0 cm^{-3}. The agreement with the low density peaks can be explained by the fact that this section of the ISM is largely regulated by SNe explosions. In the higher density peaks however, PI is the dominant process that regulates the densities at which the first SNe explode. Considering the timings of the SNe, in a given cluster we saw from Fig. 5.8 and Fig. 5.9 that the first SNe to explode do so in the higher densities peak, followed by several SNe in the lower density peak, the number of which increased with the mass of the FoF group. The SN that explodes in the first peak explodes in an environment with newly formed stars which has not yet been disturbed by SN, but has been affected heavily by PI. There is then a decrease in the fraction of SN ambient densities which roughly coincides with the peak in the ISM ambient densities. The reasoning for this is that the SN explode either at the highest densities as the first SN in their environment, and then the subsequent SNe explode at lower densities in the cavities generated by previous SNe, therefore mostly skipping these intermediate densities. There is a very small but clear trend with $\epsilon_{\rm ff}$, as was also discussed in Sec. 5.4.1 and in Chapter 3. At the lowest $\epsilon_{\rm ff}$, `PI_SN_0%`, there are more SNe in the lowest density peak and less in the higher density peak, owing to the enhanced clustering. More stars are born in clusters, meaning there are more SNe exploding in the low density regions of previous SNe.

Fig. 5.16 shows the same as Fig. 5.15 but for the different feedbacks. We show again the volume-weighted density distribution of the ISM as well as the distribution of ambient densities of the SNe (for the runs that include SNe). As before, the fiducial `PI_SN` run is shown on both plots (orange lines) for comparison. Firstly discussing the ambient densities of the SNe, without PI, the densities at which the SNe explode are much higher, overlapping substantially with the ambient densities at which the stars form. They also extend to lower densities, reaching 10^{-6} cm^{-3}, much lower than the typical densities of the overall gas. This distribution of the SN ambient densities for the `noPI_SN` and `noPI_01SN` are both very similar regardless of the SN energy injected. Comparing the SN distributions with and without PI, for the `noPI_SN` and `noPI_01SN` runs, there is no noticeable peak at 10^0 cm^{-3} as in the `PI_SN` case. Instead, the SNe that would have exploded in this peak are instead at the higher densities up to $n_{\rm gas} > 10^4$ cm^{-3}. PI is the process which regulates the densities above 10^1 cm^{-3}. For the volume-weighted density

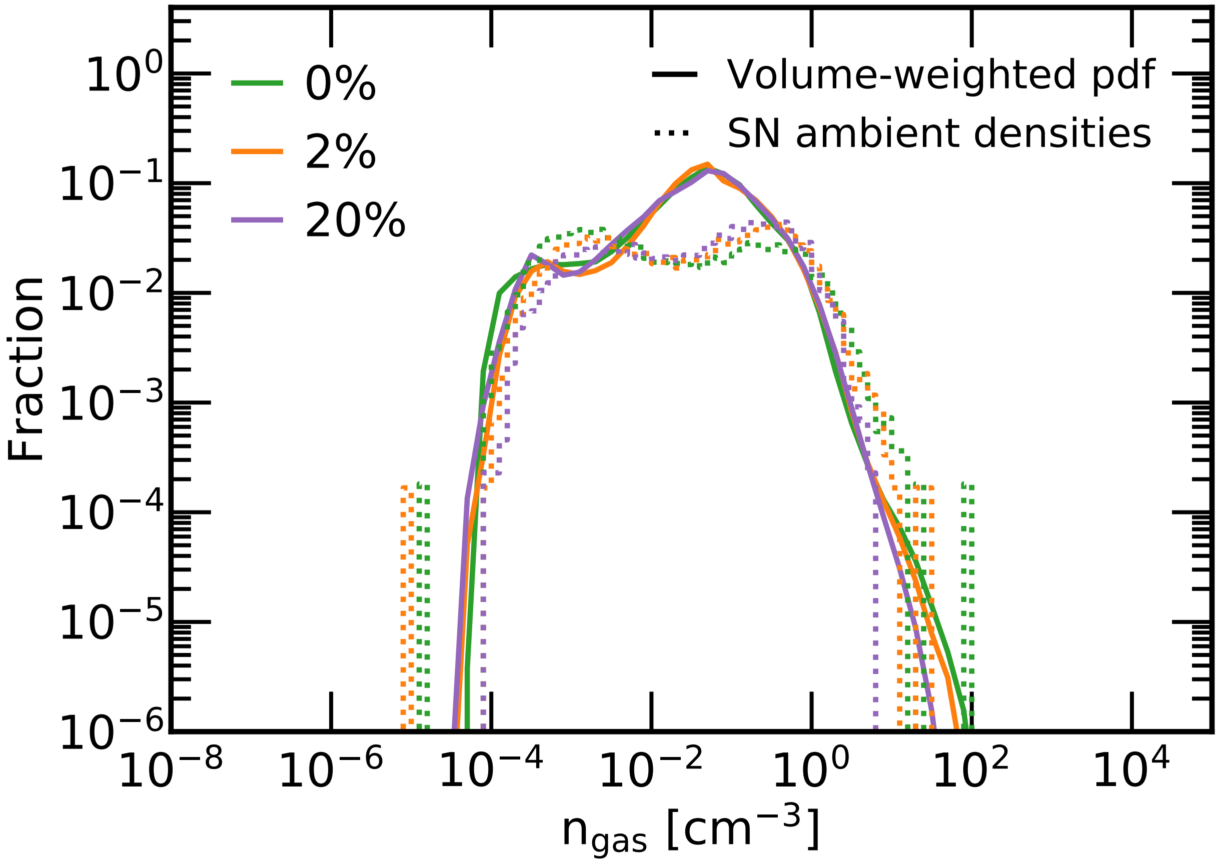

Figure 5.15: Volume-weighted densities (solid lines) and SN ambient densities (dotted lines) for each of the simulations (PI_SN_0%, PI_SN and PI_SN_20%) with the varied ϵ_{ff}. The galaxy is binned in space in bins of (50 pc)^3 for the region of extent 3 kpc $\times$ 3 kpc in the x-y plane and 1 kpc in the z-direction. The total kernel-weighted mass in each spatial region is summed and divided by the volume of the region. Dividing by the total number of bins then allows us to plot the fraction of bins in each density range. For the SN ambient density distributions, we histogram the number of SNe at each ambient density and divide by the number of SNe. This allows us to compare normalised distributions of volume-weighted densities and SNe in order to compare their distributions. The distributions of both the volume-weighed densities and SN ambient densities are very similar between all simulations, with only some subtle differences. All models here include PI and SNe, and as long as these processes are including the density distributions are fairly regulated, regardless of the clustering properties of the stars.

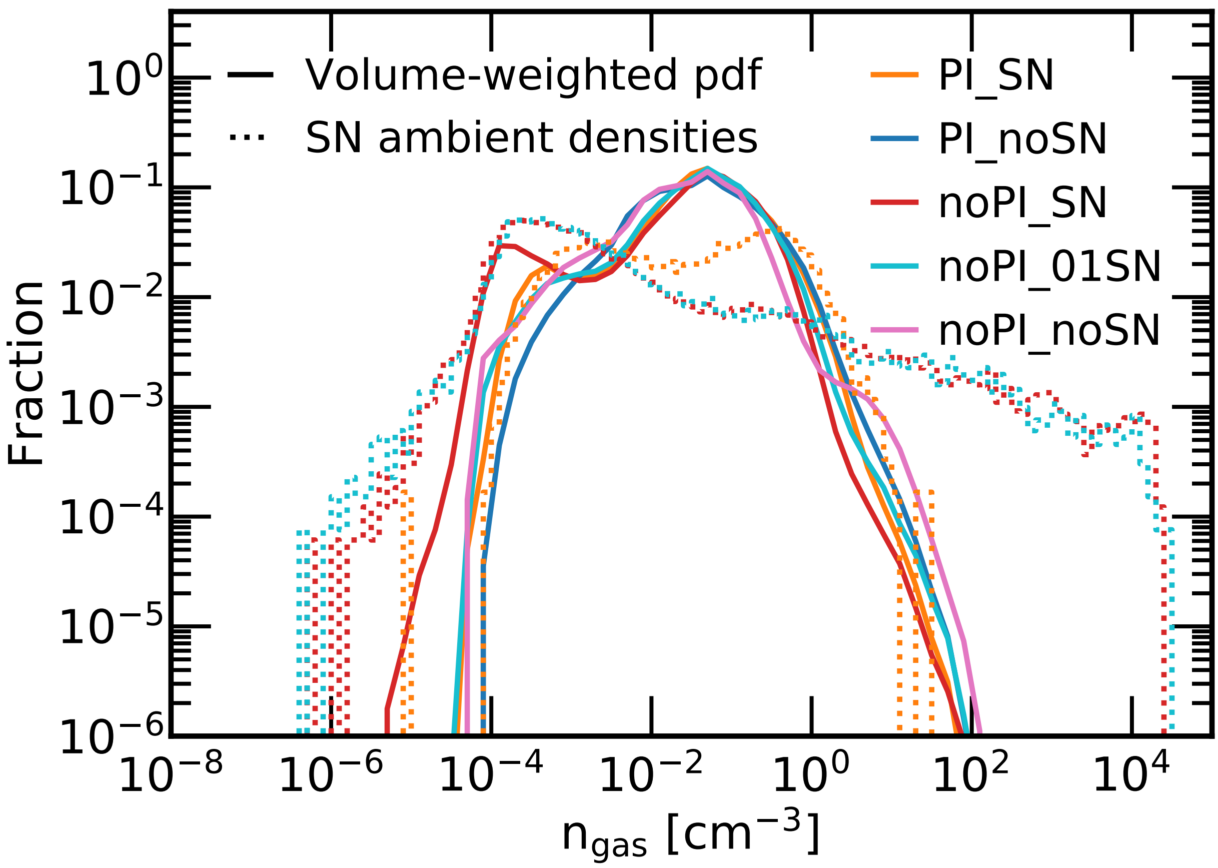

Figure 5.16: Volume-weighted densities (solid lines) and SN ambient densities (dotted lines) as in Fig. 5.15, but this time for the different simulations with different feedback. We show all of the volume-weighted densities but of course we can only show the SN density distributions for the simulations that include SNe. Nonetheless we include the volume-weighted densities for all of the feedback runs for comparison. The density distributions are all very similar at high densities, but with some distinct differences at densities below $\sim 10^{-2}$ cm^{-3}. The effect of excluding PI can be seen when comparing the SN distributions, where the SN densities extend to densities exceeding 10^{4} cm^{-3} for the `noPI_SN` and `noPI_01SN` runs when excluding PI.

distributions, at the higher densities ($> 10^{-2}$ cm^{-3}) the distributions are quite similar for all runs. The runs without SNe lack the low density peak. For the `noPI_SN` run, the densities extend to lower densities by around an order of magnitude, as well as a peak at a lower density of $\sim 10^{-4}$ cm^{-3}. In this simulation, the lack of PI results in a high number of clustered SNe which are able to drive large, low density bubbles for many future SNe to explode in, enhancing the lower density end of the distribution.

5.6 Properties of outflows

We have already seen that the different feedback models are able to produce very different star formation and outflow properties in Sec. 5.3. Enhancing outflows has often be attributed to the fact that the different feedback models produce different stellar clustering properties. We therefore test this hypothesis by discussing in more depth the outflow properties for all of the different feedback combinations presented as well as the different clustering. This will allow us to identify if it is the stellar clustering, or if this is a property set by the feedback included.

5.6.1 Mass, Energy & Momentum loading

We describe the way in which the mass, energy and momentum loading are defined, in agreement with Fielding and Bryan (2022) and Steinwandel et al. (2022a). All outflow rates are measured at a certain height above the disk, where we identify particles below this height, and calculate if in a time dt, its position will be above this height. The conditions therefore to identify these particles are that:

$$|\mathbf{z}_i| < H, \tag{5.5}$$

where $\mathbf{z}_i$ is the ith particle's positional z-vector and H is the height at which we wish to measure the outflows, and

$$|\mathbf{z}_i + (\mathbf{v}_{z,i} \cdot \mathrm{d}t)| > H, \tag{5.6}$$

where $\mathbf{v}_{z,i}$ is the ith particle's velocity in the z-direction and dt is the time in which we measure the outflow rates (we use 10 Myr). Output timesteps in our simulations are 1 Myr. Their product is therefore simply the incremental chance in the velocity in the z-direction in a time dt. By taking the magnitude of the positions in these conditions, we consider outflows both above and below the disk.

The outflow rates are therefore calculated for mass as

$$\dot{M}_{\mathrm{outflow}} = \sum_j m_j / \mathrm{d}t, \tag{5.7}$$

for energy as

$$\dot{E}_{\mathrm{outflow}} = \sum_j (m_j v_j^2) / \mathrm{d}t, \tag{5.8}$$

and for momentum as

$$\dot{p}_{\mathrm{outflow}} = \sum_j (m_j v_j) / \mathrm{d}t, \tag{5.9}$$

where j denotes particles that satisfy the conditions outlined in eq. 5.5 and eq. 5.6, m_j is the mass of these particles and v_j is their velocity. It should be noted here that the energy outflow rate is only considering the kinetic energy, and not the internal energy nor the ionisation energy transferred to particles from stellar feedback.

The mass, energy and momentum loading are thus calculated as follows:

$$\text{Mass loading} : \eta_{\mathrm{M}} = \dot{M}_{\mathrm{out}}/\overline{\mathrm{SFR}}, \tag{5.10}$$

$$\text{Energy loading} : \eta_{\mathrm{E}} = \dot{E}_{\mathrm{out}}/(E_{\mathrm{SN}}\dot{N}_{\mathrm{SN}}), \tag{5.11}$$

$$\text{Momentum loading} : \eta_{\mathrm{p}} = \dot{p}_{\mathrm{out}}/(p_{\mathrm{SN}}\dot{N}_{\mathrm{SN}}), \tag{5.12}$$

where $E_{\mathrm{SN}} = 10^{51}$ erg is the canonical supernova energy (except noPI_01SN where $E_{\mathrm{SN}} = 10^{50}$ erg), $p_{\mathrm{SN}} = 1 \times 10^5$ $\mathrm{M}_{\odot}$ km/s ($p_{\mathrm{SN}} = 3 \times 10^4$ $\mathrm{M}_{\odot}$ km/s for noPI_01SN) derived from the canonical SN energy and the average SN progenitor mass, and the rate of supernovae is $\dot{N}_{\mathrm{SN}} = \overline{\mathrm{SFR}}/(100\mathrm{M}_{\odot})$ using the assumption that the rate of SNe being produced is 1 per cent of the current SFR.

The mass, energy and momentum loading are shown in Fig. 5.17. We show these now at two different heights above and below the disk, 2 kpc and 10 kpc. We already saw the mass loadings in Sec. 5.3, but now we can examine how this evolves with height. For all of the runs including PI and SNe (PI_SN_0%, PI_SN and PI_SN_20%), the mass loading is very similar between all three runs at 2 kpc, reaching $\eta_M \sim 10$ at 100 Myr and declining slightly to $\eta_M \sim 3$ by 200 Myr. This is sustained at 10 kpc above and below the disk as well, once the outflows have reached this height at around 100 Myr, the mass loading stays constant at $\eta_M \sim 3$. There is perhaps a very small trend with ϵ_{ff}, such that there is a spread in the mass loading of ± 1 or so, with the lowest ϵ_{ff} (PI_SN_0%) having the higher mass loading, but the trend is very negligible. Somewhat surprisingly, the mass loading at both 2 kpc and 10 kpc for the noPI_SN run is very similar to the corresponding PI_SN run that does include PI. We know that the noPI_SN run has enhanced outflows, but it also has an increased number of stars and number of SNe, and so the mass loadings are very similar. This suggests that not including PI does not actually enhance outflows inherently, but just results in an enhanced SFR and SN rate. The noPI_noSN run has a higher SFR than PI_noSN, resulting in a lower mass loading. At 10 kpc above the disk, the story is the same, with a very weak initial mass loading which decreases steadily due to no SNe to continue driving outflows. For the noPI_01SN run, the outflow rates were lower than the noPI_SN run, but the SFR was higher, resulting in a mass loading around an order of magnitude lower than noPI_SNat both 2 kpc and 10 kpc.

The energy loading allows us to understand the impact of the SNe by quantifying the kinetic energy carried away in the outflowing material as a fraction of the energy injected by SNe. We already compared the energy injected by the SNe in Sec. 5.4.3, and found that for the different feedback runs, the energy injected by the noPI_SN run was approximately 5 times more than that of the PI_SN and noPI_01SN runs, which had similar total energy injections. Comparing the average energy loading (calculated from 100 Myr onwards once values have settled), at 2 kpc, PI_SN has an average of 0.11, noPI_01SN of 0.23 and noPI_SN of 0.26. Despite the equal overall energy injection by the PI_SN and noPI_01SN models, the noPI_01SN has double the energy loading, with values very close to that of the noPI_SN run which injected 5 times more energy. This is not sustained so much up to 10 kpc however, where the average energy loading (again calculated from 100 Myr onwards) is 0.27 for `PI_SN`, 0.46 for `noPI_01SN` and 0.93 for `noPI_SN`. Between the different $\epsilon_{\rm ff}$ models, we again see a very small trend with $\epsilon_{\rm ff}$, with the `PI_SN_0%` run having higher energy loading than the `PI_SN_20%` run by a factor of ~2 at 2 kpc and a factor of 3 at 10 kpc.

Finally we can compare the momentum loading, which quantifies the momentum of the outflowing gas in comparison to the momentum injected by the SNe. Between the different $\epsilon_{\rm ff}$ runs, there is relatively little different at 2 kpc, with the averages (Time > 100 Myr) all around 0.5. At 10 kpc however there is again a slight trend. Increasing $\epsilon_{\rm ff}$ takes the average momentum loading from 0.98 to 0.80 to 0.46 for the `PI_SN_0%`, `PI_SN` and `PI_SN_20%` runs, respectively. The lowering in clustering appears to result in slightly lower mass, energy and momentum loading at large heights (10 kpc), whilst making relatively little difference at lower heights (2 kpc). Comparing the runs with different feedback, again, we can ignore the `PI_noSN` and `noPI_noSN` runs, as any outflowing gas at 2 kpc or 10 kpc is simply left over from turbulent driving and not relevant the current state of the disk. For the runs with SNe, again comparing the `PI_SN`, `noPI_SN` and `noPI_01SN`, at 2 kpc, the `PI_SN` and `noPI_SN` have similar averages of 0.59 and 0.68 respectively, but the `noPI_01SN` has around half at only 0.3. This is then continued at 10 kpc, where the `noPI_SN` has a visibly much higher overall momentum loading of 1.45 in comparison to `PI_SN` which has 0.80 and `noPI_01SN` which has 0.45.

The `noPI_SN` run produces more than three times the energy loading and nearly double the momentum loading in the outflows at 10 kpc in comparison to the fiducial `PI_SN` which does include PI. Whilst there appears to be a small trend with $\epsilon_{\rm ff}$, such that higher clustering results in higher mass, energy and momentum loading at both 2 kpc and 10 kpc, the impact is much smaller than that of the feedback used.

5.6.2 Height evolution of outflow phases

Having looked at the outflows, and their components of mass, energy and momentum, we also look at the outflows in terms of their gas temperature (summarised in Table 5.2), shown in Fig. 5.18. For each gas phase we show the average outflow rates through two planes parallel to our galactic disc sitting ± 200pc, 2kpc and 10 kpc above and below the galaxy's mid-plane. 200 pc represents the region just at the edge of the ISM, therefore giving some idea of the typical gas phases present in the plane of the disk. We again compare the different $\epsilon_{\rm ff}$ runs which control the clustering, as well as the different feedbacks.

For the $\epsilon_{\rm ff}$ runs, we see that for cold, warm, warm-hot and hot gas, there is a trend with $\epsilon_{\rm ff}$, thus there is a trend with the clustering. At the plane of the disk, all values for the 'outflows' (in practice, this captures more the phases at the edge of the ISM rather than an outflow rate) are very similar, with `PI_SN_0%`, `PI_SN` and `PI_SN_20%` having values of 0.08, 0.07 and 0.08 $M_\odot$/yr for cold gas, 0.15, 0.13 and 0.15 $M_\odot$/yr for warm gas, 0.0009 $M_\odot$/yr for all runs for warm-hot gas, and 0.0007 $M_\odot$/yr for all runs for hot gas.

At 2 kpc and 10 kpc however, in all gas phases, the `PI_SN_0%` run has higher outflow rates than `PI_SN`, which has higher outflow rates than `PI_SN_20%`. For the cold gas, the outflows for the `PI_SN_0%` run at 10 kpc are double that of the `PI_SN_20%` run. For the hot gas, the

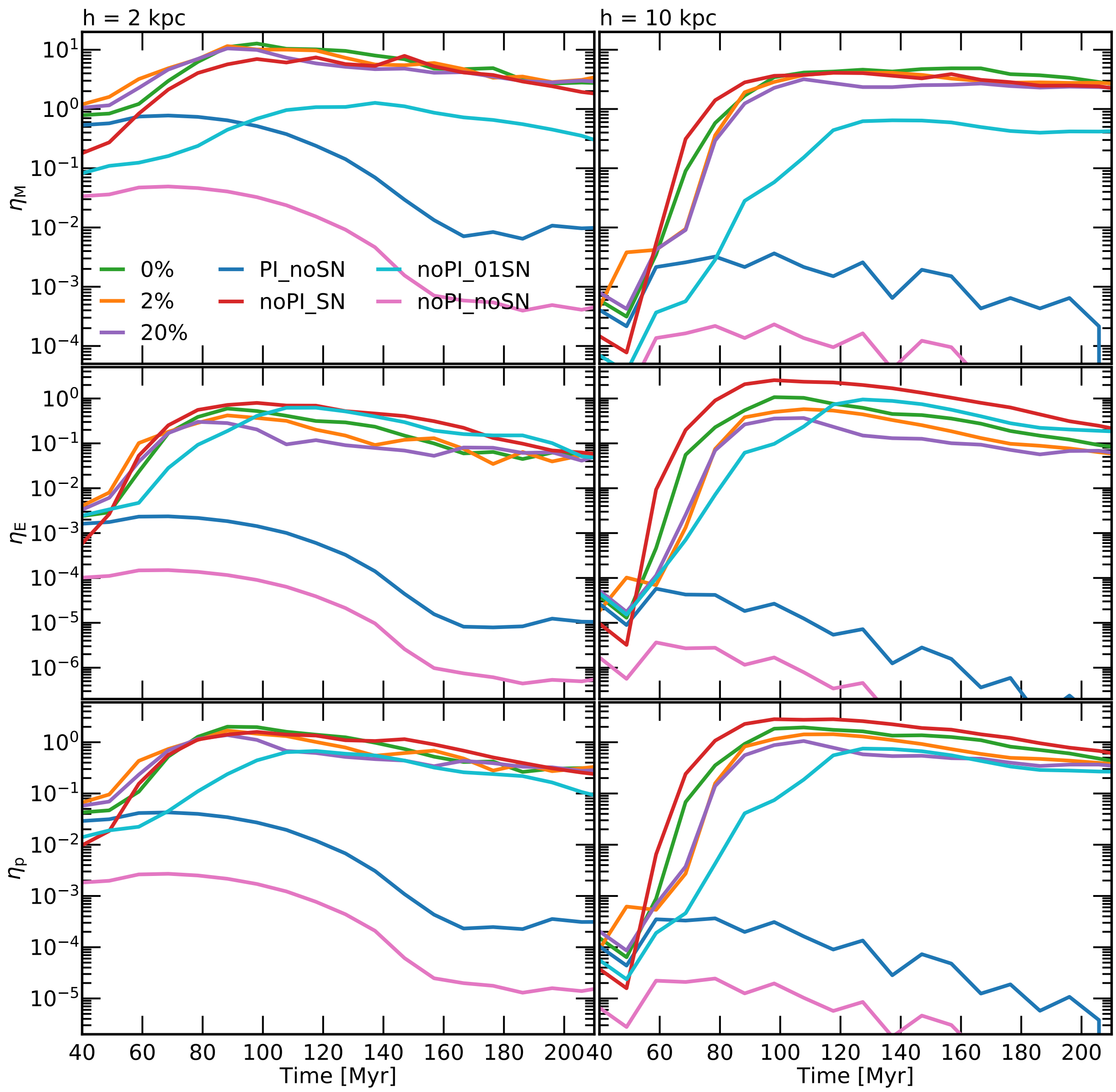

Figure 5.17: Mass, Energy and Momentum loading measured at 2 kpc and 10 kpc above and below the disk for all of the simulations. We show the different star formation efficiency simulations (`PI_SN_0%`, `PI_SN` and `PI_SN_20%`) as well as the simulations with the different feedback combinations. *Top row*: The mass loading, as already shown in Fig. 5.2 and Fig. 5.3 now shown different heights above the disk in order to show the evolution with the height above the disk. *Middle row*: The energy loading again showed for the different heights above the disk. *Bottom row*: The momentum loading. Each of these quantities is calculated as described in Sec. 5.6.1.

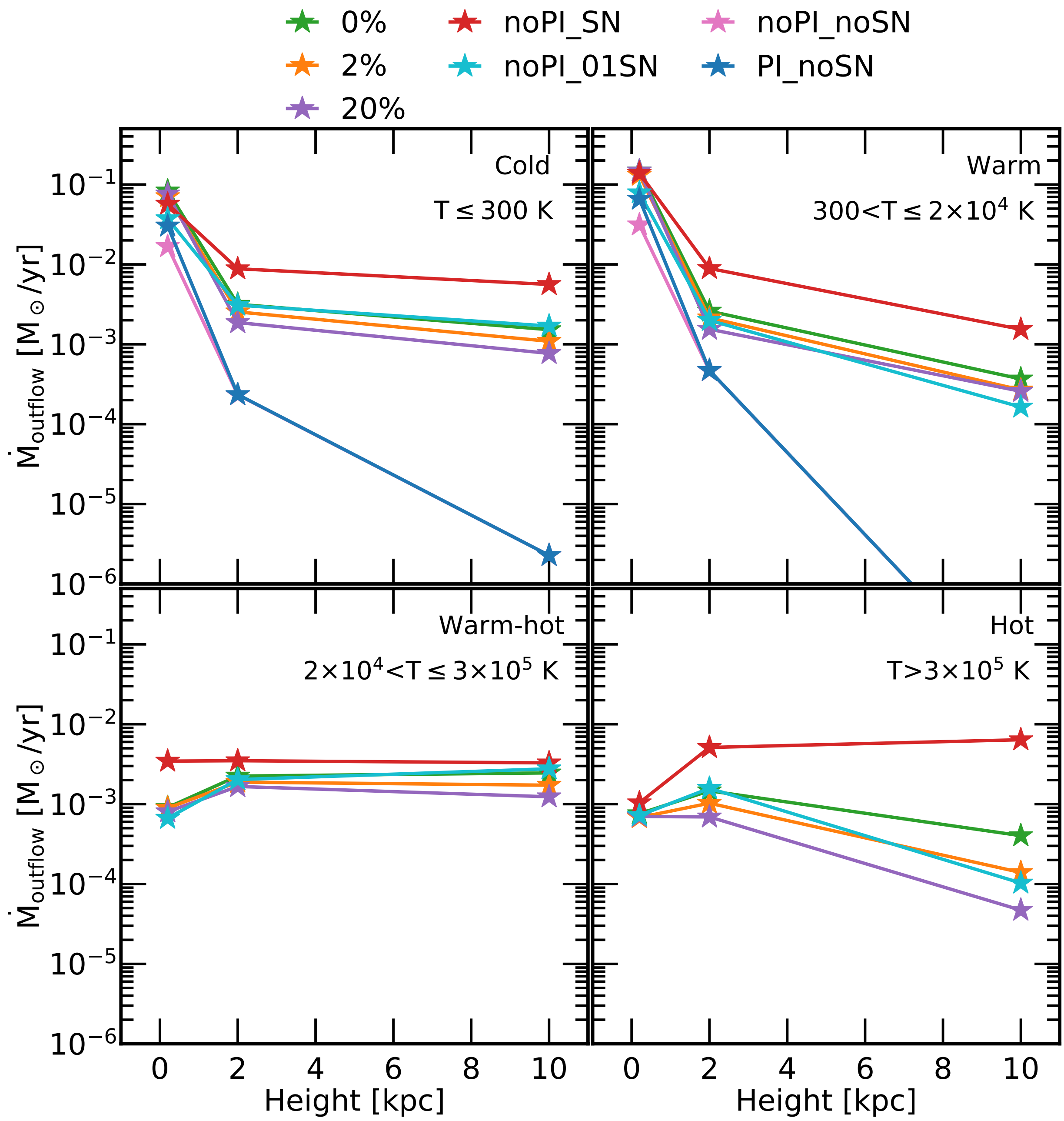

Figure 5.18: Average outflow rates between 200-500 Myr at 200 pc, 2 kpc and 10 kpc above and below the plane of the disk for the cold, warm, warm-hot and hot phases of the gas. We show the average property in this case as the outflow rates between stay roughly constant between 200-500 Myr.

outflows are a factor of >8 times greater for the PI_SN_0% run in comparison to PI_SN_20%. Enhanced clustering results in enhanced outflows, and this effect is increased as we increase in gas temperature. This is because more clustered SNe mean more SNe exploding in previous SN bubbles driving larger cavities and more hot outflows.

To compare the different feedback runs, we keep the PI_noSN and noPI_noSN runs in for completeness, but see that they drop off substantially at 2 kpc and 10 kpc for the cold and warm phases, and are not present at all as there is no presence of any gas above 2×10^4 K in these runs. Within the ISM (±200 pc), the runs including PI and SNe have the highest outflows of cold gas, followed by noPI_SN, PI_noSN, then noPI_noSN. It becomes less straightforward here to compare the ISM, as we saw in the z-projection gas distributions in Fig. 5.5, the run with no feedback (noPI_noSN) produces an extremely thin gas and stellar disk, meaning that the scale of the ISM in each of these runs is not the same. So long as one remembers that this is a caveat, we can still examine the typical ISM phases.

Comparing the phases of the outflows above 2 kpc, we primarily contrast the PI_SN, noPI_SN and noPI_01SN runs for the reasons described before. For all gas phases, the noPI_SN run has higher outflow rates, with the effect being increased with gas temperature. At 2 kpc, the outflow rates for the noPI_SN run in comparison to the PI_SN are increased by a factor 4 for warm gas, 3 for warm-hot gas and 5 for hot gas. At 10 kpc, this factor is 5 for warm gas, 2 for warm gas and 46 for hot gas. Remembering that the total amount of energy injected by the PI_SN and noPI_01SN runs was very similar (see Sec. 5.4.3), the mass outflows for the noPI_01SN run at 10 kpc for the hot gas is actually slightly less than the PI_SN. Disentangling this is an interesting topic in understanding how energy and momentum are injected into the gas, and moreover what that energy then translates to in terms of the temperature of the gas and how sustained the outflows are over time and space. For example, looking at the hot outflows for the noPI_01SN run again, at 2 kpc, it produces higher outflow rates than the PI_SN run, but these outflow rates are not sustained up to 10 kpc. The lower SN energy results in not being able to drive the same large hot bubbles to such heights above the disk.

5.6.3 Radial outflow trends

Another way we can distinguish the effect of feedback on the outflows is to look at the outflow rates and the SN rates as a function of radius. On the outer parts of the disk, the potential is more shallow and so outflows should in principle be easier to drive from these regions, should the SNe explode there. To explore this we show the outflow rate as a function of radius for the fiducial 2 per cent model with the different feedback prescriptions.

Fig. 5.19 shows the radial outflow rates and the number of SN in order to explore if we can see firstly a radial trend but also to see if there is a visual correlation between the outflow rates and the number of SNe, which we expect to be the main drivers of outflows. On the outskirts of the disk, the potential is more shallow, meaning SNe exploding in this area, irrespective of the ambient densities, will be more effective in driving outflows. Looking at the radial distributions of the outflows, if we compare the PI_SN and noPI_noSN runs, at all radii the outflow rates are very similar. There is a slight enhancement by a factor of ~ 2 between around 0.5 and 1.25 kpc. Comparing then PI_SN with noPI_SN, the outflow rates from noPI_SN are very enhanced.

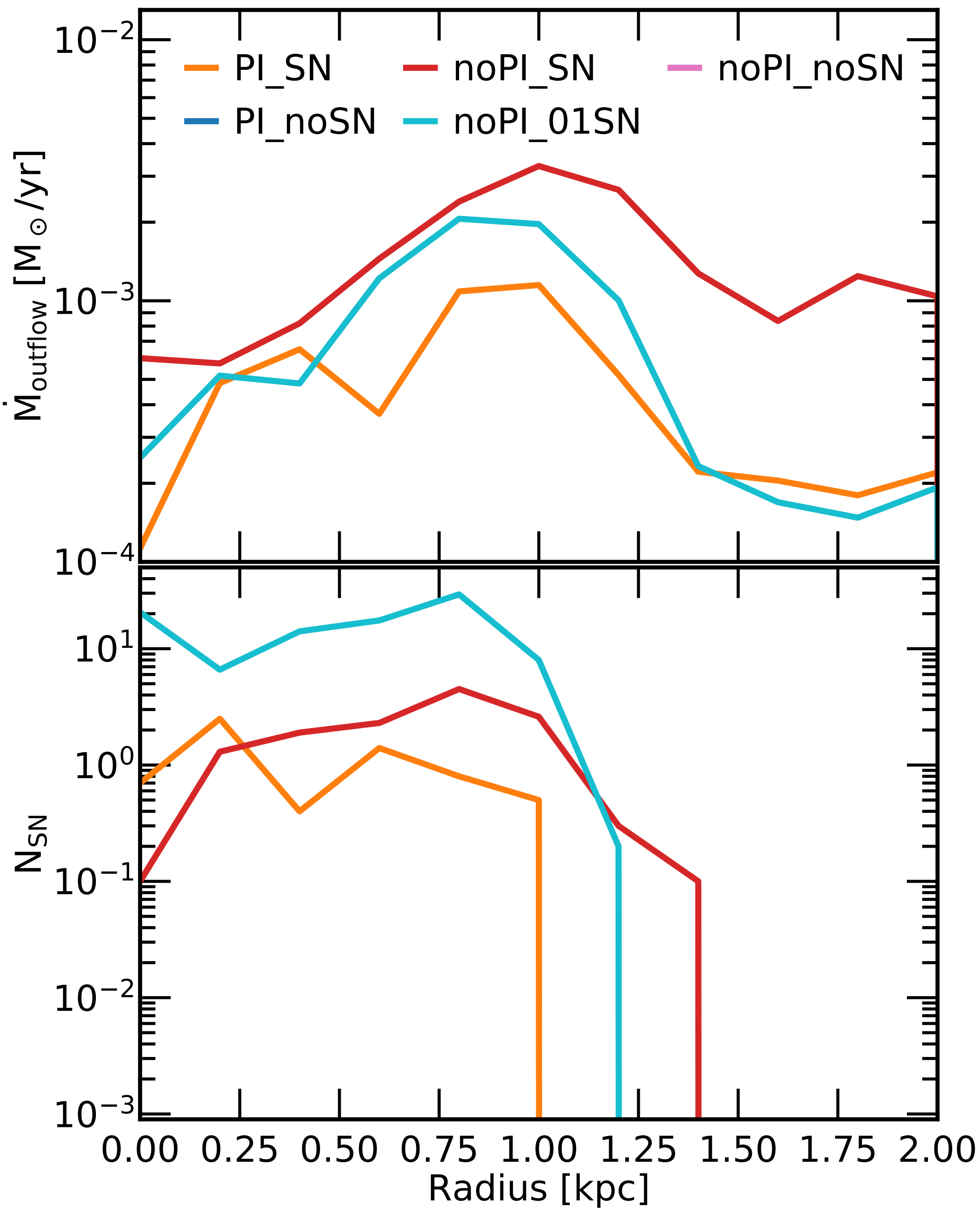

Figure 5.19: *Top panel:* The outflow rates measured at 1 kpc above and below the disk as a function of radius from the centre of the galaxy for the runs with a $\epsilon_{\rm ff}$ of 2 per cent but with the different feedback combinations. The radius is measured out to 2 kpc in 200 pc bins. *Bottom panel:* The radial distribution of the SNe for the runs with SNe included. Both the outflows and the SNe here are shown at 200 Myr in the simulation. The SNe shown are explosions between 150 and 160 Myr, then normalised by dividing by 10 to show a SN number distribution for 1 Myr in the simulation.

This is measured at 200 Myr, and so the outflows are somewhat left over from the enhanced SFR previously. After ~150 Myr is when the SFR becomes similar between these two runs.

Despite the many more SNe seen in the `noPI_01SN` run in comparison to the `PI_SN` run, we know that the overall amount of energy injected by the SNe is roughly the same in the two models (see Sec. 5.4.3). The outflow rates reflect this, where the outflow rates are very similar at all radii. We can now link the radial outflow profiles to the radial profiles of the SNe. We show here the outflows and the number of SN at the same time in the simulation, but one must remember that the current outflows are driven by SNe some Myr ago (exactly how long ago will depend on the ambient densities at which they explode). Nevertheless, at all times, the distributions of the outflows and SNe are quite similar, therefore we just show for this particular simulation time but assume that the distributions are related. In the central 1 kpc, there are roughly a factor of 10 more SNe in the `noPI_01SN` in comparison to the `PI_SN` run, but with a SN energy a factor of 10 lower, the energy injected within the central kpc is the same, reflected in the similar outflows. The outflow rates are not identical however, owing to the different heights at which the SN explode in Sec. 5.6.4.

5.6.4 Height of SNe

We can also look at the height distribution of the SNe in each of the simulations, shown in Fig. 5.20. Most of the SNe explode within the 180 pc above and below the disk, but without PI, the `noPI_SN` and the `noPI_01SN` runs both show a broader distribution of SNe out to 250 pc above and below the disk. The normalisation of SNe in the plane of the disk between the `PI_SN` and `noPI_SN` runs is very similar, and the additional number of SNe present in `noPI_SN` are just distributed at higher and lower heights. The extended distribution of SNe to increased heights above the disk can also be seen when looking back to the z-distribution of the stars in Fig. 5.4. The further away from the centre you are, whether in radius or height from the disk, the potential is decreased. SNe therefore, separately from the ambient density of the gas (although this does correlate with the radius and height) are more effective in driving outflows as the gas is able to escape from the disk more easily. The height distribution of the SNe is therefore important to consider. For a typical FoF group (seen in Fig. 5.8) with a fixed number of SNe exploding in this SN ambient density distribution, it would be interesting to quantify and understand the outflows this cluster is able to drive. Particularly, to quantify how the outflow properties would change dependent on the cluster position and height from the plane of the disk. This is not something we can pin down in this study, but would be the topic of future work in order to understand really how clustering contributes to the outflows.

5.7 Discussion

5.7.1 The role of photoionisation

PI works to regulate the ambient densities of the ISM, particularly at high densities around star formation. By the time that SNe explode, the gas densities at which the stars formed ($>10^2$

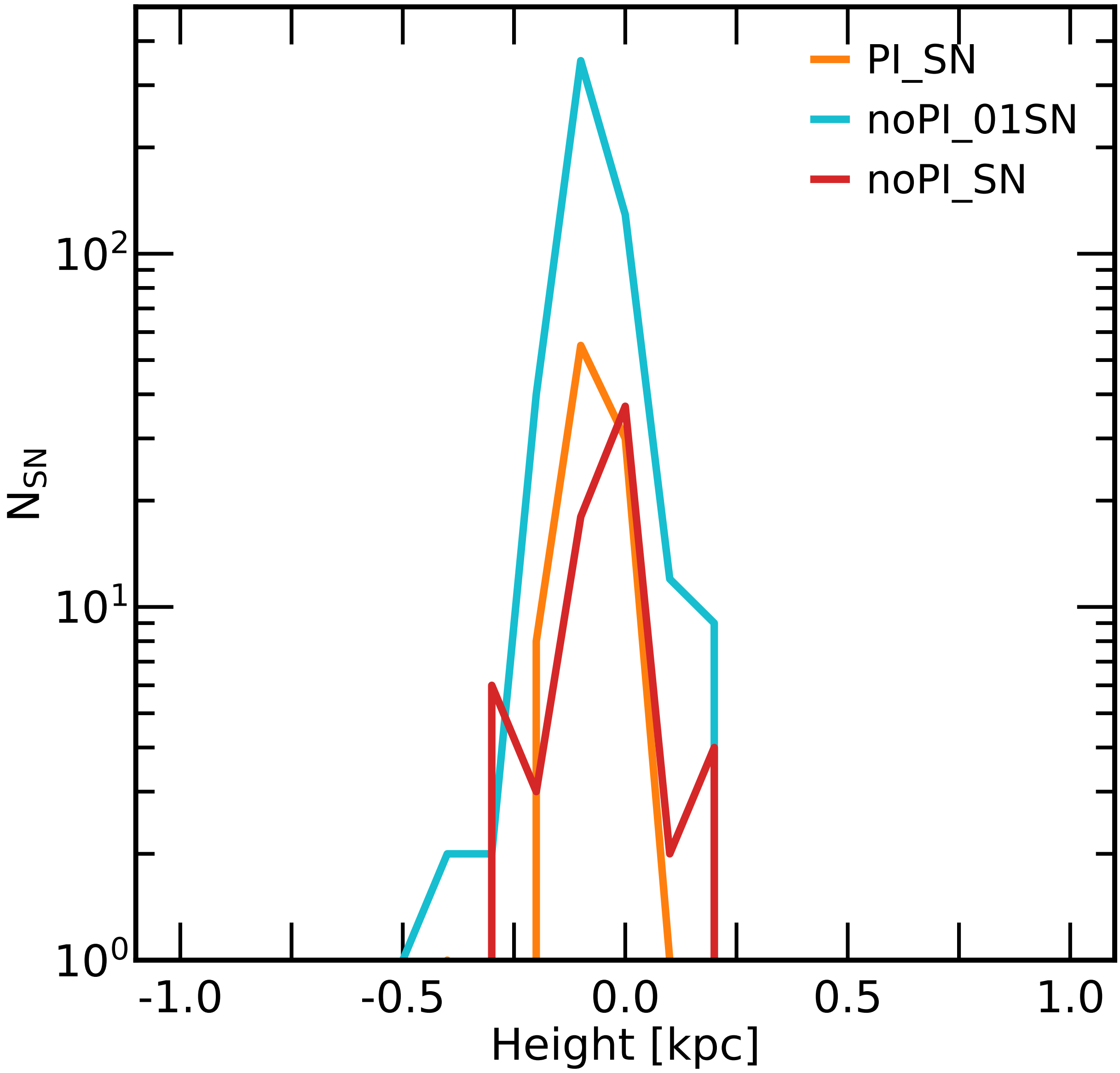

Figure 5.20: The height distribution of SNe in the different feedback runs that include SN feedback measured over a 10 Myr timeframe between 190 and 200 Myr in the simulation. Comparing the run with PI (`PI_SN`) with the runs excluding PI (`noPI_SN` and `noPI_01SN`), one can notice a slight broadening in the distribution of SNe explosions, with SNe exploding further above and below the disk when excluding PI. The normalisation over a 10 Myr period is similar for the `PI_SN` and `noPI_SN` runs, but a distinct increase in SNe can be seen for the `noPI_01SN` run.

cm^{-3} at least) have been reduced significantly, as seen in the SN ambient densities in Fig. 5.6. It can be seen from the comparison of SN ambient densities with different feedbacks in Fig. 5.7 that without PI, there is a substantial tail of SNe up to densities significantly overlapping with the ambient densities of star formation. Dale et al. (2012, 2014) investigate the impact of PI in hydrodynamical simulations of massive star clusters (10^4-10^6 $M_\odot$) by exploring the dynamical effects of the ionising feedback on the star forming cloud. They find that the most massive clouds are mostly dynamically unaffected, but that this feedback has a profound effect on the lower density 10^4 and 10^5 $M_\odot$ clouds, creating large bubbles and expelling tens of per cent of the neutral gas within 3 Myr, before the first SNe. It is not consistent between all of the studies, but some studies (e.g. Haid et al., 2019) find that PI is effective in reducing the overall star formation efficiency, and strongly advocate for the inclusion of PI in order to explain the low-observed star formation efficiencies in molecular clouds. Walch and Naab (2015) study the impact of single SN explosions on isolated dense gas clouds that have either been pre-ionised or not, and find that if the cloud has been ionised, the SN shock moves faster and the momentum input is increased by a factor of ~50 perc cent. Ali et al. (2022) explored the effect of PI in simulations of a section of a spiral arm in a Milky Way-type galaxy and found that PI is the dominant feedback mechanism that disrupts the spiral arm section, while stellar winds play a negligible role. It is worth noting that these simulations also use sink-based star formation prescription, showing that this effect is seen also using different star formation recipes. They find that including PI acts to breakup the large-scale gas structure and injects energy into the ISM, resulting in more clouds, increasing the number of low-mass clusters and reducing the number of high-mass, a result also found by Rathjen et al. (2021). Many simulations neglect PI (e.g. Gatto et al., 2017; Andersson et al., 2020), meaning the tails of the ambient densities of SNe extends much higher. In the absence of PI, we have shown that SNe are effective also in regulating the densities of the ISM above $\sim 10^0$ cm^{-3}, however they do so in a much more aggressive way than PI which can have a strong effect on cluster formation. This should be careful considered in studies of cluster formation neglecting PI.

5.7.2 What about stellar winds?

We have addressed feedback and its effects on the properties of the clustering and outflows, but by ‘feedback’ we have only examined the simulations in the absence of SNe and PI. Stellar winds are of course another component of stellar feedback, which is always included in our models but we have not tested the effects of neglecting them in the same way we have done with PI and SNe. Ali et al. (2022) also explored the effect of stellar winds and found that they did not affect the SFR or star formation efficiency, but did affect somewhat the distribution of mass in their sink-based star formation and drive small-scale cavities (~10-30 pc). In slight contrast, Gatto et al. (2017) found that stellar winds did decrease the star formation efficiency and SFR, resulting in more low-mass clusters over timescales of 10s of Myr in simulations of a vertical slice of a Milky Way-type disk where they test the contribution of stellar winds and SNe. However, it is worth considering that the impact of stellar winds can be exaggerated in the absence of PI, as Geen et al. (2021) show that the effect of stellar winds decreases when PI is included.

5.7.3 The Strömgren-sphere approximation

As discussed in Sec. 5.2.2, our simulations employ a Strömgren (1939)-sphere approximation for PI. This is also the approach in many other similar simulations (e.g. Hopkins et al., 2011; Hu et al., 2016, 2017; Keller et al., 2022) due to the computational expense of including full radiative transfer at these resolutions. Other studies inject some form of energy or momentum localised to the region immediately around a star particle (e.g. Agertz et al., 2013; Ceverino et al., 2014; Roškar et al., 2014; Forbes et al., 2016). Emerick et al. (2018) discuss how even though some of these methods do account for the long-range effects of diffuse radiation (Hopkins et al., 2012, 2018), most cases only consider the local effects of radiation, thus neglecting any effects of ionisation beyond the particles surrounding the ionisation source. Simulations that do include stellar radiation through radiative transfer or radiative-hydrodynamics schemes find it to be effective in regulating star formation and driving galactic winds (e.g. Wise et al., 2012; Kim et al., 2013; Sales et al., 2014; O'Shea et al., 2015; Pawlik et al., 2015; Rosdahl et al., 2015; Ocvirk et al., 2016; Peters et al., 2017; Geen et al., 2021). But this is what we also find in our simulations using the Strömgren (1939)-sphere approximation, and so one can ask how well this approximation captures this process, both on large and small scales. Emerick et al. (2018) test the importance of following stellar ionising radiation with an adaptive ray-tracing radiative transfer method on regulating star formation and driving outflows, by comparing the full-range radiation with only short-range radiation (as well as no radiation feedback). They find that local stellar radiation feedback (limited to 20 pc around each star particles) is effective in regulating star formation on short timescales by destroying cold, dense gas around young, hot stars, but is not sufficient to drive galactic outflows in isolated, low-mass galaxies.

5.8 Conclusions

Understanding how outflows are driven from galaxies and the relation to stellar clustering is an interesting topic, particularly on the scales of dwarf galaxies where the potential is more shallow. Recent studies have found that altering the feedback alters the clustering of the stars, which they accredit to enhanced or reduced outflows (e.g. Smith et al., 2021; Keller et al., 2022). We try to disentangle this argument to understand if it is a consequence of the clustering alone, or if it is an inherent consequence of the feedback. We address this topic by examining the SN properties, which are the main drivers of outflows, with the outflows properties themselves. We compare 7 simulations in total, 3 of which have the fiducial feedback implementation (PI and SNe) but vary the $\epsilon_{\rm ff}$ parameter, which is a very effective way of significantly changing the clustering properties of the stars without changing the global properties (see Chapter 3). The other 4 simulations vary in the feedback used, excluding PI, SNe or both, as well as reducing the SN energy by an order of magnitude.

We summarise our results by comparing the effect of varying the clustering (by changing $\epsilon_{\rm ff}$) and varying the feedback on the overall global properties, SN clustering, ISM properties and outflow properties.

Global properties (Sec. 5.3):

- Changing the clustering of the stars by varying $\epsilon_{\rm ff}$ results in very similar SFRs, as shown in Fig. 5.2. The outflow rates are slightly enhanced when the stars are more clustered.

- The simulations including PI have the lowest SFRs, settling at $\sim 10^{-3}$ $M_\odot$/yr. SNe alone manage to regulate star formation in our simulations. This, however, takes longer ($\sim$ 100 Myr) in comparison with the simulations including PI. The simulation without PI and without SNe has the highest SFR of $\sim 3 \times 10^{-2}$ $M_\odot$/yr, as seen in Fig. 5.3.

- The stellar and gas surface density distributions (Fig. 5.4 and Fig. 5.5) are highly impacted by the feedback used. Without SNe, the stellar and gas disks are very thin, with no extension at all in the z-direction, as well as being more compact in the x-y distribution. PI helps to puff out the disk and prevent the very large clumps seen in the `noPI_noSN` run. When excluding PI and including SNe only, there is very little definition left in the gas disk, and the z-projection shows the most outflows of all the models.

Clustering of the SNe (Sec. 5.4):

- For all $\epsilon_{\rm ff}$ runs, the SNe ambient densities are distributed into two peaks, at $\sim 10^0$ cm^{-3} and $\sim 10^{-3}$ cm^{-3}, shown in Fig. 5.6. Increasing the clustering of the stars increases the number of SNe in the lower density peak and decreases the number of SNe in the high density peak. More clustered stars gives more clustered SNe, meaning that more SNe explode in low density bubbles created by previous SNe.

- Excluding PI results in higher SFRs and thus more SNe. The shape of the distributions of the SN ambient densities are also very different to the runs with PI. Fig. 5.7 shows how the ambient densities of SNe exceed 10^4 cm^{-3}, due to the fact that PI has not pre-processed the ISM surrounding the star forming regions prior to the first SNe. The SNe explode at higher densities and are more numerous, are able to drive more and larger hot, low density bubbles than the runs with PI, shown by the fact that the majority of the SNe explode at densities $\sim 10^{-4}$ cm^{-3} for the `noPI_SN` run.

- We also look at the ambient density distribution of SNe in individual FoF groups in Fig. 5.8 and Fig. 5.9, and find that for all of the clusters in all of the simulations, there is a similar trend with the FoF group mass. All FoF groups, irrespective of mass, only have around 1 SN explosion at higher densities. All of the rest of the SNe explode in the lower density peak of the distribution, with this number increasing with the FoF group mass. This also adds to the explanation of why increased clustering results in more low-density SNe in comparison to runs with lower clustering.

ISM properties (Sec. 5.5):

- For the $\epsilon_{\rm ff}$ runs, the temperature and density structure of the gas disk do not show significant differences with the different clustering properties (Fig. 5.10). This is also reflected in the very similar phase diagrams (Fig. 5.11).

- The effect of the feedback is very clear in the gas temperature density maps (Fig. 5.10) and the phase diagrams (Fig. 5.11). Excluding PI but including SNe results in a more extended gas disk with relatively little cold structure and large low-density cavities. Including PI but excluding SNe results a less extended gas disk, with lots of cold gas structure, particularly around the perimeter of the disk. Excluding both PI and SNe results in a compact, highly structured disk of cold gas.

- Fig. 5.12 shows how increasing the clustering of stars increases the hot gas volume fraction and increases the cold gas mass fraction in the ISM.

- Without SNe, there is no gas volume or mass for gas above 2×10^4 K. When including SNe, turning off PI increases the volume filling fraction of hot gas by more than a factor of 2, as seen in Fig. 5.13.

- Changing the clustering of the stars does not alter the overall density distribution of the ISM or the SNe significantly. The feedback however has a strong effect. At high densities, the density distributions of the ISM are similar. The differences exist primarily at the lower densities. Excluding PI but including SNe results in an extension of the ISM to lower densities as very low density regions are generated by a large number of spatially correlated SNe. Without SNe, the lower density peak of the ISM ambient density mostly disappears, showing this density regime is almost solely regulated by SNe.

Outflow properties (Sec. 5.6):

- There is a subtle trend with $\epsilon_{\rm ff}$, where more clustering was able to drive more sustained outflows up to heights of 10 kpc, especially in the hot phase of the gas (Fig. 5.17 and Fig. 5.18). Simulations without SN feedback were not able to drive any outflows for any temperature of gas. The `noPI_SN` run drove the most outflows in all gas phases, especially the hot phase.

- Excluding PI but including SNe results in a higher number of SNe overall. These SNe extend to larger radii from the centre of the disk and subsequently higher outflow rates further away from the centre of the disk.

- The z-distribution of the SNe is extended to increased heights above the disk when excluding PI. These SNe therefore explode at typically lower densities than are found in the plane of the disk. Being further away from the centre of the disk, both in radius and in height allows SNe to drive more outflows with the same amount of energy as the ambient density is lower and the gravitational potential is more shallow.

The aim of this study was to disentangle the relevance of SN clustering, which has often been accredited to enhancing outflows, with the specific effects of different feedback prescriptions. Turning off photoionising feedback does increase clustering of stars and SNe, but it also dramatically changes the densities at which the SNe explode, as well as extending their radial and height distribution. We can then address the question: Do we see enhanced outflows because of SN clustering, or are the densities at which the SNe explode more important in dictating the outflow properties? For the dependence on clustering alone, outflows are enhanced with more clustered star formation, but by a very small amount. Clustering is not the (only) answer. Altering the feedback has a much more complicated role, as it changes the spatial distribution of SNe, as well as significantly impacting the overall density structure of the ISM, which in turn results in drastically different outflow properties.

"Sometimes I'll start a sentence and I don't even know where it's going, I just hope I find it along the way."

Michael Scott - The Office

6 Outlook

In this thesis, I have presented simulations of isolated dwarf galaxies, with a primary focus on understanding the physical processes dictating star cluster formation, as well as the impact of the clustering of stars on the evolution of the galaxy itself. I show now some preliminary results from simulations of dwarf minor mergers including an intermediate mass black hole (IMBH) in the centre of the most massive galaxy. These simulations involve the same simulation framework as described in Chapter 2, but with the inclusion of KETJU which allows the dynamics of the particles within small regions of the galaxy around a black hole to be integrated as collisional systems. We introduce this alteration to the model in more detail in Sec 6.1 and show some results. Sec. 6.2 then highlights some of the missing physics of these simulations, with suggestions of how this will alter the results and ideas for future implementations.

6.1 KETJU + GADGET

KETJU is an extension to the GADGET-3 code (Springel, 2005). Introduced in Rantala et al. (2017), and then modified in Rantala et al. (2019). It has been used extensively in cosmological simulations presented in Mannerkoski et al. (2019, 2021, 2022), it allows for the inclusion of algorithmically regularised regions around every black hole. The power of this is in resolving the dynamics of black holes, binary black holes and the surrounding stellar particles on subparsec scales at the same time as following global galactic-scale dynamical and astrophysical processes. This is demonstrated in Fig. 6.1, which shows an illustration of a 'KETJU region', where the central black hole is surrounded by regularised particles. The particles of interest, in our case this is stars, are identified using a user-input radius r_{KETJU} surrounding the black hole. In the original implementation from Rantala et al. (2017), these particles are then included as 'chain particles', and these along with the black hole form the chain subsystem. This only allowed for a

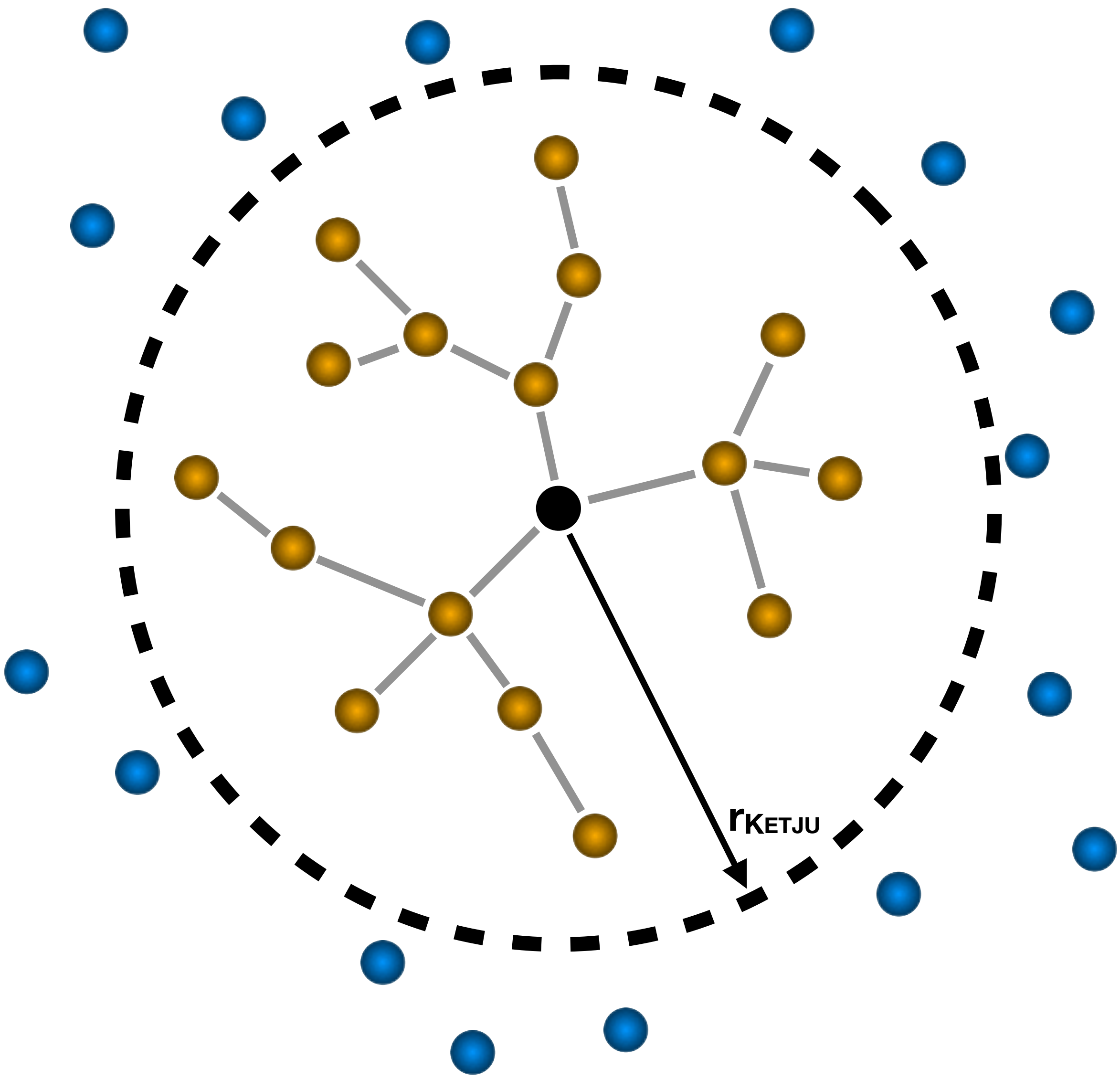

Figure 6.1: Illustration of the KETJU subsystem with a single black hole (black circle) in the centre, surrounded by ketju region particles (orange circles) and ordinary tree particles (blue circles). The particles within the ketju region are defined as particles within the radius r_{KETJU} shown by the black arrow. The grey lines linking together the particles within the KETJU region show the minimum spanning tree, as described in Rantala et al. (2019).

few hundred particles to be efficiently treated in the regularised chain regions. This motivated the implementation of a minimum spanning tree method allowing for much larger particle numbers in the region (see Rantala et al., 2019, for a more detailed explanation). Tree particles outside of r_{KETJU} are treated as usual by GADGET-3. The individual particles within the subsystem are no longer treated by the usual force calculations in GADGET-3. Instead, their common centre-of-mass is treated as a macro-particle and behaves as a usual collisionless particles within the simulation.

KETJU has a very convenient functionality in that the stellar softening within the KETJU regularised region can be turned on or off. With the stellar softening kept on, only the dynamics between the stars with the black hole are calculated directly, whilst the star-star interactions within the regularised region remain softened. With stellar softening off, the forces between all stars along with the black hole are all unsoftened, creating an N-body region embedded in a galactic context. Both setups can be extremely useful. Naturally keeping the softening on between the stars makes the calculations much less computationally expensive. The aim will be to use KETJU to approach two different problems.

The first would be to use it exactly as described above, which is to introduce a black hole in either isolated or minor merger simulations of dwarf galaxies, and to follow black hole evolution and its impact on the surrounding galaxy. This can naturally be done with the inclusion of a black hole without using KETJU at all, but where KETJU would come in would be looking into the formation of nuclear star clusters (NSCs) and the co-evolution of NSCs with central black holes. This is thought to be a common occurance (e.g. Graham and Spitler, 2009; Reines et al., 2013; Ahn et al., 2017; Neumayer et al., 2020; Baldassare et al., 2022). I discuss some preliminary results below in Sec. 6.1.1.

The secondary use would be to follow the evolution of star clusters to examine the impact of resolved internal stellar dynamics in order to study cluster disruption. It is extremely computationally expensive for galactic scale simulations to calculate the forces directly for every single particle. This is one of the primary reasons that we employ gravitational softening, as discussed in Sec. 2.1. This is useful for approximating the dynamics for a large system such as a galaxy, but if one is interested in the small-scale dynamics on the pc scales of star clusters for example, this can become problematic. It was discussed throughout this thesis about the concern of cluster disruption. We introduced some physically motivated alterations to the sub-resolution star formation prescription in Chapter 4, and found that they did have an effect on the spatial properties of the galaxies, which can make these clusters more or less susceptible to cluster disruption. The clusters that were seen to disrupt in our simulations typically had surface densities quite a lot lower than what is observed, indicating that whilst we could achieve a model showing disruption, it was because our clusters were too diffuse and not bound.

As presented in Sec. 1.5, a cluster's disruption is typically set by its boundedness, as well as its initial gas fraction. If clusters survive the initial gas expulsion, its disruption usually comes from stellar evolution and then tidal relaxation. All of the cluster disruption mechanisms can also be impacted by interactions with their environment. If we consider a cluster, with a mass of a few thousand solar masses within a radius of a few parsecs, the inter-stellar separation is much less than the 0.1 pc gravitational softening length adopted in all of the simulations presented in this thesis. It should therefore be clear that once the stellar cluster is formed and all gas is expelled, there are no internal processes within the cluster anymore that can influence the destruction of

Name	M_{BH} [10^5 $M_\odot$]	KETJU integration
BH_int	1	yes
BH_noint	1	no
noBH	0	no

Table 6.1: Summary of the setup for each of the three minor merger simulations.

the cluster at all.

Including a KETJU region around a stellar cluster as it evolves embedded in the galactic disk provides the power to understand the relative impact of external and internal processes on cluster disruption. As KETJU regions are currently required to surround a black hole, this can be implemented by the inclusion of a zero mass black hole tracing a cluster, which would involve running for example FoF on the fly during the simulation. This will be the topic of future work, to evolve stellar clusters with full internal dynamics resolved in a galactic context.

6.1.1 Minor merger simulations

We ran a trio of minor merger (10:1) simulations in order to explore the impact of the black hole on the dwarf galaxies, as well as the inclusion of unsoftened interactions between the black hole and surrounding stellar particles. The different simulation setups are described in Table 6.1. For two of the simulations, we include an IMBH in the centre of the most massive galaxy. The larger of the two galaxies is identical to that presented in this thesis, with M_{DM} = 2 $\times 10^{10}$ $M_\odot$, M_* = 2 $\times 10^7$ $M_\odot$ and M_{gas} = 4 $\times 10^7$ $M_\odot$. The smaller of the two galaxies has M_{DM} = 2 $\times 10^9$ $M_\odot$, M_* = 2 $\times 10^6$ $M_\odot$ and M_{gas} = 4 $\times 10^6$ $M_\odot$.

The initial conditions of the individual galaxies are generated using MAKEDISKGALAXY presented in Springel et al. (2005). The initial conditions for the larger of the two galaxies is identical to that of Chapter 3, Chapter 4 and Chapter 5, but with the inclusion of a 10^5 $M_\odot$ black hole in the centre for the `BH_Int` and `BH_noInt` runs. Following the generation of this isolated galaxy, turbulent driving is run for 30 Myr (as described in Sec. 2.2.4, as well as within the chapters). For the smaller galaxy, this is generated in the same way but without a black hole and with all of the total masses of the system one tenth of that of the fiducial system. The individual particle masses for both systems are the same, at 4 $M_\odot$ for the baryonic particles with 0.1 pc gravitational softening and 6.8×10^3 $M_\odot$ for the dark matter particles, with a gravitational softening of 62 pc. For the smaller galaxy, we did not run turbulent driving, as for this low-mass system, the 10^{51} erg energy injection to drive the turbulence completely disrupts the disk completely for a system with such a shallow potential well. As we are primarily interested in the star formation in the centre of the larger galaxy, the role of the smaller galaxy is mostly as a gravitational perturber and a supply of gas. We therefore do not worry about the lack of turbulent driving in the smaller galaxy, but this would certainly be some consideration for future studies.

Once we have the two individual galaxy initial conditions, they are setup as a merger with a pericentre distance r_p = 0.5 kpc and an initial separation r_{sep} = 2 kpc. The inclination and argument of pericentre are chosen off-plane as $\{i_1, i_2\} = \{60^o, 60^o\}$ and $\{\omega_1, \omega_1\} = \{30^o, 60^o\}$,

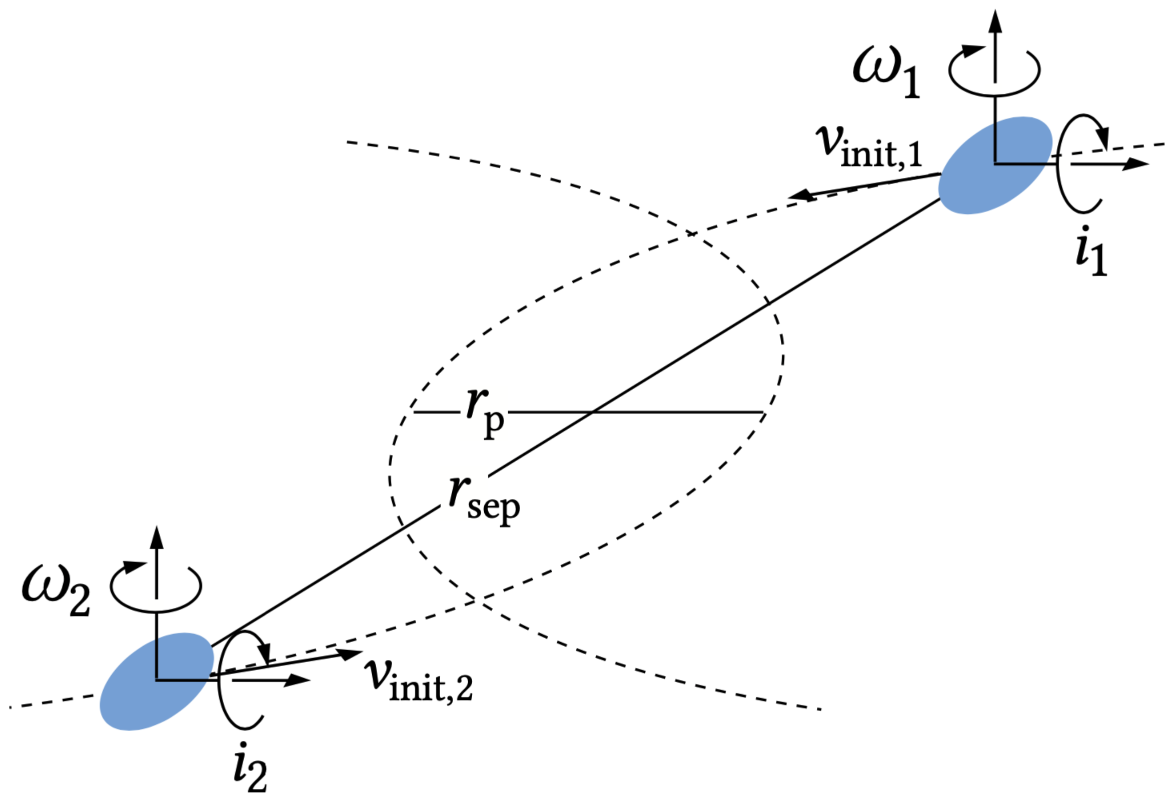

Figure 6.2: Diagram showing the merger setup parameters. Figure taken from Lahén (2020).

consistent with Lahén et al. (2018); Lahén et al. (2019). The setup configuration can be seen in Fig. 6.2.

For both of the simulation that include a black hole, we use KETJU. For one of these simulations however (`BH_noInt`) we do not employ the KETJU integration between the black hole and the stars. KETJU in this case only 'monitors' this region, but does not alter any of the force calculations at all, and they remain purely computed by GADGET-3. For `BH_Int`, the forces between the stars and the black hole are calculated using KETJU. In both cases, we use a KETJU region with radius $r_{\mathrm{ketju}} = 10$ pc. We evolve all of the simulations for 300 Myr. By comparing the three simulations presented here, there are multiple goals. The primary interest is understanding the impact of including a central IMBH on a dwarf galaxy minor merger (by comparing `noBH` and `BH_noInt`) and the impact of including KETJU which calculates directly the forces between the black hole and its surrounding stellar particles (by comparing `BH_noInt` and `BH_Int`).

6.1.2 Gas & stellar surface densities

We show the time evolution of the gas components of the minor merger in Fig. 6.3 for the `BH_noInt` simulation (although the other simulations look identical). The top left panel shows the initial setup. For this panel only, small white symbols guide the eye to show the initial positions of the two galaxies. Following the interaction between the two galaxies, we see a substantial trigger of outflows from the larger galaxy at 50 Myr, as well as the trajectory of the smaller galaxy as it has its gas stripped. We also see the effects of stellar feedback on the gas stream as stars are formed from the high pressures of the colliding gas. By 100 Myr, the larger galaxy is seen to have a much more structure appearance with less dramatic outflows. The long extent of gas from the interacting small galaxy shows gaps from supernovae explosions. By 300 Myr, there is no more trace of the smaller galaxy, and we are left with a single disk from the massive galaxy.

We examine the final snapshot at 300 Myr for the `BH_noInt` run in more detail in Fig. 6.4, which shows the gas as well as the stellar surface densities, now also looking at a much smaller region to examine the detailed results of the merger event on the larger galaxy.

6.1.3 KETJU region

Owing to the fact that KETJU can still be used but with the integration switched off, for both of the simulations including the black hole, `BH_noInt` and `BH_Int`, we can examine the 10 pc region surrounding the black hole in order to directly see the impact of including unsoftened interactions between the black hole and the stars. Fig. 6.5 shows the number of stars in the 10 pc radius surrounding the black hole. For the simulation including integration `BH_Int`, the number of stars in the region is consistently higher, with a substantial jump at around 150 Myr where it oscillates at around 60 particles in the region for the next 150 Myr until the end of the simulation runtime. For the simulation without integration turned on, the number of particles is less than 10 for the whole simulation, up until around 280 Myr where the number makes a modest jump to around 25. The explanation for this is not yet robust, but the first observation can be that the KETJU integration makes a difference to the particles within the surroundings of the black hole.

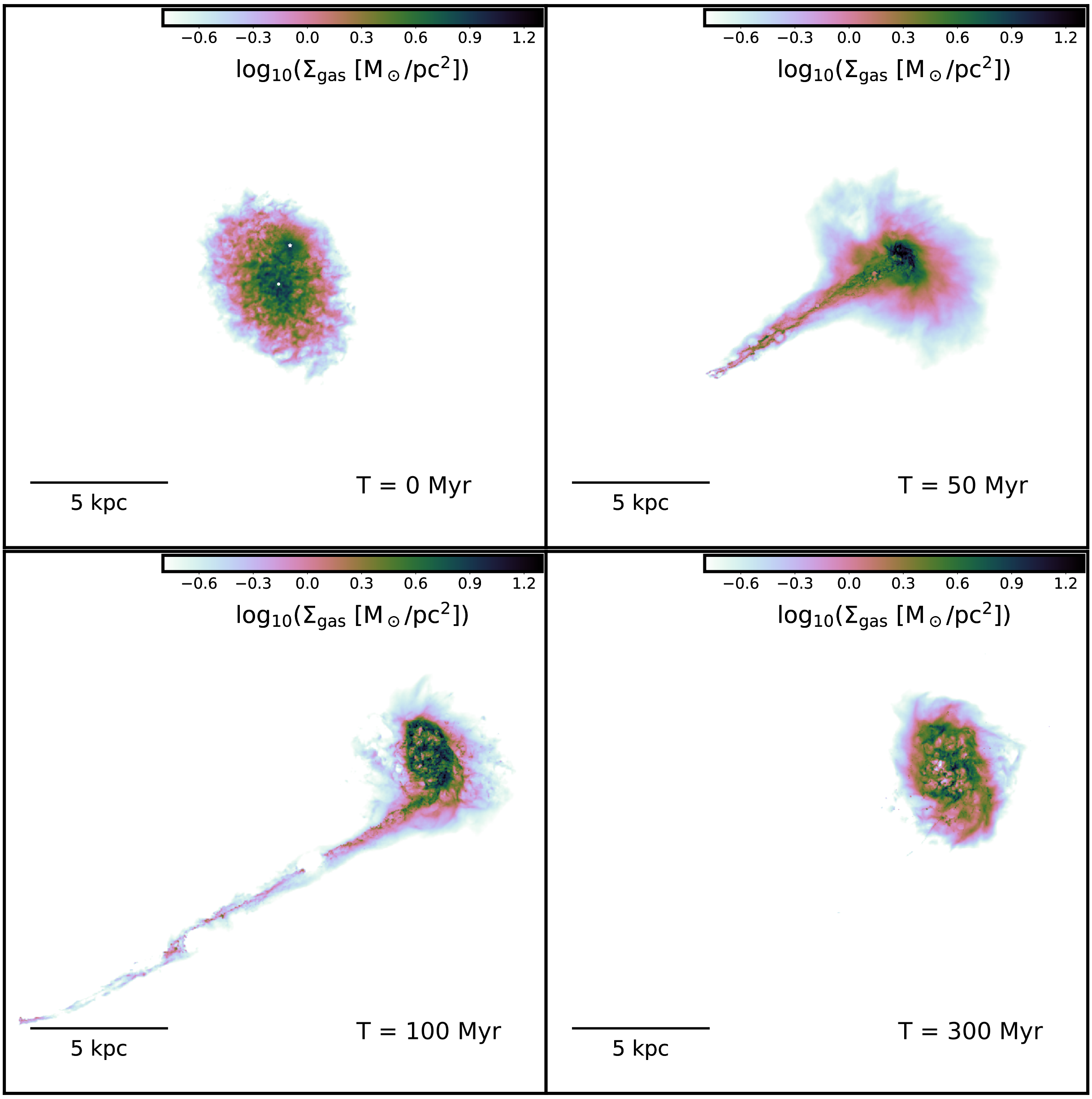

Figure 6.3: The time evolution of the minor merger configuration, here shown for the `BH_noInt` simulation. We show the gas surface density at the beginning (T = 0 Myr), then after 50, 100 and 300 Myr, as indicated by the time in the bottom right corner of each panel.

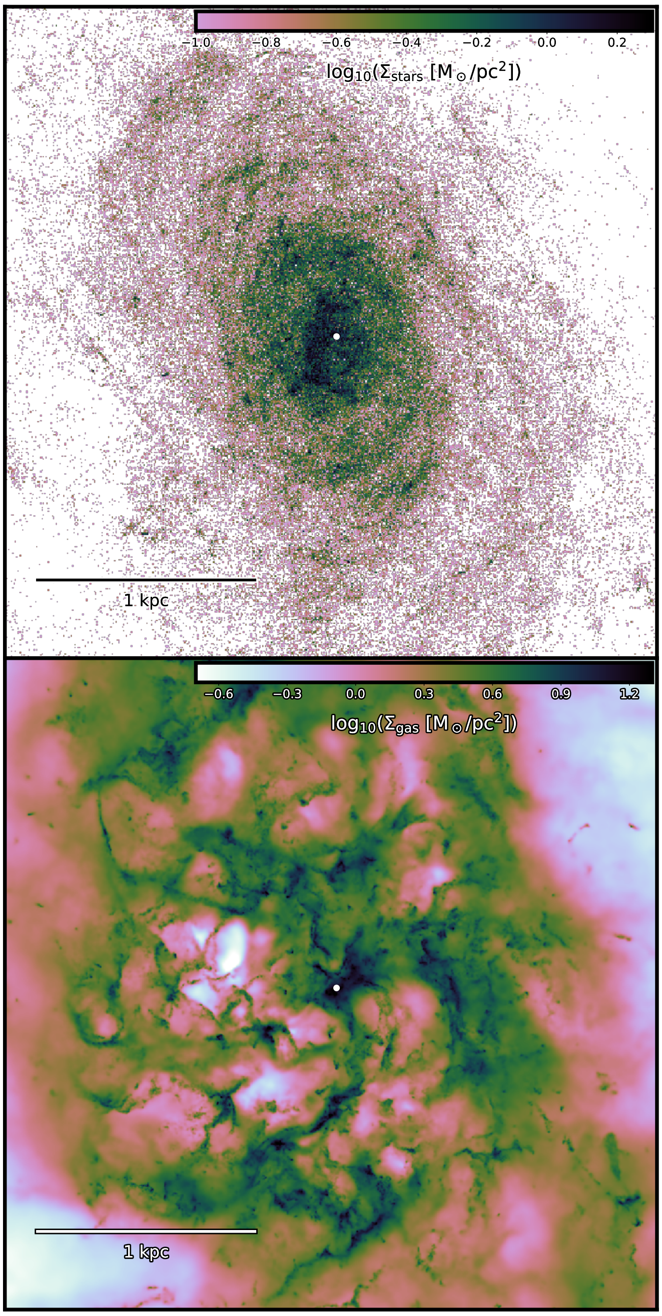

Figure 6.4: The stellar (upper) and gas (lower) surface densities of the larger galaxy in the `BH_noInt` simulation at 300 Myr. Both images show a 3 kpc × 3 kpc region. The colourbars on each respective plot show the surface density of stars and gas. The position of the black hole is marked in both plots by a small white dot.

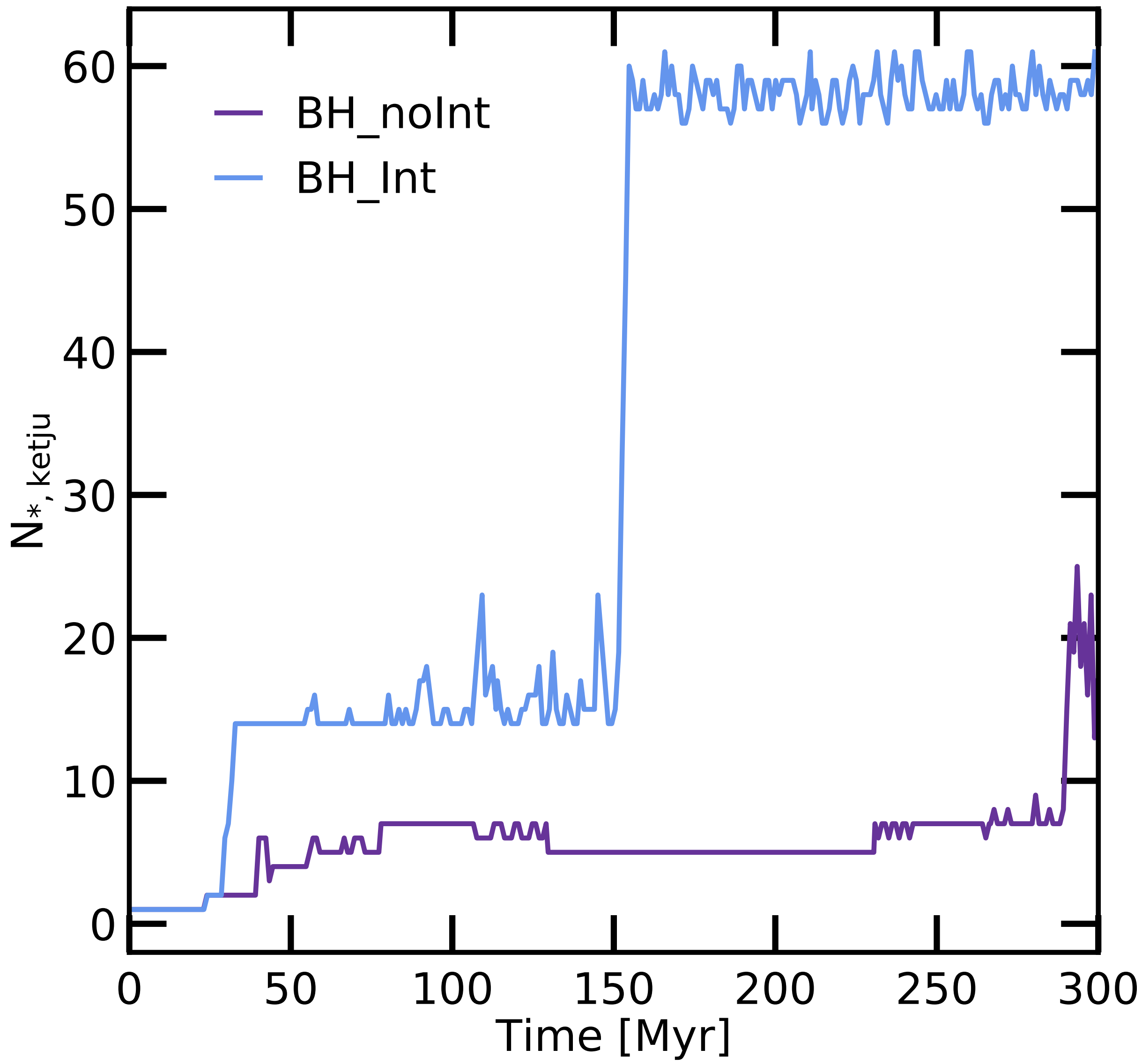

Figure 6.5: The time evolution of the number of stars in the KETJU region for both of the simulations that include a black hole.

Without integration, at <10 pc separation, the forces between the black hole and the stars are heavily softened. This allows star particles to pass through the KETJU region without necessarily being 'captured' by the black hole. With KETJU integration turned on however, the region is able to collect more star particles and keep them there. Something interesting happens for the `BH_Int` simulation at 150 Myr where it accumulates more than 3 times more stars than it had previously. We can examine this in more detail by looking at the gas and star particles surrounding the black hole for both the `BH_noInt` and `BH_Int` simulations.

Fig. 6.6 shows the surface density of the gas colour-coded by temperature between 148 and 153 Myr. We examine this period in order to understand the jump in the number of stars in the KETJU region seen in Fig. 6.5. Over plotted are the star particles, with massive stars marked in yellow and lower mass stars in orange. Symbols with black centres show star particles which have 'exploded'. Each of the timesteps in this plot are 1 Myr (the output frequency of the simulations), and we can see the evolution of the central region surrounding the black hole which is in the direct centre of each image. We can see an encounter with a collection of gas particles. These gas particles appear to 'stick' to the black hole and form stars in the very central region.

Aside from understanding the evolution of the region around the black hole, this is also a really beautiful demonstration of the feedback. At 148 Myr (top left panel), there are 19 low mass stars, including 8 AGB stars that have emitted winds into their surrounding medium previously, with a total mass of 71 $M_\odot$. Surrounding the vicinity of the black hole is 696 $M_\odot$ of cold gas which begins to form stars. This gas mass increases to 812 $M_\odot$ by 150 Myr, and the stellar mass increases to 164 $M_\odot$. From the stars formed, 2 of these are massive stars (≥ 8 $M_\odot$) which appear at 151 Myr right in the centre at the location of the black hole. The feedback from these massive stars decrease the gas mass to 344 $M_\odot$, whilst the stellar mass continues to increase substantially, with 235 $M_\odot$ of stars by 153 Myr, which is an increase of 164 $M_\odot$ in 6 Myr.

There is also a jump in the number of particles in the KETJU region for the `BH_noInt` run just before 300 Myr, so we can also examine what occurs here in Fig. 6.7. A similar series of events happens here, where a region with 103 $M_\odot$ of pre-existing stars is surrounded by a largely cold region of ~ 700 $M_\odot$ of gas at 298 Myr, which begins to form stars. By 300 Myr, the region has formed 5 low mass stars and 1 massive star, with still a huge reservoir of 1404 $M_\odot$ of gas. 1 Myr later, at 301 Myr, it has formed 3 more low mass stars and another massive star, bringing the total stellar mass in the region to 179 $M_\odot$. The stellar feedback from the first massive star has already begun however, and so the gas mass has decreased to 936 $M_\odot$. So we now see again the effect of 2 massive stars photoionising their surrounding gas. By 303 Myr, it has heated all the surrounding gas leaving 281 $M_\odot$ of gas remaining, with 188 $M_\odot$ of stars, which is an increase of 85 $M_\odot$ in the space of 6 Myr.

The difference between Fig. 6.6 and Fig. 6.7 is whether or not KETJU integration is included. We also look at the region at different times for both simulations, as we chose a time at which both IMBHs encounter a large reservoir of gas. For the simulations overall, the star formation rates are identical between `BH_Int`, `BH_noInt` and `noBH`. For the simulation including integration (`BH_Int`, Fig. 6.6), the region around the black hole has 60 stellar particles in the region at 151 Myr. 57 of these are low mass stars (18 of which have exploded as AGB stars) and 3 are high mass stars, one of which is a previously exploded supernova (not included in the plot as it is no longer active and distracts from the other massive photoionising sources). For the simulation

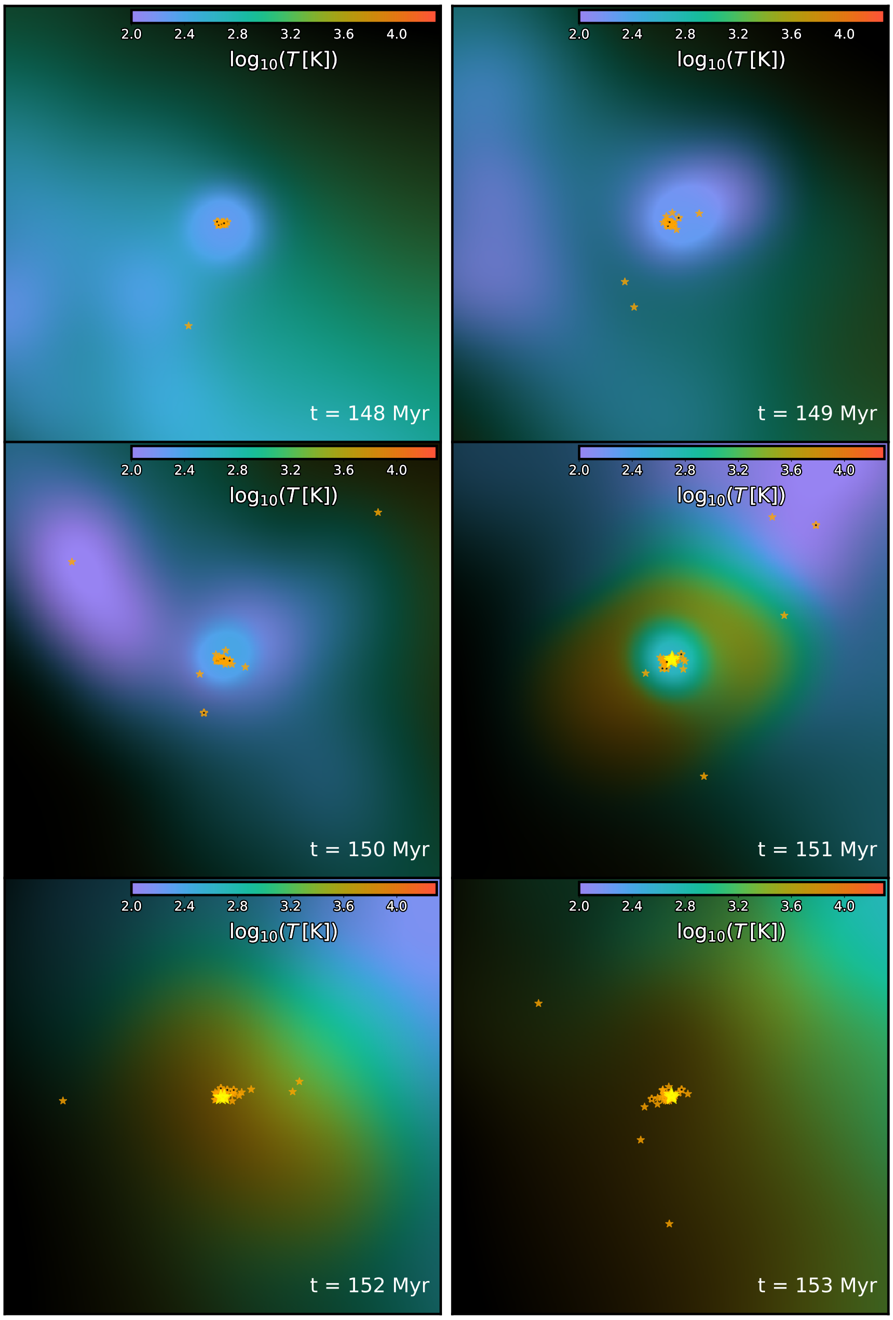

Figure 6.6: The gas surface density colored by the gas temperature for 148-153 Myr, as shown in the bottom right-hand corner of each panel. The field of view is 20×20 pc^2 and is centred on the black hole. The plotting here takes into account the kernel sizes of the SPH particles. Over plotted on top of the gas distribution are the stellar particles, shown by the star symbols. Low mass stars ($M < 8\ M_\odot$) are shown in orange, and high mass stars ($M \geq 8\ M_\odot$) are shown in yellow. The centre of the respective markers turns black if a star has 'exploded', either as a supernova for the high mass stars, or as an AGB star for the low mass stars.

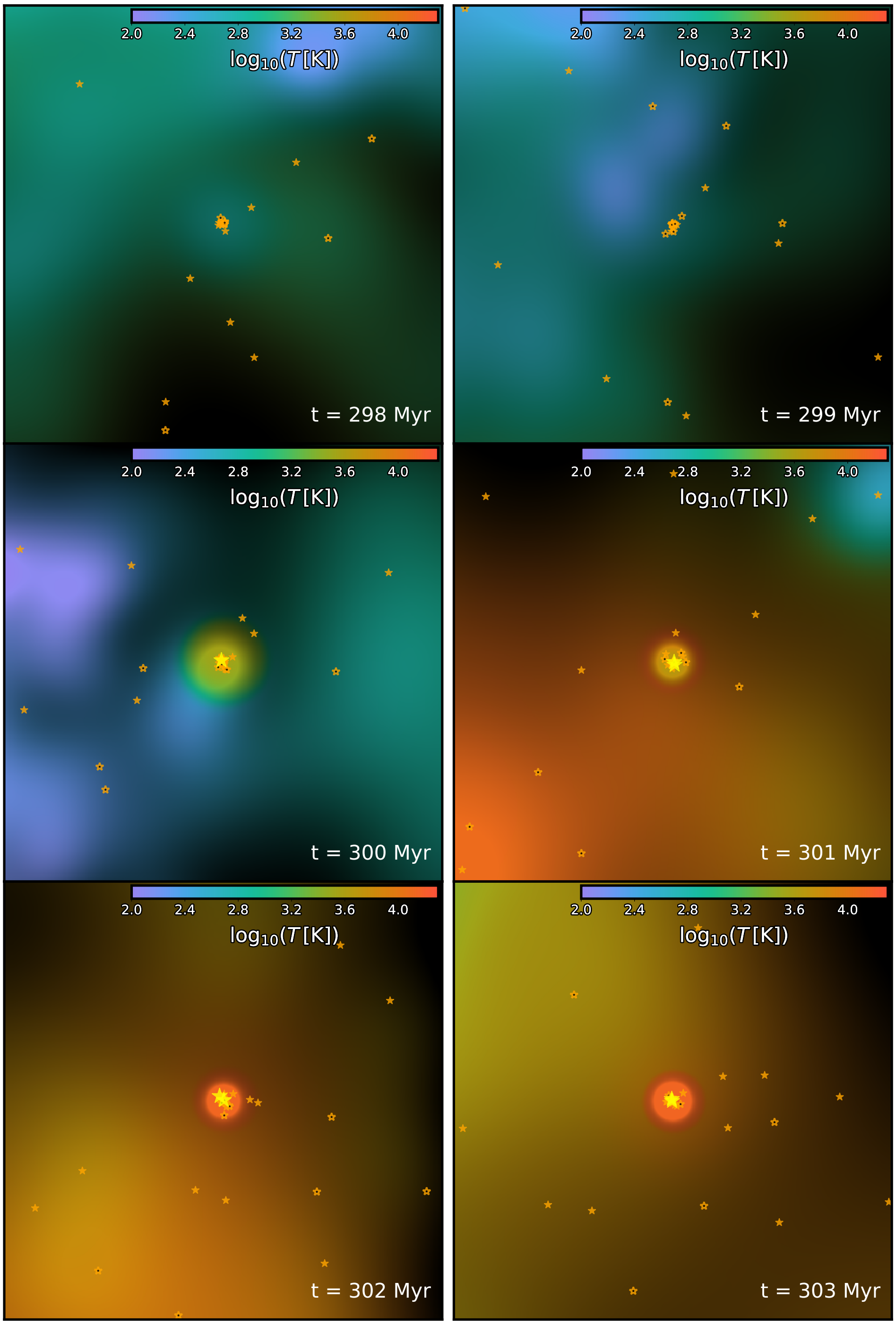

Figure 6.7: The gas surface density coloured by the gas temperature for the `BH_noInt` simulation from 298 to 303 Myr in 1 Myr intervals. As in Fig. 6.6, low mass stars ($M < 8\ M_\odot$) are shown in orange, high mass stars ($M \geq 8\ M_\odot$) are shown in yellow and the centres of each respective type turn black when they have exploded as either AGB stars or SNe.

without integration (BH_noInt, Fig. 6.7), at 301 Myr, the region has 35 stellar particles. 33 of these are low mass stars, 10 of which are ABGs. And there are 2 massive stars, neither of which have exploded as SNe. The fraction of the relative types of stars is an inherent property from the fact that both simulations sample the IMF in the same way. The BH_Int simulation however does appear to form stars much more efficiently within the KETJU region.

Also from Fig. 6.5, there appears to be an effect of including integration such that the black hole retains more of the star particles formed around it. However really understanding if this is somewhat random or really an effect of the integration will require more investigation. From a gravity point of view, the stars undoubtedly ‘stick’ to the black hole from the deepening of the potential well, forming a group of stars with a total mass of 235 $M_{\odot}$, in comparison to 188 $M_{\odot}$ for the BH_noInt simulation. This is particularly interesting considering that the BH_noInt region had almost double the amount of gas before the star formation episode.

6.1.4 Summary & Conclusions

We introduce a trio of 10:1 minor merger simulations, with the goal of exploring the formation of star clusters under the influence of an IMBH, as well as the formation of nuclear star clusters and their co-evolution with black holes. We include the KETJU extension to the GADGET-3 code in order to allow for direct N-body unsoftened force calculations between the black hole and the stars within a 10 pc spherical region surrounding the central black hole. So far we have demonstrated the functionality of the coupling of GADGET-3 and KETJU, and motivated the potential of this setup for the problems described. We have shown that including KETJU integration has an impact on the region surrounding the black hole and the way in which the stars form and remain in this region, and makes little difference to the star formation history, as it should.

Moving forwards with this project, I would like to further explore nuclear star cluster formation, with and without the presence of an IMBH, which is a widely uncertain area of research that is not yet well-understood. The combination of GADGET-3 and KETJU presented here is a powerful tool in order to answer pending questions in this area of research. A natural extension to this would then be to explore the inclusion of a black hole that does not only behave gravitationally, but accretes as well as imparts feedback on surrounding gas particles. The combination of these models will build a picture of nuclear star cluster formation in dwarf galaxies with an interacting black hole.

6.2 Future work

The simulations presented in this thesis include physical implementations that have been shown to be extremely important. Using a non-equilibrium chemistry network has been shown to be vital to capture the interstellar medium (e.g. Richings et al., 2014a,b; Hu et al., 2016), particularly on the topic of star formation, as H_2 remains out of equilibrium at all times (Hu et al., 2016). The cooling and heating processes which are vital for shaping the multi-phase structure of the interstellar medium and the conditions for star formation are also in non-equilibrium, as they depend on the chemical abundances of species within the gas, as well as the local density and temperature.

In Chapter 3, I presented the challenge of simulating the star cluster population of dwarf galaxies. Alongside the primary aim of understanding the physics that governs the formation and evolution of star clusters, we would also naturally like to produce star cluster populations in agreement with observations. With our current star formation model (described in detail in Sec. 2.2.1), the gas collapses to bound clouds which then translates to bound star clusters that appear to be unable to disrupt (by mechanisms described in Sec. 1.5). The collapse of gas before star formation was shown to be well controlled by changing the star formation efficiency parameter. Forming clusters susceptible to disruption as well as with cluster formation efficiencies in agreement with observations could only result from forming clusters with spatial properties, such as surface densities that were too low and inconsistent with observations. For star cluster formation, ideas on addressing this were already discussed in Chapter 3, and I implemented some changes to the star formation model in Chapter 4 and showed the improvement on the star cluster properties. Another way to address this however would be to move away from the Schmidt-type star formation model all together and move towards a model that accounts more for the dynamical properties of the gas, as opposed to solely the temperature and density. This has been explored in cloud scale simulations in Hopkins et al. (2013b), where they found that all of the models tested produced identical star formation rates, but the predicted spatial and density distribution of stars depends strongly on the star formation criteria. As for the evolution of the star clusters, this can be explored using KETJU as discussed in Sec. 6.1.

Chapter 5 disentangled the relative contributions of feedback to stellar clustering to driving outflows. As discussed in Sec. 5.6.4, I would like to further understand how supernovae drive outflows in a clustered environment. This would involve directly tracing the stellar clusters, from their birth out of cold, dense gas and following the feedback from the individual stars. Using this method, one can measure the outflows driven by clusters of different masses. This would have a dependency on the initial gas fraction of the cluster, as well as the ambient density of the cluster as a whole. The hypothesis in this case would be that there is a minimum cluster mass for a given cluster ambient density that is capable of driving outflows. This would also be somewhat dependent additionally on the distance of the cluster from the centre of the disk, both in height and radius. I will thus quantify which kinds of clusters can drive outflows, allowing for comparison with observations, as well as lower resolution simulations resolving stellar populations (or clusters) with single particles.

There are additionally some components of galaxies that are not included in our model that can play a vital role on both galactic scales and small scale properties, which as we have shown in this thesis are heavily interlinked. Chapter 5 particularly discussed the effects of stellar feedback on cluster properties as well as galactic outflows. It highlighted the strong impact of photoionising feedback on the densities of the ISM (see also Sec. 6.1 for a nice demonstration of photoionsation on a star forming region). The modelling of photoionising feedback as Strömgren spheres is a reasonable assumption, but it is argued in (e.g. Emerick et al., 2018) that a full radiative transfer approach is required in many cases. Cosmic rays have been shown to be another important source of feedback, influencing the properties of the interstellar medium (Padovani et al., 2020; Farcy et al., 2022; Simpson et al., 2022) and impacting star formation (Hanasz et al., 2013; Jacob et al., 2018). They can also alter the dynamics of supernova blast waves (Girichidis et al., 2014; Pais et al., 2018), and have a strong impact on driving and sustaining outflows (Uhlig et al., 2012; Pakmor et al., 2016; Simpson et al., 2016; Girichidis et al., 2016, 2018a, 2022; Steinwandel et al., 2020, 2022b). However, this has been typically demonstrated on Milky Way mass scales, whilst the effects of cosmic rays in dwarf galaxies has been shown to be relatively weak (e.g. Hopkins et al., 2020a). Magnetic fields are also observed in the interstellar medium, and have been shown to impact the formation of molecular clouds by preventing fragmentation of gas (Girichidis et al., 2018b), and can slow down star formation in dense gas (Pakmor and Springel, 2013; Kim and Ostriker, 2015) making it inefficient (Federrath and Klessen, 2012, 2013; Federrath, 2015), as well as altering the evolution of supernova remnants (Thompson, 2000; Kim and Ostriker, 2015).

Summary

In this thesis, I examine the formation of star clusters and outflows, as well as the link between them in a series of high-resolution isolated dwarf galaxy simulations run with SPHGal, an improved version of Gadget-3. The simulations include non-equilibrium heating and cooling processes and chemistry, and interstellar radiation field varying in space and time, a density and temperature dependent star formation criteria forming individual massive stars owing to the 4 $M_\odot$ baryonic mass resolution, modelling of H II regions as well as resolved supernova explosions. By altering the sub-resolution modelling of star formation and the feedback prescriptions used, I explore the impact of these sub-resolution models on both the global and the small-scale properties of the galaxy.

Chapter 3 looked at the effect of the sub-resolution modelling of star formation, specifically the star formation efficiency which describes the fraction of star forming gas that is realised into stars. Varying the star formation efficiency is an effective way to alter the densities at which stars form in our simulation. Higher star formation efficiencies causing more star formation occurring at lower densities resulting in more extended and less bound star clusters, whilst the low star formation efficiency models result in a high fraction of stars born in compact, dense star clusters. The star formation rates and outflow rates were independent of the star formation efficiency adopted. All simulations formed star clusters with power law mass functions in broad agreement with observations, with the normalisation of the mass function decreasing with increasing star formation efficiency. None of the models produced clusters with reasonable agreement with observed cluster sizes. Whilst the clusters from the high star formation efficiency models show signs of cluster disruption, they do so due to the fact that they were too diffuse. This motivates more accurate modelling of internal evolutionary processes of star clusters.

Chapter 4 introduces some physically motivated alterations to the star formation sub-resolution model. The aim is to address some of the results highlighted in Chapter 3, namely the difficulty of getting star clusters with spatial properties as well as cluster formation efficiencies in agreement with observations. We tested two different alterations separately. The first is to apply a small velocity kick (up to 3 km/s) to each newly formed star particle, to mimic effects from unresolved gas turbulence and stellar interactions. With increasing kick velocity, star formation is less clustered, and the clusters that do form are more extended with lower surface densities. Introducing the kick also prevents the pile up of low-mass, tightly bound star clusters noted in Chapter 3. Stellar kicks may be an important ingredient to consider for future modelling of star formation. The second alteration to the star formation model was to delay the photoionising feedback from massive stars by a typical free-fall time (10^4-10^6 years) of the star-forming gas particle to account for the cloud core collapse timescale. Increasing the delay time resulted in a moderate enhancement

of stellar clustering, as well as a mild increase in the median velocity dispersion of the formed clusters. Delaying the feedback by even the shortest delay time resulted in more extended and less dense clusters, bringing the spatial properties into agreement with observations. Stellar feedback, particularly photoionisation, plays an important role in regulating star formation, as shown also in Chapter 5. Accounting for cloud core collapse timescales which delays the onset of photoionisation is therefore an important consideration for modelling star formation.

Chapter 5 disentangled the effect of stellar clustering and the feedback prescriptions employed on the properties of galactic outflows. To probe the impact of stellar clustering, we use simulations with varied the star formation efficiency, shown in Chapter 3 to alter the clustering properties of the stars. To study the impact of feedback, we particularly focused on photoionising feedback and core-collapse supernovae. Including feedback from core-collapse supernovae but excluding photoionising feedback increases the stellar clustering, but also significantly changes the densities of the interstellar medium, which in turn dictates the densities at which the supernovae explode, having a strong effect on the outflow properties of the galaxy. To understand the relative contributions to the enhanced outflows from stellar clustering and the changes in the densities of the interstellar medium, we compare to the runs with varied star formation efficiency. We found that the stellar clustering makes relatively little difference to any of the global properties, including outflows, as well as having a minor impact on the phases of the outflows as well as the mass and volume fractions in the interstellar medium. Including or excluding photoionisation and/or supernova feedback however had a substantial impact on the overall density and temperature structure of both the interstellar medium as well as the outflows. We therefore conclude that whilst changing the feedback does alter the clustering properties of the stars, it also alters the density and temperature properties of the interstellar medium, and it is the properties of the interstellar medium in which the supernovae explode which are the dominant influence on galactic outflows.

Chapter 6 introduces a powerful combination of Gadget-3 and Ketju allowing for the simultaneous modelling of small regions of direct N-body unsoftened force calculations between stellar particles and a black hole, along with large scale galaxy evolution. This combined model allows us to follow important dynamical processes such as stellar interactions within clusters as well as resolved stellar feedback in a full galactic context. Additionally, this also allows for the modelling of intermediate mass black holes and the build up of nuclear star clusters.

I have demonstrated the importance of the sub-resolution modelling of star formation on the dynamical and spatial properties of star clusters, as well as the impact of photoionising feedback and supernova feedback on stellar clustering and galactic outflows. Using a combination of both hydrodynamical simulations coupled with unsoftened N-body force calculations will allow us to capture the observed properties of star clusters. My research so far has expanded our understanding of the physical processes shaping star cluster formation and evolution, along with its impact on galaxies as a whole. Moving forwards, I will address the questions raised in this thesis in order to contribute towards building a more robust theory of cluster formation and destruction in galaxies.

Bibliography

Adamo, A. and Bastian, N. (2018). The Lifecycle of Clusters in Galaxies. In Stahler, S., editor, *The Birth of Star Clusters*, volume 424 of *Astrophysics and Space Science Library*, page 91.

Adamo, A., Hollyhead, K., Messa, M., Ryon, J. E., Bajaj, V., Runnholm, A., Aalto, S., Calzetti, D., Gallagher, J. S., Hayes, M. J., Kruijssen, J. M. D., König, S., Larsen, S. S., Melinder, J., Sabbi, E., Smith, L. J., and Östlin, G. (2020a). Star cluster formation in the most extreme environments: insights from the HiPEEC survey. *Monthly Notices of the Royal Astronomical Society*, 499(3):3267–3294.

Adamo, A., Kruijssen, J. M. D., Bastian, N., Silva-Villa, E., and Ryon, J. (2015). Probing the role of the galactic environment in the formation of stellar clusters, using M83 as a test bench. *Monthly Notices of the Royal Astronomical Society*, 452(1):246–260.

Adamo, A., Östlin, G., and Zackrisson, E. (2011). Probing cluster formation under extreme conditions: massive star clusters in blue compact galaxies. *Monthly Notices of the Royal Astronomical Society*, 417(3):1904–1912.

Adamo, A., Ryon, J. E., Messa, M., Kim, H., Grasha, K., Cook, D. O., Calzetti, D., Lee, J. C., Whitmore, B. C., Elmegreen, B. G., Ubeda, L., Smith, L. J., Bright, S. N., Runnholm, A., Andrews, J. E., Fumagalli, M., Gouliermis, D. A., Kahre, L., Nair, P., Thilker, D., Walterbos, R., Wofford, A., Aloisi, A., Ashworth, G., Brown, T. M., Chandar, R., Christian, C., Cignoni, M., Clayton, G. C., Dale, D. A., de Mink, S. E., Dobbs, C., Elmegreen, D. M., Evans, A. S., Gallagher, J. S., I., Grebel, E. K., Herrero, A., Hunter, D. A., Johnson, K. E., Kennicutt, R. C., Krumholz, M. R., Lennon, D., Levay, K., Martin, C., Nota, A., Östlin, G., Pellerin, A., Prieto, J., Regan, M. W., Sabbi, E., Sacchi, E., Schaerer, D., Schiminovich, D., Shabani, F., Tosi, M., Van Dyk, S. D., and Zackrisson, E. (2017). Legacy ExtraGalactic UV Survey with The Hubble Space Telescope: Stellar Cluster Catalogs and First Insights Into Cluster Formation and Evolution in NGC 628. *The Astrophysical Journal*, 841(2):131.

Adamo, A., Zeidler, P., Kruijssen, J. M. D., Chevance, M., Gieles, M., Calzetti, D., Charbonnel, C., Zinnecker, H., and Krause, M. G. H. (2020b). Star Clusters Near and Far; Tracing Star Formation Across Cosmic Time. *Space Science Reviews*, 216(4):69.

Agertz, O. and Kravtsov, A. V. (2015). On the Interplay between Star Formation and Feedback in Galaxy Formation Simulations. *The Astrophysical Journal*, 804(1):18.

Agertz, O. and Kravtsov, A. V. (2016). The Impact of Stellar Feedback on the Structure, Size, and Morphology of Galaxies in Milky-Way-sized Dark Matter Halos. *The Astrophysical Journal*, 824(2):79.

Agertz, O., Kravtsov, A. V., Leitner, S. N., and Gnedin, N. Y. (2013). Toward a Complete Accounting of Energy and Momentum from Stellar Feedback in Galaxy Formation Simulations. *The Astrophysical Journal*, 770(1):25.

Agertz, O., Moore, B., Stadel, J., Potter, D., Miniati, F., Read, J., Mayer, L., Gawryszczak, A., Kravtsov, A., Nordlund, Å., Pearce, F., Quilis, V., Rudd, D., Springel, V., Stone, J., Tasker, E., Teyssier, R., Wadsley, J., and Walder, R. (2007). Fundamental differences between SPH and grid methods. *Monthly Notices of the Royal Astronomical Society*, 380(3):963–978.

Agertz, O., Pontzen, A., Read, J. I., Rey, M. P., Orkney, M., Rosdahl, J., Teyssier, R., Verbeke, R., Kretschmer, M., and Nickerson, S. (2020). EDGE: the mass-metallicity relation as a critical test of galaxy formation physics. *Monthly Notices of the Royal Astronomical Society*, 491(2):1656–1672.

Ahn, C. P., Seth, A. C., den Brok, M., Strader, J., Baumgardt, H., van den Bosch, R., Chilingarian, I., Frank, M., Hilker, M., McDermid, R., Mieske, S., Romanowsky, A. J., Spitler, L., Brodie, J., Neumayer, N., and Walsh, J. L. (2017). Detection of Supermassive Black Holes in Two Virgo Ultracompact Dwarf Galaxies. *The Astrophysical Journal*, 839(2):72.

Ali, A. A., Bending, T. J. R., and Dobbs, C. L. (2022). Stellar winds and photoionization in a spiral arm. *Monthly Notices of the Royal Astronomical Society*, 510(4):5592–5602.

Andersen, M., Zinnecker, H., Moneti, A., McCaughrean, M. J., Brandl, B., Brandner, W., Meylan, G., and Hunter, D. (2009). The Low-Mass Initial Mass Function in the 30 Doradus Starburst Cluster. *The Astrophysical Journal*, 707(2):1347–1360.

Andersson, E. P., Agertz, O., and Renaud, F. (2020). How runaway stars boost galactic outflows. *Monthly Notices of the Royal Astronomical Society*, 494(3):3328–3341.

Aumer, M., White, S. D. M., Naab, T., and Scannapieco, C. (2013). Towards a more realistic population of bright spiral galaxies in cosmological simulations. *Monthly Notices of the Royal Astronomical Society*, 434:3142–3164.

Bakes, E. L. O. and Tielens, A. G. G. M. (1994). The Photoelectric Heating Mechanism for Very Small Graphitic Grains and Polycyclic Aromatic Hydrocarbons. *The Astrophysical Journal*, 427:822.

Baldassare, V. F., Stone, N. C., Foord, A., Gallo, E., and Ostriker, J. P. (2022). Massive Black Hole Formation in Dense Stellar Environments: Enhanced X-Ray Detection Rates in High-velocity Dispersion Nuclear Star Clusters. *The Astrophysical Journal*, 929(1):84.

Barmby, P., McLaughlin, D. E., Harris, W. E., Harris, G. L. H., and Forbes, D. A. (2007). Structural Parameters for Globular Clusters in M31 and Generalizations for the Fundamental Plane. *The Astronomical Journal*, 133(6):2764–2786.

Barnes, A. T., Chandar, R., Kreckel, K., Glover, S. C. O., Scheuermann, F., Belfiore, F., Bigiel, F., Blanc, G. A., Boquien, M., den Brok, J., Congiu, E., Chevance, M., Dale, D. A., Deger, S., Kruijssen, J. M. D., Egorov, O. V., Eibensteiner, C., Emsellem, E., Grasha, K., Groves, B., Klessen, R. S., Hannon, S., Hassani, H., Lee, J. C., Leroy, A. K., Lopez, L. A., McLeod, A. F., Pan, H., Sánchez-Blázquez, P., Schinnerer, E., Sormani, M. C., Thilker, D. A., Ubeda, L., Watkins, E. J., and Williams, T. G. (2022). Linking stellar populations to H II regions across nearby galaxies. I. Constraining pre-supernova feedback from young clusters in NGC 1672. *Astronomy & Astrophysics*, 662:L6.

Barnes, A. T., Henshaw, J. D., Fontani, F., Pineda, J. E., Cosentino, G., Tan, J. C., Caselli, P., Jiménez-Serra, I., Law, C. Y., Avison, A., Bigiel, F., Feng, S., Kong, S., Longmore, S. N., Moser, L., Parker, R. J., Sánchez-Monge, Á., and Wang, K. (2021). ALMA-IRDC: dense gas mass distribution from cloud to core scales. *Monthly Notices of the Royal Astronomical Society*, 503(3):4601–4626.

Barnes, J. and Hut, P. (1986). A hierarchical O(N log N) force-calculation algorithm. *Nature*, 324(6096):446–449.

Bartko, H., Martins, F., Trippe, S., Fritz, T. K., Genzel, R., Ott, T., Eisenhauer, F., Gillessen, S., Paumard, T., Alexander, T., Dodds-Eden, K., Gerhard, O., Levin, Y., Mascetti, L., Nayakshin, S., Perets, H. B., Perrin, G., Pfuhl, O., Reid, M. J., Rouan, D., Zilka, M., and Sternberg, A. (2010). An Extremely Top-Heavy Initial Mass Function in the Galactic Center Stellar Disks. *The Astrophysical Journal*, 708(1):834–840.

Bastian, N. (2008). On the star formation rate - brightest cluster relation: estimating the peak star formation rate in post-merger galaxies. *Monthly Notices of the Royal Astronomical Society*, 390(2):759–768.

Bastian, N. (2011). Cluster Disruption: From Infant Mortality to Long Term Survival. In *Stellar Clusters & Associations: A RIA Workshop on Gaia*, pages 85–97.

Bastian, N., Adamo, A., Gieles, M., Silva-Villa, E., Lamers, H. J. G. L. M., Larsen, S. S., Smith, L. J., Konstantopoulos, I. S., and Zackrisson, E. (2012). Stellar clusters in M83: formation, evolution, disruption and the influence of the environment. *Monthly Notices of the Royal Astronomical Society*, 419(3):2606–2622.

Bastian, N. and Gieles, M. (2008). Cluster Disruption: Combining Theory and Observations. In de Koter, A., Smith, L. J., and Waters, L. B. F. M., editors, *Mass Loss from Stars and the Evolution of Stellar Clusters*, volume 388 of *Astronomical Society of the Pacific Conference Series*, page 353.

Bastian, N., Gieles, M., Efremov, Y. N., and Lamers, H. J. G. L. M. (2005). Hierarchical star formation in M 51: star/cluster complexes. *Astronomy & Astrophysics*, 443(1):79–90.

Bastian, N. and Goodwin, S. P. (2006). Evidence for the strong effect of gas removal on the internal dynamics of young stellar clusters. *Monthly Notices of the Royal Astronomical Society*, 369(1):L9–L13.

Bauer, A. and Springel, V. (2012). Subsonic turbulence in smoothed particle hydrodynamics and moving-mesh simulations. *Monthly Notices of the Royal Astronomical Society*, 423(3):2558–2578.

Baugh, C. M., Cole, S., and Frenk, C. S. (1996a). Evolution of the Hubble sequence in hierarchical models for galaxy formation. *Monthly Notices of the Royal Astronomical Society*, 283(4):1361–1378.

Baugh, C. M., Cole, S., and Frenk, C. S. (1996b). Faint galaxy counts as a function of morphological type in a hierarchical merger model. *Monthly Notices of the Royal Astronomical Society*, 282(1):L27–L32.

Baumgardt, H. (2009). Dissolution of Globular Clusters. In Richtler, T. and Larsen, S., editors, *Globular Clusters - Guides to Galaxies*, page 387.

Baumgardt, H. and Hilker, M. (2018). A catalogue of masses, structural parameters, and velocity dispersion profiles of 112 Milky Way globular clusters. *Monthly Notices of the Royal Astronomical Society*, 478(2):1520–1557.

Baumgardt, H. and Kroupa, P. (2007). A comprehensive set of simulations studying the influence of gas expulsion on star cluster evolution. *Monthly Notices of the Royal Astronomical Society*, 380(4):1589–1598.

Baumgardt, H. and Makino, J. (2003). Dynamical evolution of star clusters in tidal fields. *Monthly Notices of the Royal Astronomical Society*, 340(1):227–246.

Baumgardt, H., Parmentier, G., Anders, P., and Grebel, E. K. (2013). The star cluster formation history of the LMC. *Monthly Notices of the Royal Astronomical Society*, 430:676–685.

Belokurov, V., Erkal, D., Evans, N. W., Koposov, S. E., and Deason, A. J. (2018). Co-formation of the disc and the stellar halo. *Monthly Notices of the Royal Astronomical Society*, 478(1):611–619.

Bending, T. J. R., Dobbs, C. L., and Bate, M. R. (2020). Photoionizing feedback in spiral arm molecular clouds. *Monthly Notices of the Royal Astronomical Society*, 495(2):1672–1691.

Benson, A. J. (2010). Galaxy formation theory. *Physics Reports*, 495(2-3):33–86.

Bergin, E. A., Hartmann, L. W., Raymond, J. C., and Ballesteros-Paredes, J. (2004). Molecular Cloud Formation behind Shock Waves. *The Astrophysical Journal*, 612(2):921–939.

Bertoldi, F. and McKee, C. F. (1992). Pressure-confined Clumps in Magnetized Molecular Clouds. *The Astrophysical Journal*, 395:140.

Besla, G., Kallivayalil, N., Hernquist, L., van der Marel, R. P., Cox, T. J., and Kereš, D. (2012). The role of dwarf galaxy interactions in shaping the Magellanic System and implications for Magellanic Irregulars. *Monthly Notices of the Royal Astronomical Society*, 421(3):2109–2138.

Besla, G., Martínez-Delgado, D., van der Marel, R. P., Beletsky, Y., Seibert, M., Schlafly, E. F., Grebel, E. K., and Neyer, F. (2016). Low Surface Brightness Imaging of the Magellanic System: Imprints of Tidal Interactions between the Clouds in the Stellar Periphery. *The Astrophysical Journal*, 825(1):20.

Bigiel, F., Leroy, A., Walter, F., Brinks, E., de Blok, W. J. G., Madore, B., and Thornley, M. D. (2008). The Star Formation Law in Nearby Galaxies on Sub-Kpc Scales. *The Astronomical Journal*, 136(6):2846–2871.

Bik, A., Lamers, H. J. G. L. M., Bastian, N., Panagia, N., and Romaniello, M. (2003). Clusters in the inner spiral arms of M 51: The cluster IMF and the formation history. *Astronomy & Astrophysics*, 397:473–486.

Binney, J. and Tremaine, S. (2008). *Galactic dynamics*. Princeton University Press.

Bisbas, T. G., Haworth, T. J., Williams, R. J. R., Mackey, J., Tremblin, P., Raga, A. C., Arthur, S. J., Baczynski, C., Walch, S., and Wünsch, R. (2015). STARBENCH: the D-type expansion of an H II region. *Monthly Notices of the Royal Astronomical Society*, 453:17.

Blaauw, A. (1961). On the origin of the O- and B-type stars with high velocities (the “run-away” stars), and some related problems. , 15:265.

Boily, C. M. and Kroupa, P. (2003a). The impact of mass loss on star cluster formation - I. Analytical results. *Monthly Notices of the Royal Astronomical Society*, 338(3):665–672.

Boily, C. M. and Kroupa, P. (2003b). The impact of mass loss on star cluster formation - II. Numerical N-body integration and further applications. *Monthly Notices of the Royal Astronomical Society*, 338(3):673–686.

Bolatto, A. D. (2019). Interstellar Medium and Star Formation in Dwarf Galaxies. In McQuinn, K. B. W. and Stierwalt, S., editors, *Dwarf Galaxies: From the Deep Universe to the Present*, volume 344, pages 233–239.

Bolatto, A. D., Leroy, A. K., Jameson, K., Ostriker, E., Gordon, K., Lawton, B., Stanimirović, S., Israel, F. P., Madden, S. C., Hony, S., Sandstrom, K. M., Bot, C., Rubio, M., Winkler, P. F., Roman-Duval, J., van Loon, J. T., Oliveira, J. M., and Indebetouw, R. (2011). The State of the Gas and the Relation between Gas and Star Formation at Low Metallicity: The Small Magellanic Cloud. *The Astrophysical Journal*, 741(1):12.

Bonnell, I. A. and Bate, M. R. (2006). Star formation through gravitational collapse and competitive accretion. *Monthly Notices of the Royal Astronomical Society*, 370(1):488–494.

Boutloukos, S. G. and Lamers, H. J. G. L. M. (2003). Star cluster formation and disruption timescales - I. An empirical determination of the disruption time of star clusters in four galaxies. *Monthly Notices of the Royal Astronomical Society*, 338(3):717–732.

Braspenning, J., Schaye, J., Borrow, J., and Schaller, M. (2022). Sensitivity of non-radiative cloud-wind interactions to the hydrodynamics solver. *arXiv e-prints*, page arXiv:2203.13915.

Bressert, E., Bastian, N., Gutermuth, R., Megeath, S. T., Allen, L., Evans, Neal J., I., Rebull, L. M., Hatchell, J., Johnstone, D., Bourke, T. L., Cieza, L. A., Harvey, P. M., Merin, B., Ray, T. P., and Tothill, N. F. H. (2010). The spatial distribution of star formation in the solar neighbourhood: do all stars form in dense clusters? *Monthly Notices of the Royal Astronomical Society*, 409(1):L54–L58.

Brook, C. B., Stinson, G., Gibson, B. K., Wadsley, J., and Quinn, T. (2012). MaGICC discs: matching observed galaxy relationships over a wide stellar mass range. *Monthly Notices of the Royal Astronomical Society*, 424(2):1275–1283.

Brown, G. and Gnedin, O. Y. (2021). Radii of young star clusters in nearby galaxies. *Monthly Notices of the Royal Astronomical Society*, 508(4):5935–5953.

Bryan, G. L., Norman, M. L., O'Shea, B. W., Abel, T., Wise, J. H., Turk, M. J., Reynolds, D. R., Collins, D. C., Wang, P., Skillman, S. W., Smith, B., Harkness, R. P., Bordner, J., Kim, J.-h., Kuhlen, M., Xu, H., Goldbaum, N., Hummels, C., Kritsuk, A. G., Tasker, E., Skory, S., Simpson, C. M., Hahn, O., Oishi, J. S., So, G. C., Zhao, F., Cen, R., Li, Y., and Enzo Collaboration (2014). ENZO: An Adaptive Mesh Refinement Code for Astrophysics. *The Astrophysical Journal, Supplement*, 211(2):19.

Burbidge, E. M., Burbidge, G. R., and Rubin, V. C. (1964). A Study of the Velocity Field in M82 and its Bearing on Explosive Phenomena in that Galaxy. *The Astrophysical Journal*, 140:942.

Butler, M. J., Tan, J. C., Teyssier, R., Rosdahl, J., Van Loo, S., and Nickerson, S. (2017). Kiloparsec-scale Simulations of Star Formation in Disk Galaxies. IV. Regulation of Galactic Star Formation Rates by Stellar Feedback. *The Astrophysical Journal*, 841(2):82.

Campbell, M. A., Evans, C. J., Mackey, A. D., Gieles, M., Alves, J., Ascenso, J., Bastian, N., and Longmore, A. J. (2010). VLT-MAD observations of the core of 30 Doradus. *Monthly Notices of the Royal Astronomical Society*, 405(1):421–435.

Ceverino, D., Klypin, A., Klimek, E. S., Trujillo-Gomez, S., Churchill, C. W., Primack, J., and Dekel, A. (2014). Radiative feedback and the low efficiency of galaxy formation in low-mass haloes at high redshift. *Monthly Notices of the Royal Astronomical Society*, 442(2):1545–1559.

Chabrier, G. (2003). Galactic Stellar and Substellar Initial Mass Function. *Publications of the Astronomical Society of the Pacific*, 115(809):763–795.

Chandar, R., Fall, S. M., and Whitmore, B. C. (2015). The link between the formation rates of clusters and stars in galaxies. *The Astrophysical Journal*, 810(1):1.

Chandar, R., Fall, S. M., Whitmore, B. C., and Mulia, A. J. (2017). The Fraction of Stars That Form in Clusters in Different Galaxies. *The Astrophysical Journal*, 849(2):128.

Chandar, R., Whitmore, B. C., Dinino, D., Kennicutt, R. C., Chien, L. H., Schinnerer, E., and Meidt, S. (2016). The Age, Mass, and Size Distributions of Star Clusters in M51. *The Astrophysical Journal*, 824(2):71.

Chandrasekhar, S. (1931). The Maximum Mass of Ideal White Dwarfs. *The Astrophysical Journal*, 74:81.

Chernoff, D. F. and Weinberg, M. D. (1990). Evolution of Globular Clusters in the Galaxy. *The Astrophysical Journal*, 351:121.

Chevance, M., Kruijssen, J. M. D., Hygate, A. P. S., Schruba, A., Longmore, S. N., Groves, B., Henshaw, J. D., Herrera, C. N., Hughes, A., Jeffreson, S. M. R., Lang, P., Leroy, A. K., Meidt, S. E., Pety, J., Razza, A., Rosolowsky, E., Schinnerer, E., Bigiel, F., Blanc, G. A., Emsellem, E., Faesi, C. M., Glover, S. C. O., Haydon, D. T., Ho, I. T., Kreckel, K., Lee, J. C., Liu, D., Querejeta, M., Saito, T., Sun, J., Usero, A., and Utomo, D. (2020). The lifecycle of molecular clouds in nearby star-forming disc galaxies. *Monthly Notices of the Royal Astronomical Society*, 493(2):2872–2909.

Chevance, M., Kruijssen, J. M. D., Krumholz, M. R., Groves, B., Keller, B. W., Hughes, A., Glover, S. C. O., Henshaw, J. D., Herrera, C. N., Kim, J., Leroy, A. K., Pety, J., Razza, A., Rosolowsky, E., Schinnerer, E., Schruba, A., Barnes, A. T., Bigiel, F., Blanc, G. A., Dale, D. A., Emsellem, E., Faesi, C. M., Grasha, K., Klessen, R. S., Kreckel, K., Liu, D., Longmore, S. N., Meidt, S. E., Querejeta, M., Saito, T., Sun, J., and Usero, A. (2022). Pre-supernova feedback mechanisms drive the destruction of molecular clouds in nearby star-forming disc galaxies. *Monthly Notices of the Royal Astronomical Society*, 509(1):272–288.

Chieffi, A. and Limongi, M. (2004). Explosive Yields of Massive Stars from Z = 0 to Z = Z_{solar}. *The Astrophysical Journal*, 608(1):405–410.

Cole, S. (1991). Modeling Galaxy Formation in Evolving Dark Matter Halos. *The Astrophysical Journal*, 367:45.

Collins, M. L. M. and Read, J. I. (2022). Observational constraints on stellar feedback in dwarf galaxies. *Nature Astronomy*, 6:647–658.

Conroy, C., Wechsler, R. H., and Kravtsov, A. V. (2007). The Hierarchical Build-Up of Massive Galaxies and the Intracluster Light since z = 1. *The Astrophysical Journal*, 668(2):826–838.

Cook, D. O., Seth, A. C., Dale, D. A., Johnson, L. C., Weisz, D. R., Fouesneau, M., Olsen, K. A. G., Engelbracht, C. W., and Dalcanton, J. J. (2012). The ACS Nearby Galaxy Survey

Treasury. X. Quantifying the Star Cluster Formation Efficiency of nearby Dwarf Galaxies. *The Astrophysical Journal*, 751(2):100.

Cullen, L. and Dehnen, W. (2010). Inviscid smoothed particle hydrodynamics. *Monthly Notices of the Royal Astronomical Society*, 408:669–683.

Daddi, E., Elbaz, D., Walter, F., Bournaud, F., Salmi, F., Carilli, C., Dannerbauer, H., Dickinson, M., Monaco, P., and Riechers, D. (2010). Different Star Formation Laws for Disks Versus Starbursts at Low and High Redshifts. *The Astrophysical Journal, Letters*, 714(1):L118–L122.

Dale, D. A., Cohen, S. A., Johnson, L. C., Schuster, M. D., Calzetti, D., Engelbracht, C. W., Gil de Paz, A., Kennicutt, R. C., Lee, J. C., Begum, A., Block, M., Dalcanton, J. J., Funes, J. G., Gordon, K. D., Johnson, B. D., Marble, A. R., Sakai, S., Skillman, E. D., van Zee, L., Walter, F., Weisz, D. R., Williams, B., Wu, S. Y., and Wu, Y. (2009). The Spitzer Local Volume Legacy: Survey Description and Infrared Photometry. *The Astrophysical Journal*, 703(1):517–556.

Dale, J. E. and Bonnell, I. A. (2008). The effect of stellar winds on the formation of a protocluster. *Monthly Notices of the Royal Astronomical Society*, 391(1):2–13.

Dale, J. E., Ercolano, B., and Bonnell, I. A. (2012). Ionizing feedback from massive stars in massive clusters - II. Disruption of bound clusters by photoionization. *Monthly Notices of the Royal Astronomical Society*, 424(1):377–392.

Dale, J. E., Ngoumou, J., Ercolano, B., and Bonnell, I. A. (2014). Before the first supernova: combined effects of H II regions and winds on molecular clouds. *Monthly Notices of the Royal Astronomical Society*, 442(1):694–712.

Davé, R., Anglés-Alcázar, D., Narayanan, D., Li, Q., Rafieferantsoa, M. H., and Appleby, S. (2019). SIMBA: Cosmological simulations with black hole growth and feedback. *Monthly Notices of the Royal Astronomical Society*, 486(2):2827–2849.

Davis, M., Efstathiou, G., Frenk, C. S., and White, S. D. M. (1985). The evolution of large-scale structure in a universe dominated by cold dark matter. *The Astrophysical Journal*, 292:371–394.

de Grijs, R. and Anders, P. (2006). How well do we know the age and mass distributions of the star cluster system in the Large Magellanic Cloud? *Monthly Notices of the Royal Astronomical Society*, 366(1):295–307.

de Grijs, R., Bastian, N., and Lamers, H. J. G. L. M. (2003). Star cluster formation and disruption time-scales - II. Evolution of the star cluster system in the fossil starburst of M82. *Monthly Notices of the Royal Astronomical Society*, 340(1):197–209.

Dehnen, W. and Aly, H. (2012). Improving convergence in smoothed particle hydrodynamics simulations without pairing instability. *Monthly Notices of the Royal Astronomical Society*, 425(2):1068–1082.

Dekel, A. and Birnboim, Y. (2006). Galaxy bimodality due to cold flows and shock heating. *Monthly Notices of the Royal Astronomical Society*, 368(1):2–20.

Dobbs, C. L., Adamo, A., Few, C. G., Calzetti, D., Dale, D. A., Elmegreen, B. G., Evans, A. S., Gouliermis, D. A., Grasha, K., Grebel, E. K., Johnson, K. E., Kim, H., Lee, J. C., Messa, M., Ryon, J. E., Smith, L. J., Thilker, D., Ubeda, L., and Whitmore, B. (2017). The properties, origin and evolution of stellar clusters in galaxy simulations and observations. *Monthly Notices of the Royal Astronomical Society*, 464(3):3580–3596.

Dobbs, C. L., Bending, T. J. R., Pettitt, A. R., and Bate, M. R. (2022). The formation of massive stellar clusters in converging galactic flows with photoionization. *Monthly Notices of the Royal Astronomical Society*, 509(1):954–973.

Draine, B. T. (2011). *Physics of the Interstellar and Intergalactic Medium*. Princeton University Press.

Dubois, Y., Pichon, C., Welker, C., Le Borgne, D., Devriendt, J., Laigle, C., Codis, S., Pogosyan, D., Arnouts, S., Benabed, K., Bertin, E., Blaizot, J., Bouchet, F., Cardoso, J. F., Colombi, S., de Lapparent, V., Desjacques, V., Gavazzi, R., Kassin, S., Kimm, T., McCracken, H., Milliard, B., Peirani, S., Prunet, S., Rouberol, S., Silk, J., Slyz, A., Sousbie, T., Teyssier, R., Tresse, L., Treyer, M., Vibert, D., and Volonteri, M. (2014). Dancing in the dark: galactic properties trace spin swings along the cosmic web. *Monthly Notices of the Royal Astronomical Society*, 444(2):1453–1468.

Durier, F. and Dalla Vecchia, C. (2012). Implementation of feedback in smoothed particle hydrodynamics: towards concordance of methods. *Monthly Notices of the Royal Astronomical Society*, 419:465–478.

Efstathiou, G. (1992). Suppressing the formation of dwarf galaxies via photoionization. *Monthly Notices of the Royal Astronomical Society*, 256(2):43P–47P.

Ejdetjärn, T., Agertz, O., Östlin, G., Renaud, F., and Romeo, A. B. (2022). From giant clumps to clouds - III. The connection between star formation and turbulence in the ISM. *Monthly Notices of the Royal Astronomical Society*, 514(1):480–496.

Elmegreen, B. G. (2007). On the Rapid Collapse and Evolution of Molecular Clouds. *The Astrophysical Journal*, 668(2):1064–1082.

Elmegreen, B. G. (2011). Star Formation Patterns and Hierarchies. In Charbonnel, C. and Montmerle, T., editors, *EAS Publications Series*, volume 51 of *EAS Publications Series*, pages 31–44.

Elmegreen, B. G. and Efremov, Y. N. (1997). A Universal Formation Mechanism for Open and Globular Clusters in Turbulent Gas. *The Astrophysical Journal*, 480(1):235–245.

Elmegreen, B. G. and Hunter, D. A. (2015). A Star Formation Law for Dwarf Irregular Galaxies. *The Astrophysical Journal*, 805(2):145.

Emerick, A., Bryan, G. L., and Low, M.-M. M. (2018). Stellar Radiation Is Critical for Regulating Star Formation and Driving Outflows in Low-mass Dwarf Galaxies. *The Astrophysical Journal*, 865:L22.

Emerick, A., Bryan, G. L., and Mac Low, M.-M. (2020). The Role of Stellar Feedback in the Chemical Evolution of a Low Mass Dwarf Galaxy. *arXiv e-prints*, page arXiv:2007.03702.

Evans, Neal J., I. (1999). Physical Conditions in Regions of Star Formation. *Annual Review of Astronomy & Astrophysics*, 37:311–362.

Evans, Neal J., I., Dunham, M. M., Jørgensen, J. K., Enoch, M. L., Merín, B., van Dishoeck, E. F., Alcalá, J. M., Myers, P. C., Stapelfeldt, K. R., Huard, T. L., Allen, L. E., Harvey, P. M., van Kempen, T., Blake, G. A., Koerner, D. W., Mundy, L. G., Padgett, D. L., and Sargent, A. I. (2009). The Spitzer c2d Legacy Results: Star-Formation Rates and Efficiencies; Evolution and Lifetimes. *The Astrophysical Journal, Supplement*, 181(2):321–350.

Evans, Neal J., I., Heiderman, A., and Vutisalchavakul, N. (2014). Star Formation Relations in Nearby Molecular Clouds. *The Astrophysical Journal*, 782(2):114.

Faesi, C. M., Lada, C. J., and Forbrich, J. (2016). Resolving Giant Molecular Clouds in NGC 300: A First Look with the Submillimeter Array. *The Astrophysical Journal*, 821(2):125.

Faesi, C. M., Lada, C. J., and Forbrich, J. (2018). The ALMA View of GMCs in NGC 300: Physical Properties and Scaling Relations at 10 pc Resolution. *The Astrophysical Journal*, 857(1):19.

Faesi, C. M., Lada, C. J., Forbrich, J., Menten, K. M., and Bouy, H. (2014). Molecular Cloud-scale Star Formation in NGC 300. *The Astrophysical Journal*, 789(1):81.

Fahrion, K., Leaman, R., Lyubenova, M., and van de Ven, G. (2022). Disentangling the formation mechanisms of nuclear star clusters. *Astronomy & Astrophysics*, 658:A172.

Fall, S. M. and Chandar, R. (2012). Similarities in populations of star clusters. *The Astrophysical Journal*, 752(7pp):96.

Fall, S. M., Chandar, R., and Whitmore, B. C. (2005). The Age Distribution of Massive Star Clusters in the Antennae Galaxies. *The Astrophysical Journal, Letters*, 631(2):L133–L136.

Fantin, N. J., Côté, P., McConnachie, A. W., Bergeron, P., Cuillandre, J.-C., Dufour, P., Gwyn, S. D. J., Ibata, R. A., and Thomas, G. F. (2021). The Mass and Age Distribution of Halo White Dwarfs in the Canada-France Imaging Survey. *The Astrophysical Journal*, 913(1):30.

Farcy, M., Rosdahl, J., Dubois, Y., Blaizot, J., and Martin-Alvarez, S. (2022). Radiation-magnetohydrodynamics simulations of cosmic ray feedback in disc galaxies. *Monthly Notices of the Royal Astronomical Society*, 513(4):5000–5019.

Faucher-Giguère, C.-A. and Kaspi, V. M. (2006). Birth and Evolution of Isolated Radio Pulsars. *The Astrophysical Journal*, 643(1):332–355.

Federrath, C. (2015). Inefficient star formation through turbulence, magnetic fields and feedback. *Monthly Notices of the Royal Astronomical Society*, 450(4):4035–4042.

Federrath, C. and Klessen, R. S. (2012). The Star Formation Rate of Turbulent Magnetized Clouds: Comparing Theory, Simulations, and Observations. *The Astrophysical Journal*, 761(2):156.

Federrath, C. and Klessen, R. S. (2013). On the Star Formation Efficiency of Turbulent Magnetized Clouds. *The Astrophysical Journal*, 763(1):51.

Field, G. B., Goldsmith, D. W., and Habing, H. J. (1969). Cosmic-Ray Heating of the Interstellar Gas. *The Astrophysical Journal, Letters*, 155:L149.

Fielding, D. B. and Bryan, G. L. (2022). The Structure of Multiphase Galactic Winds. *The Astrophysical Journal*, 924(2):82.

Forbes, J. C., Krumholz, M. R., Goldbaum, N. J., and Dekel, A. (2016). Suppression of star formation in dwarf galaxies by photoelectric grain heating feedback. *Nature*, 535(7613):523–525.

Fouesneau, M., Johnson, L. C., Weisz, D. R., Dalcanton, J. J., Bell, E. F., Bianchi, L., Caldwell, N., Gouliermis, D. A., Guhathakurta, P., Kalirai, J., Larsen, S. S., Rix, H.-W., Seth, A. C., Skillman, E. D., and Williams, B. F. (2014). The Panchromatic Hubble Andromeda Treasury. V. Ages and Masses of the Year 1 Stellar Clusters. *The Astrophysical Journal*, 786(2):117.

Franeck, A., Wünsch, R., Martínez-González, S., Orlitová, I., Boorman, P., Svoboda, J., Szécsi, D., and Douna, V. (2022). X-Ray Emission from Star-cluster Winds in Starburst Galaxies. *The Astrophysical Journal*, 927(2):212.

Frenk, C. S., White, S. D. M., Bode, P., Bond, J. R., Bryan, G. L., Cen, R., Couchman, H. M. P., Evrard, A. E., Gnedin, N., Jenkins, A., Khokhlov, A. M., Klypin, A., Navarro, J. F., Norman, M. L., Ostriker, J. P., Owen, J. M., Pearce, F. R., Pen, U. L., Steinmetz, M., Thomas, P. A., Villumsen, J. V., Wadsley, J. W., Warren, M. S., Xu, G., and Yepes, G. (1999). The Santa Barbara Cluster Comparison Project: A Comparison of Cosmological Hydrodynamics Solutions. *The Astrophysical Journal*, 525(2):554–582.

Fukui, Y., Tsuge, K., Sano, H., Bekki, K., Yozin, C., Tachihara, K., and Inoue, T. (2017). Formation of the young massive cluster R136 triggered by tidally-driven colliding H i flows. *Publications of the Astronomical Society of Japan*, 69(3):L5.

Fukushige, T. and Heggie, D. C. (1995). Pre-collapse evolution of galactic globular clusters. *Monthly Notices of the Royal Astronomical Society*, 276(1):206–218.

Galilei, G. (1610). *Sidereus nuncius*. Apud Thomam Baglionum.

Gallagher, John S., I. and Smith, L. J. (1999). Stellar populations and ages of M82 super star clusters. *Monthly Notices of the Royal Astronomical Society*, 304(3):540–548.

Gallegos-Garcia, M., Burkhart, B., Rosen, A. L., Naiman, J. P., and Ramirez-Ruiz, E. (2020). Winds in Star Clusters Drive Kolmogorov Turbulence. *The Astrophysical Journal, Letters*, 899(2):L30.

Gascoigne, S. C. B. (1966). Colour-magnitude diagrams for nine globular-like clusters in the Magellanic Clouds. *Monthly Notices of the Royal Astronomical Society*, 134:59.

Gatto, A., Walch, S., Naab, T., Girichidis, P., Wünsch, R., Glover, S. C., Klessen, R. S., Clark, P. C., Peters, T., Derigs, D., Baczynski, C., and Puls, J. (2017). The SILCC project - III. Regulation of star formation and outflows by stellar winds and supernovae. *Monthly Notices of the Royal Astronomical Society*, 466(2):1903–1924.

Geen, S., Bieri, R., Rosdahl, J., and de Koter, A. (2021). The geometry and dynamical role of stellar wind bubbles in photoionized H II regions. *Monthly Notices of the Royal Astronomical Society*, 501(1):1352–1369.

Genzel, R., Tacconi, L. J., Gracia-Carpio, J., Sternberg, A., Cooper, M. C., Shapiro, K., Bolatto, A., Bouché, N., Bournaud, F., Burkert, A., Combes, F., Comerford, J., Cox, P., Davis, M., Förster Schreiber, N. M., Garcia-Burillo, S., Lutz, D., Naab, T., Neri, R., Omont, A., Shapley, A., and Weiner, B. (2010). A study of the gas-star formation relation over cosmic time. *Monthly Notices of the Royal Astronomical Society*, 407(4):2091–2108.

Georgy, C., Ekström, S., Eggenberger, P., Meynet, G., Haemmerlé, L., Maeder, A., Granada, A., Groh, J. H., Hirschi, R., Mowlavi, N., Yusof, N., Charbonnel, C., Decressin, T., and Barblan, F. (2013). Grids of stellar models with rotation. III. Models from 0.8 to 120 $M_{\odot}$ at a metallicity Z = 0.002. *Astronomy & Astrophysics*, 558:A103.

Geyer, M. P. and Burkert, A. (2001). The effect of gas loss on the formation of bound stellar clusters. *Monthly Notices of the Royal Astronomical Society*, 323(4):988–994.

Gieles, M. (2009). The early evolution of the star cluster mass function. *Monthly Notices of the Royal Astronomical Society*, 394(4):2113–2126.

Gieles, M. (2010). Star cluster disruption. In de Grijs, R. and Lépine, J. R. D., editors, *Star Clusters: Basic Galactic Building Blocks Throughout Time and Space*, volume 266, pages 69–80.

Gieles, M., Baumgardt, H., Heggie, D. C., and Lamers, H. J. G. L. M. (2010a). On the mass-radius relation of hot stellar systems. *Monthly Notices of the Royal Astronomical Society*, 408(1):L16–L20.

Gieles, M. and Portegies Zwart, S. F. (2011). The distinction between star clusters and associations. *Monthly Notices of the Royal Astronomical Society*, 410(1):L6–L7.

Gieles, M., Sana, H., and Portegies Zwart, S. F. (2010b). On the velocity dispersion of young star clusters: super-virial or binaries? *Monthly Notices of the Royal Astronomical Society*, 402(3):1750–1757.

Gingold, R. A. and Monaghan, J. J. (1977). Smoothed particle hydrodynamics: theory and application to non-spherical stars. *Monthly Notices of the Royal Astronomical Society*, 181:375–389.

Girichidis, P., Naab, T., Hanasz, M., and Walch, S. (2018a). Cooler and smoother - the impact of cosmic rays on the phase structure of galactic outflows. *Monthly Notices of the Royal Astronomical Society*, 479(3):3042–3067.

Girichidis, P., Naab, T., Walch, S., and Hanasz, M. (2014). Anisotropic transport and early dynamical impact of Cosmic Rays around Supernova remnants. *arXiv e-prints*, page arXiv:1406.4861.

Girichidis, P., Pfrommer, C., Pakmor, R., and Springel, V. (2022). Spectrally resolved cosmic rays - II. Momentum-dependent cosmic ray diffusion drives powerful galactic winds. *Monthly Notices of the Royal Astronomical Society*, 510(3):3917–3938.

Girichidis, P., Seifried, D., Naab, T., Peters, T., Walch, S., Wünsch, R., Glover, S. C. O., and Klessen, R. S. (2018b). The SILCC project - V. The impact of magnetic fields on the chemistry and the formation of molecular clouds. *Monthly Notices of the Royal Astronomical Society*, 480(3):3511–3540.

Girichidis, P., Walch, S., Naab, T., Gatto, A., Wünsch, R., Glover, S. C. O., Klessen, R. S., Clark, P. C., Peters, T., Derigs, D., and Baczynski, C. (2016). The SILCC (SImulating the LifeCycle of molecular Clouds) project - II. Dynamical evolution of the supernova-driven ISM and the launching of outflows. *Monthly Notices of the Royal Astronomical Society*, 456(4):3432–3455.

Glover, S. C. O. and Clark, P. C. (2012). Approximations for modelling CO chemistry in giant molecular clouds: a comparison of approaches. *Monthly Notices of the Royal Astronomical Society*, 421:116–131.

Glover, S. C. O. and Mac Low, M.-M. (2007). Simulating the Formation of Molecular Clouds. I. Slow Formation by Gravitational Collapse from Static Initial Conditions. *The Astrophysical Journal, Supplement*, 169(2):239–268.

Goddard, Q. E., Bastian, N., and Kennicutt, R. C. (2010). On the fraction of star clusters surviving the embedded phase. *Monthly Notices of the Royal Astronomical Society*, 405(2):857–869.

González-Lópezlira, R. A., Pflamm-Altenburg, J., and Kroupa, P. (2012). Gas Surface Density, Star Formation Rate Surface Density, and the Maximum Mass of Young Star Clusters in a Disk Galaxy. I. The Flocculent Galaxy M 33. *The Astrophysical Journal*, 761(2):124.

Goodwin, S. P. (1997a). Residual gas expulsion from young globular clusters. *Monthly Notices of the Royal Astronomical Society*, 284(4):785–802.

Goodwin, S. P. (1997b). The initial conditions of young globular clusters in the Large Magellanic Cloud. *Monthly Notices of the Royal Astronomical Society*, 286(3):669–680.

Goodwin, S. P. (2011). The theory of young cluster disruption. In Alves, J., Elmegreen, B. G., Girart, J. M., and Trimble, V., editors, *Computational Star Formation*, volume 270, pages 283–286.

Governato, F., Brook, C., Mayer, L., Brooks, A., Rhee, G., Wadsley, J., Jonsson, P., Willman, B., Stinson, G., Quinn, T., and Madau, P. (2010). Bulgeless dwarf galaxies and dark matter cores from supernova-driven outflows. *Nature*, 463(7278):203–206.

Graham, A. W. and Spitler, L. R. (2009). Quantifying the coexistence of massive black holes and dense nuclear star clusters. *Monthly Notices of the Royal Astronomical Society*, 397(4):2148–2162.

Grond, J. J., Woods, R. M., Wadsley, J. W., and Couchman, H. M. P. (2019). TREVR: A general N $\log^2$N radiative transfer algorithm. *Monthly Notices of the Royal Astronomical Society*, 485(3):3681–3695.

Grudić, M. Y., Guszejnov, D., Hopkins, P. F., Offner, S. S. R., and Faucher-Giguère, C.-A. (2021). STARFORGE: Towards a comprehensive numerical model of star cluster formation and feedback. *Monthly Notices of the Royal Astronomical Society*, 506(2):2199–2231.

Guillard, N., Emsellem, E., and Renaud, F. (2018). The impact of radiation feedback on the assembly of star clusters in a galactic context. *Monthly Notices of the Royal Astronomical Society*, 477(4):5001–5010.

Guszejnov, D., Markey, C., Offner, S. S. R., Grudić, M. Y., Faucher-Giguère, C.-A., Rosen, A. L., and Hopkins, P. F. (2022). Cluster assembly and the origin of mass segregation in the STARFORGE simulations. *Monthly Notices of the Royal Astronomical Society*, 515(1):167–184.

Gutcke, T. A., Pakmor, R., Naab, T., and Springel, V. (2021). LYRA - I. Simulating the multiphase ISM of a dwarf galaxy with variable energy supernovae from individual stars. *Monthly Notices of the Royal Astronomical Society*, 501(4):5597–5615.

Gutcke, T. A., Pakmor, R., Naab, T., and Springel, V. (2022). LYRA - II. Cosmological dwarf galaxy formation with inhomogeneous Population III enrichment. *Monthly Notices of the Royal Astronomical Society*, 513(1):1372–1385.

Haardt, F. and Madau, P. (2001). Modelling the UV/X-ray cosmic background with CUBA. In Neumann, D. M. and Tran, J. T. V., editors, *Clusters of Galaxies and the High Redshift Universe Observed in X-rays*, page 64.

Hacar, A., Clark, S., Heitsch, F., Kainulainen, J., Panopoulou, G., Seifried, D., and Smith, R. (2022). Initial Conditions for Star Formation: A Physical Description of the Filamentary ISM. *arXiv e-prints*, page arXiv:2203.09562.

Haid, S., Walch, S., Seifried, D., Wünsch, R., Dinnbier, F., and Naab, T. (2018). The relative impact of photoionizing radiation and stellar winds on different environments. *Monthly Notices of the Royal Astronomical Society*, 478(4):4799–4815.

Haid, S., Walch, S., Seifried, D., Wünsch, R., Dinnbier, F., and Naab, T. (2019). SILCC-Zoom: The early impact of ionizing radiation on forming molecular clouds. *Monthly Notices of the Royal Astronomical Society*, 482(3):4062–4083.

Hanasz, M., Lesch, H., Naab, T., Gawryszczak, A., Kowalik, K., and Wóltański, D. (2013). Cosmic Rays Can Drive Strong Outflows from Gas-rich High-redshift Disk Galaxies. *The Astrophysical Journal, Letters*, 777(2):L38.

Hartmann, L. (2001). On Age Spreads in Star-forming Regions. *The Astronomical Journal*, 121(2):1030–1039.

Henkel, C., Javanmardi, B., Martínez-Delgado, D., Kroupa, P., and Teuwen, K. (2017). DGSAT: Dwarf Galaxy Survey with Amateur Telescopes. II. A catalogue of isolated nearby edge-on disk galaxies and the discovery of new low surface brightness systems. *Astronomy & Astrophysics*, 603:A18.

Hennebelle, P. and Audit, E. (2007). On the structure of the turbulent interstellar atomic hydrogen. I. Physical characteristics. Influence and nature of turbulence in a thermally bistable flow. *Astronomy & Astrophysics, Supplement*, 465(2):431–443.

Hennebelle, P., Audit, E., and Miville-Deschênes, M. A. (2007). On the structure of the turbulent interstellar atomic hydrogen. II. First comparison between observation and theory. Are the characteristics of molecular clouds determined early in the turbulent 2-phase atomic gas? *Astronomy & Astrophysics*, 465(2):445–456.

Hewitt, J. W. and Yusef-Zadeh, F. (2009). Discovery of new interacting supernova remnants in the inner galaxy. *The Astrophysical Journal*, 694:16–20.

Heyer, M. and Dame, T. M. (2015). Molecular Clouds in the Milky Way. *Annual Review of Astronomy & Astrophysics*, 53:583–629.

Heyer, M., Gutermuth, R., Urquhart, J. S., Csengeri, T., Wienen, M., Leurini, S., Menten, K., and Wyrowski, F. (2016). The rate and latency of star formation in dense, massive clumps in the Milky Way. *Astronomy & Astrophysics*, 588:A29.

Hills, J. G. (1980). The effect of mass loss on the dynamical evolution of a stellar system - Analytic approximations. *The Astrophysical Journal*, 235:986–991.

Hirai, Y., Fujii, M. S., and Saitoh, T. R. (2021). SIRIUS project. I. Star formation models for star-by-star simulations of star clusters and galaxy formation. *Publications of the Astronomical Society of Japan*, 73(4):1036–1056.

Hislop, J. M., Naab, T., Steinwandel, U. P., Lahén, N., Irodotou, D., Johansson, P. H., and Walch, S. (2022). The challenge of simulating the star cluster population of dwarf galaxies with resolved interstellar medium. *Monthly Notices of the Royal Astronomical Society*, 509(4):5938–5954.

Hodge, P. (1987). Clusters of the Small Magellanic Cloud. II. Age distributions. *Publications of the Astronomical Society of the Pacific*, 99:724–729.

Hopkins, P. F. (2013). A general class of Lagrangian smoothed particle hydrodynamics methods and implications for fluid mixing problems. *Monthly Notices of the Royal Astronomical Society*, 428:2840–2856.

Hopkins, P. F. (2013). A general theory of turbulent fragmentation. *Monthly Notices of the Royal Astronomical Society*, 430(3):1653–1693.

Hopkins, P. F. (2015). A new class of accurate, mesh-free hydrodynamic simulation methods. *Monthly Notices of the Royal Astronomical Society*, 450(1):53–110.

Hopkins, P. F., Chan, T. K., Garrison-Kimmel, S., Ji, S., Su, K.-Y., Hummels, C. B., Kereš, D., Quataert, E., and Faucher-Giguère, C.-A. (2020a). But what about...: cosmic rays, magnetic fields, conduction, and viscosity in galaxy formation. *Monthly Notices of the Royal Astronomical Society*, 492(3):3465–3498.

Hopkins, P. F., Grudić, M. Y., Wetzel, A., Kereš, D., Faucher-Giguère, C.-A., Ma, X., Murray, N., and Butcher, N. (2020b). Radiative stellar feedback in galaxy formation: Methods and physics. *Monthly Notices of the Royal Astronomical Society*, 491(3):3702–3729.

Hopkins, P. F., Kereš, D., Oñorbe, J., Faucher-Giguère, C.-A., Quataert, E., Murray, N., and Bullock, J. S. (2014). Galaxies on FIRE (Feedback In Realistic Environments): stellar feedback explains cosmologically inefficient star formation. *Monthly Notices of the Royal Astronomical Society*, 445(1):581–603.

Hopkins, P. F., Narayanan, D., and Murray, N. (2013a). The meaning and consequences of star formation criteria in galaxy models with resolved stellar feedback. *Monthly Notices of the Royal Astronomical Society*, 432(4):2647–2653.

Hopkins, P. F., Narayanan, D., and Murray, N. (2013b). The meaning and consequences of star formation criteria in galaxy models with resolved stellar feedback. *Monthly Notices of the Royal Astronomical Society*, 432(4):2647–2653.

Hopkins, P. F., Quataert, E., and Murray, N. (2011). Self-regulated star formation in galaxies via momentum input from massive stars. *Monthly Notices of the Royal Astronomical Society*, 417(2):950–973.

Hopkins, P. F., Quataert, E., and Murray, N. (2012). Stellar feedback in galaxies and the origin of galaxy-scale winds. *Monthly Notices of the Royal Astronomical Society*, 421(4):3522–3537.

Hopkins, P. F., Wetzel, A., Kereš, D., Faucher-Giguère, C.-A., Quataert, E., Boylan-Kolchin, M., Murray, N., Hayward, C. C., Garrison-Kimmel, S., Hummels, C., Feldmann, R., Torrey, P., Ma, X., Anglés-Alcázar, D., Su, K.-Y., Orr, M., Schmitz, D., Escala, I., Sanderson, R., Grudić, M. Y., Hafen, Z., Kim, J.-H., Fitts, A., Bullock, J. S., Wheeler, C., Chan, T. K., Elbert, O. D., and Narayanan, D. (2018). FIRE-2 simulations: physics versus numerics in galaxy formation. *Monthly Notices of the Royal Astronomical Society*, 480(1):800–863.

Hu, C.-Y. (2019). Supernova-driven winds in simulated dwarf galaxies. *Monthly Notices of the Royal Astronomical Society*, 483(3):3363–3381.

Hu, C.-Y., Naab, T., Glover, S. C. O., Walch, S., and Clark, P. C. (2017). Variable interstellar radiation fields in simulated dwarf galaxies: supernovae versus photoelectric heating. *Monthly Notices of the Royal Astronomical Society*, 471:2151–2173.

Hu, C.-Y., Naab, T., Walch, S., Glover, S. C. O., and Clark, P. C. (2016). Star formation and molecular hydrogen in dwarf galaxies: a non-equilibrium view. *Monthly Notices of the Royal Astronomical Society*, 458:3528–3553.

Hu, C.-Y., Naab, T., Walch, S., Moster, B. P., and Oser, L. (2014). SPHGal: smoothed particle hydrodynamics with improved accuracy for galaxy simulations. *Monthly Notices of the Royal Astronomical Society*, 443:1173–1191.

Hu, C.-Y., Schruba, A., Sternberg, A., and van Dishoeck, E. F. (2022a). Dependence of X $_{CO}$ on Metallicity, Intensity, and Spatial Scale in a Self-regulated Interstellar Medium. *The Astrophysical Journal*, 931(1):28.

Hu, C.-Y., Smith, M. C., Teyssier, R., Bryan, G. L., Verbeke, R., Emerick, A., Somerville, R. S., Burkhart, B., Li, Y., Forbes, J. C., and Starkenburg, T. (2022b). Code Comparison in Galaxy Scale Simulations with Resolved Supernova Feedback: Lagrangian vs. Eulerian Methods. *arXiv e-prints*, page arXiv:2208.10528.

Hu, C.-Y., Sternberg, A., and van Dishoeck, E. F. (2021). Metallicity Dependence of the H/H_2 and C^+/C/CO Distributions in a Resolved Self-regulating Interstellar Medium. *The Astrophysical Journal*, 920(1):44.

Hu, Y., Federrath, C., Xu, S., and Mathew, S. S. (2022c). The velocity statistics of turbulent clouds in the presence of gravity, magnetic fields, radiation, and outflow feedback. *Monthly Notices of the Royal Astronomical Society*, 513(2):2100–2110.

Hunter, D. A., Elmegreen, B. G., Dupuy, T. J., and Mortonson, M. (2003). Cluster Mass Functions in the Large and Small Magellanic Clouds: Fading and Size-of-Sample Effects. *The Astronomical Journal*, 126(4):1836–1848.

Hunter, D. A., Ficut-Vicas, D., Ashley, T., Brinks, E., Cigan, P., Elmegreen, B. G., Heesen, V., Herrmann, K. A., Johnson, M., Oh, S.-H., Rupen, M. P., Schruba, A., Simpson, C. E., Walter, F., Westpfahl, D. J., Young, L. M., and Zhang, H.-X. (2012). Little Things. *The Astronomical Journal*, 144(5):134.

Iwamoto, K., Brachwitz, F., Nomoto, K., Kishimoto, N., Umeda, H., Hix, W. R., and Thielemann, F.-K. (1999). Nucleosynthesis in Chandrasekhar Mass Models for Type IA Supernovae and Constraints on Progenitor Systems and Burning-Front Propagation. *The Astrophysical Journal, Supplement*, 125(2):439–462.

Jacob, S., Pakmor, R., Simpson, C. M., Springel, V., and Pfrommer, C. (2018). The dependence of cosmic ray-driven galactic winds on halo mass. *Monthly Notices of the Royal Astronomical Society*, 475(1):570–584.

Jameson, K. E., Bolatto, A. D., Leroy, A. K., Meixner, M., Roman-Duval, J., Gordon, K., Hughes, A., Israel, F. P., Rubio, M., Indebetouw, R., Madden, S. C., Bot, C., Hony, S., Cormier, D., Pellegrini, E. W., Galametz, M., and Sonneborn, G. (2016). The Relationship Between Molecular Gas, H I, and Star Formation in the Low-mass, Low-metallicity Magellanic Clouds. *The Astrophysical Journal*, 825(1):12.

Janka, H.-T. (2012). Explosion Mechanisms of Core-Collapse Supernovae. *Annual Review of Nuclear and Particle Science*, 62(1):407–451.

Jeans, J. H. (1902). The Stability of a Spherical Nebula. *Philosophical Transactions of the Royal Society of London Series A*, 199:1–53.

Jeffreson, S. M. R., Keller, B. W., Winter, A. J., Chevance, M., Kruijssen, J. M. D., Krumholz, M. R., and Fujimoto, Y. (2021). A scaling relation for the molecular cloud lifetime in Milky Way-like galaxies. *Monthly Notices of the Royal Astronomical Society*, 505(2):1678–1698.

Johnson, L. C., Seth, A. C., Dalcanton, J. J., Beerman, L. C., Fouesneau, M., Lewis, A. R., Weisz, D. R., Williams, B. F., Bell, E. F., Dolphin, A. E., Larsen, S. S., Sandstrom, K., and Skillman, E. D. (2016). Panchromatic Hubble Andromeda Treasury. XVI. Star Cluster Formation Efficiency and the Clustered Fraction of Young Stars. *The Astrophysical Journal*, 827(1):33.

Johnson, L. C., Seth, A. C., Dalcanton, J. J., Caldwell, N., Fouesneau, M., Gouliermis, D. A., Hodge, P. W., Larsen, S. S., Olsen, K. A. G., San Roman, I., Sarajedini, A., Weisz, D. R., Williams, B. F., Beerman, L. C., Bianchi, L., Dolphin, A. E., Girardi, L., Guhathakurta, P., Kalirai, J., Lang, D., Monachesi, A., Nanda, S., Rix, H.-W., and Skillman, E. D. (2012). PHAT Stellar Cluster Survey. I. Year 1 Catalog and Integrated Photometry. *The Astrophysical Journal*, 752(2):95.

Kannan, R., Marinacci, F., Simpson, C. M., Glover, S. C. O., and Hernquist, L. (2020). Efficacy of early stellar feedback in low gas surface density environments. *Monthly Notices of the Royal Astronomical Society*, 491(2):2088–2103.

Kannan, R., Stinson, G. S., Macciò, A. V., Hennawi, J. F., Woods, R., Wadsley, J., Shen, S., Robitaille, T., Cantalupo, S., Quinn, T. R., and Christensen, C. (2014). Galaxy formation with local photoionization feedback - I. Methods. *Monthly Notices of the Royal Astronomical Society*, 437(3):2882–2893.

Karachentsev, I. D. and Kaisina, E. I. (2019). Dwarf Galaxies in the Local Volume. *Astrophysical Bulletin*, 74(2):111–127.

Karakas, A. I. (2010). Updated stellar yields from asymptotic giant branch models. *Monthly Notices of the Royal Astronomical Society*, 403(3):1413–1425.

Katz, N. (1992). Dissipational Galaxy Formation. II. Effects of Star Formation. *The Astrophysical Journal*, 391:502.

Keller, B. W. and Kruijssen, J. M. D. (2022). Uncertainties in supernova input rates drive qualitative differences in simulations of galaxy evolution. *Monthly Notices of the Royal Astronomical Society*, 512(1):199–215.

Keller, B. W., Kruijssen, J. M. D., and Chevance, M. (2022). Empirically motivated early feedback: momentum input by stellar feedback in galaxy simulations inferred through observations. *Monthly Notices of the Royal Astronomical Society*, 514(4):5355–5374.

Kennicutt, Robert C., J. (1998). The Global Schmidt Law in Star-forming Galaxies. *The Astrophysical Journal*, 498(2):541–552.

Kennicutt, R. C. and Evans, N. J. (2012). Star Formation in the Milky Way and Nearby Galaxies. *Annual Review of Astronomy & Astrophysics*, 50:531–608.

Kharchenko, N. V., Piskunov, A. E., Schilbach, E., Röser, S., and Scholz, R. D. (2013). Global survey of star clusters in the Milky Way. II. The catalogue of basic parameters. *Astronomy & Astrophysics*, 558:A53.

Kim, C.-G. and Ostriker, E. C. (2015). Momentum Injection by Supernovae in the Interstellar Medium. *The Astrophysical Journal*, 802(2):99.

Kim, J.-h., Krumholz, M. R., Wise, J. H., Turk, M. J., Goldbaum, N. J., and Abel, T. (2013). Dwarf Galaxies with Ionizing Radiation Feedback. I. Escape of Ionizing Photons. *The Astrophysical Journal*, 775(2):109.

Kirby, E. N., Xie, J. L., Guo, R., de los Reyes, M. A. C., Bergemann, M., Kovalev, M., Shen, K. J., Piro, A. L., and McWilliam, A. (2019). Evidence for Sub-Chandrasekhar Type Ia Supernovae from Stellar Abundances in Dwarf Galaxies. *The Astrophysical Journal*, 881(1):45.

Klessen, R. S. and Glover, S. C. O. (2016). Physical Processes in the Interstellar Medium. *Saas-Fee Advanced Course*, 43:85.

Konstantopoulos, I. S., Bastian, N., Smith, L. J., Westmoquette, M. S., Trancho, G., and Gallagher, J. S., I. (2009). A Spectroscopic Census of the M82 Stellar Cluster Population. *The Astrophysical Journal*, 701(2):1015–1031.

Koudmani, S., Henden, N. A., and Sijacki, D. (2021). A little FABLE: exploring AGN feedback in dwarf galaxies with cosmological simulations. *Monthly Notices of the Royal Astronomical Society*, 503(3):3568–3591.

Koudmani, S., Sijacki, D., Bourne, M. A., and Smith, M. C. (2019). Fast and energetic AGN-driven outflows in simulated dwarf galaxies. *Monthly Notices of the Royal Astronomical Society*, 484(2):2047–2066.

Koudmani, S., Sijacki, D., and Smith, M. C. (2022). Two can play at that game: constraining the role of supernova and AGN feedback in dwarf galaxies with cosmological zoom-in simulations. *arXiv e-prints*, page arXiv:2206.11274.

Kravtsov, A. V. (1999). *High-resolution simulations of structure formation in the universe*. PhD thesis, New Mexico State University.

Kreckel, K., Faesi, C., Kruijssen, J. M. D., Schruba, A., Groves, B., Leroy, A. K., Bigiel, F., Blanc, G. A., Chevance, M., Herrera, C., Hughes, A., McElroy, R., Pety, J., Querejeta, M., Rosolowsky, E., Schinnerer, E., Sun, J., Usero, A., and Utomo, D. (2018). A 50 pc Scale View of Star Formation Efficiency across NGC 628. *The Astrophysical Journal, Letters*, 863(2):L21.

Kretschmer, M., Dekel, A., and Teyssier, R. (2022). On the origin of surprisingly cold gas discs in galaxies at high redshift. *Monthly Notices of the Royal Astronomical Society*, 510(3):3266–3275.

Kroupa, P. (2001). On the variation of the initial mass function. *Monthly Notices of the Royal Astronomical Society*, 322(2):231–246.

Kroupa, P., Aarseth, S., and Hurley, J. (2001). The formation of a bound star cluster: from the Orion nebula cluster to the Pleiades. *Monthly Notices of the Royal Astronomical Society*, 321:699–712.

Kroupa, P. and Boily, C. M. (2002). On the mass function of star clusters. *Monthly Notices of the Royal Astronomical Society*, 336(4):1188–1194.

Kruijssen, J. M. D. (2009). The evolution of the stellar mass function in star clusters. *Astronomy & Astrophysics*, 507(3):1409–1423.

Kruijssen, J. M. D. (2012). On the fraction of star formation occurring in bound stellar clusters. *Monthly Notices of the Royal Astronomical Society*, 426:3008–3040.

Kruijssen, J. M. D. and Bastian, N. (2016). Pitfalls when observationally characterizing the relative formation rates of stars and stellar clusters in galaxies. *Monthly Notices of the Royal Astronomical Society*, 457(1):L24–L28.

Kruijssen, J. M. D., Schruba, A., Chevance, M., Longmore, S. N., Hygate, A. P. S., Haydon, D. T., McLeod, A. F., Dalcanton, J. J., Tacconi, L. J., and van Dishoeck, E. F. (2019). Fast and inefficient star formation due to short-lived molecular clouds and rapid feedback. *Nature*, 569(7757):519–522.

Krumholz, M. R. (2014). The big problems in star formation: The star formation rate, stellar clustering, and the initial mass function. *Physics Reports*, 539:49–134.

Krumholz, M. R., Dekel, A., and Mckee, C. F. (2012). A universal, local star formation law in galactic clouds, nearby galaxies, high-redshift disks, and starbursts. *The Astrophysical Journal*, 745(16pp):69.

Krumholz, M. R., McKee, C. F., and Bland-Hawthorn, J. (2019). Star Clusters Across Cosmic Time. *Annual Review of Astronomy & Astrophysics*, 57:227–303.

Krumholz, M. R. and Tan, J. C. (2007). Slow star formation in dense gas: evidence and implications. *The Astrophysical Journal*, 654:304–315.

Kuhn, M. A., Hillenbrand, L. A., Sills, A., Feigelson, E. D., and Getman, K. V. (2019). Kinematics in Young Star Clusters and Associations with Gaia DR2. *The Astrophysical Journal*, 870(1):32.

Lada, C. J. and Lada, E. A. (2003). Embedded clusters in molecular clouds. *Annu. Rev. Astron. Astrophys*, 41:57–115.

Lahén, N. (2020). *Hydrodynamical simulations and synthetic observations of merging galaxies*. PhD thesis, University of Helsinki.

Lahén, N., Johansson, P. H., Rantala, A., Naab, T., and Frigo, M. (2018). The fate of the Antennae galaxies. *Monthly Notices of the Royal Astronomical Society*, 475(3):3934–3958.

Lahén, N., Naab, T., Johansson, P. H., Elmegreen, B., Hu, C.-Y., and Walch, S. (2019). The Formation of Low-metallicity Globular Clusters in Dwarf Galaxy Mergers. *The Astrophysical Journal*, 879(2).

Lahén, N., Naab, T., Johansson, P. H., Elmegreen, B., Hu, C.-Y., and Walch, S. (2020). Structure and Rotation of Young Massive Star Clusters in a Simulated Dwarf Starburst. *The Astrophysical Journal*, 904(1):71.

Lahén, N., Naab, T., Johansson, P. H., Elmegreen, B., Hu, C.-Y., Walch, S., Steinwandel, U. P., and Moster, B. P. (2020). The GRIFFIN Project-Formation of Star Clusters with Individual Massive Stars in a Simulated Dwarf Galaxy Starburst. *The Astrophysical Journal*, 891(1).

Lamb, J. B., Oey, M. S., Werk, J. K., and Ingleby, L. D. (2010). The Sparsest Clusters with O Stars. *The Astrophysical Journal*, 725(2):1886–1902.

Lamers, H. J. G. L. M., Baumgardt, H., and Gieles, M. (2010). Mass-loss rates and the mass evolution of star clusters. *Monthly Notices of the Royal Astronomical Society*, 409(1):305–328.

Lancaster, L., Ostriker, E. C., Kim, J.-G., and Kim, C.-G. (2021). Star Formation Regulation and Self-pollution by Stellar Wind Feedback. *The Astrophysical Journal, Letters*, 922(1):L3.

Landy, S. D. and Szalay, A. S. (1993). Bias and Variance of Angular Correlation Functions. *The Astrophysical Journal*, 412:64.

Larsen, S. S. (2009). The mass function of young star clusters in spiral galaxies. *Astronomy & Astrophysics*, 494(2):539–551.

Larsen, S. S. and Richtler, T. (2000). Young massive star clusters in nearby spiral galaxies. III. Correlations between cluster populations and host galaxy properties. *Astronomy & Astrophysics*, 354:836–846.

Larson, R. B. (1974). Effects of supernovae on the early evolution of galaxies. *Monthly Notices of the Royal Astronomical Society*, 169:229–246.

Larson, R. B. (1981). Turbulence and star formation in molecular clouds. *Monthly Notices of the Royal Astronomical Society*, 194:809–826.

Larson, R. B. (1998). Early star formation and the evolution of the stellar initial mass function in galaxies. *Monthly Notices of the Royal Astronomical Society*, 301(2):569–581.

Lee, E. J., Miville-Deschênes, M.-A., and Murray, N. W. (2016). Observational Evidence of Dynamic Star Formation Rate in Milky Way Giant Molecular Clouds. *The Astrophysical Journal*, 833(2):229.

Lee, J., Whitmore, B., Thilker, D., Deger, S., Chandar, R., Larson, K., Dale, D., Turner, J., Ubeda, L., Anand, G., Boquien, M., Schinnerer, E., Leroy, A., and Phangs Team (2021). The PHANGS-HST Survey: A Census of Star Clusters and Multi-Scale Stellar Associations in Nearby Spiral Galaxies. In *American Astronomical Society Meeting Abstracts*, volume 53 of *American Astronomical Society Meeting Abstracts*, page 331.04.

Lejeune, T., Cuisinier, F., and Buser, R. (1997). Standard stellar library for evolutionary synthesis. I. Calibration of theoretical spectra. *Astronomy & Astrophysics*, 125:229–246.

Leroy, A. K., Bolatto, A. D., Ostriker, E. C., Walter, F., Gorski, M., Ginsburg, A., Krieger, N., Levy, R. C., Meier, D. S., Mills, E., Ott, J., Rosolowsky, E., Thompson, T. A., Veilleux, S., and Zschaechner, L. K. (2018). Forming Super Star Clusters in the Central Starburst of NGC 253. *The Astrophysical Journal*, 869(2):126.

Leroy, A. K., Hughes, A., Schruba, A., Rosolowsky, E., Blanc, G. A., Bolatto, A. D., Colombo, D., Escala, A., Kramer, C., Kruijssen, J. M. D., Meidt, S., Pety, J., Querejeta, M., Sandstrom, K., Schinnerer, E., Sliwa, K., and Usero, A. (2016). A Portrait of Cold Gas in Galaxies at 60 pc Resolution and a Simple Method to Test Hypotheses That Link Small-scale ISM Structure to Galaxy-scale Processes. *The Astrophysical Journal*, 831(1):16.

Leroy, A. K., Schinnerer, E., Hughes, A., Kruijssen, J. M. D., Meidt, S., Schruba, A., Sun, J., Bigiel, F., Aniano, G., Blanc, G. A., Bolatto, A., Chevance, M., Colombo, D., Gallagher, M., Garcia-Burillo, S., Kramer, C., Querejeta, M., Pety, J., Thompson, T. A., and Usero, A. (2017). Cloud-scale ISM Structure and Star Formation in M51. *The Astrophysical Journal*, 846(1):71.

Leroy, A. K., Walter, F., Brinks, E., Bigiel, F., De Blok, W. J. G., Madore, B., and Thornley, M. D. (2008). The star formaiton efficiency in nearby galaxies: measuring where gas forms stars effectively. *The Astrophysical Journal*, 136:2782–2845.

Li, H., Gnedin, O. Y., and Gnedin, N. Y. (2018). Star Cluster Formation in Cosmological Simulations. II. Effects of Star Formation Efficiency and Stellar Feedback. *The Astrophysical Journal*, 861(2):107.

Li, H., Gnedin, O. Y., Gnedin, N. Y., Meng, X., Semenov, V. A., and Kravtsov, A. V. (2017). Star Cluster Formation in Cosmological Simulations. I. Properties of Young Clusters. *The Astrophysical Journal*, 834(1):69.

Li, H., Vogelsberger, M., Marinacci, F., and Gnedin, O. Y. (2019). Disruption of giant molecular clouds and formation of bound star clusters under the influence of momentum stellar feedback. *Monthly Notices of the Royal Astronomical Society*, 487(2):364–380.

Li, H., Vogelsberger, M., Marinacci, F., Sales, L. V., and Torrey, P. (2020). The effects of subgrid models on the properties of giant molecular clouds in galaxy formation simulations. *Monthly Notices of the Royal Astronomical Society*, 499(4):5862–5872.

Longmore, S. N., Kruijssen, J. M. D., Bastian, N., Bally, J., Rathborne, J., Testi, L., Stolte, A., Dale, J., Bressert, E., and Alves, J. (2014). The Formation and Early Evolution of Young Massive Clusters. In Beuther, H., Klessen, R. S., Dullemond, C. P., and Henning, T., editors, *Protostars Planets VI*, pages 291–314. University of Arizona Press.

Lopez, L. A., Krumholz, M. R., Bolatto, A. D., Prochaska, J. X., and Ramirez-Ruiz, E. (2011). What Drives the Expansion of Giant H II Regions?: A Study of Stellar Feedback in 30 Doradus. *The Astrophysical Journal*, 731(2):91.

Lucy, L. B. (1977). A numerical approach to the testing of the fission hypothesis. *The Astronomical Journal*, 82:1013–1024.

Lynds, C. R. and Sandage, A. R. (1963). Evidence for an Explosion in the Center of the Galaxy M82. *The Astrophysical Journal*, 137:1005.

Ma, X., Grudić, M. Y., Quataert, E., Hopkins, P. F., Faucher-Giguère, C.-A., Boylan-Kolchin, M., Wetzel, A., Kim, J.-h., Murray, N., and Kereš, D. (2020). Self-consistent proto-globular cluster formation in cosmological simulations of high-redshift galaxies. *Monthly Notices of the Royal Astronomical Society*, 493(3):4315–4332.

Mannerkoski, M., Johansson, P. H., Pihajoki, P., Rantala, A., and Naab, T. (2019). Gravitational Waves from the Inspiral of Supermassive Black Holes in Galactic-scale Simulations. *The Astrophysical Journal*, 887(1):35.

Mannerkoski, M., Johansson, P. H., Rantala, A., Naab, T., and Liao, S. (2021). Resolving the Complex Evolution of a Supermassive Black Hole Triplet in a Cosmological Simulation. *The Astrophysical Journal, Letters*, 912(2):L20.

Mannerkoski, M., Johansson, P. H., Rantala, A., Naab, T., Liao, S., and Rawlings, A. (2022). Signatures of the Many Supermassive Black Hole Mergers in a Cosmologically Forming Massive Early-type Galaxy. *The Astrophysical Journal*, 929(2):167.

Maoz, D. and Mannucci, F. (2012). Type-Ia Supernova Rates and the Progenitor Problem: A Review. *Publications of the Astronomical Society of Australia*, 29(4):447–465.

Marinacci, F., Sales, L. V., Vogelsberger, M., Torrey, P., and Springel, V. (2019). Simulating the interstellar medium and stellar feedback on a moving mesh: implementation and isolated galaxies. *Monthly Notices of the Royal Astronomical Society*, 489(3):4233–4260.

Markova, N., Puls, J., Repolust, T., and Markov, H. (2004). Bright OB stars in the Galaxy. I. Mass-loss and wind-momentum rates of O-type stars: A pure Hanalysis accounting for line-blanketing. *Astronomy & Astrophysics*, 413:693–709.

Marks, M., Kroupa, P., Dabringhausen, J., and Pawlowski, M. S. (2012). Evidence for top-heavy stellar initial mass functions with increasing density and decreasing metallicity. *Monthly Notices of the Royal Astronomical Society*, 422(3):2246–2254.

Martin, C. L. (1998). The Impact of Star Formation on the Interstellar Medium in Dwarf Galaxies. II. The Formation of Galactic Winds. *The Astrophysical Journal*, 506(1):222–252.

Massey, P. and Hunter, D. A. (1998). Star Formation in R136: A Cluster of O3 Stars Revealed by Hubble Space Telescope Spectroscopy. *The Astrophysical Journal*, 493(1):180–194.

Mateo, M. L. (1998). Dwarf Galaxies of the Local Group. *Annual Review of Astronomy & Astrophysics*, 36:435–506.

Mathew, S. S. and Federrath, C. (2021). The IMF and multiplicity of stars from gravity, turbulence, magnetic fields, radiation, and outflow feedback. *Monthly Notices of the Royal Astronomical Society*, 507(2):2448–2467.

McConnachie, A. W. (2012). The Observed Properties of Dwarf Galaxies in and around the Local Group. *The Astronomical Journal*, 144(1):4.

McCrady, N. and Graham, J. R. (2007). Super Star Cluster Velocity Dispersions and Virial Masses in the M82 Nuclear Starburst. *The Astrophysical Journal*, 663(2):844–856.

McKee, C. F. and Ostriker, J. P. (1977). A theory of the interstellar medium: three components regulated by supernova explosions in an inhomogeneous substrate. *The Astrophysical Journal*, 218:148–169.

McKee, C. F., Parravano, A., and Hollenbach, D. J. (2015). Stars, Gas, and Dark Matter in the Solar Neighborhood. *The Astrophysical Journal*, 814(1):13.

McQuinn, K. B. W., Skillman, E. D., Dalcanton, J. J., Dolphin, A. E., Cannon, J. M., Holtzman, J., Weisz, D. R., and Williams, B. F. (2012). Observational Constraints on the Molecular Gas Content in Nearby Starburst Dwarf Galaxies. *The Astrophysical Journal*, 751(2):127.

McQuinn, K. B. W., van Zee, L., and Skillman, E. D. (2019). Galactic Winds in Low-mass Galaxies. *The Astrophysical Journal*, 886(1):74.

Meidt, S. E., Glover, S. C. O., Kruijssen, J. M. D., Leroy, A. K., Rosolowsky, E., Hughes, A., Schinnerer, E., Schruba, A., Usero, A., Bigiel, F., Blanc, G., Chevance, M., Pety, J., Querejeta, M., and Utomo, D. (2020). A Model for the Onset of Self-gravitation and Star Formation in Molecular Gas Governed by Galactic Forces. II. The Bottleneck to Collapse Set by Cloud-Environment Decoupling. *The Astrophysical Journal*, 892(2):73.

Meidt, S. E., Schinnerer, E., García-Burillo, S., Hughes, A., Colombo, D., Pety, J., Dobbs, C. L., Schuster, K. F., Kramer, C., Leroy, A. K., Dumas, G., and Thompson, T. A. (2013). Gas Kinematics on Giant Molecular Cloud Scales in M51 with PAWS: Cloud Stabilization through Dynamical Pressure. *The Astrophysical Journal*, 779(1):45.

Melo, V. P., Muñoz-Tuñón, C., Maíz-Apellániz, J., and Tenorio-Tagle, G. (2005). Young Super Star Clusters in the Starburst of M82: The Catalog. *The Astrophysical Journal*, 619(1):270–290.

Mihalas, D. and Binney, J. (1981). *Galactic astronomy. Structure and kinematics*. Freeman.

Monaghan, J. J. (1992). Smoothed particle hydrodynamics. *Annual Review of Astronomy & Astrophysics*, 30:543–574.

Monaghan, J. J. (1997). SPH and Riemann Solvers. *J. Comput. Phys.*, 136:298–307.

Monaghan, J. J. and Lattanzio, J. C. (1985). A refined particle method for astrophysical problems. *Astronomy & Astrophysics*, 149(1):135–143.

Moster, B. P., Naab, T., and White, S. D. M. (2013). Galactic star formation and accretion histories from matching galaxies to dark matter haloes. *Monthly Notices of the Royal Astronomical Society*, 428(4):3121–3138.

Moster, B. P., Somerville, R. S., Maulbetsch, C., van den Bosch, F. C., Macciò, A. V., Naab, T., and Oser, L. (2010). Constraints on the Relationship between Stellar Mass and Halo Mass at Low and High Redshift. *The Astrophysical Journal*, 710(2):903–923.

Muratov, A. L., Kereš, D., Faucher-Giguère, C.-A., Hopkins, P. F., Quataert, E., and Murray, N. (2015). Gusty, gaseous flows of FIRE: galactic winds in cosmological simulations with explicit stellar feedback. *Monthly Notices of the Royal Astronomical Society*, 454(3):2691–2713.

Naab, T. and Ostriker, J. P. (2017). Theoretical Challenges in Galaxy Formation. *Annu. Rev. Astron. Astrophys.*, 55(1):59–109.

Navarro, J. F., Frenk, C. S., and White, S. D. M. (1997). A Universal Density Profile from Hierarchical Clustering. *The Astrophysical Journal*, 490(2):493–508.

Neistein, E., van den Bosch, F. C., and Dekel, A. (2006). Natural downsizing in hierarchical galaxy formation. *Monthly Notices of the Royal Astronomical Society*, 372(2):933–948.

Nelson, R. P. and Langer, W. D. (1997). The dynamics of low-mass molecular clouds in external radiation fields. *The Astrophysical Journal*, 482:796–826.

Nelson, R. P. and Papaloizou, J. C. B. (1994). Variable Smoothing Lengths and Energy Conservation in Smoothed Particle Hydrodynamics. *Monthly Notices of the Royal Astronomical Society*, 270:1.

Neumayer, N., Seth, A., and Böker, T. (2020). Nuclear star clusters. *Astronomy & Astrophysics Reviews*, 28(1):4.

Nordlund, Å. and Padoan, P. (2003). Star Formation and the Initial Mass Function. In Falgarone, E. and Passot, T., editors, *Turbulence and Magnetic Fields in Astrophysics*, volume 614, pages 271–298.

O'Connell, R. W., Gallagher, John S., I., Hunter, D. A., and Colley, W. N. (1995). Hubble Space Telescope Imaging of Super Star Clusters in M82. *The Astrophysical Journal, Letters*, 446:L1.

Ocvirk, P., Gillet, N., Shapiro, P. R., Aubert, D., Iliev, I. T., Teyssier, R., Yepes, G., Choi, J.-H., Sullivan, D., Knebe, A., Gottlöber, S., D'Aloisio, A., Park, H., Hoffman, Y., and Stranex, T. (2016). Cosmic Dawn (CoDa): the First Radiation-Hydrodynamics Simulation of Reionization and Galaxy Formation in the Local Universe. *Monthly Notices of the Royal Astronomical Society*, 463(2):1462–1485.

Oh, S. and Kroupa, P. (2016). Dynamical ejections of massive stars from young star clusters under diverse initial conditions. *Astronomy & Astrophysics*, 590:A107.

Oort, J. H. (1958). Summary - From the Astronomical Point of View. *Ricerche Astronomiche*, 5:507.

O'Shea, B. W., Nagamine, K., Springel, V., Hernquist, L., and Norman, M. L. (2005). Comparing AMR and SPH Cosmological Simulations. I. Dark Matter and Adiabatic Simulations. *The Astrophysical Journal, Supplement*, 160(1):1–27.

O'Shea, B. W., Wise, J. H., Xu, H., and Norman, M. L. (2015). Probing the Ultraviolet Luminosity Function of the Earliest Galaxies with the Renaissance Simulations. *The Astrophysical Journal, Letters*, 807(1):L12.

Padovani, M., Ivlev, A. V., Galli, D., Offner, S. S. R., Indriolo, N., Rodgers-Lee, D., Marcowith, A., Girichidis, P., Bykov, A. M., and Kruijssen, J. M. D. (2020). Impact of Low-Energy Cosmic Rays on Star Formation. *Space Science Reviews*, 216(2):29.

Pais, M., Pfrommer, C., Ehlert, K., and Pakmor, R. (2018). The effect of cosmic ray acceleration on supernova blast wave dynamics. *Monthly Notices of the Royal Astronomical Society*, 478(4):5278–5295.

Pakmor, R., Pfrommer, C., Simpson, C. M., and Springel, V. (2016). Galactic Winds Driven by Isotropic and Anisotropic Cosmic-Ray Diffusion in Disk Galaxies. *The Astrophysical Journal, Letters*, 824(2):L30.

Pakmor, R. and Springel, V. (2013). Simulations of magnetic fields in isolated disc galaxies. *Monthly Notices of the Royal Astronomical Society*, 432(1):176–193.

Pawlik, A. H., Schaye, J., and Dalla Vecchia, C. (2015). Spatially adaptive radiation-hydrodynamical simulations of galaxy formation during cosmological reionization. *Monthly Notices of the Royal Astronomical Society*, 451(2):1586–1605.

Peacock, M. B., Zepf, S. E., and Finzell, T. (2013). Signatures of Multiple Stellar Populations in Unresolved Extragalactic Globular/Young Massive Star Clusters. *The Astrophysical Journal*, 769(2):126.

Peters, T., Naab, T., Walch, S., Glover, S. C. O., Girichidis, P., Pellegrini, E., Klessen, R. S., Wünsch, R., Gatto, A., and Baczynski, C. (2017). The SILCC project-IV. Impact of dissociating and ionizing radiation on the interstellar medium and Hα emission as a tracer of the star formation rate. *Monthly Notices of the Royal Astronomical Society*, 466:3293–3308.

Piotto, G., Villanova, S., Bedin, L. R., Gratton, R., Cassisi, S., Momany, Y., Recio-Blanco, A., Lucatello, S., Anderson, J., King, I. R., Pietrinferni, A., and Carraro, G. (2005). Metallicities on the Double Main Sequence of ω Centauri Imply Large Helium Enhancement. *The Astrophysical Journal*, 621(2):777–784.

Plummer, H. C. (1911). On the problem of distribution in globular star clusters. *Monthly Notices of the Royal Astronomical Society*, 71:460–470.

Pokhrel, R., Gutermuth, R. A., Krumholz, M. R., Federrath, C., Heyer, M., Khullar, S., Thomas Megeath, S., Myers, P. C., Offner, S. S. R., Pipher, J. L., Fischer, W. J., Henning, T., and Hora, J. L. (2021). The Single-cloud Star Formation Relation. *The Astrophysical Journal*, 912(1):L19.

Portegies Zwart, S. F., Mcmillan, S. L. W., and Gieles, M. (2010). Young Massive Star Clusters. *Annu. Rev. Astron. Astrophys*, 48:431–493.

Pouteau, Y., Motte, F., Nony, T., Galván-Madrid, R., Men'shchikov, A., Bontemps, S., Robitaille, J. F., Louvet, F., Ginsburg, A., Herpin, F., López-Sepulcre, A., Dell'Ova, P., Gusdorf, A., Sanhueza, P., Stutz, A. M., Brouillet, N., Thomasson, B., Armante, M., Baug, T., Bonfand, M., Busquet, G., Csengeri, T., Cunningham, N., Fernández-López, M., Liu, H. L., Olguin, F., Towner, A. P. M., Bally, J., Braine, J., Bronfman, L., Joncour, I., González, M., Hennebelle, P., Lu, X., Menten, K. M., Moraux, E., Tatematsu, K., Walker, D., and Whitworth, A. P. (2022). ALMA-IMF. III. Investigating the origin of stellar masses: top-heavy core mass function in the W43-MM2&MM3 mini-starburst. *Astronomy & Astrophysics*, 664:A26.

Poveda, A., Ruiz, J., and Allen, C. (1967). Run-away Stars as the Result of the Gravitational Collapse of Proto-stellar Clusters. *Boletin de los Observatorios Tonantzintla y Tacubaya*, 4:86–90.

Power, C. and Knebe, A. (2006). The impact of box size on the properties of dark matter haloes in cosmological simulations. *Monthly Notices of the Royal Astronomical Society*, 370(2):691–701.

Ramírez-Tannus, M. C., Backs, F., de Koter, A., Sana, H., Beuther, H., Bik, A., Brandner, W., Kaper, L., Linz, H., Henning, T., and Poorta, J. (2021). A relation between the radial velocity dispersion of young clusters and their age. Evidence for hardening as the formation scenario of massive close binaries. *Astronomy & Astrophysics*, 645:L10.

Rantala, A., Johansson, P. H., Naab, T., Thomas, J., and Frigo, M. (2019). The Simultaneous Formation of Cored, Tangentially Biased, and Kinematically Decoupled Centers in Massive Early-type Galaxies. *The Astrophysical Journal, Letters*, 872(2):L17.

Rantala, A., Naab, T., and Springel, V. (2021). frost: a momentum-conserving CUDA implementation of a hierarchical fourth-order forward symplectic integrator. *Monthly Notices of the Royal Astronomical Society*, 502(4):5546–5562.

Rantala, A., Pihajoki, P., Johansson, P. H., Naab, T., Lahén, N., and Sawala, T. (2017). Post-Newtonian Dynamical Modeling of Supermassive Black Holes in Galactic-scale Simulations. *The Astrophysical Journal*, 840(1):53.

Rathjen, T.-E., Naab, T., Girichidis, P., Walch, S., Wünsch, R., Dinnbier, F., Seifried, D., Klessen, R. S., and Glover, S. C. O. (2021). SILCC VI - Multiphase ISM structure, stellar clustering, and outflows with supernovae, stellar winds, ionizing radiation, and cosmic rays. *Monthly Notices of the Royal Astronomical Society*, 504(1):1039–1061.

Read, J. I., Hayfield, T., and Agertz, O. (2010). Resolving mixing in smoothed particle hydrodynamics. *Monthly Notices of the Royal Astronomical Society*, 405:1513–1530.

Reina-Campos, M., Keller, B. W., Kruijssen, J. M. D., Gensior, J., Trujillo-Gomez, S., Jeffreson, S. M. R., Pfeffer, J. L., and Sills, A. (2022). Introducing EMP-Pathfinder: modelling the simultaneous formation and evolution of stellar clusters in their host galaxies. *arXiv e-prints*, page arXiv:2202.06961.

Reines, A. E., Greene, J. E., and Geha, M. (2013). Dwarf Galaxies with Optical Signatures of Active Massive Black Holes. *The Astrophysical Journal*, 775(2):116.

Renaud, F., Bournaud, F., and Duc, P.-A. (2015). A parsec-resolution simulation of the Antennae galaxies: formation of star clusters during the merger. *Monthly Notices of the Royal Astronomical Society*, 446(2):2038–2054.

Rhode, K. L., Salzer, J. J., Westpfahl, D. J., and Radice, L. A. (1999). A Test of the Standard Hypothesis for the Origin of the H I Holes in Holmberg II. *The Astronomical Journal*, 118(1):323–336.

Richings, A. J., Faucher-Giguere, C.-A., Gurvich, A. B., Schaye, J., and Hayward, C. C. (2022). The effects of local stellar radiation and dust depletion on non-equilibrium interstellar chemistry. *arXiv e-prints*, page arXiv:2208.02288.

Richings, A. J., Schaye, J., and Oppenheimer, B. D. (2014a). Non-equilibrium chemistry and cooling in the diffuse interstellar medium - I. Optically thin regime. *Monthly Notices of the Royal Astronomical Society*, 440(4):3349–3369.

Richings, A. J., Schaye, J., and Oppenheimer, B. D. (2014b). Non-equilibrium chemistry and cooling in the diffuse interstellar medium - II. Shielded gas. *Monthly Notices of the Royal Astronomical Society*, 442(3):2780–2796.

Rosdahl, J., Schaye, J., Teyssier, R., and Agertz, O. (2015). Galaxies that shine: radiation-hydrodynamical simulations of disc galaxies. *Monthly Notices of the Royal Astronomical Society*, 451(1):34–58.

Rosen, A. L., Offner, S. S. R., Foley, M. M., and Lopez, L. A. (2021). Blowing Bubbles around Intermediate-Mass Stars: Feedback from Main-Sequence Winds is not Enough. *arXiv e-prints*, page arXiv:2107.12397.

Roškar, R., Teyssier, R., Agertz, O., Wetzstein, M., and Moore, B. (2014). A systematic look at the effects of radiative feedback on disc galaxy formation. *Monthly Notices of the Royal Astronomical Society*, 444(3):2837–2853.

Rubio, M., Elmegreen, B. G., Hunter, D. A., Brinks, E., Cortés, J. R., and Cigan, P. (2015). Dense cloud cores revealed by CO in the low metallicity dwarf galaxy WLM. *Nature*, 525(7568):218–221.

Ryon, J. E., Bastian, N., Adamo, A., Konstantopoulos, I. S., Gallagher, J. S., Larsen, S., Hollyhead, K., Silva-Villa, E., and Smith, L. J. (2015). Sizes and shapes of young star cluster light profiles in M83. *Monthly Notices of the Royal Astronomical Society*, 452(1):525–539.

Ryon, J. E., Gallagher, J. S., Smith, L. J., Adamo, A., Calzetti, D., Bright, S. N., Cignoni, M., Cook, D. O., Dale, D. A., Elmegreen, B. E., Fumagalli, M., Gouliermis, D. A., Grasha, K., Grebel, E. K., Kim, H., Messa, M., Thilker, D., and Ubeda, L. (2017). Effective Radii of Young, Massive Star Clusters in Two LEGUS Galaxies. *The Astrophysical Journal*, 841(2):92.

Saitoh, T. R. and Makino, J. (2009). A necessary condition for individual time steps in SPH simulations. *The Astrophysical Journal*, 697:99–102.

Saitoh, T. R. and Makino, J. (2013). A Density-independent Formulation of Smoothed Particle Hydrodynamics. *The Astrophysical Journal*, 768(1):44.

Sales, L. V., Marinacci, F., Springel, V., and Petkova, M. (2014). Stellar feedback by radiation pressure and photoionization. *Monthly Notices of the Royal Astronomical Society*, 439(3):2990–3006.

Salpeter, E. E. (1955). The Luminosity Function and Stellar Evolution. *The Astrophysical Journal*, 121:161.

Schaye, J., Crain, R. A., Bower, R. G., Furlong, M., Schaller, M., Theuns, T., Dalla Vecchia, C., Frenk, C. S., McCarthy, I. G., Helly, J. C., Jenkins, A., Rosas-Guevara, Y. M., White, S. D. M., Baes, M., Booth, C. M., Camps, P., Navarro, J. F., Qu, Y., Rahmati, A., Sawala, T., Thomas, P. A., and Trayford, J. (2015). The EAGLE project: simulating the evolution and assembly of galaxies and their environments. *Monthly Notices of the Royal Astronomical Society*, 446(1):521–554.

Schaye, J. and Dalla Vecchia, C. (2008). On the relation between the Schmidt and Kennicutt-Schmidt star formation laws and its implications for numerical simulations. *Monthly Notices of the Royal Astronomical Society*, 383(3):1210–1222.

Schinnerer, E., Hughes, A., Leroy, A., Groves, B., Blanc, G. A., Kreckel, K., Bigiel, F., Chevance, M., Dale, D., Emsellem, E., Faesi, C., Glover, S., Grasha, K., Henshaw, J., Hygate, A., Kruijssen, J. M. D., Meidt, S., Pety, J., Querejeta, M., Rosolowsky, E., Saito, T., Schruba, A., Sun, J., and Utomo, D. (2019). The Gas-Star Formation Cycle in Nearby Star-forming Galaxies. I. Assessment of Multi-scale Variations. *The Astrophysical Journal*, 887(1):49.

Schmidt, M. (1959). The Rate of Star Formation. *The Astrophysical Journal*, 129:243.

Schruba, A., Leroy, A. K., Kruijssen, J. M. D., Bigiel, F., Bolatto, A. D., de Blok, W. J. G., Tacconi, L., van Dishoeck, E. F., and Walter, F. (2017). Physical Properties of Molecular Clouds at 2 pc Resolution in the Low-metallicity Dwarf Galaxy NGC 6822 and the Milky Way. *The Astrophysical Journal*, 835(2):278.

Schruba, A., Leroy, A. K., Walter, F., Bigiel, F., Brinks, E., de Blok, W. J. G., Kramer, C., Rosolowsky, E., Sandstrom, K., Schuster, K., Usero, A., Weiss, A., and Wiesemeyer, H. (2012). Low CO Luminosities in Dwarf Galaxies. *The Astronomical Journal*, 143(6):138.

Semenov, V. A., Kravtsov, A. V., and Gnedin, N. Y. (2018). How Galaxies Form Stars: The Connection between Local and Global Star Formation in Galaxy Simulations. *The Astrophysical Journal*, 861(1):4.

Semenov, V. A., Kravtsov, A. V., and Gnedin, N. Y. (2021). Spatial Decorrelation of Young Stars and Dense Gas as a Probe of the Star Formation-Feedback Cycle in Galaxies. *The Astrophysical Journal*, 918(1):13.

Shen, S., Madau, P., Conroy, C., Governato, F., and Mayer, L. (2014). The Baryon Cycle of Dwarf Galaxies: Dark, Bursty, Gas-rich Polluters. *The Astrophysical Journal*, 792(2):99.

Silk, J. (2017). Feedback by Massive Black Holes in Gas-rich Dwarf Galaxies. *The Astrophysical Journal, Letters*, 839(1):L13.

Silva-Villa, E. and Larsen, S. S. (2011). The star cluster-field star connection in nearby spiral galaxies II. Field star and cluster formation histories and their relation. *Astronomy & Astrophysics*, 529:25.

Simpson, C. M., Pakmor, R., Marinacci, F., Pfrommer, C., Springel, V., Glover, S. C. O., Clark, P. C., and Smith, R. J. (2016). The Role of Cosmic-Ray Pressure in Accelerating Galactic Outflows. *The Astrophysical Journal, Letters*, 827(2):L29.

Simpson, C. M., Pakmor, R., Pfrommer, C., Glover, S. C. O., and Smith, R. (2022). How Cosmic Rays Mediate the Evolution of the Interstellar Medium. *arXiv e-prints*, page arXiv:2204.02410.

Smith, M. C., Bryan, G. L., Somerville, R. S., Hu, C.-Y., Teyssier, R., Burkhart, B., and Hernquist, L. (2021). Efficient early stellar feedback can suppress galactic outflows by reducing supernova clustering. *Monthly Notices of the Royal Astronomical Society*, 506(3):3882–3915.

Snaith, O., Haywood, M., Di Matteo, P., Lehnert, M. D., Combes, F., Katz, D., and Gómez, A. (2015). Reconstructing the star formation history of the Milky Way disc(s) from chemical abundances. *Astronomy & Astrophysics*, 578:A87.

Solomon, P. M., Rivolo, A. R., Barrett, J., and Yahil, A. (1987). Mass, Luminosity, and Line Width Relations of Galactic Molecular Clouds. *The Astrophysical Journal*, 319:730.

Somerville, R. S. and Davé, R. (2015). Physical Models of Galaxy Formation in a Cosmological Framework. *Annual Review of Astronomy & Astrophysics*, 53:51–113.

Spitzer, L. (1998). *Physical processes in the interstellar medium*. Wiley.

Springel, V. (2005). The cosmological simulation code GADGET-2. *Monthly Notices of the Royal Astronomical Society*, 364:1105–1134.

Springel, V. (2010). E pur si muove: Galilean-invariant cosmological hydrodynamical simulations on a moving mesh. *Monthly Notices of the Royal Astronomical Society*, 401(2):791–851.

Springel, V., Di Matteo, T., and Hernquist, L. (2005). Modelling feedback from stars and black holes in galaxy mergers. *Monthly Notices of the Royal Astronomical Society*, 361(3):776–794.

Springel, V. and Hernquist, L. (2002). Cosmological smoothed particle hydrodynamics simulations: the entropy equation. *Monthly Notices of the Royal Astronomical Society*, 333(3):649–664.

Springel, V. and Hernquist, L. (2003). Cosmological smoothed particle hydrodynamics simulations: a hybrid multiphase model for star formation. *Monthly Notices of the Royal Astronomical Society*, 339(2):289–311.

Springel, V., Pakmor, R., Pillepich, A., Weinberger, R., Nelson, D., Hernquist, L., Vogelsberger, M., Genel, S., Torrey, P., Marinacci, F., and Naiman, J. (2018). First results from the IllustrisTNG simulations: matter and galaxy clustering. *Monthly Notices of the Royal Astronomical Society*, 475(1):676–698.

Springel, V., Yoshida, N., and White, S. D. M. (2001). GADGET: a code for collisionless and gasdynamical cosmological simulations. *New Astronomy*, 6(2):79–117.

Stasińska, G. (1990). A grid of model HII regions for extragalactic studies. *Astronomy & Astrophysics, Supplement*, 83:501.

Steinwandel, U. P., Bryan, G. L., Somerville, R. S., Hayward, C. C., and Burkhart, B. (2022a). On the impact of runaway stars on dwarf galaxies with resolved interstellar medium. *arXiv e-prints*, page arXiv:2205.09774.

Steinwandel, U. P., Dolag, K., Lesch, H., and Burkert, A. (2022b). Driving Galactic Outflows with Magnetic Fields at Low and High Redshift. *The Astrophysical Journal*, 924(1):26.

Steinwandel, U. P., Dolag, K., Lesch, H., Moster, B. P., Burkert, A., and Prieto, A. (2020). On the origin of magnetic driven winds and the structure of the galactic dynamo in isolated galaxies. *Monthly Notices of the Royal Astronomical Society*, 494(3):4393–4412.

Steinwandel, U. P., Moster, B. P., Naab, T., Hu, C.-Y., and Walch, S. (2020). Hot phase generation by supernovae in ISM simulations: resolution, chemistry, and thermal conduction. *Monthly Notices of the Royal Astronomical Society*, 495:1035–1060.

Stinson, G. S., Brook, C., Macciò, A. V., Wadsley, J., Quinn, T. R., and Couchman, H. M. P. (2013). Making Galaxies In a Cosmological Context: the need for early stellar feedback. *Monthly Notices of the Royal Astronomical Society*, 428(1):129–140.

Strömgren, B. (1939). The Physical State of Interstellar Hydrogen. *The Astrophysical Journal*, 89:526.

Sun, J., Leroy, A. K., Schinnerer, E., Hughes, A., Rosolowsky, E., Querejeta, M., Schruba, A., Liu, D., Saito, T., Herrera, C. N., Faesi, C., Usero, A., Pety, J., Kruijssen, J. M. D., Ostriker, E. C., Bigiel, F., Blanc, G. A., Bolatto, A. D., Boquien, M., Chevance, M., Dale, D. A., Deger, S., Emsellem, E., Glover, S. C. O., Grasha, K., Groves, B., Henshaw, J., Jimenez-Donaire, M. J., Kim, J. J., Klessen, R. S., Kreckel, K., Lee, J. C., Meidt, S., Sandstrom, K., Sardone, A. E., Utomo, D., and Williams, T. G. (2020). Molecular Gas Properties on Cloud Scales across the Local Star-forming Galaxy Population. *The Astrophysical Journal, Letters*, 901(1):L8.

Sun, J., Leroy, A. K., Schruba, A., Rosolowsky, E., Hughes, A., Kruijssen, J. M. D., Meidt, S., Schinnerer, E., Blanc, G. A., Bigiel, F., Bolatto, A. D., Chevance, M., Groves, B., Herrera, C. N., Hygate, A. P. S., Pety, J., Querejeta, M., Usero, A., and Utomo, D. (2018). Cloud-scale Molecular Gas Properties in 15 Nearby Galaxies. *The Astrophysical Journal*, 860(2):172.

Tacconi, L. J., Genzel, R., and Sternberg, A. (2020). The Evolution of the Star-Forming Interstellar Medium Across Cosmic Time. *Annual Review of Astronomy & Astrophysics*, 58:157–203.

Tacconi, L. J., Neri, R., Genzel, R., Combes, F., Bolatto, A., Cooper, M. C., Wuyts, S., Bournaud, F., Burkert, A., Comerford, J., Cox, P., Davis, M., Förster Schreiber, N. M., García-Burillo, S., Gracia-Carpio, J., Lutz, D., Naab, T., Newman, S., Omont, A., Saintonge, A., Shapiro Griffin, K., Shapley, A., Sternberg, A., and Weiner, B. (2013). Phibss: Molecular gas content and scaling relations in z $\sim$ 1-3 massive, main-sequence star-forming galaxies. *The Astrophysical Journal*, 768(1):74.

Takahashi, K. and Portegies Zwart, S. F. (2000). The Evolution of Globular Clusters in the Galaxy. *The Astrophysical Journal*, 535(2):759–775.

Teyssier, R. (2002). Cosmological hydrodynamics with adaptive mesh refinement. A new high resolution code called RAMSES. *Astronomy & Astrophysics*, 385:337–364.

Thompson, C. (2000). Accretional Heating of Asymmetric Supernova Cores. *The Astrophysical Journal*, 534(2):915–933.

Tremonti, C. A., Heckman, T. M., Kauffmann, G., Brinchmann, J., Charlot, S., White, S. D. M., Seibert, M., Peng, E. W., Schlegel, D. J., Uomoto, A., Fukugita, M., and Brinkmann, J. (2004). The Origin of the Mass-Metallicity Relation: Insights from 53,000 Star-forming Galaxies in the Sloan Digital Sky Survey. *The Astrophysical Journal*, 613(2):898–913.

Trumpler, R. J. (1930). Preliminary results on the distances, dimensions and space distribution of open star clusters. *Lick Observatory Bulletin*, 420:154–188.

Tutukov, A. V. (1978). Early Stages of Dynamical Evolution of Star Cluster Models. *Astronomy & Astrophysics*, 70:57.

Uhlig, M., Pfrommer, C., Sharma, M., Nath, B. B., Enßlin, T. A., and Springel, V. (2012). Galactic winds driven by cosmic ray streaming. *Monthly Notices of the Royal Astronomical Society*, 423(3):2374–2396.

van den Bergh, S. (1971). The Post-Eruptive Galaxy M 82. *Astronomy & Astrophysics*, 12:474.

van den Bergh, S. (2006). Diameters of Open Star Clusters. *The Astronomical Journal*, 131(3):1559–1564.

Vansevičius, V., Kodaira, K., Narbutis, D., Stonkutė, R., Bridžius, A., Deveikis, V., and Semionov, D. (2009). Compact Star Clusters in the M31 Disk. *The Astrophysical Journal*, 703(2):1872–1883.

Vázquez-Semadeni, E., Colín, P., Gómez, G. C., Ballesteros-Paredes, J., and Watson, A. W. (2010). Molecular Cloud Evolution. III. Accretion Versus Stellar Feedback. *The Astrophysical Journal*, 715(2):1302–1317.

Veilleux, S., Cecil, G., and Bland-Hawthorn, J. (2005). Galactic Winds. *Annual Review of Astronomy & Astrophysics*, 43(1):769–826.

Veilleux, S., Maiolino, R., Bolatto, A. D., and Aalto, S. (2020). Cool outflows in galaxies and their implications. *Astronomy & Astrophysics Reviews*, 28(1):2.

Villanova, S., Piotto, G., King, I. R., Anderson, J., Bedin, L. R., Gratton, R. G., Cassisi, S., Momany, Y., Bellini, A., Cool, A. M., Recio-Blanco, A., and Renzini, A. (2007). The Multiplicity of the Subgiant Branch of ω Centauri: Evidence for Prolonged Star Formation. *The Astrophysical Journal*, 663(1):296–314.

Vogelsberger, M., Genel, S., Springel, V., Torrey, P., Sijacki, D., Xu, D., Snyder, G., Bird, S., Nelson, D., and Hernquist, L. (2014). Properties of galaxies reproduced by a hydrodynamic simulation. *Nature*, 509(7499):177–182.

Vogelsberger, M., Marinacci, F., Torrey, P., and Puchwein, E. (2020). Cosmological simulations of galaxy formation. *Nature Reviews Physics*, 2(1):42–66.

Vutisalchavakul, N., Evans, Neal J., I., and Heyer, M. (2016). Star Formation Relations in the Milky Way. *The Astrophysical Journal*, 831(1):73.

Walch, S., Girichidis, P., Naab, T., Gatto, A., Glover, S. C. O., Wünsch, R., Klessen, R. S., Clark, P. C., Peters, T., Derigs, D., and Baczynski, C. (2015). The SILCC (SImulating the LifeCycle of molecular Clouds) project-I. Chemical evolution of the supernova-driven ISM. *Monthly Notices of the Royal Astronomical Society*, 454:238–268.

Walch, S. and Naab, T. (2015). The energy and momentum input of supernova explosions in structured and ionized molecular clouds. *Monthly Notices of the Royal Astronomical Society*, 451(3):2757–2771.

Walch, S., Whitworth, A. P., Bisbas, T. G., Hubber, D. A., and Wünsch, R. (2015). Comparing simulations of ionization triggered star formation and observations in RCW 120. *Monthly Notices of the Royal Astronomical Society*, 452(3):2794–2803.

Walch, S. K., Whitworth, A. P., Bisbas, T., Wünsch, R., and Hubber, D. (2012). Dispersal of molecular clouds by ionizing radiation. *Monthly Notices of the Royal Astronomical Society*, 427(1):625–636.

Weigelt, G. and Baier, G. (1985). R 136a in the 30 Doradus nebula resolved by holographic speckle interferometry. *Astronomy & Astrophysics*, 150:L18–L20.

Weisz, D. R., Dalcanton, J. J., Williams, B. F., Gilbert, K. M., Skillman, E. D., Seth, A. C., Dolphin, A. E., McQuinn, K. B. W., Gogarten, S. M., Holtzman, J., Rosema, K., Cole, A., Karachentsev, I. D., and Zaritsky, D. (2011). The ACS Nearby Galaxy Survey Treasury. VIII. The Global Star Formation Histories of 60 Dwarf Galaxies in the Local Volume. *The Astrophysical Journal*, 739(1):5.

Wendland, H. (1995). Piecewise polynomial, positive definite and compactly supported radial functions of minimal degree. *Advances in computational Mathematics*, 4(1):389–396.

Westera, P., Lejeune, T., Buser, R., Cuisinier, F., and Bruzual, G. (2002). A standard stellar library for evolutionary synthesis. III. Metallicity calibration. *Astronomy & Astrophysics*, 381:524–538.

Whitmore, B. C. (2003). The formation of star clusters. In Livio, M., Noll, K., and Stiavelli, M., editors, *A Decade of Hubble Space Telescope Science*, volume 14, pages 153–178.

Whitmore, B. C. and Schweizer, F. (1995). Hubble Space Telescope Observations of Young Star Clusters in NGC 4038/4039, "The Antennae" Galaxies. *The Astronomical Journal*, 109:960.

Whitmore, B. C., Zhang, Q., Leitherer, C., Fall, S. M., Schweizer, F., and Miller, B. W. (1999). The Luminosity Function of Young Star Clusters in "the Antennae" Galaxies (NGC 4038-4039). *The Astronomical Journal*, 118(4):1551–1576.

Wielen, R. (1971). The Age Distribution and Total Lifetimes of Galactic Clusters. *Astronomy & Astrophysics*, 13:309–322.

Wiersma, R. P. C., Schaye, J., and Smith, B. D. (2009). The effect of photoionization on the cooling rates of enriched, astrophysical plasmas. *Monthly Notices of the Royal Astronomical Society*, 393:99–107.

Williams, B. A., Walker, D. L., Longmore, S. N., Barnes, A. T., Battersby, C., Garay, G., Ginsburg, A., Gomez, L., Henshaw, J. D., Ho, L. C., Kruijssen, J. M. D., Lu, X., Mills, E. A. C., Petkova, M. A., and Zhang, Q. (2022). The initial conditions for young massive cluster formation in the Galactic Centre: convergence of large-scale gas flows. *Monthly Notices of the Royal Astronomical Society*, 514(1):578–595.

Williams, J. P., Blitz, L., and McKee, C. F. (2000). The Structure and Evolution of Molecular Clouds: from Clumps to Cores to the IMF. In Mannings, V., Boss, A. P., and Russell, S. S., editors, *Protostars and Planets IV*, page 97.

Williams, J. P. and McKee, C. F. (1997). The Galactic Distribution of OB Associations in Molecular Clouds. *The Astrophysical Journal*, 476(1):166–183.

Wise, J. H., Abel, T., Turk, M. J., Norman, M. L., and Smith, B. D. (2012). The birth of a galaxy - II. The role of radiation pressure. *Monthly Notices of the Royal Astronomical Society*, 427(1):311–326.

Wolfire, M. G., McKee, C. F., Hollenbach, D., and Tielens, A. G. G. M. (2003). Neutral Atomic Phases of the Interstellar Medium in the Galaxy. *The Astrophysical Journal*, 587(1):278–311.

Wood, P. R., Olivier, E. A., and Kawaler, S. D. (2004). Long Secondary Periods in Pulsating Asymptotic Giant Branch Stars: An Investigation of their Origin. *The Astrophysical Journal*, 604(2):800–816.

Wu, J., Evans, Neal J., I., Shirley, Y. L., and Knez, C. (2010). The Properties of Massive, Dense Clumps: Mapping Surveys of HCN and CS. *The Astrophysical Journal, Supplement*, 188(2):313–357.

Zhang, Q. and Fall, S. M. (1999). The Mass Function of Young Star Clusters in the “Antennae” Galaxies. *The Astrophysical Journal, Letters*, 527(2):L81–L84.

Zuckerman, B. and Palmer, P. (1974). Radio radiation from interstellar molecules. *Annual Review of Astronomy & Astrophysics*, 12:279–313.

"You're an interesting species. An interesting mix. You're capable of such beautiful dreams, and such horrible nightmares. You feel so lost, so cut off, so alone, only you're not. See, in all our searching, the only thing we've found that makes the emptiness bearable, is each other."

Alien, talking about humans - Contact (1997)

Acknowledgements

A substantial part of this thesis work was completed during the COVID-19 pandemic. I am sincerely grateful to all of the key workers who kept the world going and risked their lives doing so whilst I worked from the safety of my home.

I would like to thank my supervisor, Thorsten Naab, for your advice and support. Your expertise and knowledge has been invaluable and I'm grateful for your guidance throughout this thesis, both scientifically and otherwise.

I must also acknowledge my undergraduate and masters supervisor, Peter Thomas, for starting me off on this journey. You always expected a lot from me, and it really made me believe in myself and strive to be better. You taught me so much that I have carried through with me during my PhD and I'm eternally grateful.

Scientifically, there are several people I would like to thank for shaping and contributing to the ideas and results here. Thank you to Dimitrios, Rebekka, Christian and Thorsten for reading and providing comments on significant parts of this thesis, and to Jakob and Christian for help with translating the abstract. I'm grateful also to all of the people with whom I've managed to have scientific discussions with, either at conferences, summer schools or visits who have influenced this work and kept me excited about science: Eric Andersson, Greg Bryan, Thales Gutcke, Sarah Jeffreson, Peter Johansson, Ben Keller, Sophie Koudmani, Hui Li, Matt Orr, Vadim Semenov, Matthew Smith and Steffi Walch.

Moving on from science, on a personal level, there are so many people I have to credit for getting me through this PhD. Thank you to my group, both old and current. Thank you to Rob Yates for being the greatest friend and support when I moved to Germany and for the hours and hours of chats and table tennis. To Constantina & Eirini for being wonderful friends. Thank you to Ulli for so much help throughout my PhD and helping me to navigate the joys of Gadget and academic life. I have been lucky enough to have some incredible role models, noteably Francesca and Rebekka - I cannot thank you both enough for being such incredible friends. And to everyone I interacted with at MPA - the environment is something I will miss so much. Thank you to everyone for making it such a wonderful place to spend the past 4 years.

The last year or so of my PhD was made somewhat bearable by the best group of coffee, beer and cocktail guzzling friends I could have wished for. Those little breaks really kept me going. Special thanks must go to Daniela, Adam, Miha, Aniket & Christian for a lot of science chats, support and laughs, and for keeping me sane(ish) during the final thesis writing stages. Words cannot express how much I will miss seeing you all everyday.

Thank you to all of my U.K. friends. To SOT, for more than 20 years of friendship. Thank you for celebrating every single one of my small successes, for all of the FaceTimes, and for just being there for me even when I was far away.

Mum & Dad, Gela, Rossy Boy, and all of my family - thank you for believing in me and for being such a solid support system when I needed you.

Finally, I would like to thank my colleague, best friend and partner, Mitsos. Thank you for embarking on a long-distance relationship with me, for sticking with me through all the good and bad times. I'm so proud of us for surviving it and I'm so excited for our future. Thank you for supporting me and empowering me through the times I didn't think I could finish this PhD. I couldn't have done it without you.